ARISTOTLE UNIVERSITY OF THESSALONIKI
FACULTY OF SCIENCES
SCHOOL OF GEOLOGY

PETROS NEOFOTISTOS
MSc Geologist

GEOLOGY AND DEFORMATION OF THE NORTHERN PART OF THE ATHOS PENINSULA, NORTHERN GREECE

DISSERTATION THESIS

THESSALONIKI
2020

ΑΡΙΣΤΟΤΕΛΕΙΟ ΠΑΝΕΠΙΣΤΗΜΙΟ ΘΕΣΣΑΛΟΝΙΚΗΣ
ΣΧΟΛΗ ΘΕΤΙΚΩΝ ΕΠΙΣΤΗΜΩΝ
ΤΜΗΜΑ ΓΕΩΛΟΓΙΑΣ

ΠΕΤΡΟΣ ΝΕΟΦΩΤΙΣΤΟΣ
MSc Γεωλόγος

ΓΕΩΛΟΓΙΑ ΚΑΙ ΠΑΡΑΜΟΡΦΩΣΗ ΤΟΥ ΒΟΡΕΙΟΥ ΤΜΗΜΑΤΟΣ ΤΗΣ ΧΕΡΣΟΝΗΣΟΥ ΤΟΥ ΑΓΙΟΥ ΟΡΟΥΣ, ΒΟΡΕΙΑ ΕΛΛΑΔΑ

ΔΙΔΑΚΤΟΡΙΚΗ ΔΙΑΤΡΙΒΗ

ΘΕΣΣΑΛΟΝΙΚΗ
2020

PETROS NEOFOTISTOS
MSc Geologist

GEOLOGY AND DEFORMATION OF THE NORTHERN PART OF THE ATHOS PENINSULA, NORTHERN GREECE

It was carried out at the Geology Department of the School of Geology A.U.TH.
It was submitted at the School of Geology A.U.TH. in March 2020.

Date of Dissertation Defense: 22/04/2020

Annex number of the Scientific Annals of School of Geology N°: 205

Advisory Committee

Professor Tranos Markos, Supervisor
Emer. Professor Pavlides Spyridon, Member of the Advisory Committee
Emer. Professor Heilbronner Renée, Member of the Advisory Committee

Examination Committee

Assoc. Professor, Tranos Markos
Emer. Professor, Pavlides Spyridon
Emer. Professor, Heilbronner Renée
Assoc. Professor, Lozios Stylianos
Assoc. Professor, Kokkalas Sotirios
Assoc. Professor, Xypolias Paraskevas
Assoc. Professor, Markos Athanasas Konstantinos

Citation:
Neofotistos P. G., 2020. – Geology and deformation of the Northern part of the Athos Peninsula, Northern Greece. Ph.D. Thesis, School of Geology, Aristotle University of Thessaloniki, Annex Number of Scientific Annals of the School of Geology No 205, 244 pp.
Νεοφώτιστος Π. Γ., 2020. – Γεωλογία και παραμόρφωση του βορείου τμήματος της Χερσονήσου του Αγίου Όρους, Βόρεια Ελλάδα. Διδακτορική Διατριβή, Τμήμα Γεωλογίας Α.Π.Θ., Αριθμός Παραρτήματος Επιστημονικής Επετηρίδας Τμ. Γεωλογίας Νο 205, 244 σελ.

Contents

Chapter 1. Introduction

1.1. Introduction

The Hellenic Hinterland is located between the Carpatho-Balkan and Dinaric-Hellenic mountain belts (Fig. 1.1a) both being part of the Alpine orogen and resulting from the convergence-related processes between the Eurasian plate and Gondwana-derived continental blocks (e.g., Dercourt et al., 1993; Stampfli and Borel, 2002), during Mesozoic and Cenozoic times. It comprises of crystalline rocks that were initially attributed Precambrian age and were considered to build up an already consolidated, stable part of crust, unaffected by the Alpine orogenic processes (Kober, 1928; Dimitrievic, 1966, 1974). In Greece, these rocks have been grouped in the Rhodope massif, and the Serbo-Macedonian massif, covering the area from its western margin, located east of the Axios zone in Central Macedonia as far to the east as the Thrace basin (Fig. 1.1b). These crystalline massifs occupy large regions in Bulgaria, as well. However later studies indicated that the Hellenic Hinterland has undergone significant reworking and metamorphism due to Alpine orogeny (e.g. Ivanov, 1988; Burg et al., 1990, 1996; Kilias et al., 1999; Brun and Sokoutis, 2007). As a result, nowadays it is considered rather as a complex pile of Mesozoic, syn-metamophic nappes stacked in an active Alpine margin, and later on during Tertiary, this pile was subjected to extension causing the exhumation of high-grade metamorphic rocks and the formation of several metamorphic core complexes (Dinter and Royden, 1993; Sokoutis et al., 1993; Brun and Sokoutis, 2007). The most interesting, however, issue, is that this re-assessment is accompanied by the difficulty to correctly assign the multi-deformed and multi-metamorphosed rocks to specific geological (map) units, and, because of this fact, different re-assignments of main geological contacts and boundaries and diverse structural interpretations have been proposed (Burg et al., 1995; 1996; 2012; Kilias et al., 1999; Brun and Sokoutis, 2007; Himmerkus et al., 2011, Plougarlis and Tranos, 2014; Kydonakis et al., 2015).

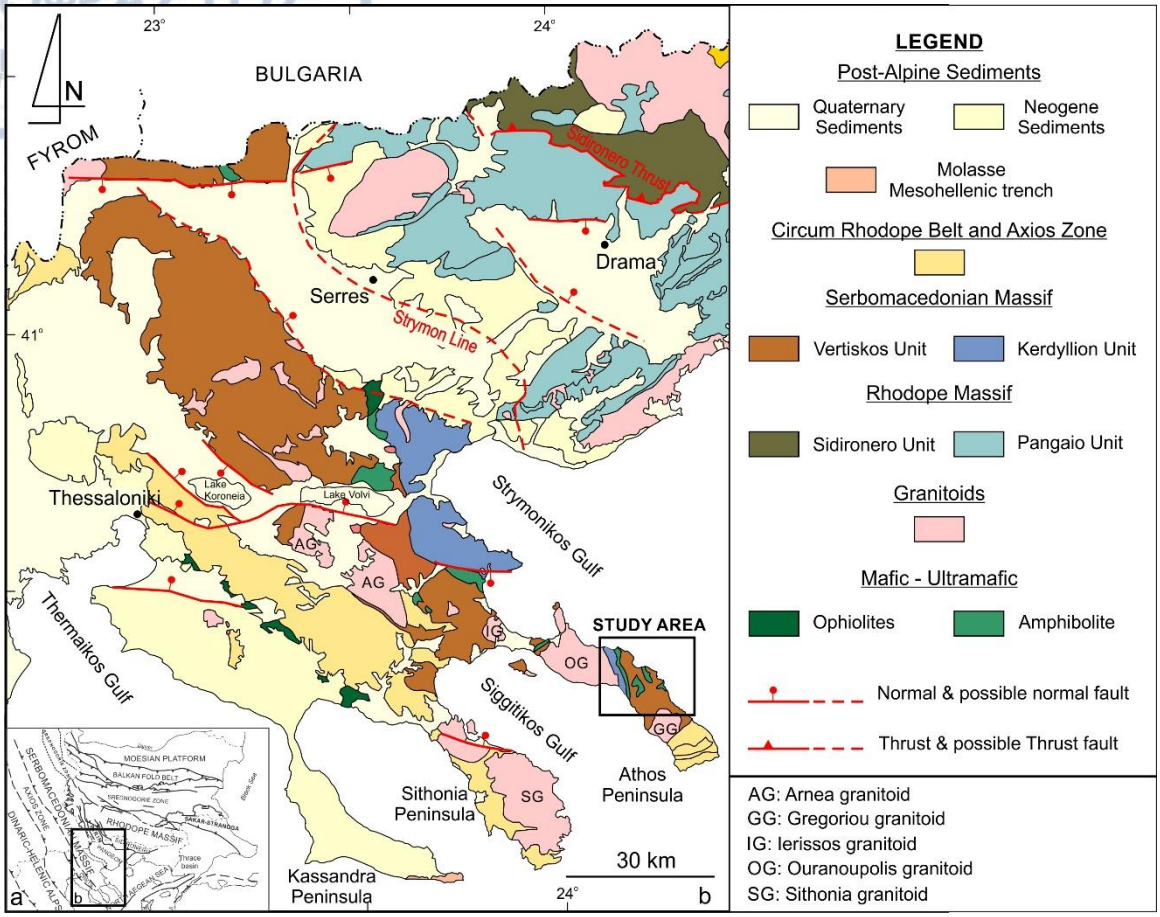

Fig. 1.1. Simplified geological maps of: a) the main geotectonic framework of the Eastern Mediterranean region, including the Dinarides-Hellenides and Balkanides, as the main Alpine orogenic belts. Modified after Tranos and Lacombe (2014); b) the Internal Hellenides and their innermost part, represented by the Serbo-Macedonian and the Rhodope massifs. The study area is also indicated at the northern part of the Athos Peninsula. Modified after Kockel et al. (1977) and Plougarlis and Tranos (2014).

The present PhD thesis focuses on the northern part of the Athos peninsula, which is the easternmost part of the wider Chalkidiki peninsula in Central Macedonia, Greece, and protrudes 50 km into the Aegean Sea. The Athos Peninsula was originally mapped by Kockel and Mollat (1978) (Fig. 1.2), who assigned the rocks comprising the basement of the central and northern part of the peninsula to the Vertiskos and Kerdyllion Units of the Serbo-Macedonian massif. The contact between the two units was initially considered as normal whereas the amphibolites and ultra-mafics were indiscriminately described as igneous and meta-igneous rocks. Himmerkus et al. (2011) grouped the rocks of the study area into the Kerdyllion Unit and the Athos-Volvi Suture Zone (Himmerkus et al., 2005), based solely on dating methods and geochemistry. There is, therefore, an absence of a

purely structural study from the area which will, not only clarify and determine the Alpine reworking, documented in other parts of the Serbo-Macedonian massif, but also examine this afore-mentioned re-assessment, by assigning the rocks of the Athos peninsula to specific (map) units. This is the gap this dissertation attempts to fill, by identifying, analyzing and clarifying structural relationships, concerning an integral part of the Hellenic orogen.

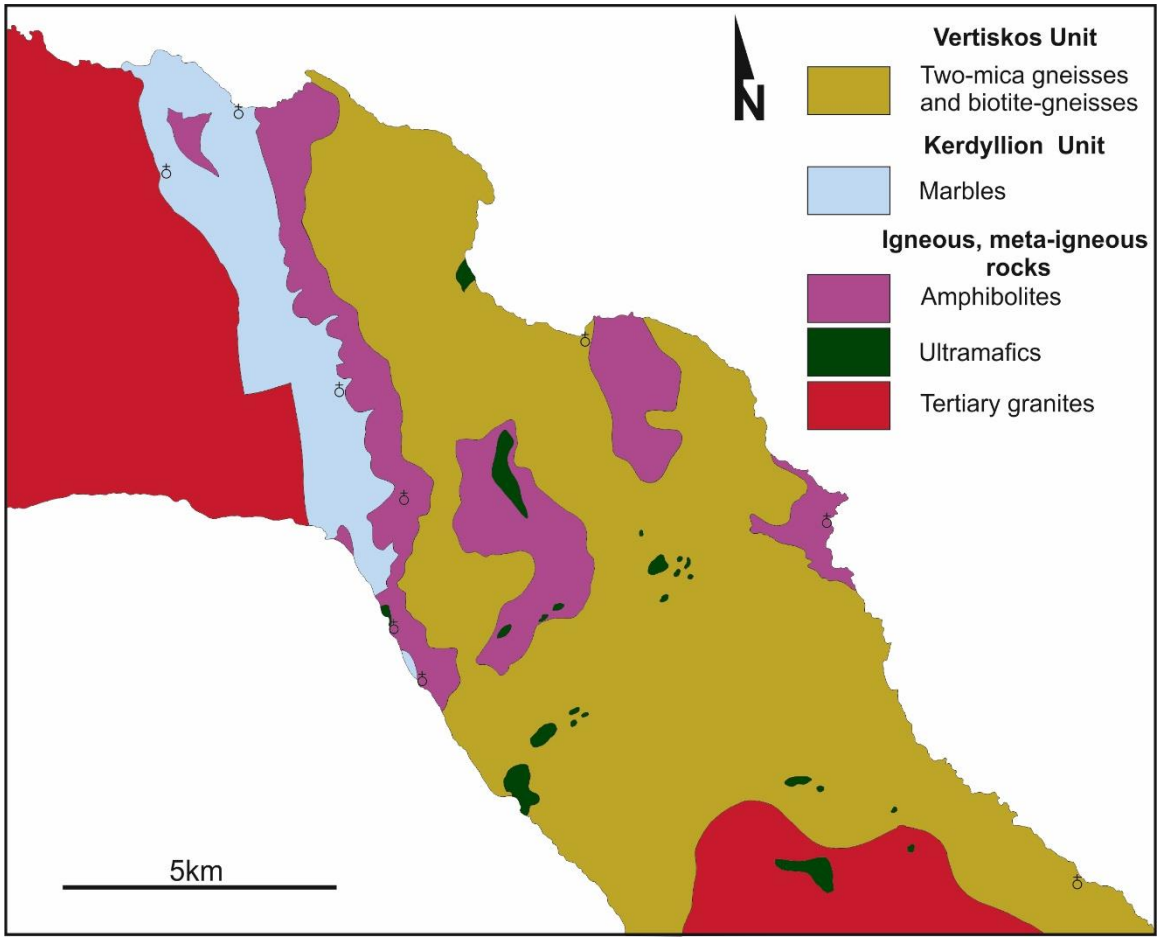

Fig. 1.2. Geological map of the study area (based on the geological mapping and lithological descriptions of Kockel and Mollat (1969) and published by the Publication Department of Geological Maps of I.G.M.R. (1978)).

1.2. Geological setting

1.2.1 Serbo-Macedonian massif

The Serbo-Macedonian massif was separated from the Rhodope massif during the decade of 60's (Kockel and Walther, 1965; Dimitrievic, 1963). More precisely, Kockel and Walther (1965) who mapped the wider area of the Chalkidiki peninsula in central Greece defined the Serbo-Macedonian massif as covering the area east of the Axios zone until

the Strymon River (Fig. 1.1). Furthermore, they subdivided the Serbo-Macedonian Massif into two distinct geological units: a) the structurally upper Vertiskos Unit to the west, which occupies the largest part of the Serbo-Macedonian Massif, and consists mainly of gneisses and schists, and b) the structurally lower Kerdyllion Unit to the east, which comprises mainly of biotite gneisses, migmatitic gneisses, amphibolites and marbles (Kockel et al., 1977; Sakellariou, 1989; Burg et al., 1995).

1.2.1.1 Lithologies

More specifically the Vertiskos Unit consists mainly of monotonous, fine- to medium-grained, muscovite-biotite gneiss and biotite-muscovite gneiss; we called them two-mica gneiss. Subsidiary, lithologies like muscovite gneiss, augen gneiss, biotite gneiss, biotite-hornblende gneiss and amphibolite intercalate with the two-mica gneiss, whereas marbles and other carbonate rocks are exceedingly rare. These rocks have been interpreted as an originally thick series of greywackes, arkoses and shales (Kockel et al. 1977, Sakellariou, 1989). On the contrary, Himmerkus et al., (2006); Himmerkus et al., (2009a) interpreted them as representing a mainly orthogneissic sequence of continental magmatic-arc origin. The amphibolites exhibit a great variability from fine-grained to coarser, thick-layered, often bearing anatexitic feldspathic layers. Their mineralogical compositions also vary as far as the biotite concentration is concerned, leading to biotite-hornblende intercalations at places. Occasionally thin layers of calc-silicate schists are found intercalating these amphibolitic bodies. The amphibolites, in their entirety, have been interpreted as meta-ophiolitic bodies with ultrabasic, gabbroic and volcanic subdivisions, of tholeitic magma origin (Kockel et al. 1977, Kasoli-Fournaraki, 1981). Since the amphibolites are found to be interlayered with the two-mica gneiss, their emplacement was considered to be synchronous with the deposition of the afore-mentioned meta-sediments and of Precambrian age (Kockel et al. 1977). As far as the ultra-basic bodies are concerned, they consist mainly of pyroxene peridotites, with signs of extensive serpentinization and their contacts with the surrounding rocks (two-mica gneisses sequence and amphibolites) have been interpreted as tectonic in all localities (Kockel et al. 1977). These ultra-basic bodies were grouped into the Therma-Gomati-Volvi

complex by Dixon and Dimitriadis (1984) and were considered as remnants of an oceanic crust.

The Kerdyllion Unit consists mainly of fine to medium-grained biotite gneisses, with a very well-developed metamorphic banding and signs of extensive regional anatexis at places. Concordant intercalations of other rock types are commonly found within the dominant biotite gneiss sequence and include: muscovite-biotite, garnet-bearing gneisses, hornblende-biotite and biotite-hornblende gneisses with a less pronounced layering, as well as various types of fine to coarse-grained, more massive, flaser amphibolites, often accompanied by anatexitic feldspathic bands and layers of garnet-epidote-rich and calc-silicate rocks. The second most characteristic rock type of the Kerdyllion Unit are the marbles which comprise of three distinct horizons: the lower, intermediate and upper horizon, of similar lithology among all three horizons, but also an overall distinct facies differentiation, from predominating bluish, coarse-grained, thick-bedded types to thinly bedded, slaty varieties. Intercalations, predominantly with biotite-hornblende gneisses and amphibolites, along with actinolite-calc-schists, calcite-bearing amphibolites, epidote-actinolite-schists and banded biotite-actinolite-calc-schists, are quite common within the three marble horizons. The Kerdyllion Unit has been interpreted as an originally monotonous greywacke-arkose and occasionally marl series of great thickness, with embedded limestone horizons, whereas the amphibolites have been assigned both sedimentary (marls) as well as igneous (tholeitic magma) origin, depending on the researcher (Kockel et al., 1977; Kasoli-Fournaraki, 1981; Sakellariou, 1989).

1.2.1.2 Metamorphism

Both units of the Serbo-Macedonian massif are characterized by a multi-phase metamorphic history, which has been subject to various interpretations by researchers. The first metamorphic phase has been identified in relict forms as a possible eclogite-facies, based on the co-existence of titanite and rutile in the basalt-origin amphibolites (Hellman and Green, 1979) from both Vertiskos and Kerdyllion Units (Kassoli-Fournaraki, 1981; Dimitriadis, 1974), as well as the microanalysis of garnets from the same amphibolites, whose composition points to A-type eclogites (Sakellariou, 1989). This relict eclogite-facies was not initially assigned any specific age, other than pre-Mesozoic (Sakellariou, 1989), whereas later studies identified graphite pseudoforms after

diamonds, within amphibolite xenoliths within the Arnea granite and the vicinity of the Vertiskos Unit, pointing to an ultra-high pressure, eclogite-facies metamorphic event that was attributed Carboniferous age (Kostopoulos et al., 2000). The latter metamorphic event could be correlated with the Late Carboniferous-Early Permian mica ages, for the Vertiskos Unit, dated by Borci et al. (1965) within pegmatoid intrusive bodies, even though these ages were initially interpreted as the effect of a thermal rejuvenation event throughout Vertiskos Unit (Kockel et al., 1977). An analogous relict eclogite-facies was also identified in garnet-staurolite-mica schists which, according to some researchers, represent former Mesozoic sedimentary sequences initially deposited on the Serbo-Macedonian Palaeozoic basement (Kockel et al., 1977; Dixon and Dimitriadis, 1984), thus assigning Mesozoic age to this HP metamorphic phase (Kydonakis et al., 2015).

A consequent second metamorphic event of medium amphibolite grade was recognized in the Vertiskos Unit meta-sedimentary rocks by Sakellariou (1989), that was considered syn-tectonic to either the Cimmeric orogenic processes (Sengör, 1984) or a possible neo-Paleozoic orogenic event (Sakellariou, 1989).

The predominant metamorphic fabric, characterizing both the Vertiskos and Kerdyllion Units, has been attributed to a third syn/post-tectonic regional metamorphic event under lower-medium grade amphibolite facies (Kockel et. al, 1977; Dixon and Dimitriadis, 1984; Sakellariou, 1989), post-dating and overprinting the afore-mentioned metamorphic phase. This metamorphic phase is considered generally responsible for the intense Mesozoic reworking of a previously believed inert crustal part since the Paleozoic by earlier researchers, such as Kockel et al. (1977). Its dating varies according to the existing geochronological data (Borsi et al., 1965; Christofides et al., 1999, 2007; De Wet et al., 1989; Harre et al., 1968; Lips et al., 2000; Papadopoulos and Kilias, 1985) and the researchers ranging from Middle-Late Jurassic (Dixon and Dimitriadis, 1984; Sakellariou, 1989) to Middle-Late Cretaceous (Papadopoulos and Kilias, 1985; Kilias et al., 1999).

This predominant lower-middle amphibolite facies has been found to have retrograded to an upper greenschist, syntectonic facies, characterizing this fourth metamorphic phase, affecting both Vertiskos and Kerdyllion Units. The age of this metamorphic event is considered as Early Cretaceous (De Wet et al., 1987; Sakellariou, 1989) and is based on the already-mentioned, geochronological data of mainly micas

(Harre et al., 1968; De Wet et al., 1989; Lips et al., 2000). However, some researchers attribute the latter geochronological data to the previous amphibolite facies event, even though these mica ages are generally considered to represent cooling ages and seem to be more fit with this retrograde greenschist facies.

The fifth and final, youngest metamorphic phase is represented by a syn-tectonic, retrograde, lower greenschist facies of Tertiary-Eocene age (Kockel et al., 1977; Kassoli-Fournaraki 1981; Dixon and Dimitriadis 1984; Chatzidimitriadis et al., 1985; Papadopoulos and Kilias 1985; Sakellariou 1989), affecting the basement rocks as well as the afore-mentioned Eocene granitoids of Sithonia, Ouranoupolis etc. and being in accordance with the main Late Eocene mica cooling ages by Harre et al. (1968).

Various mica ages from pegmatoids and Vertiskos-Kerdyllion Units could have recorded any stage from the afore-mentioned late-Alpine metamorphic, syntectonic phases.

1.2.1.3 Magmatism

Magmatism in the Serbo-Macedonian massif has been generally assigned four phases, even though the ages involved vary from researcher to researcher, depending on the existence or not of geochronological data as well as the dating methods applied. The first magmatic phase has been already described and is related to the protolith of the widespread amphibolites both in the Kerdyllion as well as the meta-ophiolitic, basic and ultra-basic bodies within the Vertiskos Unit. They are considered as metamorphic products of a pre-Alpine, probably Precambrian basic-ultra-basic magmatic event (Kockel et al., 1977, Kasoli-Fournaraki, 1981), even though another group of researchers have identified great part of this meta-ophiolitic sequence as an in-situ Mesozoic rift complex, namely Therma-Gomati-Volvi ophiolite complex (Dixon and Dimitriadis, 1984), or a Mesozoic ophiolithic suture, namely Athos-Volvi Suture zone (Himmerkus et al., 2005).

A subsequent, second magmatic phase is represented by the plagioclase-microcline gneiss, concordantly incorporated in both the Vertiskos and more extensively the Kerdyllion Unit. This plagioclase-microcline gneiss corresponds to syn-orogenic, leucocratic, biotite-muscovite granite intrusions, whereas their dominant fabric was considered as pre- or syn-kinematic with the dominant regional metamorphism of the

Serbo-Macedonian massif (Kockel et al., 1977, Plougarlis and Tranos, 2014). Much younger ages of Eocene to Oligocene times (55.8 to 33.9 Ma), calculated via radiometric dating of K/Ar and Rb/Sr on muscovite and biotite from this plagioclase-microcline gneiss (Harre et al., 1968). This dating might represent thermal rejuvenation ages associated with the widespread acidic intrusions throughout the Serbo-Macedonian massif (Kockel et al., 1977). However, the oldest dated magmatic phase is of Silurian age, based on zircon dating, and it is considered to represent a continental magmatic arc having as a result the primary granite intrusions in the Vertiskos Unit (Himmerkus et al., 2006; Himmerkus et al., 2009a). Obviously, this age contradicts both the initial Precambrian age assigned to the same rocks, as well as the predominantly sedimentary origin of the Serbo-Macedonian massif (Dimitrievic, 1966, 1974; Kockel et al., 1977).

The third magmatic phase is of Mesozoic age, identified in the Vertiskos Unit, and consists mainly of large, medium- to coarse-grained, monotonous biotite-muscovite granites, like the Arnea, Kerkini and Monopigadon granites, accompanied by smaller intrusions, dykes and apophyses. The age assigned to this magmatic phase is a matter of dispute as two distinct ages have been identified: A Late Jurassic age (Kockel et al., 1977), based primarily on mica ages (Dixon and Dimitriadis, 1984; Papadopoulos and Kilias, 1985; DeWet et al., 1989; Ricou et al., 1998; Christofides et al., 1999; Lips et al., 2000), and a Triassic age based on zircon dating (Himmerkus et al., 2008; 2009; 2011). This difference between the two recorded ages has been attributed by researchers to the low closure temperature of micas (300°C to 450°C), which, for the first age group, could correspond to cooling, exhumation ages of the Vertiskos terrain, whereas zircon ages, being much less prone to resetting by thermal events, represent primary crystallization ages for the granites (Himmerkus et al., 2009 and references therein), possibly associated with the Triassic rifting of a passive continental margin (Stais and Ferriere, 1991). Himmerkus et al. (2011) also dated a Late-Jurassic magmatic arc event in rocks occupying the Athos peninsula, which were initially assigned to the Vertiskos Unit (Kockel et al., 1977) and later to the Kerdyllion Unit and the Rhodope massif (Brun and Sokoutis, 2007, Himmerkus et al., 2011).

The fourth and youngest magmatic phase, recognized throughout the Serbo-Macedonian massif, consists of granitoid rocks, e.g. Sithonia, Ouranoupolis, Gregoriou,

Ierissos plutons, that intruded the basement of the Serbo-Macedonian massif during Eocene times (DeWet et al., 1989, Christofides et al., 1990), and were also considered responsible for Eocene-Oligocene thermal rejuvenation ages of micas from basement rocks (Harre et al., 1968; Kockel et al., 1977).

1.2.1.4 Deformation

The Serbo-Macedonian massif constitutes a geotectonic assemblage not only of multi-phase metamorphic and magmatic history, but also deformation, since most of this history was attributed to specific tectonic events mostly related to the complex plate convergence between the Gondwana-derived continental blocks and Eurasia.

Sakellariou (1989) defined five syn-metamorphic deformational phases, as afore-mentioned, for both the Vertiskos and Kerdyllion Units. The first deformational phase, which is the oldest, has been linked with relict forms found within amphibolites and correlated with an eclogite facies metamorphism. The second deformational phase has been linked with a medium-grade amphibolite facies metamorphism and is characterized by isoclinal folds, generally trending NW-SE, and a parallel trending stretching lineation, both structural elements characterized by a strong later parallelism with the third, consequent deformational event. Sakellariou (1989) assigned a Neo-Paleozoic age to this deformational event. The third deformational phase took place under lower amphibolite grade conditions and was characterized by the researcher as the main event, which gave rise to the metamorphic and deformational fabric of both units, as well as the Mesozoic Arnea granite. It is characterized by isoclinal folds, re-folding previous structures, also trending NW-SE. Parallel to these axes is the stretching lineation. The age that was assigned to this deformational event was Mid- to Late-Jurassic. The fourth deformational phase, which was related with an upper greenschist metamorphic facies, was characterized by close folds, trending N-S to NNE-SSW, and an intersection lineation of parallel orientation, mainly expressed as microfold rodding axes. This metamorphic phase was attributed a Lower Cretaceous age. The last syn-metamorphic deformational phase was of a lowermost greenschist metamorphic grade, and was characterized by open to close folds trending E-W, and it was attributed an Eocene age.

Patras et al. (1989) also report five deformational events for the Serbo-Macedonian massif. The first deformational phase is represented by isoclinal folds trending NW-SE to

NNW-SSE (135° to 170°) and associated with an axial planar foliation. The second deformational phase is represented by isoclinal to tight, asymmetric folds, trending 125°-155° and a formation of an intersection lineation. The third deformational phase mainly includes large-scale, open to close folds, trending NNE-SSW, frequently asymmetric and verging towards the SE. The fourth deformational event includes NW-SE trending, open to gentle folds. The fifth deformational event is represented by N-S trending, kink folds.

Sidiropoulos (1991) concluded four deformational events for the Serbo-Macedonian massif. The first deformational event is related with migmatization processes and the initial orientation of its deformational fabric could not be established due to the intense over-printing of the subsequent deformational event. It was assigned a Hercynian age. The second deformational event is characterized by an intense mylonitization, a discrete planar fabric, parallel to the pre-existing foliation related with the first deformationa event, and the presence of tight to isoclinal folds, dated in the Permo-Triassic. The third deformational event led to asymmetric, tight, recumbent folds trending NW-SE and NE-SW and both intersection and sliding lineations. This event has been dated as Late-Jurassic. The fourth deformational event is related with generally upright, open folds, trending NNE-SSW and ENE-WSW as well, the development of a synchronous planar fabric and sliding lineations, assigned a post-Jurassic age.

Kilias et al. (1999) also referred to two main deformational events, which affected the Serbo-Macedonian massif and were related to the afore-mentioned, alpine re-working processes that these rocks underwent. The D_{SRB} event was associated with metamorphic conditions of 4.5–7.5 kbar and 510–580°C, and refers to a predominant ductile deformation, producing a penetrative foliation, axial planar to isoclinal folds, the f-axes of which are found parallel to the equivalent stretching lineation. This stretching lineation mainly trends ENE-WSW to WNW-ESE and the studied kinematics produced an inferred top-to-the ENE to ESE ductile flow, of Cretaceous age (120–90 Ma) associated with a crustal stretching and unroofing. However, this kinematics has been also defined in the Eocene Sithonia granitoid (Tranos et al., 1993) implying that it outlasted the Eocene. The second deformational event, namely D_e, defined by Kilias et al. (1999) was associated with low-angle extensional ductile shear zones, with an inferred top-to-the NE to SW sense of

shear. This deformational event was attributed an Eocene to Miocene age, followed by a consequent NW/SE-directed shortening during its later stages.

Plougarlis and Tranos (2014) proposed five deformational events for the Serbo-Macedonian massif and their study in the Vertiskos and Kerdyllion Units. The first deformational event is characterized by an intense shearing, the development of mylonitic zones and isoclinal folds, transposed by the subsequent deformational event. The second deformational event is also characterized by isoclinal folds, trending ENE-WSW to E-W, affecting the previous structures and the associated axial planar foliation. The third deformational event includes close folds, trending WSW-ENE and the development of a crenulation cleavage. The fourth deformational event was of low intensity and produced chevron-kink folds, whereas the fifth and final deformational event described by the researchers corresponded to brittle to semi-brittle structures defining transpression-pure compression and a N-S directed shortening.

Kydonakis et al. (2015) also studied the deformation of the Vertiskos Unit and, as following previous researchers (Burg et al., 1996a; Burg et al., 1996b, Brun and Sokoutis, 2007), they incorporated the Kerdyllion Unit to the Rhodope massif. They consider Vertiskos Unit to be part of the Chalkidiki block, which underwent in overall a ductile deformational event, associated with an initial high-pressure metamorphism, followed by a thermal equilibration, under lower pressure but higher temperature metamorphic condition. This event spanned in time throughout the whole Cretaceous. They recorded a stretching lineation, dominantly trending NE-SW and a dual opposite sense of shear, both top-to-the SW and the NE, the former related with thrusting processes and the latter probably related with extensional tectonics and the exhumation of the metamorphic units.

1.2.2 Rhodope massif

1.2.2.1 Lithologies

The subdivision of the Rhodope Massif into distinct tectono-metamorphic units is not an issue that has been totally resolved, however it has been roughly divided into two units: a) The structurally lower unit which, in the central part of the Rhodope massif corresponds to the Pangeon Unit (Papanikolaou and Panagopoulos, 1981), and in the eastern part to the Lower Tectonic Unit, or LTU (Mposkos, 1998; Mposkos and Krohe,

2000). The Pangeon unit consists of augen gneisses, mica schists and amphibolite schists of variable thickness (20-300 m), underlying thick massive marbles intercalating with mica schists of relatively small thickness, usually found within the cores of large scale isoclinal synforms (Papanikolaou and Panagopoulos, 1981). The LTU, in turn, consists mainly of orthogneisses, migmatites (containing muscovite-metapegmatite lenses), pelitic gneisses, high Al-metapelites, eclogites, eclogite-amphibolites, amphibolites and rare marble intercalations, whereas large ultramafic bodies associated with eclogitised and amphibolitised gabbros are tectonically intercalated within the orthogneisses and metapelites (Mposkos, 1998); b) The structurally higher unit, corresponding to: the Sidironero Unit in the central part of the Rhodope massif, which overlies the Pangeon Unit via a WNW-ESE tectonic zone, namely Nestos thrust, and to the Upper Tectonic Unit (UTU) in the eastern part of the Rhodope massif, mainly consisting of medium to high grade augen gneisses, migmatites, metapelites, leucocratic gneisses, amphibolites, eclogite-amphibolites, mica schists, thin intercalations of marbles and a lot of pegmatite and aplite veins, whereas small ultramafic bodies occur in many places (Papanikolaou and Panagopoulos, 1981; Mposkos, 1998). In any case researchers have consistently subdivided the Rhodope massif into two different structural units. The subdivision of the Rhodope massif into the Pangeon-Sidironero Units was based on the tectonic juxtaposition of a higher amphibolite-grade metamorphic complex, having reached HP to UHP-HT peak metamorphic conditions that thrust over a lower grade metamorphic complex of generally HP-LT, upper greenschist facies. Whereas the subdivision of the Rhodope massif into the LTU and the UTU was based on the different inferred ages of successive HP, MP and LP tectonometamorphic events, with the most pronounced MP event being characterized by higher amphibolite facies in the UTU and upper greenschist-lower amphibolite facies in the LTU (Mposkos, 1989; Mposkos, 1998). As far as the overall origin of the afore-mentioned units are concerned, metasedimentary rocks are considered to be of Gondwana provenance, based on the common presence of 670-560 Ma and 2.0-2.1 Ga ages, from detrital zircons, whereas the orthogneisses in bulk are considered to be granitoids of Hercynian age (late Carboniferous-Early Permian) and the eclogite-amphibolites metagabbroid rocks of Late Permian-Early Triassic age (Liati et al., 2011 and references therein).

1.2.2.2 Metamorphism

The Rhodope massif is strongly characterized, as the Serbo-Macedonian massif, by a polyphase metamorhism. Some researchers argue for an initial Variscan metamorphism (Burg et al., 1990; 1996; Krohe and Mposkos, 2002; Peytcheva et al., 2004; von Quadt et al., 2005) attributed to protolith ages of granitoid gneisses and metapegmatites. The most recorded and best-documented metamorphic phase, however, is of Mesozoic age and constitutes an eclogite relict facies, which constitutes a preceding HP history of both sedimentary and magmatic origin rocks throughout the Rhodope massif (e.g. Mposkos, 1989; Wawrzenitz and Mposkos, 1998; Liati and Gebauer, 1999; Mposkos and Kostopoulos, 2001; Reischmann and Kostopoulos, 2002; Liati et al., 2011 and references therein). Numerous studies have identified these eclogite facies metamorphic conditions, with geochronological data placing them in a very wide time span, ranging from Early Jurassic to Late Eocene, and varying tectono-metamotamorphic interpretations, which attribute this time span to either a unique HP/(U)HP event related with a single long-lasting subduction and exhumation cycle (Mposkos and Krohe, 2006; Cornelius, 2008; Krenn et al., 2010; Turpaud and Reischmann, 2010), or a series of multiple subduction cycles during Late Jurassic, Late Cretaceous, Early Eocene and Middle-Late Eocene times respectively (Liati et al., 2011 and references therein). A subsequent metamorphic phase, overprinting the latter eclogite facies, and forming the predominant metamorphic fabric throughout the Rhodope massif, is represented by an amphibolite and at least at parts by granulite facies (Liati and Seidel, 1996 and references therein, Liati and Gebauer, 1999) for the UTU and Sidironero Unit, and an upper greenschist-lower amphibolite facies for the LTU and Pangeon Unit. The amphibolite facies has been dated, mainly in the UTU and Sidironero Unit, both in the Early Paleocene as well as in the Early-Late Eocene (Wawrzenitz et al., 1994; Mposkos and Wawrzenitz, 1995; Mposkos, 1998, Liati and Gebauer, 1999), whereas retrograde greenschist assemblages were geochronologically placed in the Late Oligocene-Early Miocene (Del Moro et al., 1990; Wawrzenitz and Krohe, 1998), in Thasos and the Pangeon Unit.

1.2.2.3 Magmatism

The Rhodope massif is also characterized by a poly-phase magmatic activity. Hercynian ages, ranging from Late Carboniferous-Early Permian, are reported as granitoid

protolith ages of orthogneisses throughout the Rhodope massif (Peytcheva and von Quadt, 1995; Wawrzenitz 1997; Liati and Gebauer 1999; Liati et al., 2002; Liati and Fanning 2005), even though some researchers have attributed the afore-mentioned granitic intrusions solely to the Pangaion or Lower Tectonic Unit (Turpaud and Reischmann, 2010). A consequent magmatic event was identified in amphibolitized eclogites from the Sidironero and the Upper Tectonic unit that was attributed Late Permian-Early Triassic age and was related with the crystallization of gabbroic protoliths (Liati and Fanning, 2005; Liati, 2005, Bauer et al., 2007). A quite well established magmatic event has been defined in the Mesozoic, and more specifically the Late Jurassic-Early Cretaceous, connected with either magmatic arc activity of corresponding granitoids or rift-related magmatic underplating in the continental crust in Central Rhodope supported by SHRIMP data, recorded in both basic and acid lithologies (Gebauer and Liati, 1997; Liati and Gebauer, 2001, Liati et al., 2002; Turpaud and Reischmann, 2010). All the existing geochronological data, however, seem to limit this Late Jurassic-Early Cretaceous magmatism to the Sidironero and UTU of the Rhodope massif. Tertiary magmatism remains a prominent characteristic of the Rhodope massif as well, and two main phases can be distinguished: a first one is restricted within the Sidironero and UTU and refers to the intrusion of granitoid rocks in the Eocene (Kilias and Mountrakis, 1998; Christofides et al., 2001; Soldatos et al., 2001). This phase could be responsible for the Late Eocene migmatization and the formation of leucosomes in orthogneisses recorded by some researchers (Liati and Gebauer 1999; Liati et al., 2004; Liati, 2005), and a second, younger one during the Oligocene-Miocene, also characterized by acid magmatism (Harre et al., 1968; Eleftheriadis et al., 2001), solely within the Pangeon Unit and it is of post-collisional nature (Christofides et al., 2001).

1.2.2.4 Deformation

The Rhodope massif, although bearing signs of an initial Variscan metamorphism, is characterized by an overall fabric developed during the alpine, nappe-stacking processes which must have stretched in time from the Upper Jurassic to the Paleogene (e.g., Burg et al., 1990; 1996; Liati and Mposkos, 1990; Dinter et al., 1995; Wawrzenitz and Mposkos, 1997; Ricou et al., 1998; Krohe and Mposkos, 2002; Liati, 2005; Mposkos and Krohe, 2006; Bauer et al., 2007; Krenn et al., 2008). Many researchers have attributed a polyphase

character to this long-lasting deformational period the Rhodope massif underwent (e.g. Meyer, 1969; Papanikolaou and Panagopoulos, 1981; Ivanov et al., 1985; Burg et al., 1990; Kilias and Mountrakis, 1990; Koukouvelas and Doutsos, 1990), while others have grouped multiple co-axial, recorded structural elements under a single progressive deformational event (Burg et al., 1996). The main fabric, which has been most prominently imprinted on the rocks of the Rhodope massif, is characterized by a generally shallow-dipping foliation, isoclinal, recumbent folds, occasionally showing signs of a sheath fold geometry and accompanied by a parallel to the afore-mentioned fold hinges stretching lineation (Burg et al., 1996; 2012, Krenn et al., 2010). This intense stretching lineation, recorded throughout the Rhodope massif, is generally NE-SW to N-S oriented (Meyer et al., 1963; Meyer, 1969; Kronberg et al., 1970; Kilias and Mountrakis, 1990; Koukouvelas and Doutsos, 1990; von Braun, 1993, Burg et al., 1996) and represents an either top-to-the SW to S sense of shearing during the alpine nappe stacking event or a SW-ward shear associated with the gravitational adjustment of this pre-existing nappe, via low-angle normal faults (Burg et al., 1996; 2012).

The later stages of Rhodope's deformational history are characterized by both crenulation and also kilometre-wavelength folds, constituting mainly E-W, S-facing folds but also and N-S, W-facing chevron folds (Burg et al., 1996; 2012). These folding structures and the produced occasional planar fabric associated with them, like a crenulation cleavage, have been found to affect and cross-cut the late- to post-tectonic Eocene to Oligocene plutons scattered throughout the Rhodope massif (Burg et al., 1996; 2012; Tranos et al. 2009).

1.3. Aim of this study

The Athos peninsula was primarily mapped by Kockel et al. (1977) (Fig. 1.2), and was considered to be mainly build up by rocks belonging to the Vertiskos and Kerdyllion Units of the Serbo-Macedonian massif. However, since then, later studies provided new subdivisions of the crystalline rocks. For example, a new unit, namely Ammouliani Unit between the Kerdyllion and Vertiskos Units, has been suggested by Plougarlis and Tranos (2014), the Kerdyllion Unit was incorporated to the Rhodope massif (Burg et al., 1995; Ricou et al., 1998; Brun and Sokoutis, 2004; 2007, Himmerkus et al., 2007; 2011), and the Vertiskos Unit was considered as a separated individual tectonic terrane (Burg et al., 1995; 1996; 2012 and references therein).

Moreover, Kockel et al. (1977), was based mainly on the interpretation of aerial photos and some cross-sections, as basic tools for their mapping and the area has not been studied in detail up to now. This fact constitutes the study area of much more interest, concerning the structural relationships between the two units, and the Alpine reworking, documented in other parts of the Serbo-Macedonian massif (e.g., its western contact with the Circum Rhodope Belt Thrust System, Tranos et al. (1999)), which led to the amalgamation of the innermost part of the Internal Hellenides.

Additionally, geochronological and geochemical data exist for the study area (Himmerkus et al., 2011), the interpretation of which has led to the extrapolation of various tectonic implications, with the actual tectonic analysis being absent. This is one of the gaps this dissertation attempts to fill, in part, using existing geochronological and geochemical data as a useful tool in an attempt to unfold the geotectonic evolution of the study area, primarily based on structural analysis.

For this purpose, I carried out fieldwork, a detailed mapping of the study area and additional microstructural analysis which allowed me to present the different lithologies and deformation structures of the area. This work aims at deciphering the overall structure, and tectono-stratigraphy of the Vertiskos and Kerdyllion Units in the northern part of the Athos Peninsula, and how the region was affected by the Alpine orogeny, also, targeting the contact between the units, so as to better understand the tectono-metamorphic history of the Serbo-Macedonian massif.

Chapter 2. Geological structure of the Northern part of the Athos peninsula

2.1. Introduction

The northern part of the peninsula is mainly composed of marbles, initially grouped into the Kerdyllion Unit and biotite gneisses and two-mica gneisses, grouped into the Vertiskos Unit, both Units belonging to the Serbo-Macedonian massif, whereas their contact was considered as a normal contact, by Kockel and Mollat (1968), during the mapping process which led to the 1978 Institute of Geology and Mineral Exploration (I.G.M.E.) of Greece (Fig. 1.2). However, amphibolites and ultramafic rocks exist along with the above mentioned rocks, making the geology and relationship between the two units much more complicated. Later Himmerkus et al. (2011) grouped the rocks of the study area into a map unit, consisting primarily of biotite gneisses, of ortho-origin, assigned solely to the Kerdyllion Unit, whereas the amphibolites and ultra-mafics were assigned to the Athos-Volvi Suture Zone, considered by the specific researchers as an ophiolitic melange zone, juxtaposed with the Therma-Volvi-Gomati complex of Dixon and Dimitriadis (1984).

During this dissertation a geological mapping of the northern part of the Athos peninsula took place, along with the collection of structural data, such as different types of foliation and lineation, fold axes and shear sense indicators and markers, in order to define the map units of the study area, to clarify the nature of their contacts and to decipher the overall structure governing this part of the Serbo-Macedonian massif. This data was introduced and processed by an appropriate Geographical Information System software and a new map was produced for the study area (Fig. 2.1).

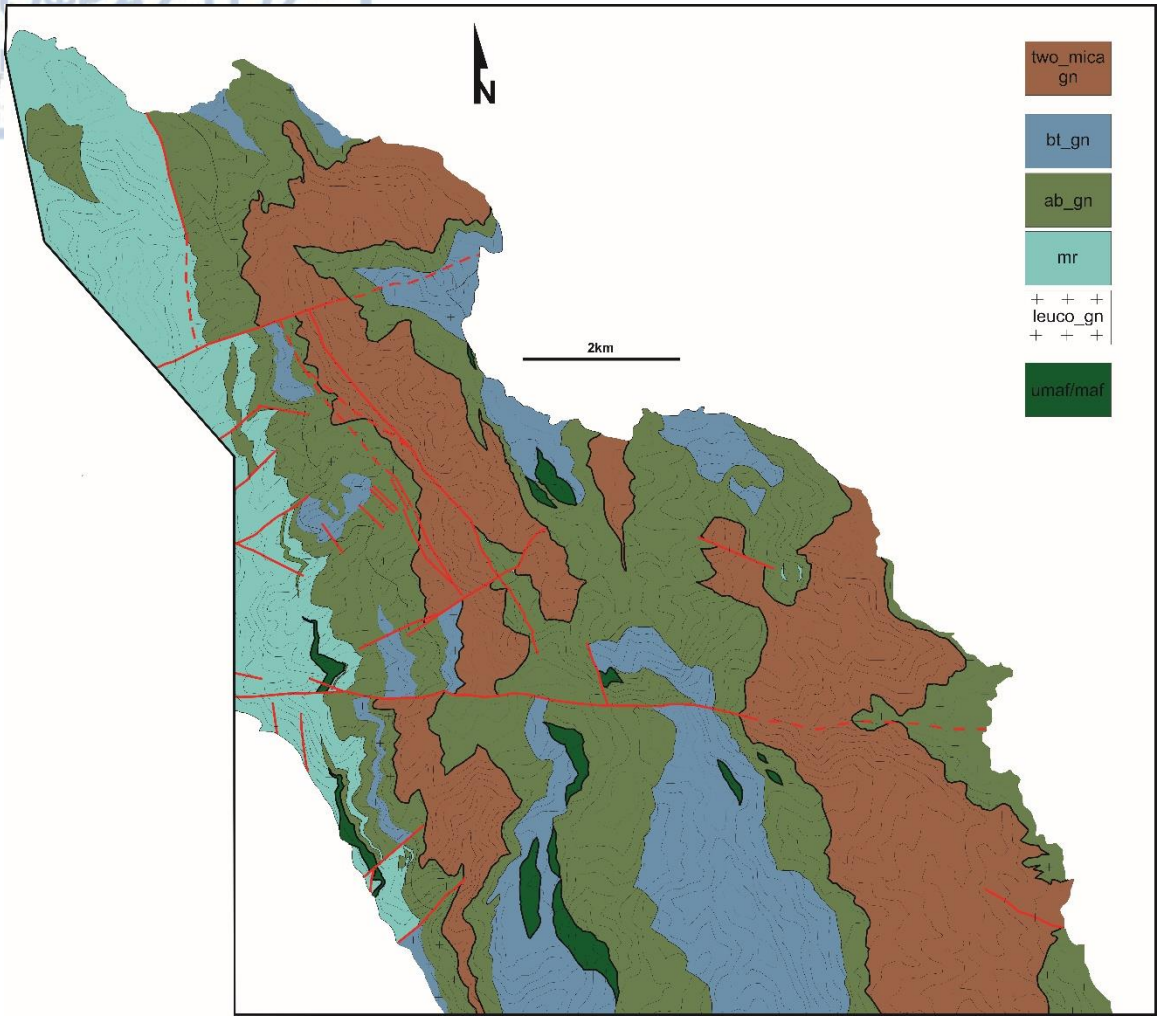

Fig. 2.1. Geological map of the study area, produced via mapping, field work and structural analysis, carried out during this dissertation.

2.2. Lithological description of the map units

The geological mapping, which was carried out, defined the main geological map units of the study area, which are: a) marbles, b) amphibolite gneiss, c) biotite gneiss, d) two mica-gneiss and g) ultra-mafics. It is worth mentioning that within the marbles, as well as the biotite and amphibolite gneiss map units underlying the two-mica gneiss, small exposures of calc-silicate rocks, of several decades of meters in length, have been observed in the field, but these exposures are too small to be mapped as a distinct map unit. Another rock-type was identified during the geological mapping; that of leucogneiss, which exposes in lenses or lensoidal interlayers of up to few hundreds of meters in length and up to decades of meters in thickness, within the amphibolite and biotite gneiss, especially along their lower boundary with the two-mica gneiss and to a much lesser

extent within biotite gneiss overlying the two-mica gneiss. This rock was also not mapped as a distinct map unit due to its relatively small exposures, even though it is indicated as a "diffused" rock-element within the above-mentioned map units, in the produced geological map.

The above map units generally dip with a very gentle angle to the ENE, and thus their description from the structurally lower to the structurally higher levels is as follows:

Marbles

The marbles, forming an N-S striking narrow stripe between the Eocene Ouranoupolis granitoid to the west and the lower amphibolite gneiss to the east, occupy the westernmost part of the study area where the monasteries of Konstamonitou, Zografou, Chiliandariou and Esfigmenou are located. Actually, the Eocene Ouranoupolis granite intruded the marbles in the west. The marbles generally dip towards E-ESE at very gentle angles underneath the amphibolite gneiss. They are mainly white and blueish gray in color, coarse-grained, strongly foliated and banded, due to the alterations between purely carbonate and more clastic layers, ranging in thickness up to tens of cm (Fig. 2.2a-h). They appear as strongly deformed rocks, under ductile flow conditions resulting in a mylonitic foliation, and at places carry overprinting relationships among multiple deformational events (it will be further analyzed and described in a following chapter). A typical mineral assemblage is calcite, biotite, epidote, quartz, and rutile as an accessory mineral. At places, some intercalations with amphibolites, calc-silicate and amphibole schists, which may reach tens of meters in thickness, have been observed into the marbles. The marbles acquire a reddish pink color when these intercalations occur. Finally, marbles also occur, as lenses in the form of tectonic slivers, few meters in thickness, along the contact of the two-mica gneiss with the amphibolite gneiss map unit.

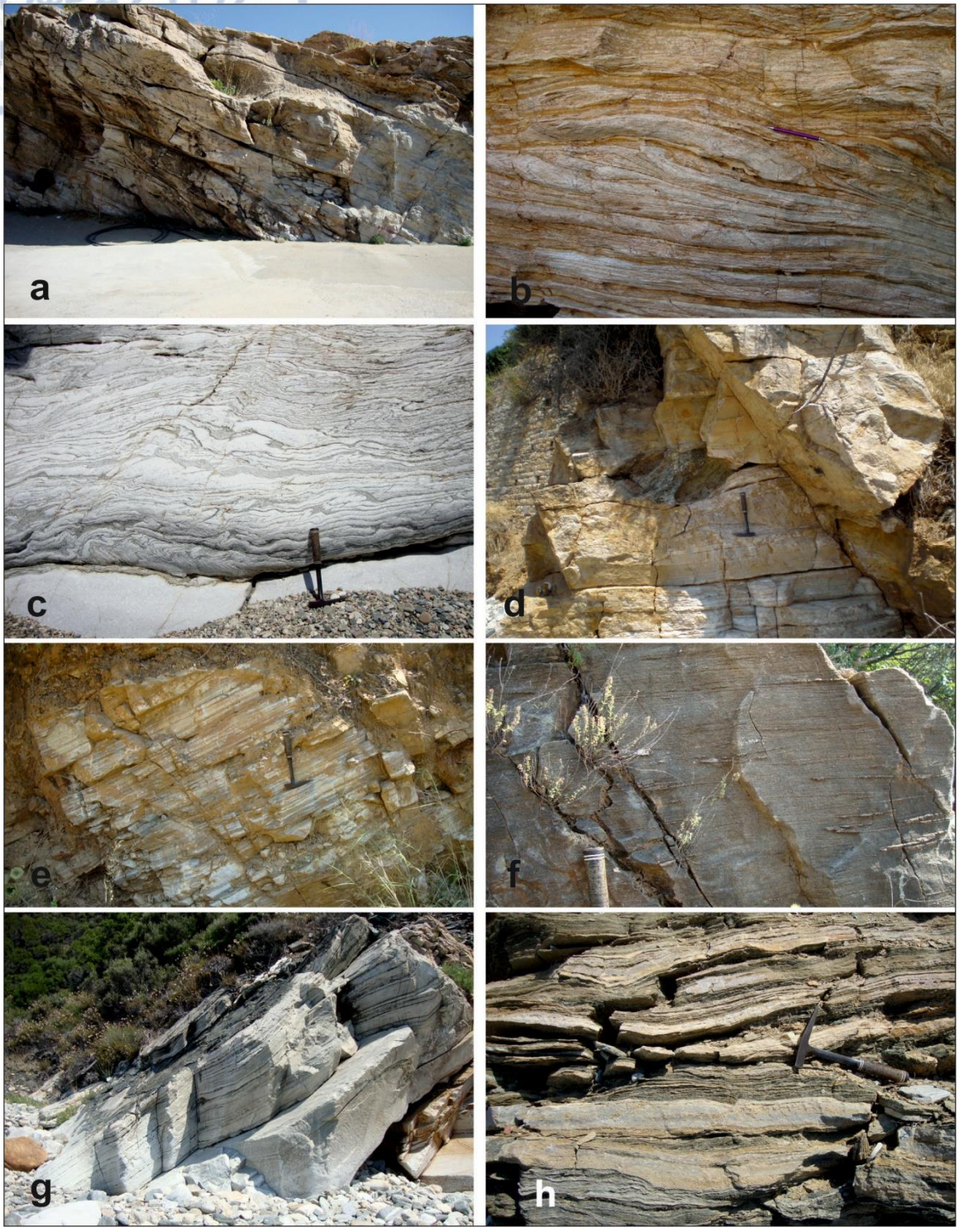

Fig. 2.2. Marbles from the study area: a) Well-foliated marbles W of Konstamonitou monastery, b) Reddish-pink, well-foliated marbles with thin calc-siliclastic intercalations, S of Zografou monastery, c) White, intensely folded, generally coarse-grained marbles, S of Zografou monastery, d) White, coarse-grained, well-foliated marble with foliation parallel shear zone, incorporating a boudinaged amphibolitic bead, at Dohiarion monastery, e) Blueish white, well-foliated, coarse-grained marble, overlying the lower amphibolite gneiss map unit, N of Dohiarion monastery, f) White-pink, coarse-grained, well-foliated marble, SSE of Dohiarion monastery, g) White, coarse-grained, well-foliated marble, intercalating with

cm-thick amphibolite layers, SSE of Xenofontos monastery, h) Blueish grey, coarse-grained marble, intercalating with calc-silica-schist inlayers, ocassionally amphibole-rich, at Xenofontos monastery.

Amphibolite gneiss

The amphibolite gneiss map unit, as already mentioned, both underlies and overlies the two mica-gneiss map unit. The underlying counterpart outcrops in the western part of the study area, i.e. the areas of Xenofontos, Dochiariou, Konstamonitou, Zografou and Esfigmenou monasteries, also overlying the marbles, whereas the overlying counterpart of the amphibolite gneiss occurs in the central part of the study area, from the area vicinity of Vatopedi monastery to Karyes. The rocks belonging to this map unit are dark green to black in color, well foliated, and in many parts, they have developed a migmatitic banding, especially at their part underlying the two mica-gneiss (Fig. 2.3a-h and Fig. 2.4a-h). They often include augens of feldspar or feldspar-quartz-aggregate. The layering ranges from 1-2 mm to approximately 10 cm in thickness and depending on their type they exhibit from coarse-grained and massive to fine-grained types, especially when thinly banded, whereas flecky and nebulitic textures are also evident in numerous localities, indicating signs of migmatization. Frequent pegmatoid bodies, constituting the leucogneiss at many localities, appear parallel or subparallel to the main foliation, forming concordant pegmatoid bands of few cm to several meters in thickness, which become much scarcer at the amphibolite gneiss part overlying the two mica gneiss. They are often boudinaged forming at places “isolated” pegmatoid beads from centimetric to metric scale. Also, near the contact with the underlying marbles, calc-silicate gneiss or schist intercalations are found within the amphibolite gneiss. It quite frequently grades from an amphibole-gneiss to an amphibole-biotite gneiss or biotite-amphibole gneiss, especially at their contact with the overlying biotite gneiss. A fact that implies the gradual passage between the amphibolite gneiss and the overlying biotite gneiss. On the other hand, they also exhibit at places sharp boundaries with the biotite gneiss, in the form of shear zones and a higher strain gradient, as well as a more pronounced gneissic to migmatitic layering, when referring to the part of the map unit underlying the two mica-gneiss. There are also some localities (i.e. Pantokratoros monastery), where they maintain a deformed pillow structure, which could point to their basaltic protolith origin. The typical mineral

assemblage consists of hornblende, plagioclase (An 20-40), epidote and zoisite, quartz, whereas garnet, rutile and titanite exist as accessory minerals.

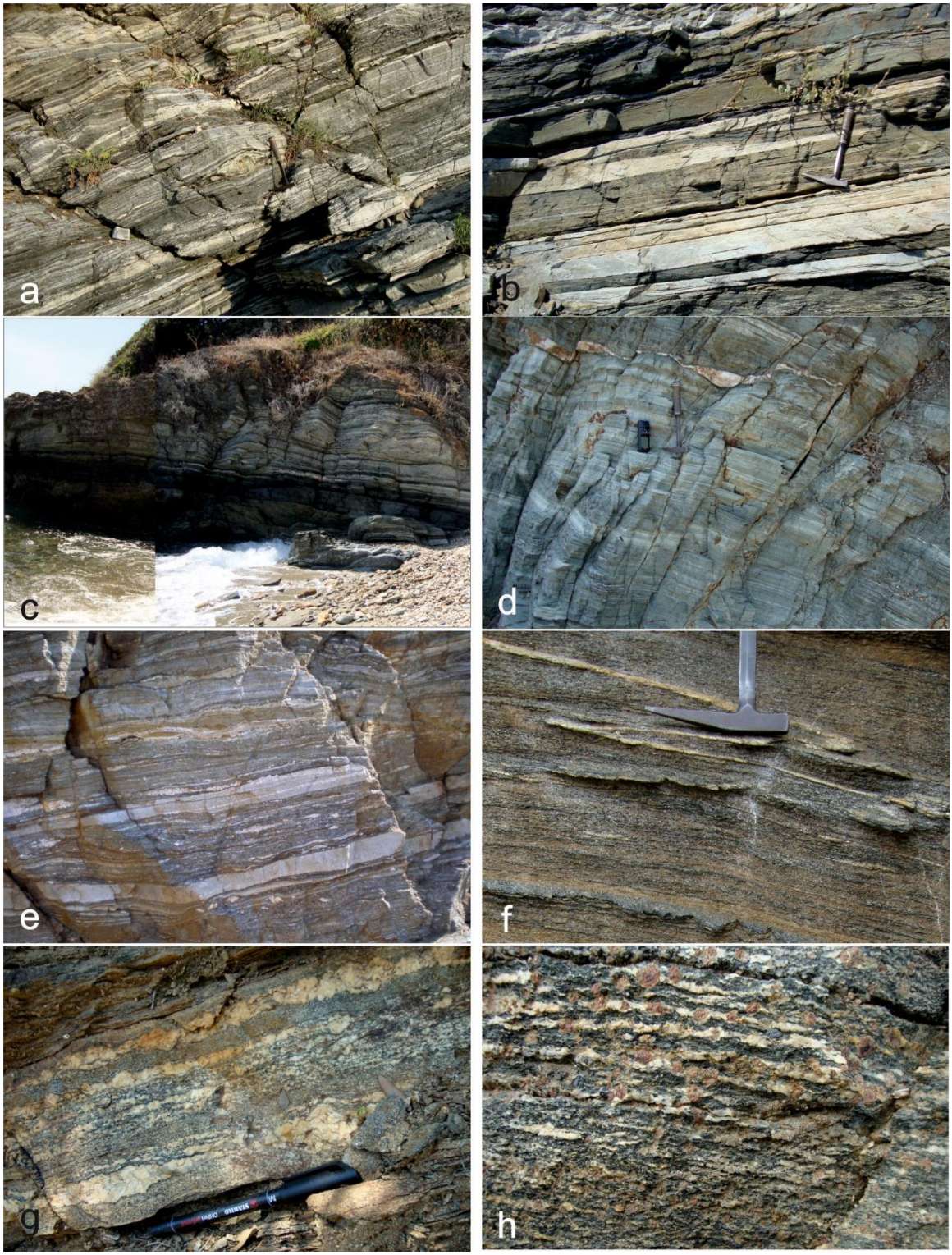

Fig. 2.3. Amphibolite gneiss images, underlying the two mica-gneiss: a) Migmatitic, well-foliated, hornblende-biotite gneiss, with boudinaged, calc-silica-gneissic lenses, parallel to the foliation, SSE of

Xenofontos monastery, b) Migmatitic, fell-foliated, layered amphibolite gneiss, SSE of Pantokratoros monastery, c) Migmatitic, fell-foliated, layered amphibolite gneiss, NNW of Iviron monastery, d) Fine-grained, thinly-foliated, amphibolite gneiss, at Iviron monastery, e) Migmatitic, coarse-grained, horneblende-biotite augen-gneiss, with inlayers of the leucogneiss and calc-silica-gneiss map unit, at Esfigmenou monastery, f) Well-foliated, horneblend-biotite amphibolite gneiss, ENE of Esfigmenou monastery, g) Migmatitic, amphibolite gneiss, E of Zografou monastery, h) Coarse-grained, garnet-amphibolite gneiss, E of Esfigmenou monastery.

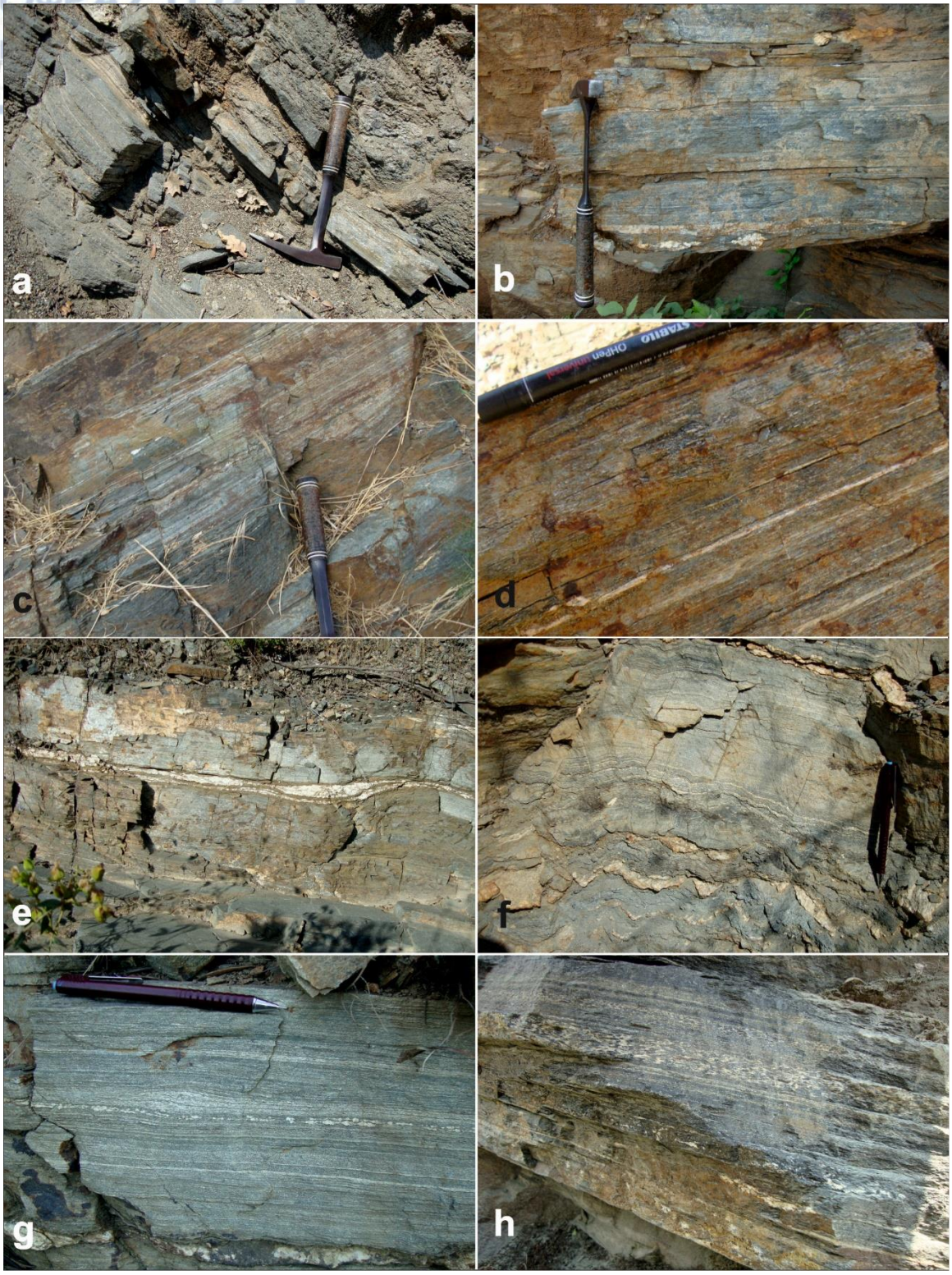

Fig. 2.4. Amphibolite gneiss map unit images, overlying the two mica gneiss map unit: a) Well-foliated, thinly banded amphibolite gneiss, WSW of Karyes, b) Well-foliated, thinly banded amphibolite gneiss, at Karyes, c) Well-foliated, thinly banded amphibolite gneiss, WNW of Vatopedi monastery, d) Well-foliated, thinly banded amphibolite gneiss, E of Vatopedi monastery, e) Well-foliated, thinly banded amphibolite gneiss, W of Vatopedi monastery, f) Well-foliated, thinly banded amphibolite gneiss, W of

Vatopedi monastery, g) Well-foliated amphibolite gneiss, W of Vatopedi monastery, h) Well-foliated, amphibolite gneiss, with occasional migmatitic layers, NNW of Pantokratoros monastery.

Biotite gneiss

The biotite gneiss, as the underlying amphibolite gneiss, also underlies and overlies the two mica-gneiss map unit. The underlying counterpart mainly appears at the western part of the study area and more specifically as an inlayer within the amphibolite gneiss, at the vicinity of Xenofontos, Konstamonitou, Zografou and Esfigmenou monasteries, occasionally coming in contact with the two-mica gneiss as well, due to the effect of an isoclinal folding, which will be described in the according chapter later on. The overlying part mainly outcrops in the central part of the study area, W-NW of Karyes, but also E and W to NW of Vatopedi monastery. It is generally dark gray to blueish gray in color, medium to coarse-grained and well-foliated (Fig. 2.5a-h). It exhibits a lithological grading towards the amphibolite gneiss, with mineralogical variations between horneblende-biotite to biotite-horneblende gneisses. The biotite gneiss, structurally located beneath the two mica-gneiss map unit, is characterized by a migmatitic texture and layering, with the occasional, characteristic appearance of feldspar augens as well as feldspar-quartz aggregate augens, ranging from few mm to several cm wide. Calc-silicate layers can also be observed at places, in this part of the map unit, quite frequently boudinaged, whereas the occurrence of concordant, leucogneissic/pegmatoid bodies is much more intense. The part of the biotite gneiss, structurally situated above the two mica-gneiss, appear more homogeneous, texture-wise (Fig. 2.6a-d). Its typical mineral assemblage consists of: plagioclase, biotite, sphene, apatite and epidote.

Fig. 2.5. Biotite gneiss map unit images, structurally underneath the two mica-gneiss map unit: a) Migmatized biotite- to biotite-horneblende gneiss, with an occasional augen texture and the presence of cm-long quartzofeldspathic aggregates, at Xenofontos monastery, Migmatized biotite-horneblende layered gneiss, with foliation-parallel leucogneissic bands, SSE of Xenofontos monastery, c) Migmatitic, augen-biotite gneiss, E of Esfigmenou monastery, d) Migmatitic, biotite-gneiss, Eof Zografou monastery,

e) Relatively homogeneous, well-foliated, biotite-horneblende gneiss with migmatitic leucogneiss inlayers, ESE of Esfigmenou monastery, f) Relatively homogeneous biotite gneiss with foliation-parallel, boudinaged, pegmatoid beads, E of Esfigmenou monastery, g) Well-foliated, migmatitic, augen-biotite gneiss, at Xenofontos monastery, h) Well-foliated, biotite augen-gneiss, E of Esfigmenou monastery.

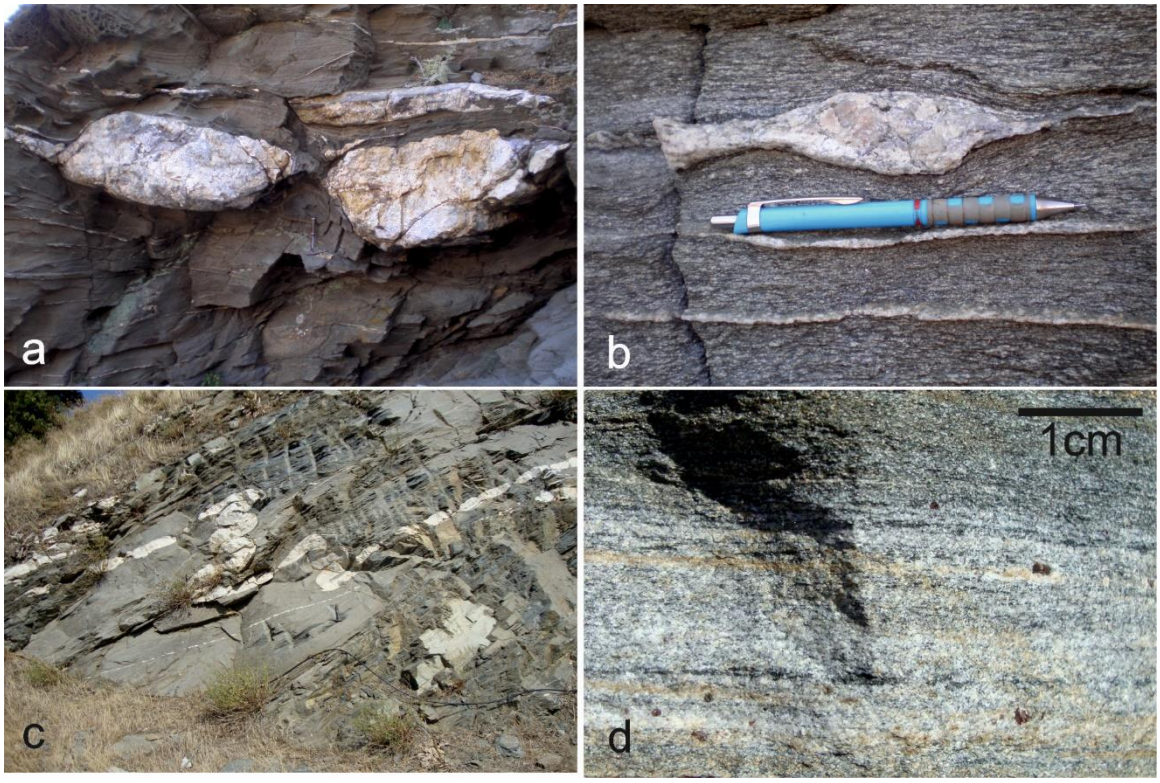

Fig. 2.6. Biotite gneiss map unit images, structurally located above the two mica gneiss map unit: a) Homogeneous, biotite gneiss with boudinaged leucogneiss inlayers, SSE of Esfigmenou monastery, b) Detail of the afore-mentioned, homogeneous, biotite-gneiss, SSE of Esfigmenou monastery, c) Homogeneous, biotite-gneiss, run-through by pegmatoid veins, folded and boudinaged, E of Karyes, d) Close-up view of fine-grained, biotite-horneblende gneiss, with occasional garnets, E of Xenofontos monastery.

Two-mica gneiss

The two-mica gneiss occurs mainly along the central part of the study area, in the areas of Xenofontos, Dochiariou, W of Vatopedi and S-SE of Esfigmenou monasteries, as well as the eastern part in the vicinity of Karyes, Stavronikita, W of Pantokratoros and S-SE of Vatopedi monasteries. It is grey to brownish grey in color, predominantly fine to medium-grained and acquires a flaser or even augen texture only at places (Fig. 2.7a-h). The ratio of the two micas, biotite and muscovite, varies from place to place, leading to an either biotite-muscovite or muscovite-biotite gneiss composition. At certain localities

the contribution of biotite to the overall mineral composition diminishes and the rock transcends to a brownish white leucocratic muscovite gneiss. The two-mica gneiss is well-foliated and banded, the thickness of the latter usually being a few cm, and it is scarcely run through by sub-parallel or concordant pegmatoid veins or boudinaged beads, ranging from tens of cm to few m in thickness. Migmatization images are not so frequent or intense as in the lower amphibolite and biotite gneiss map units and are mainly limited at the lower boundary with the afore-mentioned units. Accordingly these concordantly emplaced to the main foliation pegmatoid bodies, which have been correlated with the leucogneiss map unit, are almost completely absent from the two-mica gneiss map units. The rock mesoscopically refers to a sedimentary parent rock and origin.

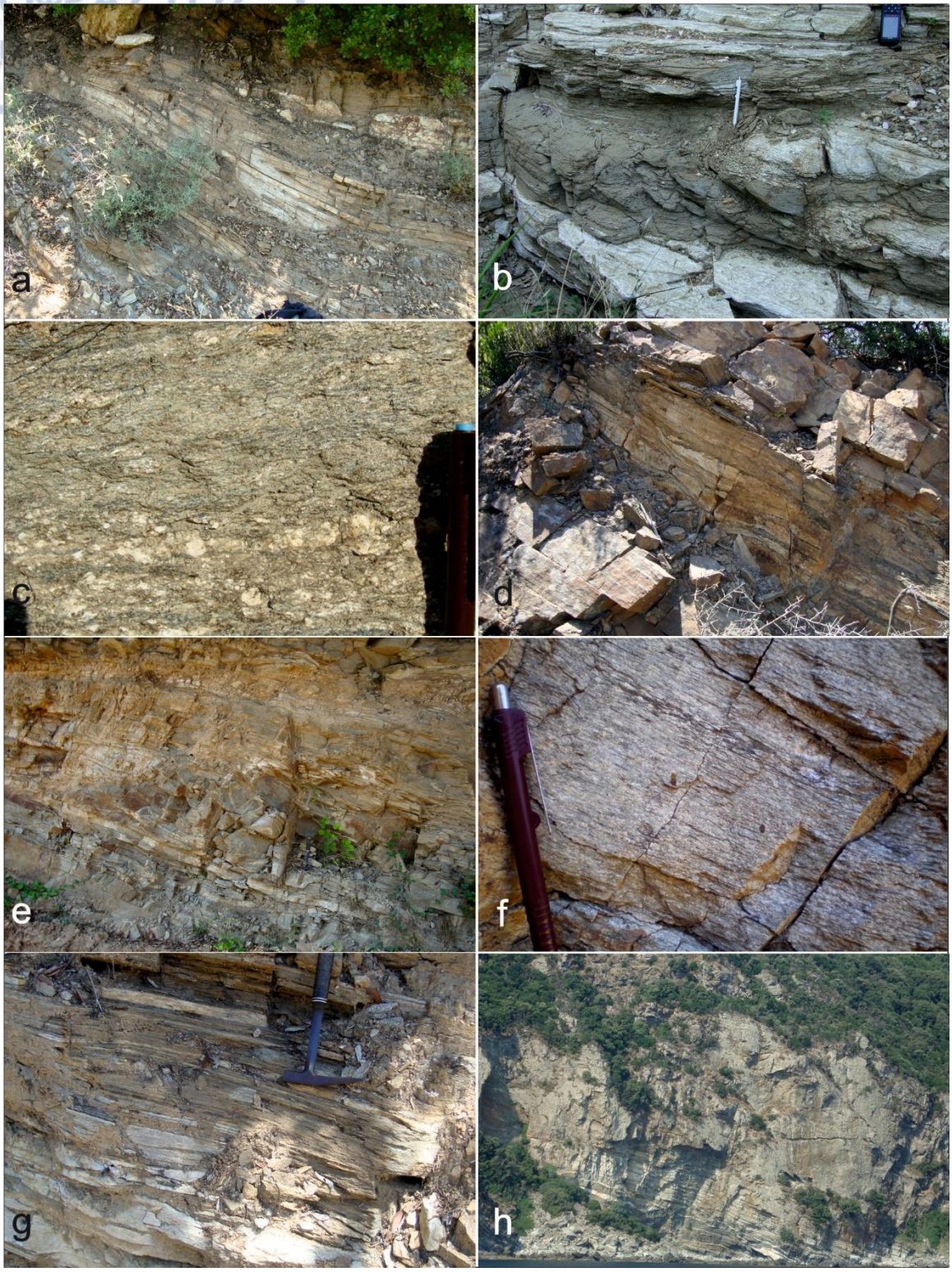

Fig. 2.7. Two mica gneiss map unit images: a) Isoclinally folded, well-foliated two-mica gneiss, E of Konstamonitou monastery, b) Isoclinally folded alterations of white, muscovite-rich gneiss layers and biotite-rich, schistose layers, both belonging to the two-mica gneiss map unit, E of Konstamonitou monastery, c) Well-foliated two-mica gneiss, WSW of Vatopedi monastery, d) Two-mica gneiss NNw of Pantokratoros monastery, e) Two-mica gneiss with very little signs of migmatization processes, E of Pantokratoros monastery, f) Well-foliated, two mica gneiss colse to the unit's upper boundary with the

amphibolite gneiss map unit. Notice the S-C fabric developed in the two-mica gneiss, g) More mesoscopic view of the well-foliated, two mica gneiss at its upper boundary with the amphibolite gneiss map unit, h) Lower boundary of the two-mica gneiss map unit with the amphibolite gneiss map unit NW of Pantokratoros monastery. Notice the migmatitic texture within the amphibolite gneiss map unit and the accumulated leucogneissic material, in the form of a m-thick layer along the contact of the two afore-mentioned map units.

Ultra-mafic/mafic map unit

The ultra-mafic/mafic map unit occurs as scattered, elongate, lenticular bodies, from tens of m to few hundreds of m in length and up to tens of m in thickness, mainly in the central part of the study area (Fig. 2.1). They are characteristically found within the amphibolite and biotite-gneiss map units, close to their contact with the two-mica gneiss map unit. They are also in contact with the marbles, whereas they are absent from within the body of the two-mica gneiss map units. They are composed of ultra-mafic to mafic rocks and more specifically dark to light green meta-peridotites, quite frequently serpentinized, lherzolitic at places, subordinated by dark green pyroxenites, often partly altered to a pale green color, meta-gabbros and pale greenish white talc-schists (Fig. 2.8a-h). It seems that their contacts follow concordantly the foliation of the country rocks, whereas they display at places intense signs of shearing and deformation, appearing as tectonic lenses/slivers within the afore mentioned map units.

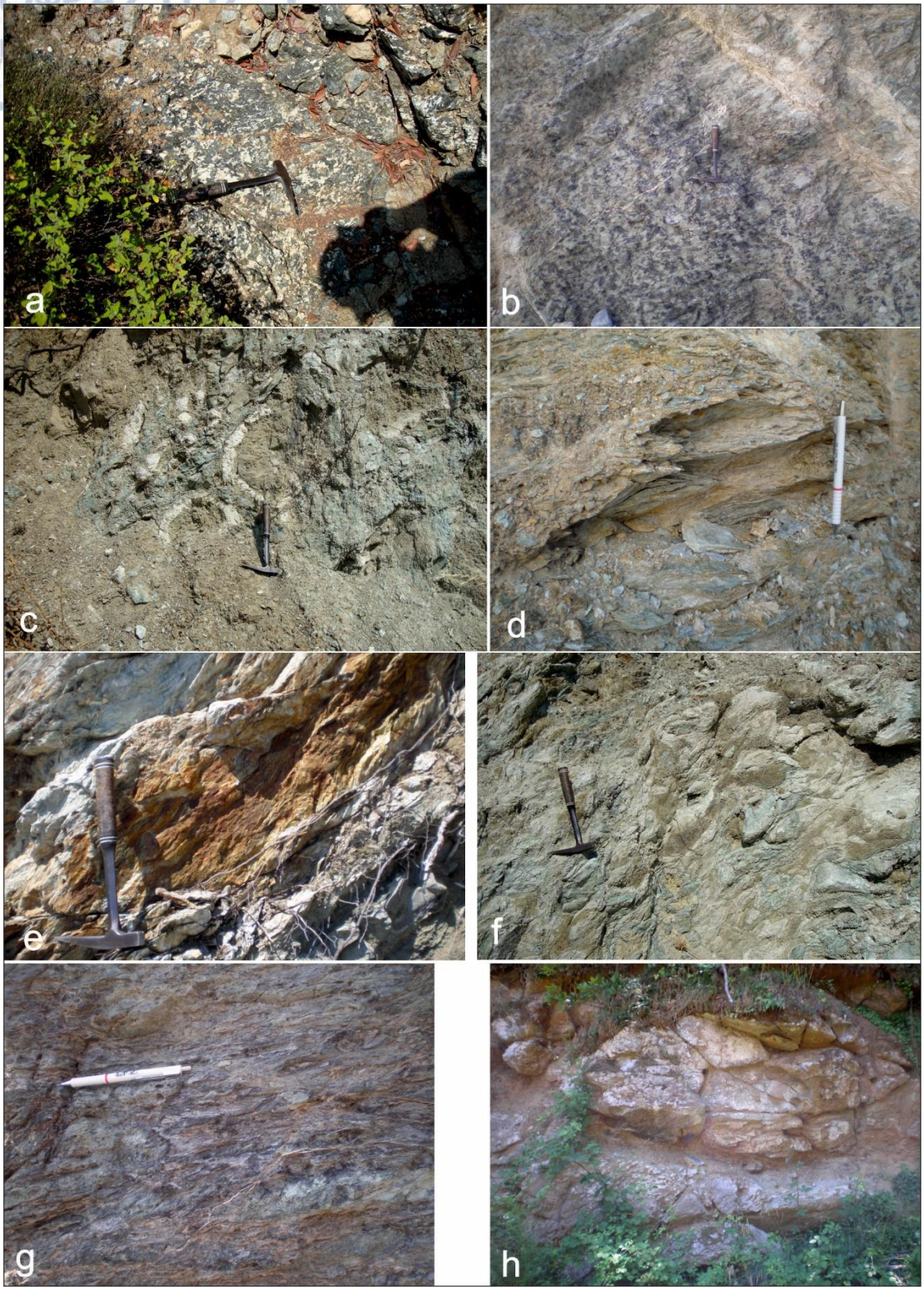

Fig. 2.8. Ultra-mafic/mafic map unit images from the study area: a) Gabbros, at the boundary of the amphibolite and biotite gneiss map units, ENE of Dohiarion monastery, b) Lherzolitic parts of the ultramafic rocks, as tectonic slivers within marbles and amphibolites intercalations, at Dohiarion monastery, c) Structures resembling pillow-lavas in the ultramafic/mafic map unit, d) Intensely sheared,

serpentinized ultramafic rocks, parts of a tectonic sliver within marbles and amphibolites intercalations, at Dohiarion monastery, e) Sheared, serpentinized, ultramafics, separating marbles and the amphibolite gneiss, NNW of Xenofontos monastery, f) Serpentinized, ultramafic counterparts, W of Xenofontos monastery, within the biotite gneiss map unit, g) Sheared lherzolititc counterparts of ultra mafic rocks, NNW of Dohiarion monastery, h) Ultramafic tectonic lense within the amphibolite gneiss map unit, few m above its contact with the two-mica gneiss map unit, NE of Karyes.

Below follow the lithological descriptions of the leucogneiss and the calc-silicate rocks, which were identified in the study area, but were not mapped as separate map-units:

Leucogneiss

The leucogneiss mainly occurs both along the western and eastern contact of the amphibolite gneiss and biotite gneiss map units with the overlying two-mica gneisses and its main exposure is in the vicinity of Esfigmenou, Zografou, Konstamonitou and Xenofontos monasteries to the W and Pantokratoros, Stavronikita, Iviron monasteries to the E. It is a coarse-grained leucocratic biotite-muscovite quartzofeldspathic gneiss that at places has a flaser to augen gneiss texture (Fig. 3.9a-f). It is generally well-foliated, appearing as cm to meters thick bands mostly within the lower amphibolites and biotite gneiss map units and their boundary with the two-mica gneiss, is always parallel or sub-parallel to the main foliation. Banding varies from few cm to several meters in thickness. The leucogneiss exhibits a characterictic increased strain gradient, usually expressed via its frequent and intense augen texture. Its typical mineral assemblage consists of microcline (occasionally bearing a perthitic texture), plagioclase (showing in specific samples a microscopic intergrowth with quartz crystals and therefore myrmekite texture), white mica, biotite, quartz and epidote, garnet and rutile, zircon as accessory minerals. It mesoscopically refers to an initial felsic melt.

Fig. 2.9. Leucogneiss map unit images from the study area: a) Large-scale, boudinaged leucogneiss bead, foliation-parallel and within the biotite gneiss map unit, SE of Esfigmenou monastery, b) m-thick bands of leucogneiss, parallel to the well foliated amphibolite and horneblende-biotite gneiss layers, E of Esfigmenou monastery, c) Detail of the afore-mentioned leucogneissic bands, within the amphibolite gneiss map unit, coarse-grained and obtaining an intense augen texture, of quartzofeldspathic material, E of Esfigmenou monastery, d) Leucogneissic bands, parallel to the well-foliated amphibolite gneiss map

unit, at Pantokratoros monastery, e) Leucogneissic band, bearing an augen texture, within the also migmatized biotite gneiss map unit, E of Zografou monastery, f) Leucogneiss band, foliation-parallel from the amphibolite gneiss map unit, E of Esfigmenou monastery.

Calc-silicates

Calc-silicate rocks appear either in the form of isolated bands or lenses and boudins within the amphibolites and the biotite-gneiss or in the form of schist-inlayers within the marbles. In the former case they are pinkish white in color, due to the plagioclase, calcite and occasional garnet, with green patches, due to the epidote and diopside at places. Within the marbles they appear as dark blueish grey schists, primarily composed of calcite, biotite, epidote and actinolite. In the western part of the study area calc-silicates appear along the contact of the structurally lower marbles with the overlying amphibolite and biotite gneiss map units, within both map units and can be used as a structural marker for the specific contact as we relocate calc-silicates within the amphibolite unit in the eastern part of the study area as well.

2.3. Contacts between map units

Marbles-Lower amphibolite gneiss contact

The contact between the marbles map unit and the overlying lower amphibolite gneisses can be observed at the westernmost part of the study area. It is generally normal, in the vast majority of the locations it was observed. It does not show signs of shearing, even though, the whole body of the rocks comprising the study area are generally strongly deformed and sheared. Moreover the existence of calc-silicates, both within the marbles map unit, mainly as intercalations of calc-silicate, amphibole schists, and within the lower amphibolite gneisses, mainly in the form of calc-silicate gneiss inlayers, points towards a diffusion between these two map units and along their normal contact. In the northwestern part of the study area, at the vicinity of Esfigmenou monastery, the contact between the marbles and the amphibolite gneiss is tectonic due to a later NNW-SSE trending, high angle fault-zone, few m in thickness, which has displaced the initial contact.

Amphibolite gneiss-Biotite gneiss contacts

The contact between the amphibolite gneiss and the biotite gneiss map unit has been observed both at the structural segment underlying the two mica-gneiss as well as the overlying segment. As far as the underlying segment is concerned, the specific contact was studied in the western part of the study area and the vicinity of Xenofontos, Dohiariou, Konstamonitou, Zografou and Esfigmenou monasteries. Here the amphibolite gneiss has been found to underlie and overlie the biotite gneiss. This contact is partly characterized by intense shearing, quite frequently expressed in the form of mylonitic zones, usually tens of cm thick, where the biotite gneiss acquires an augen texture, but also in the form of thinner and sharper shear zones juxtaposing the two map units. Consequently, both map units occasionally exhibit an intense mylonitic foliation along their contact, which frequently constitutes shear zones of varying thickness, whether it is the biotite gneiss overlying the amphibolite gneiss or the opposite. However, it is very common at various localities to observe a lithological grading of one map unit into the other, with the appearance of lithologically intermediate variations of the two map units, in the form of horblende-biotite gneisses and biotite-hornblende gneisses respectively, thus leading us to overall characterize the specific contacts as normal.

The contact between the structurally higher counterparts of the amphibolite gneiss and the biotite gneiss was documented and observed mainly at the central part of the study area. The amphibolite gneiss has been found to underlie the biotite gneiss map unit. They generally exhibit, once more, a distinctive grading from one map unit to the other, as already mentioned for their structurally lower counterparts, which is more prominent due to the less overall migmatitic layering, a more thinly layered gneissic texture in the amphibolite gneiss map unit and finally a more homogeneous texture characterizing the biotite gneiss map unit, above the two mica-gneiss. In most localitites this lithological grading strongly advocates towards an overall normal contact. However, a generally high strain gradient has been documented throughout the whole body rock of this map units' counterpart as well. Moreover, numerous slivers of ultra-mafics are found along the contact between them, also indicating the presence of an intense shearing. Therefore, the two map units seem to lithologically relate to one another and to normally come in contact, yet also exhibit signs of shearing, possibly attributing their repetition at places to

shearing in combination with an isoclinal folding event (the latter will be described and analyzed in the according chapter).

Two mica-gneiss - Amphibolite gneiss contacts

The contacts between the amphibolite gneiss and the two-mica gneiss have been observed in various locations, mainly in the central part of the study area. Both underlying and overlying contacts have been recognized as tens of m thick shear zones of growing intensity towards the actual contact. The two-mica gneiss acquires an augen texture of growing intensity when reaching both contacts. The lower amphibolite gneiss also becomes intensely porphyroblastic, with garnet augens growing along its contact with the two-mica gneiss, whereas slivers of ultra-mafics and marbles have been recognized along the contact of the amphibolite gneiss overlying the two-mica-gneiss map unit. A mylonitic foliation has been documented along both contacts and thinner, more district shear zones also occur within the afore-mentioned map units themselves. An interesting observation concerning these contacts was that the leucogneiss map unit, even though strongly evident and showing signs of intense shearing within the amphibolite and biotite gneiss map units, close to their contact with the two-mica gneiss, was almost, if not completely, absent from within the two-mica gneiss map unit.

Leucogneiss contacts

The leucogneiss map unit has been documented mainly within the amphibolite and biotite gneiss map units underlyng the two mica-gneiss, the biotite gneiss map unit, structurally situated above the two mica-gneiss. Whenever present, the leucogneiss appears sheared by a strong mylonitic foliation, parallel to sub-parallel to its neighboring units, frequently boudinaged and giving the impression of a former leucocratic magmatic body, brought into concordance with the afore-mentioned map units during an intense shearing event.

2.4. Lithological correlation with existing units

Taking into account the lithological description of the map units comprising the body rock of the study area, a correlation is attempted with the Kerdyllion and Vertiskos Units, as they were originally defined by Kockel et al. (1977), who also undertook the research and compilation of the I.G.M.E Athos Peninsula sheet (Fig. 1.2).

The blueish, generally thinly bedded marbles, with the biotite, calc-silica schists, of the study area fit very well with the Kerdyllion upper marbles horizon, as the latter was described by Kockel et al. (1977). The amphibolite and biotite gneiss map units even though they present at places non-normal contacts, in the sense that usually shear zones constitute their boundaries, they, however, exhibit a lithological relation between them, since a lithological grading can be observed from one amphibole-rich end member to the other biotite-rich end member. Moreover the description of the Kerdyllion Unit by Kockel et al. (1977) as mainly fine to medium-grained, well-banded biotite gneisses, with extensive signs of regional anatexis and concordant hornblende-biotite, biotite-hornblende gneisses and occasional garnet-epidote-rich, calc silicate rocks seems to also fit well with the amphibolite and biotite gneiss map units, also exhibiting signs of anatexis and an analogous lithological grading from one unit to the other. Bearing also in mind the fact that in various locations the contact between the lower amphibolite gneiss map unit and the marbles was not identified as sheared, plus the fact that marbles and amphibolite gneiss intercalations do exist in the study area, these three map units: marbles, lower and upper amphibolite and biotite gneisses, are considered as part of the Kerdyllion Unit.

Concerning the protolith origin of the amphibolite gneiss assigned to the Kerdyllion Unit in the study area the following can be stated: The Kerdyllion Unit has been interpreted by Kockel et al. (1977), as an originally greywacke-arkose series, also including marls and carbonate rocks. Nevertherless, according to the same authors, a characteristic lack of alluminosilicates has been observed for the rocks of the Kerdyllion Unit and the amphibolites conclusively, a fact that was also verified by this dissertation as an overall absence of alluminosilicates was observed in the respective samples. The amphibolitic rocks of the study area mesoscopically refer to an ortho-origin, rather than a sedimentary protolith. Moreover, geochemical data from amphibolitic samples of the study area (Himmerkus et al., 2011) also point towards an ortho-origin, whereas previous researchers have also argued towards a magmatic origin of the amphibolites found both in Vertiskos and Kerdyllion Units in other study areas (Kassoli-Fournaraki, 1982; Sapountzis et al., 1990).

According to the present researcher, this intercalation of marbles, amphibolite gneisses, biotite-gneisses and occasional calc-silicates (as a sign of diffusion between the

marbles and the amphibolite gneisses), assigned to the Kerdyllion Unit, could point towards a metamorphosed volcaniclastic/volcano-sedimentary sequence primarily composed of carbonate, basaltic and clay components.

Accordingly the two-mica gneiss map unit, varying between biotite-muscovite, muscovite-biotite composition, falls well within the description of Vertiskos Unit by Kockel et al. (1977). The two-mica gneiss map unit mesoscopically refers to a sedimentary parent rock and origin, as already indicated by Kockel et al. (1977), who assigned it to the Vertiskos meta-sedimentary sequence in the I.G.M.E. Athos Peninsula, geological map sheet and related it with a series of arkoses, greywackes and shales.

Kockel et al. (1977) identified the leucocratic bodies scattered within the metamorphic rocks of the study area as part of the Plagioclase-microcline gneiss map unit in their map. They considered these bodies as initial syn-orogenic granitic bodies, intruding in large sheets within both the Vertiskos and Kerdyllion Units. However, these bodies, namely herein leucogneiss, bear intense signs of anatexis and are closely related with the migmatization only within the amphibolite and biotite gneiss map units. They fit much better with the anatexites, Kockel et al. (1977) describe as a characteristic feature of the Kerdyllion Unit, and the Amoulliani Unit, described as quartzofeldspathic gneisses and anatexites-granitic gneisses by Plougarlis and Tranos (2014).

The ultra-mafic/mafic map unit can be correlated with the Therma-Volvi-Gomati complex, considered as a dismembered ophiolite by Dimitriadis (1980), occurring at the boundary between the Vertiskos and Kerdyllion Units and including both mafic and ultra-mafic rocks. The Volvi mafic counterparts of the afore-mentioned complex were interpreted as in-situ, rift-related ophiolites by Dixon and Dimitriadis (1984).

2.5. Description of cross sections

Three detailed cross-sections were constructed, after the collection of structural data and observations in the field, in the western and eastern part of the study area (Fig. 2.10), in order to better understand and consequently interpret the structural relationship between the map units and the Units they represent.

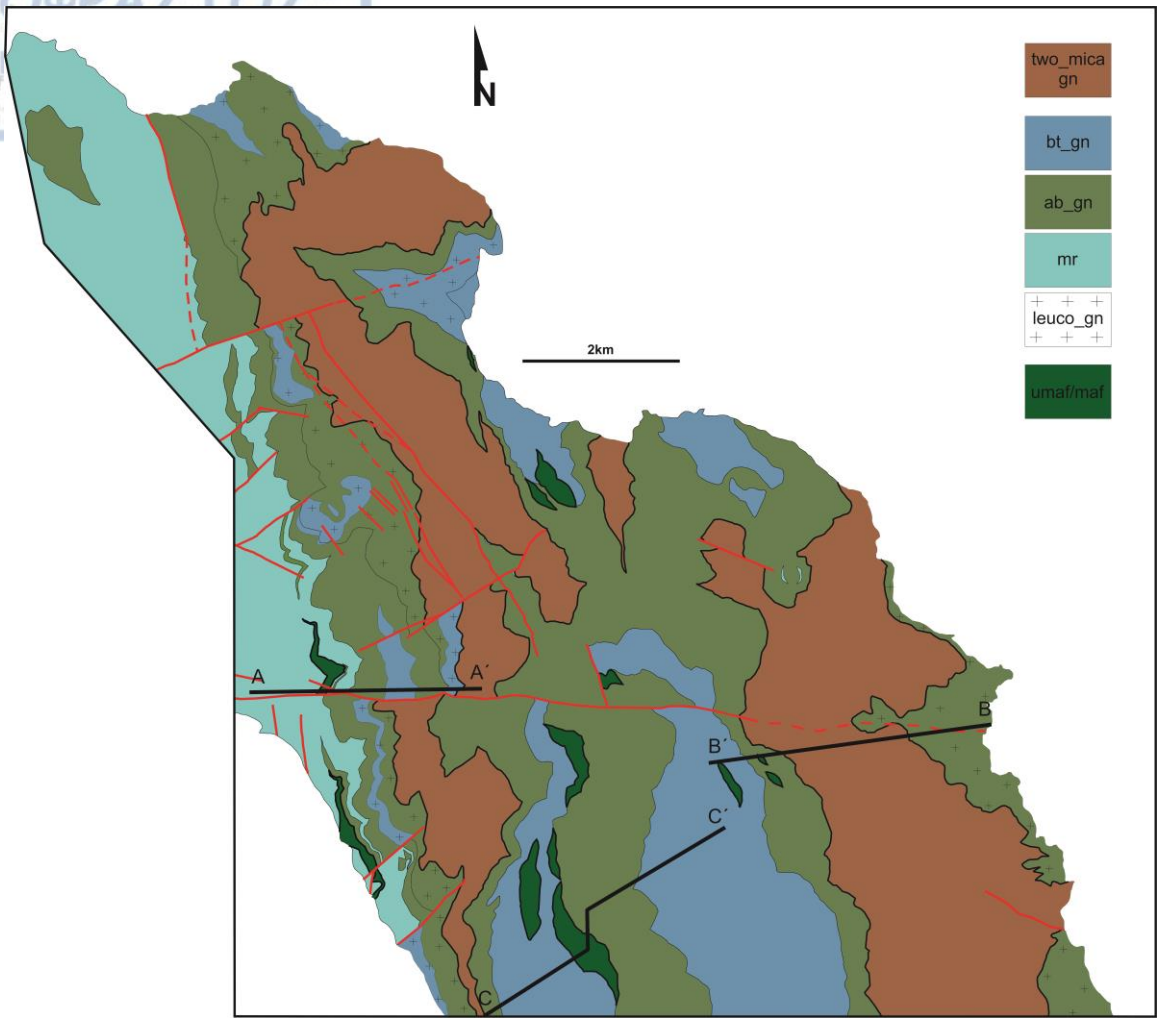

Fig. 2.10. Location of the three detailed cross-sections in the study area.

The A-A΄ cross-section refers to the western coast of the northern part of the Athos peninsula and is located at the vicinity of Konstamonitou monastery (Fig. 2.10). It trends E-W and the following can be observed, gradually moving from the W to the E and the lower to the higher structural levels (Fig. 2.11):

- At the western part of the cross-section, the marbles gently dip towards the E and underlie conformably the amphibolite gneisses. Numerous locations along this contact, where alternations of marbles and amphibolite gneisses exist, advocate for the normal contact with the overlying amphibolite gneisses. Within the marbles calc-silicates, occasionally amphibole-schists have been found, especially close to mafic-ultramafic rocks. The latter occur as tectonic slivers tectonically emplaced parallel to the main foliation of the marbles.

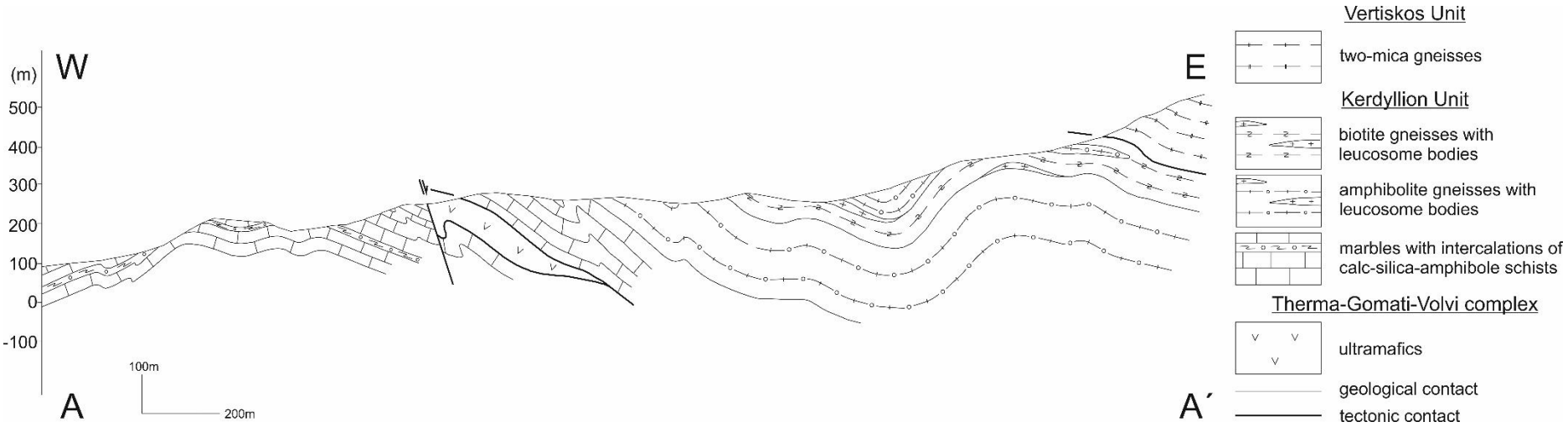

Fig. 2.11. Cross section at the vicinity of Konstamonitou monastery.

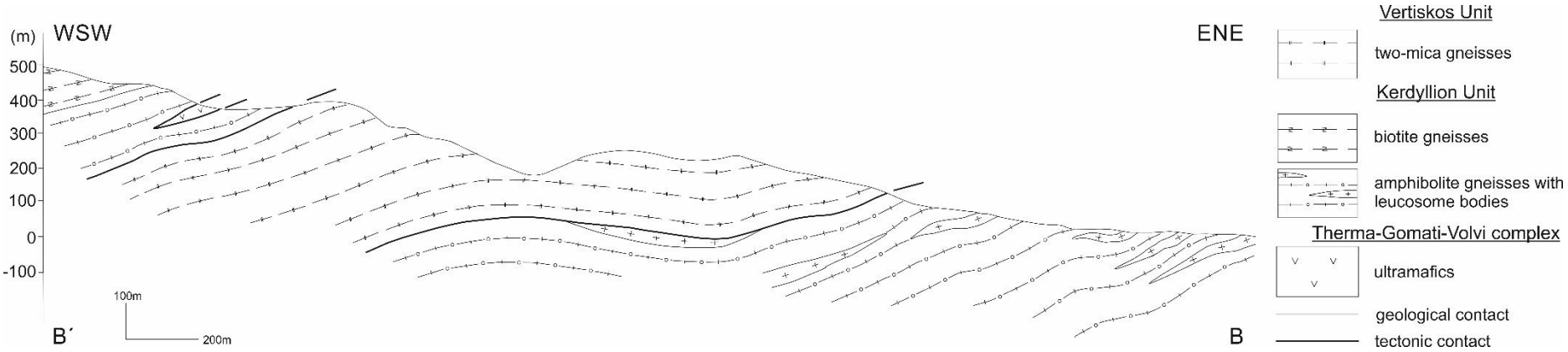

Fig. 2.12. Cross section at the vicinity of Pantokratoros monastery.

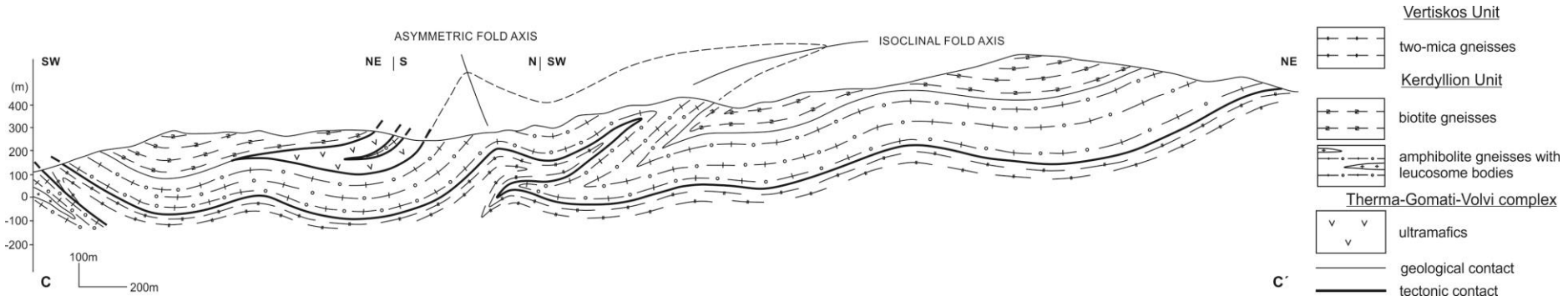

Fig. 2.13. Cross section at the vicinity of Xenofontos monastery.

- At the central part of the cross-section, the amphibolite gneisses pass upwards to biotite gneisses through successive alternations between them; a fact that advocates for the normal contact between them. However, these alternations could be further enhanced from multiplications due to isoclinal to tight folding, as shown by the many folds of this type that have been observed in both lithologies. The above-mentioned lithologies indicate intense migmatization and shearing. Because of this, abundant are the concordantly emplaced lense-shaped leucogneiss bodies, which form distinct layers being more abundant towards the uppermost part of the biotite gneiss, underlying the two-mica gneiss.

- At the easternmost part of the cross-section, the biotite gneiss gently dips to the E and underlies the two-mica gneisses. The contact is a ductile shear zone associated with an intense mylonitization and strongly imprinted stretching lineation trending N-S. Shear sense indicators observed both in the field and rock thin sections show a top-to-the S sense of shear.

- Variations on the geometry of the main foliation and deviations from the low undulating angles governing the overall structure (Fig. 2.11) are due to refolding from horizontal, inclined to inverted and close to open folds, although occasionally upright folds can be observed. These folds trend N-S to NNW-SSE and form synforms and antiforms with medium to high angles as depicted in the cross-sections with vergence mainly to the W to WSW.

The B-B′ cross-section refers to the eastern coast of the northern part of the Athos peninsula and is located at the vicinity of Pantokratoros monastery (Fig. 2.10). It trends WSW-ENE and the following can be observed, drifting upslope towards WSW and the structurally lower to the structurally higher (Fig. 2.12):

- The overlying two-mica gneiss dips to the WSW, in a gentle undulating fashion and at the western part of the cross-section, the amphibolite gneiss overlies it. Their contact reveals the same features with those described above, apart from the sense-of-shear,

which is the top-to-the N, i.e., opposite to the previously mentioned. A fact suggesting inversion of the lithologies due to isoclinal folding.

- At the western part of the cross-section, mafic-ultramafic rocks outcrop as a tectonic sliver within the amphibolite gneiss and closer to their contact with the tectonically underlying two-mica gneiss. At the westernmost part, the biotite gneiss, once more gently dipping to the WSW, overlies the amphibolite gneiss, with a normal contact.

The C-C′ cross-section refers to the southeastern coast of the northern part of the Athos peninsula and is located at the vicinity of Xenofontos monastery (Fig. 2.10). It trends SW-NE and the following can be observed, drifting upslope towards NE and the structurally lower to the structurally higher (Fig. 2.13):

- At the southwesternmost part of the cross section the amhpibolte gneiss both tectonically underlies and overlies the two-mica gneiss, with both map units following a gentle dipping geometry towards the NE. The biotite gneiss normally overlies the amphibolite gneiss and then a mafic-ultramafic tectonic sliver interferes.

- At the central part of the cross section medium to high angles have been recorded in the map units, related with an asymmetric folding, which also affects and refolds large-scale, pre-existing, isoclinal folds. The interference of these two folding events will be analyzed further on in chapter 3.3. The amphibolite has been found to normally overlie the biotite gneiss, with a relatively low angle, due to the existence of an inverted limb belonging to an anti-form and related with the afore-mentioned isoclinal folding event.

-At the northeastern part of the cross section the biotite gneiss normally overlies anew the amphibolite gneiss, whereas the two-mica gneiss has been once more found to tectonically underlie the amphibolite gneiss.

Chapter 3. Structural analysis

3.1. Foliation

The dominant planar fabric documented in the study area is the namely in this dissertation S3 foliation, frequently expressed as a mylonitic foliation, generally following gentle angles of dipping towards the ENE. The second most intensely imprinted planar fabric is represented by a later S4 crenulation cleavage, much less prominent than the afore-mentioned mylonitic foliation, dipping with intermediate to high angles towards the E to ENE or the W to WSW and related with an asymmetric to steeply-inclined folding event. Besides these two most prominent foliations, other planar fabrics were also documented, both pre-dating and post-dating the S3 and S4, either as faint or transposed remnants of overprinted structures (S1 and S2 foliations) or later non-dominant planar fabrics (S5 foliation). Their description follows from the relatively oldest to the relatively youngest, as it was documented from overprinting and cross-cutting relationships in the field.

3.1.1. S1 foliation

S1 represents a primary foliation, which was associated with pegmatoid and aplitic veins, discordantly emplaced with reference to the main planar fabric, but cross-cut by the latter foliation, within the amphibolite gneiss, the biotite gneiss and the two-mica gneiss (Fig. 3.1). Such pegmatoid and quartz veins were also assosiated with an older foliation in previous studies (Sakellariou, 1989), concerning the Serbo-Macedonian massif, characterized by eclogitic metamorphic conditions (relics of which were not able to identify microscopically in this dissertation, due to the poly-metamorphosed history of the study area and the strong overprinting of later fabrics).

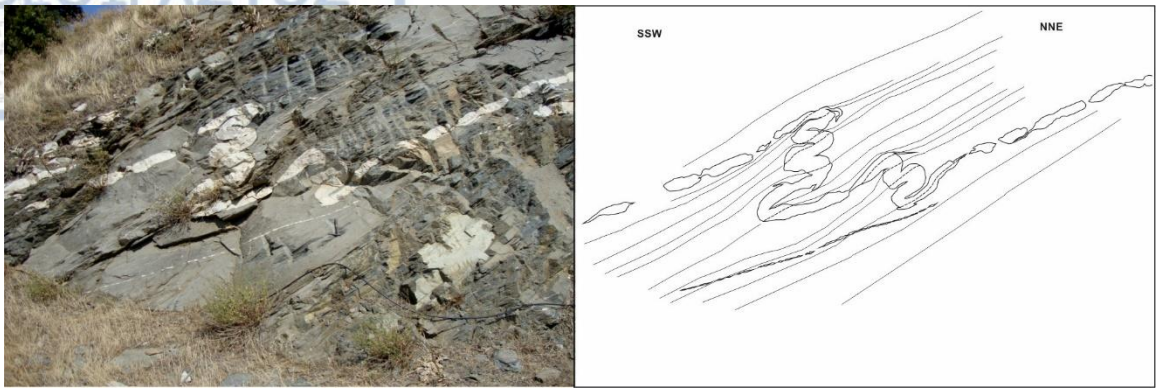

Fig. 3.1. Pegmatoid vein in the biotite gneiss, assosiated with the S1 foliation and discordantly emplaced with respect to the main planar fabric, represented by S3 foliation. Parts of the vein that are sub-parallel to the main planar fabric are boudinaged, whereas discordant parts are isoclinally folded, according to the domains of the flow regime the whole vein was later subject to. At some locations (upper central part of the photo) two successive isoclinal folding events can be distinguished related with the development of the S2 and S3 foliations respectively. Located ENE of Xenofontos monastery.

3.1.2. S2 foliation

The S2 foliation has been documented as a continuous foliation in the marbles, amphibolite gneiss, biotite gneiss and two-mica gneiss map units, but it is only locally preserved due to its overprinting by later deformational events and structures as will be discussed further on. When evident it is frequently assosiated with a recumbent to gently-dipping isoclinal folding, the latter represented by rootless, intrafolial, isoclinal folds (Figs 3.1, 3.2). Its initial orientation was not possible to determine as it has been forced into parallelism with the subsequent, dominant S3 foliation, to such an extent that it is often difficult to distinguish which structure is being observed and measured in the field. It is notably preserved in various localities where hinges, outlined by the S2 foliation occur and the S2 foliation has been deformed, cross-cut and crenulated by a later, horizontal to sub-horizontal S3 foliation (Fig. 3.2). Remnants of this S2 foliation were also recorded microscopically in the first generation of hornblende porphyroclast crystals, grown over this S2 foliation and surrounded by crystals of a second generation hornblende, of significantly smaller grain size, plagioclase and epidote mainly constituting the dominant S3 foliation, which will be described afterwards. More precisely, when observing these

older hornblende porphyroclasts in microscope, the S2 foliation is actually outlined as an internal foliation by the inclusion pattern within the hornblende porhyroclast, and has an angular relationship to the external subsequent, S3 fabric (Fig. 3.3). Even though the S2 foliation was documented in most map units, it was not documented in the ultra-mafic/mafic map unit.

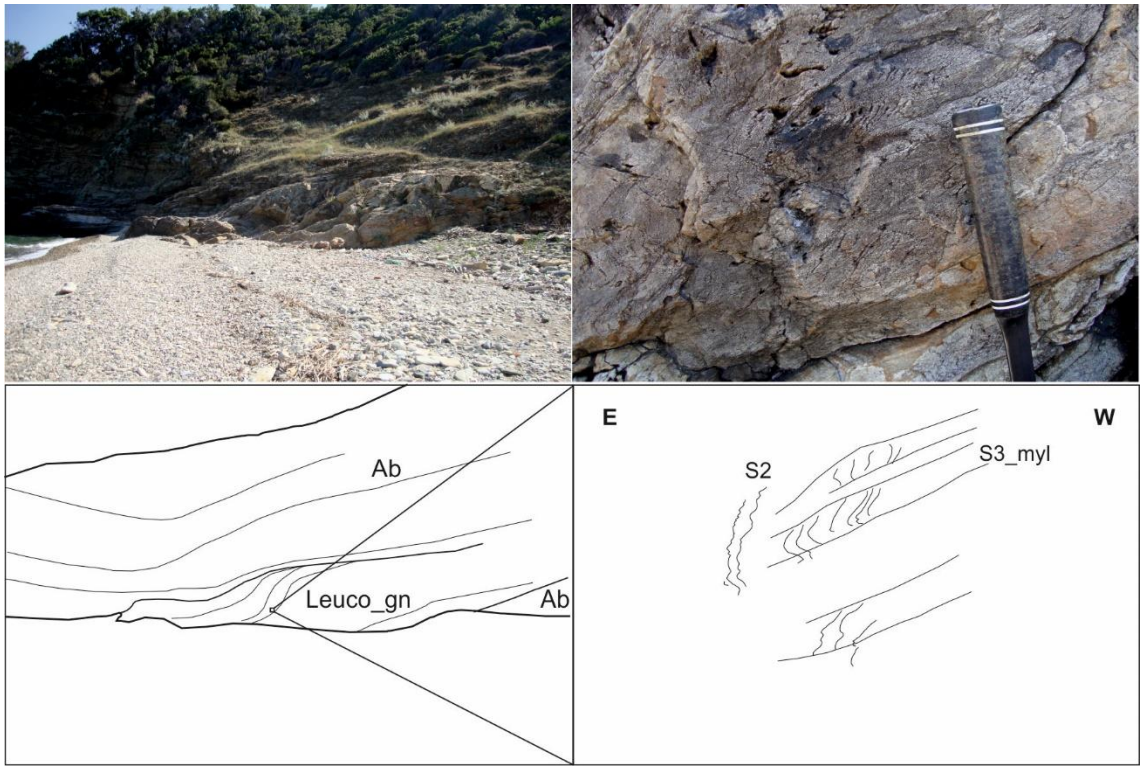

Fig. 3.2. Leucogneiss inlayer within the lower amphibolite gneiss map unit, at Pantokratoros monastery. S2 foliation has been preserved within the leucogneiss as a steeply dipping remnant fabric, probably also constituting a transpositioned F2 fold hinge. Both former structures are being sheared and transpositioned by a shallow-dipping to the E S3 mylonitic foliation, also characterizing the overlying and underlying amphibolite gneiss.

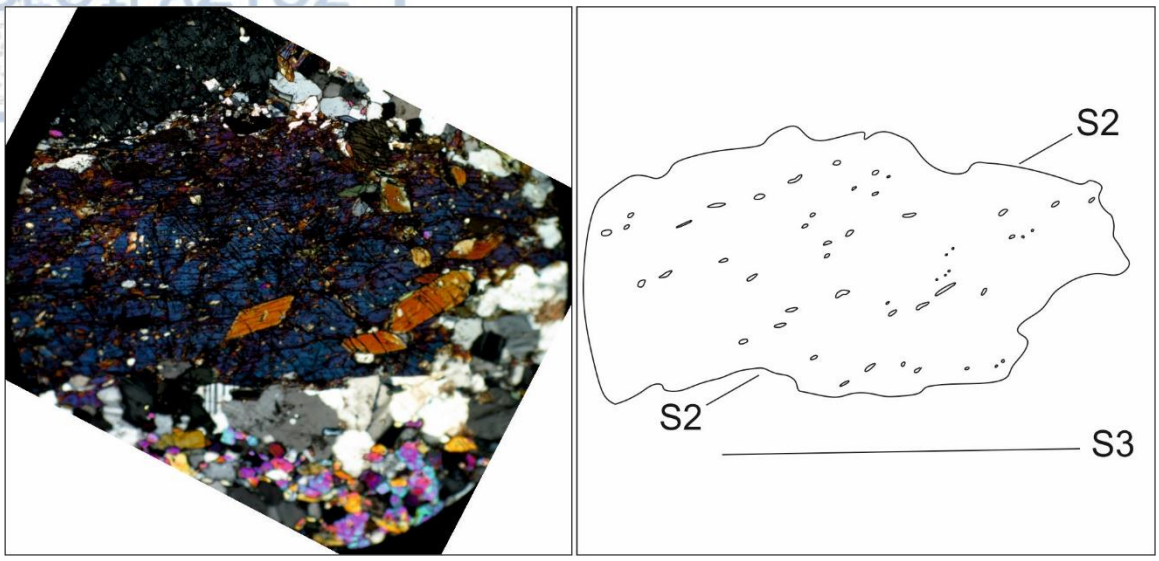

Fig. 3.3. Hornblende crystal associated with the syn-metamorphic amphibolite facies attributed to the S2 planar fabric. The inclusion pattern outlines a remnant S2 foliation in an angular relationship with the "external" horizontal S3, defined mainly by a second generation of hornblende crystals, of smaller grain size, plagioclase, epidote and quartz. Sample A_3, amphibolite gneiss underlying the two mica gneiss, NNW of Stavronikita monastery.

3.1.3. S3 foliation

S3 foliation is the dominant planar fabric in the study area recorded in all the map units of and was characterized as the "main foliation". It is a continuous foliation, comprised of the main minerals participating in the planar fabric of the majority of the map units. In the case of the ultra-mafic/mafic map unit the S3 is represented by a C-S mylonitic fabric and the development of C-type shear bands. In the rest of the map units it is frequently expressed as an active mylonitic foliation, since its fabric is strongly related with an intense syn-metamorphic shearing, which took place along with an isoclinal folding event. It has been found to affect and cross-cut pre-existing fabrics like the afore-mentioned S2 and also pegmatoid veins related with former fabrics and deformational events (Figs 3.1, 3.2). It prevails throughout the whole study area and has been the most strongly imprinted fabric on all the map units.

The S3 foliation mainly dips at low angles towards the ENE (Fig. 3.4), whereas medium to high angle surfaces also appear, but to a much lesser extent than the predominant low-angle overall structure. This low-dipping geometry can easily deviate from the ENE-

dipping norm, frequently exhibiting an undulating geometry, with the map units also dipping towards the W to WSW, but also N wards and S wards. Additionally, the spatial distribution of the S3 planes indicates the two most prominent low-angle concentrations, which suggest an overall isoclinal, recumbent folding (Fig. 3.4a), with a general N-S trending axis. The latter observation agrees with the structural data collected in the field, documenting and describing a dominant isoclinal folding of a respective geometry, which will be described later on and shows that it is not due to a statistical artifact.

Finally, bearing in mind that the study region is comprised of poly-metamorphosed, multi-deformed rocks one cannot oversee the fact such an analysis will inevitably incorporate geometries and deformational patterns that postdate the dominant structures described above and the deformation they represent. Since it has been concluded from field work observations and data that the S3 foliation is related to a general recumbent isoclinal folding and is attributed low angles, moderate and high angles, were also excluded, as shown in Fig. 3.4b, since they have been correlated with subsequent deformational events and in order to diminish their potential misleading to misinterpretations related with the dominant structure. This rationale was also followed in the further analysis of the S3 foliation performed and associated with the description of the folding (Chapter 3.3.3).

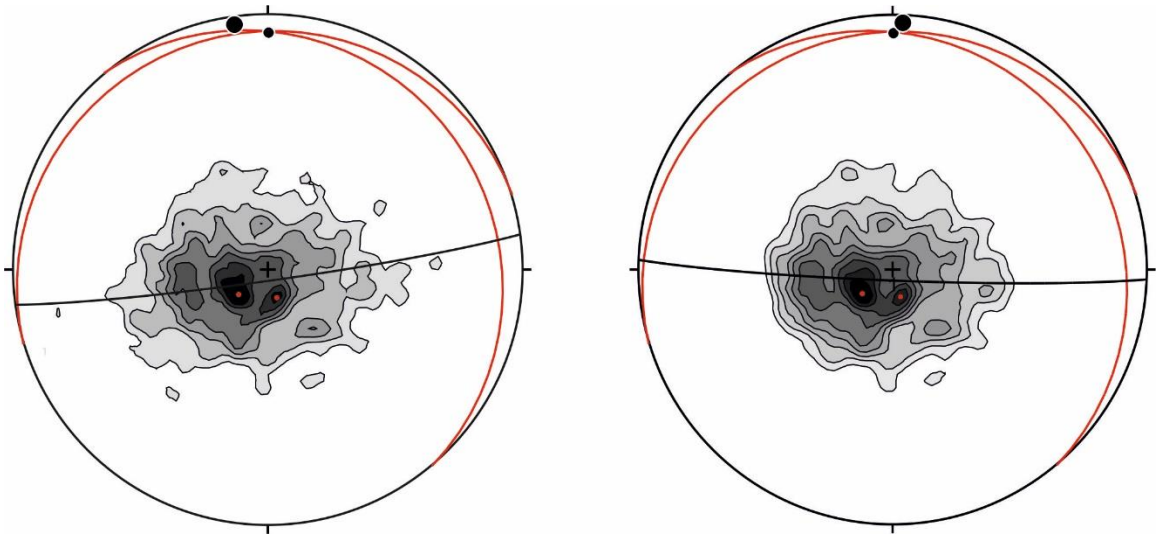

Fig. 3.4. a) S3 planes, mainly dipping towards the ENE and the two main concentrations suggesting a N-S trending isoclinal folding, sub-parallel to the symmetry axis suggested by the best-fit great circle, b)

Analogous analysis of the S3 planes, with medium and high-angles excluded and the extrapolated, N-S trending, isoclinal folding now parallel with the symmetry axis suggested by the best-fit great circle.

3.1.4. S4 foliation

The S4 foliation is a spaced cleavage, of cm- to mm-spacing, that was mainly recorded in the two-mica gneiss, biotite gneiss, marbles and less prominently the amphibolite gneiss map units, as well as the leucogneissic bodies within the amphibolite and biotite gneisses. This spaced cleavage is expressed as a crenulation cleavage and axial foliation, related with the development of mainly steeply-inclined, asymmetric to overturned folds (Figs. 3.5-3.9). It does not constitute a continuous foliation and its orientation depends on the fold geometry and in some cases the dip of the two-paired limbs of the fold, as shown in Fig. 3.9. In particular, S4 dips at medium to high angles either towards the E-ENE or the W-WSW, with 4 major concentrations distinguished (Fig. 3.5). The two concentrations representing high angle S4 planes are actual crenulation cleavage and axial foliation planes recorded in steeply-inclined to nearly upright folds, horizontal to sub-horizontal folds, whereas the other two low-to-medium angle S4 concentrations represent an analogous crenulation cleavage mainly recorded in asymmetrical, steeply inclined, and horizontal to sub-horizontal folds. As far as the latter case is concerned, S4 foliation exhibits a fan-out, producing lower angles at the steeply dipping limbs and medium to higher angles at the more gently dipping limbs of the asymmetrical folds (Fig. 3.9). Moreover, a refraction of this S4 foliation has been recorded, especially in the marbles, when alterations of coarser and more fine-grained layers occur, causing a change in the dip angle of the resulting cleavage/foliation. This refraction is more evident in the lower-angle limbs of asymmetrical folds, with coarser-grained and more competent layers, exhibiting higher refraction angles than more fine-grained and less competent layers. In both cases, whether it is a high-angle axial foliation/crenulation cleavage imprinted on steeply-inclined folds or medium-to-low angle crenulation cleavage imprinted on asymmetrical folds, a N-S to NNW-SSE geometry is concluded and a fold axis of respective orientation is suggested for this type of folds (Fig. 3.5).

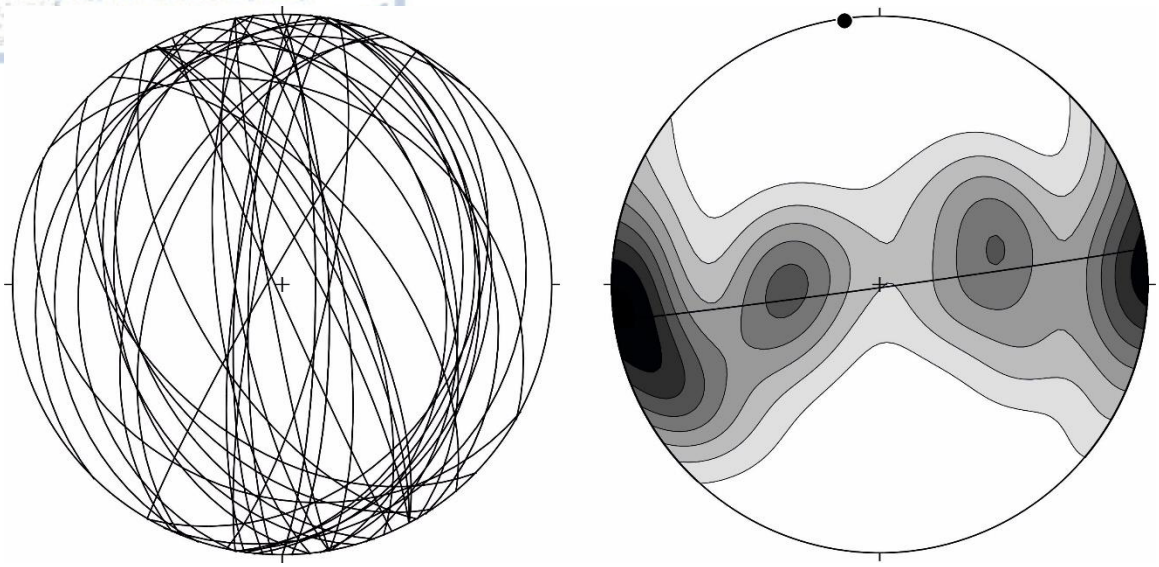

Fig. 3.5. Distribution of S4 planes, forming 4 main concentrations, representing its fan-out as a crenulation cleavage on F4 crenulation folds of diverse geometry. The best-fit great circle suggests an overall, horizontal, NNW-dipping F4 axis for these crenulation folds.

Along the S4 cleavage the common mineral is the white mica, suggesting lower-grade metamorphic conditions when higher grade minerals, e.g. hornblende, are not observed in the field as well as the microscale. Since white mica is not the main constituent mineral in the amphibolite gneiss and biotite gneiss, where migmatitic layering is more prominent, this foliation is hardly seen in these rock types. Finally, this S4 foliation and the associated structures have been found in the field to overprint and cross-cut the previously described S3 foliation (Figs 3.6-3.9).

Fig. 3.6. Steeply-inclined to nearly upright fold, within the two mica-gneiss, WNW of Vatopedi monastery. From the detailed photo a nearly vertical, non-continuous S4 crenulation cleavage/axial foliation can be defined. It cross-cuts the previously gently-dipping, now folded planes of the S3 foliation.

Fig. 3.7. S3 foliation, isoclinally folded, within the two mica gneiss map unit, alternating with pegmatoid bodies. Crenulation folds, post-dating the isoclinal ones, can be distinguished, with the development of a steeply-dipping S4 crenulation cleavage, cross-cutting the pre-existing S4 planes. Located WNW of Vatopedi monastery.

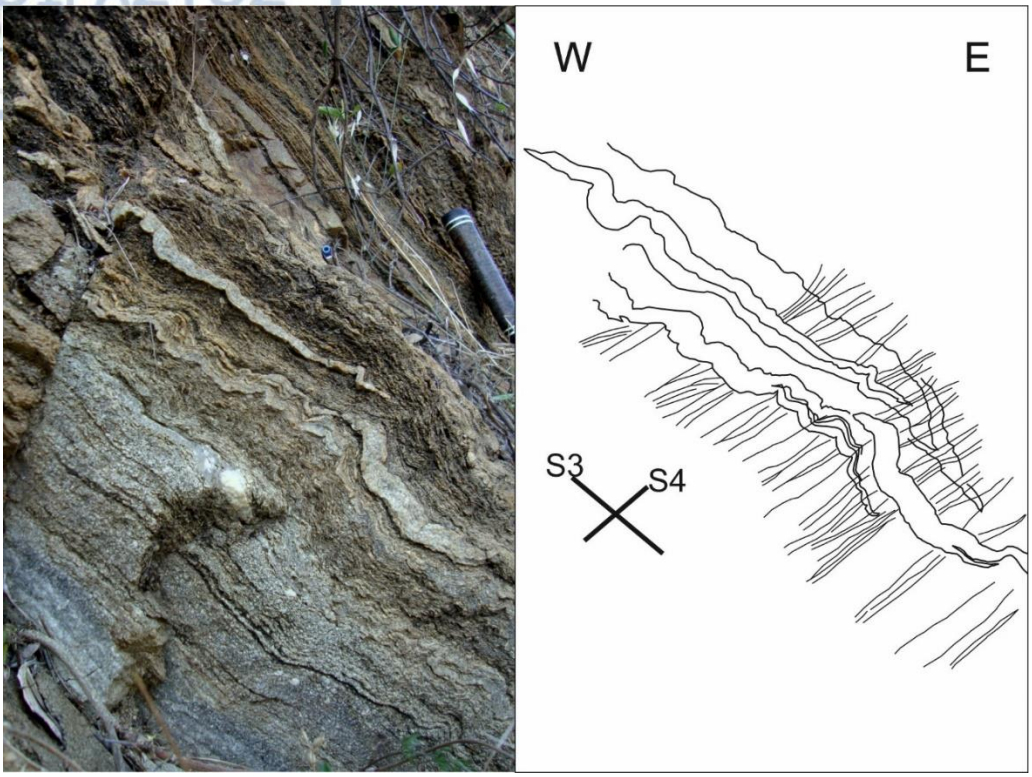

Fig. 3.8. Medium- to high-angle limb of an asymmetric fold, in the two mica gneiss map unit, W of Vatopedi monastery. The main S4 foliation has been rotated to a medium- to high-angle, along with the previously recumbent to gently-dipping isoclinal folds. Both structures are crenulated by later crenulation folds and cross-cut by a non-continuous S3 crenulation cleanage, more conspicuous within the micaceous inlayers.

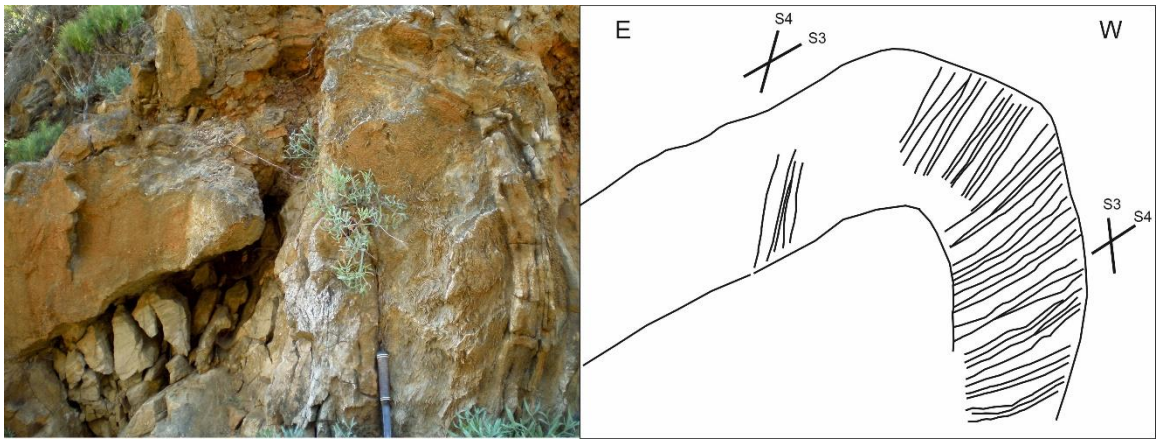

Fig. 3.9. S4 crenulation cleavage, fanning out at the two limbs of an asymmetric, steeply-inclined, overturned F4 fold, verging towards the W, at Esfigmenou monastery.

3.1.5 S5 foliation

An S5 foliation has been observed in the field forming a faint spaced or crenulation cleavage, at scarce locations and mainly within the two-mica gneiss and the leucogneiss bodies, in their less migmatitic counterparts. It is an axial cleavage to mainly E-W trending kink folds and horizontal upright or slightly asymmetric gentle to open folds, trending E-W as well (Fig. 3.11). The S5 foliation dips, at medium to high angles, usually to the south and mainly affects the dominant S3 foliation (Fig. 3.10), as well as the asymmetric folds related with the S4 foliation, in the sense that the S5 has been documented to cross-cut the limbs of the afore-mentioned geometry. (Fig. 3.13).

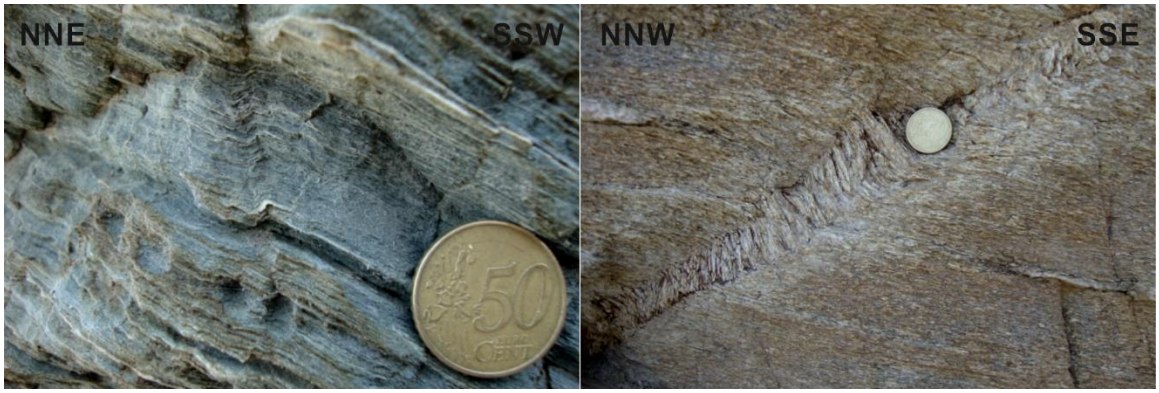

Fig. 3.10. S5 foliation as an axial foliation to kink folds observed in extremely tightly-foliated amphibolite gneiss, SSE of Stavronikita monastery, and in leucogneissic concordant bodies again within the amphibolite gneiss, underlying the two mica gneiss, SSE of Stavronikita monastery.

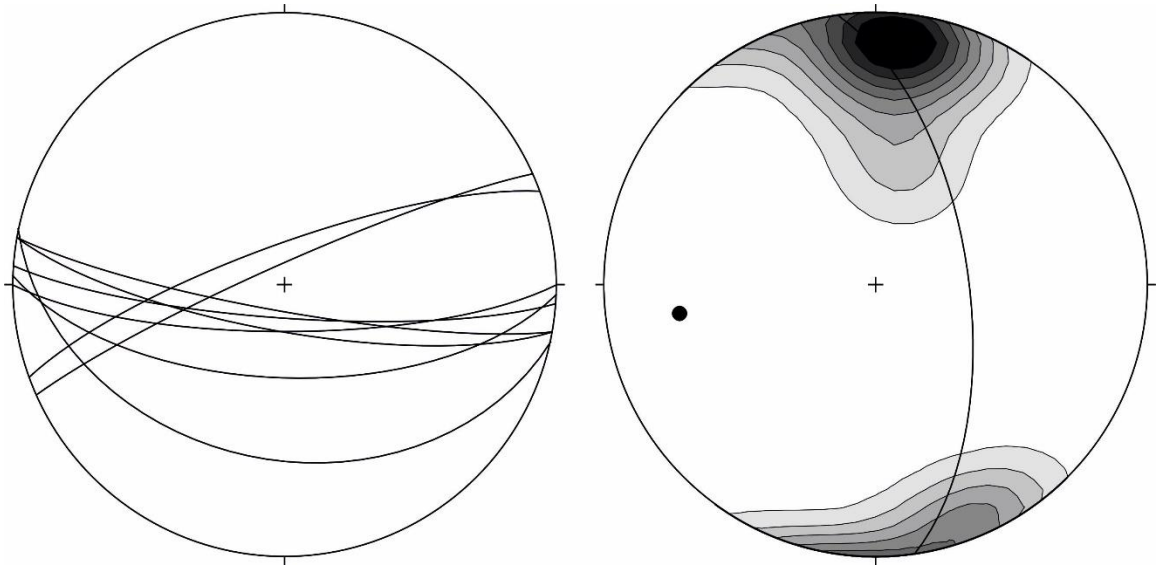

Fig. 3.11. S5 foliation planes trending about an E-W axis.

3.2. Lineation

This chapter refers to the linear fabrics recognized in the map units. The dominant linear fabric documented in the study area is the namely in this dissertation L3 lineation, expressed as a stretching/mineral lineation trending about a N-S axis. The second most intensely imprinted linear fabric is represented by a later L4 trace lineation, expressed either as a crenulation lineation or an intersection lineation, dipping with intermediate to high angles towards the E to ENE or the W to WSW and related with an asymmetric to steeply-inclined folding event. Besides these two most prominent lineations, other linear fabrics were also documented, both pre-dating and post-dating the L3 and L4, either as transposed remnants of overprinted structures (L2 lineation) or as later non-dominant linear fabrics (L5 foliation). Their description follows from the relatively oldest to the relatively youngest, as it was documented from overprinting and cross-cutting relationships in the field.

3.2.1. L1 lineation

The L1 lineation, considered herein, as a corresponding linear fabric related with the S1 foliation, was not possible to recognize in the field.

3.2.2. L2 lineation

L2 lineation was found on S2 foliation, as a stretching and mineral lineation of quartzofeldspathic aggregates, or mineral grains of feldspars, micas or amphiboles. However, as it has been already mentioned in the S2 description, the main fabric attributed to the overall structure of the study area has strongly overprinted pre-existing fabrics, like the L2 lineation, and rotated them into parallelism with its predominant geometry. Therefore, it was not made possible to recognize the initial orientation and geometry of the L2 lineation, which, when still existent on S2 relics, must have been forced into parallelism with the consequent, dominant L3 lineation.

3.2.3. L3 lineation

The dominant linear structures recognized in the field comprise the L3 lineation, and were recorded on the S3 planes. This L3 lineation has been observed as a linear fabric made up of quartzofeldspathic aggregates or elongated (stretched) grains (micas), which define a stretching lineation. In other cases, it appears as a mineral lineation formed by the needle shaped amphiboles. It has been repeatedly recorded during field work in all the map units, besides the mafics/ultramafics map unit. The L3, also indicating, as a stretching lineation, the X-axis of the strain ellipsoid (Passchier and Trouw, 2005), trends about a N-S trending axis (Fig. 3.12). More specifically, it trends NNE-SSW, when gently plunging to the north (concentration maxima at 06/011), and when plunging to the south, an additional concentrate indicates a NNW-SSE trend for the L3 (concentration maxima at 05/172).

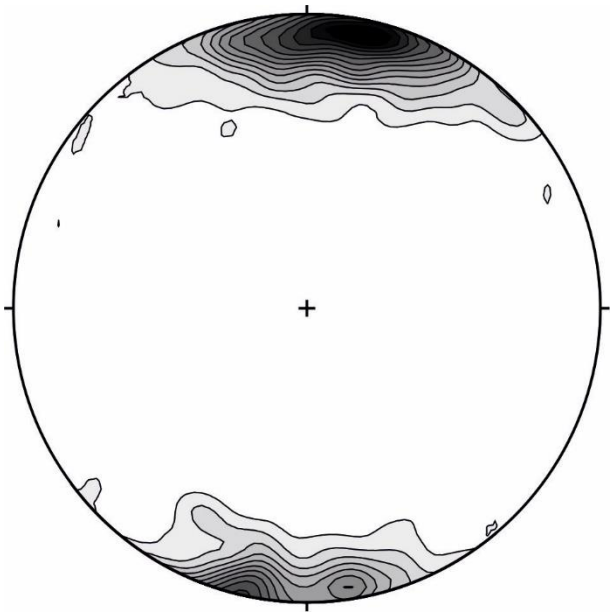

Fig. 3.12. L3 stretching and mineral lineation, distributed about a general N-S trending axis.

3.2.4. L4 lineation

A trace lineation (Piazzolo and Passchier, 2002b) has been documented in the field, post-dating the dominant L3 stretching lineation, either in the form of a crenulation

lineation, in the sense that they describe the continuity of microscopic crenulation folds on the main S3 foliation planes, or in the form of intersection lineations, between pre-existing S3 foliation planes and subsequent crenulation cleavage (axial F4 foliation). Especially in the case of intersection lineations, they can greatly vary in orientation, depending each time on the orientation of the pre-existing foliation plane, which will be over-printed. However, as far as the L4 is concerned, the most consistent structural feature which can be safely correlated with a stable geometry, is the one representing the tracing of microscopic crenulation folds, since fold axes follow, in large, a specific geometrical axis, especially if they are cylindrical, as is the case for the respective F4 folds, which will be analyzed later on.

This trace lineation concentrates mainly along a N-S to NNW-SSE trending axis and then seems to generally scatter in a wide range (Fig. 3.13). Since this L4 maxima is constituted, in its vast majority, by crenulation lineation measurements, it is considered to represent the trace of microscopic crenulation folds on pre-existing S3 surfaces.

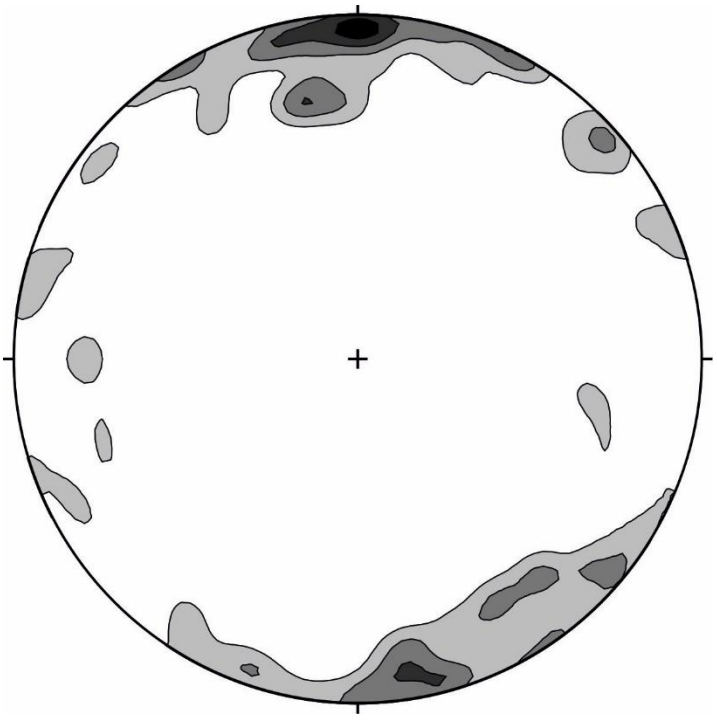

Fig. 3.12. L4 trace lineation trending mainly about a N-S axis and represented mainly by the tracing of F4 crenulation folds on S3 planes.

3.2.5. L5 lineation

The L5 lineation was also documented in the field as a trace lineation, expressed either as a crenulation lineation of kink and crenulation folds or an intersection lineation of the already described S5 foliation cross-cutting the dominant S3 planes. It was recorded in scarce locations and more significantly, in some cases it was found to co-exist with the L4 lineation on the same S3 planes (Fig. 3.14). The L5 lineation was documented to cross-cut and post-date the L4 lineation. Due to the fact that the cases of the L4 and L5 co-existing are scarce, the gross distinction between them can be done only based on the trend; the L5 trends more to the E-W to ESE-WSW, whereas the L4 to the N-S to NNW-SSE, as already described. In some cases the L5 was also recorded as an intersection lineation (of S5 on S3 planes) on both limbs of asymmetric F4 folds, post-dating the latter (Fig. 3.13). To conclude, this L5 trace lineation has been the last and least imprinted lineation on the overall fabric of all the map units and has been found to affect and post-date, as already mentioned, the S3 planar fabric, the L4 trace lineation, as well as F4 folds, which will be described in the according chapter.

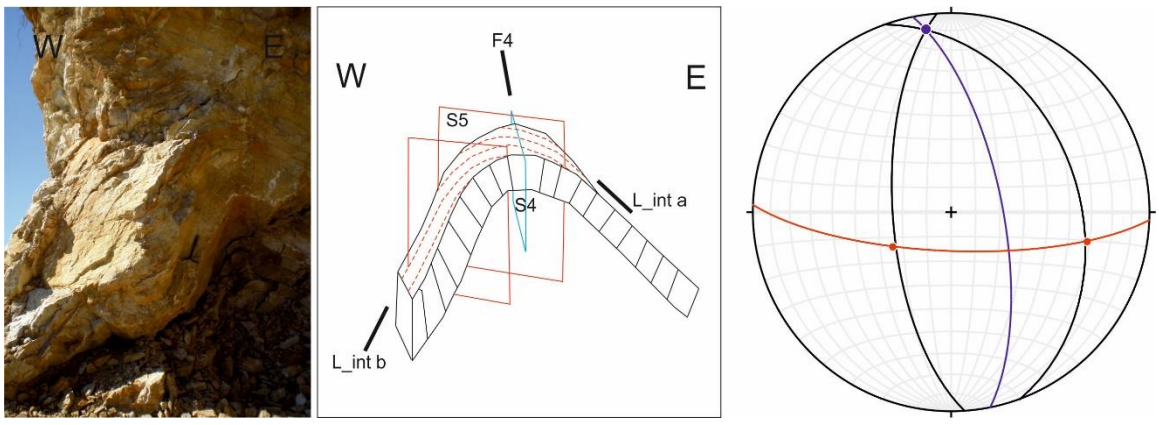

Fig. 3.13. Interpretation of an asymmetric F4 fold, trending N-S, being overprinted and cross-cut by the development of E-W trending, S5 surfaces. The intersection of the latter with the folded S3 planes, produces the L5 intersection lineation.

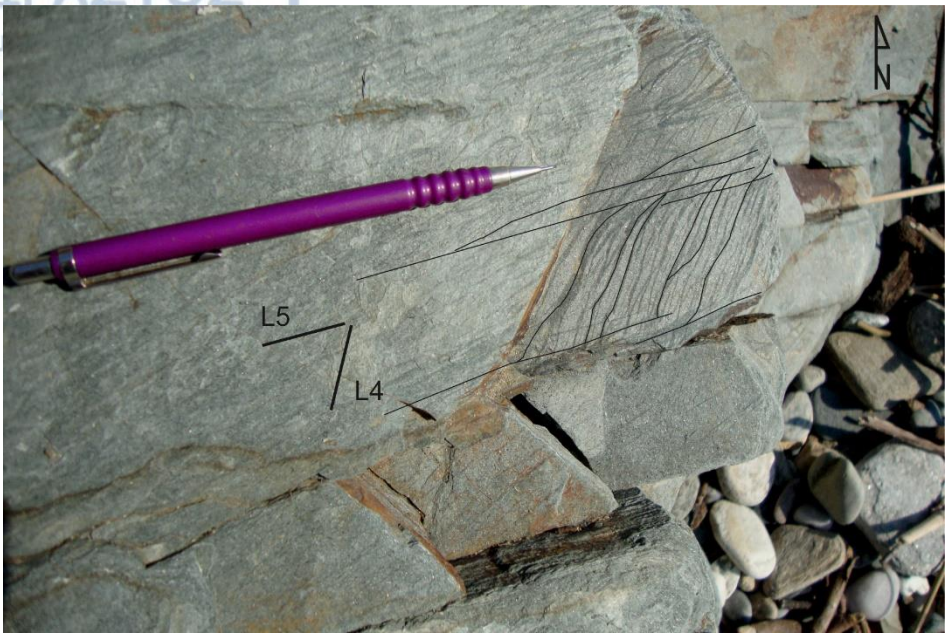

Fig. 3.14. Plan view of the foliation plane in thinly-foliated amphibole-biotite gneiss NNW of Iviron monastery, where the superposition of the later L5 intersection lineation can be distinguished on the pre-existing L4 intersection lineation, both evident due to the high content of biotite in the crenulation cleavage planes formed during the respective deformational events. Notice that the L4 lineation is generally trending NNE-SSW, whereas the L5 is trending ENE-WSW.

3.3. Folds

This chapter refers to the folding events recognized in the map units. The dominant folding event documented in the study area is represented by the namely in this dissertation F3 folds, constituting isoclinal to tight, generally recumbent folds, trending about a N-S axis. The second most intensely imprinted folding event is represented by asymmetric to steeply inclined, occasionally crenulation F4 folds, trending NNW-SSE to N-S. Besides these two most fold geometries, F2 folds were also recorded of F3-respective geometry and also scarce F5 folds, expressed as kink and open to gentle folds trending about an E-W axis. Their description follows from the relatively oldest to the relatively youngest, as it was documented from overprinting and cross-cutting relationships in the field.

3.3.1. F1 folds

F1 folds were not possible to identify and record in the field. As elements of an initial stage or stages in the multi-deformational procedure the map units underwent, they were subsequently overprinted by later deformational events to such an extent that not even relics of this folding event could be identified in the field.

3.3.2. F2 folds

F2 folds are isoclinal, intrafolial, rootless folds within the S3 foliation, implying that these folds and their associated S2 foliation have been thoroughly transposed and overprinted by F3 folds and their associated S3 planar fabric. There are many cases in the field were these F2 folds have been documented in the marbles, amphibolite and biotite gneiss, leucogneiss and two-mica gneiss map units, either as isolated, intrafolial rootless folds (Fig. 3.15) or initial isoclinal folds being isoclinally re-folded by the consequent F3 folding event (Fig.3.17). In very few cases, their hinges have been preserved as relict structures after their overprinting and transposition due to the F3 folding event and contemporaneous shearing (Figs 3.2 and 3.16).

Fig. 3.15. Rootless, intrafolial, recumbent, isoclinal F2 folds in: a) well-foliated, coarse-grained marbles SSE of Dohiarion monastery, and b) well-foliated, lower amphibolite gneiss, E of Zografou monastery, both structures transpositioned and roteted into parallelism with the subsequent F3 folds.

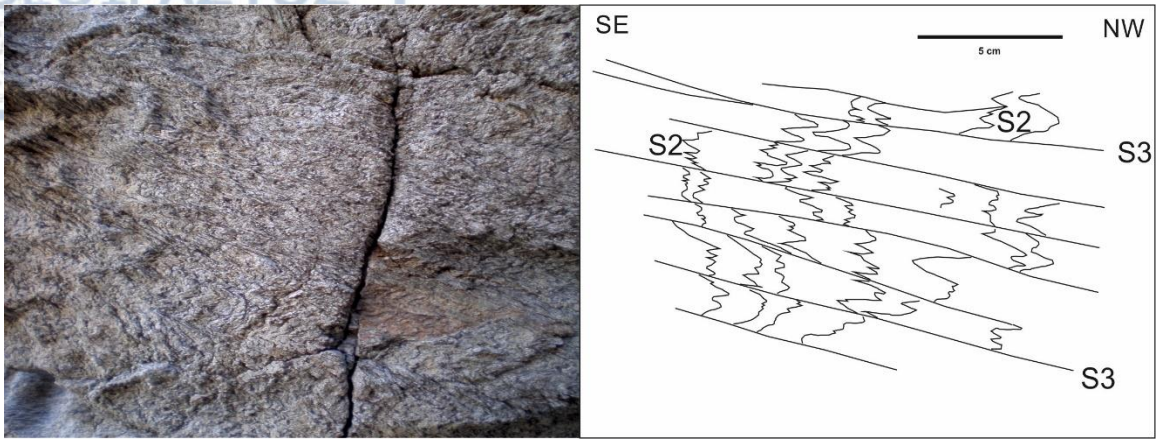

Fig. 3.16. Transposition of S2 foliation preserved in mesoscopic F2 fold hinges by a mylonitic S3 foliation, in biotite gneiss, SE of Esfigmenou monastery.

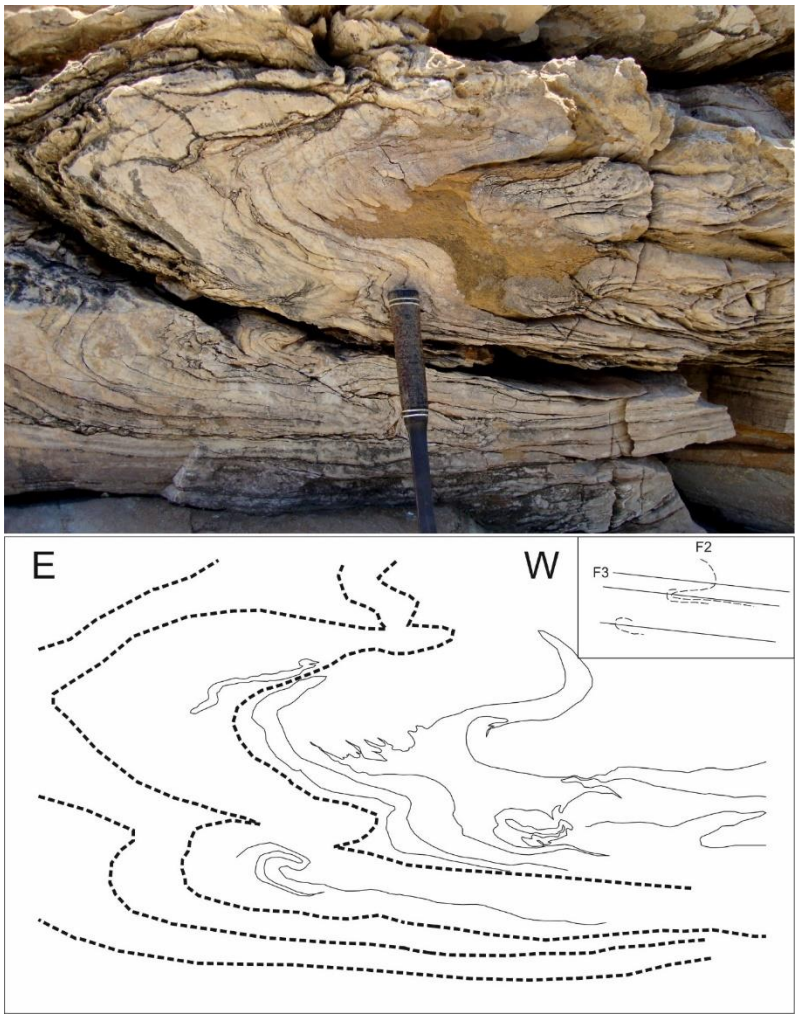

Fig 3.17. F2 isoclinal folds being isoclinally refolded and overprinted by F3 folds, within the marbles map unit, SW of Konstamonitou monastery. The lithological differentiation between purely carbonate and

more clastic-rich horizons, in the "crenulated" central part of the photo, could represent a remnant fabric of the S2 foliation, at a pre-existing upright position of an F2 fold hinge, also isoclinally refolded .

3.3.3. F3 folds

F3 folds have been recorded in all the map units of the study area, except the ultra-mafics/mafic map unit. They are mainly isoclinal to tight, horizontal, recumbent folds trending NNW-SSE (Fig. 3.18) (concentration maxima of their fold axes is at 02°/352° and NNE-SSW (concentration maxima at 01°/013°). Many of these isoclinal to tight folds constitute parasitic folds describing larger structures. They trend about a general N-S axis, also described for the L3 stretching and mineral lineation. This isoclinal folding represents the dominant meso-scale folding structure imprinted on the study area and also governs the map-scale structure of the study area (Fig. 3.19).

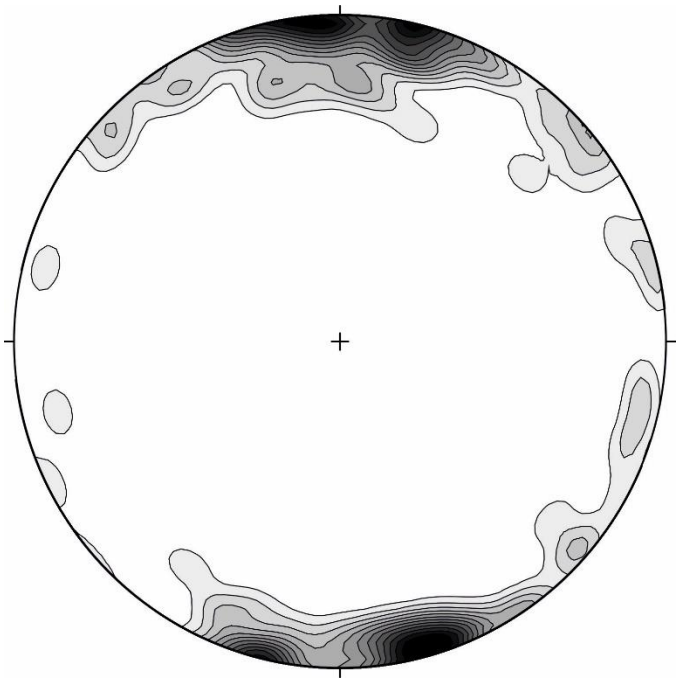

Fig. 3.18. F3 Fold axes of isoclinal to tight, generally recumbent, horizontal to sub-horizontal folds, trending parallel to the L3 stretching/mineral lineation.

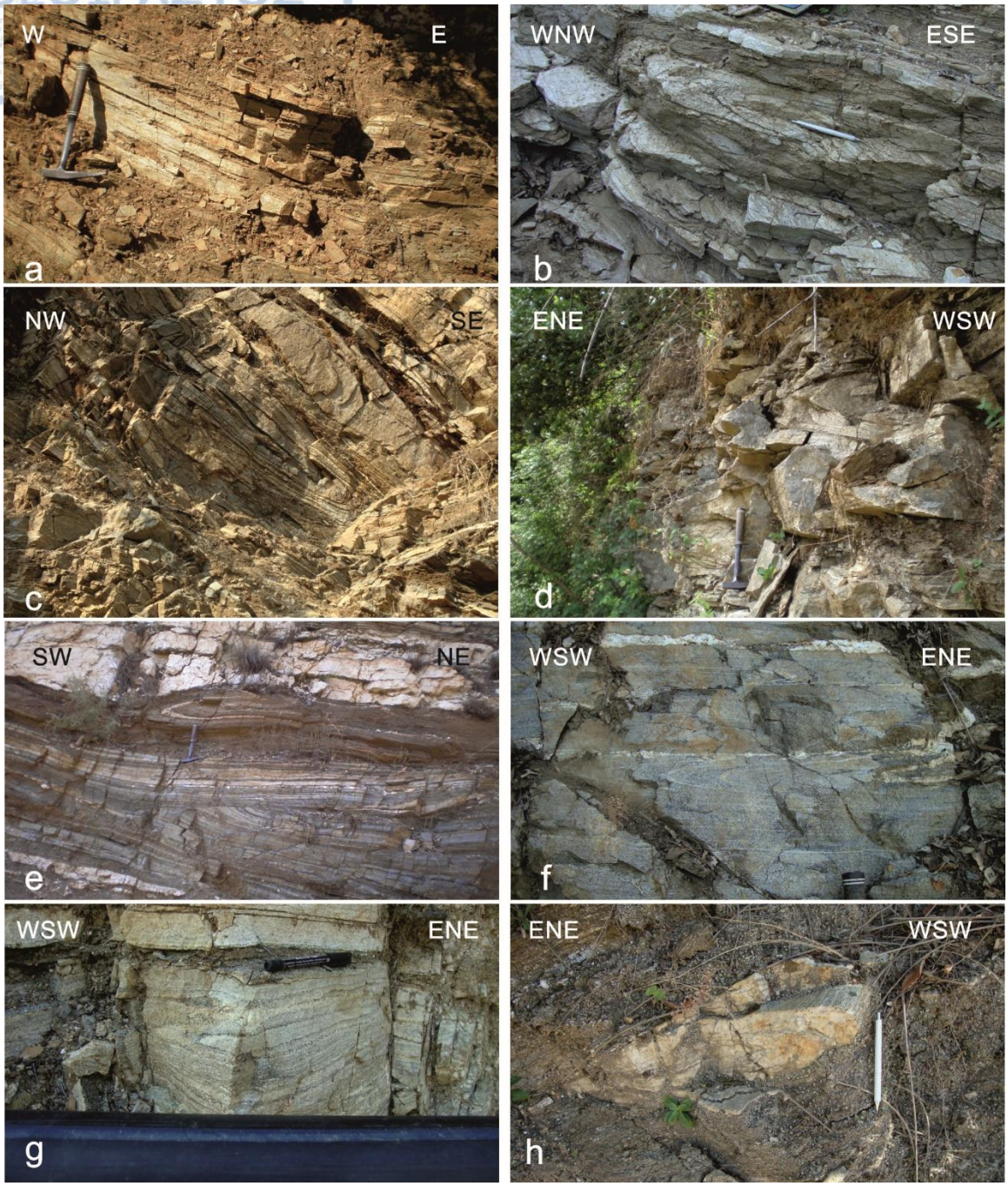

Fig. 3.19. Isoclinal folds recorded in the majority of the study area's map units, following the documented geometry of a general N-S trending F3 axis: a) Isoclinal F3 fold in two-mica gneiss map unit E of Konstamonitou monastery, b) Isoclinal F3 fold in two-mica gneiss map unit E of Konstamonitou monastery, c) Rotated isoclinal F3 fold, to a medium angle, due to later influence by the F4 folding event in two-mica gneiss map unit, E of Dohiarion monastery, d) Isoclinal F3 folds in two mica gneiss map unit W of Pantokratoros monastery, e) Isoclinal F3 fold in amphibolite gneiss map unit E of Esfigmenou monastery. Notice the cross-cutting of the S3 foliation by thin shear zones, also juxtaposing the

amphibolite gneiss with concordant, leucogneissic layers, f) Isoclinal to rootless F3 folds in the amphibolite gneiss map unit E of Zografou monastery, g) Isoclinal fold in the amphibolite gneiss map unit W of Zografou monastery, h) Isoclinal F3 fold in leucogneissic layer within the biotite gneiss map unit W of Zografou monastery.

In order to better understand this dominant structure, related with this meso- and map-scale isoclinal folding, further structural analysis has been carried out on the S3 (which constitutes the dominant planar fabric in the study area), the L3 and the F3 datasets respectively.

As far as the S3 dataset is concerned, it can be concluded from the geological mapping of the study area that the map units repeat themselves bilaterally of a rough N-S symmetry axis (Fig. 3.20), following the lithostratigraphic sequence described in the previous chapter, from the overlying, alternating amphibolite and biotite gneiss map units, to the two-mica gneiss, the underlying, alternating amphibolite and biotite gneiss and finally the lowest marbles map unit, which outcrops only at the westernmost part of the study area. The dataset was, therefore divided, according to the structural position of each map unit vertically (the amphibolite and biotite gneisses underlying and overlying the two mica gneiss were grouped and named lower and upper amphibolite and biotite gneisses respectively), as well as this N-S symmetry axis bilaterally of which the map units repeat themselves (sub-dividing the mapped area in a western and eastern segment). This first round of analysis (Fig. 3.21) shows that:

a) The best-fit great circles reveal a NNW-SSE to NNE-SSW symmetry axis. Especially the subsets belonging to the western segment show a main NNW-SSE symmetry axis, with the exception of the two-mica gneiss unit following a NNE-SSW symmetry axis, whereas the eastern segment exhibits a N-S to NNE-SSW symmetry axis. Some subsets as the western segment of the upper amphibolite and biotite gneiss units could incorporate both geometries, meaning both a NNW-SSE and NNE-SSW symmetry axis. Therefore, a structural pattern is repeated on each sub-set, revealing either a NNW-SSE or a NNE-SSW symmetry axis, depending on the rock type as well as its structural position.

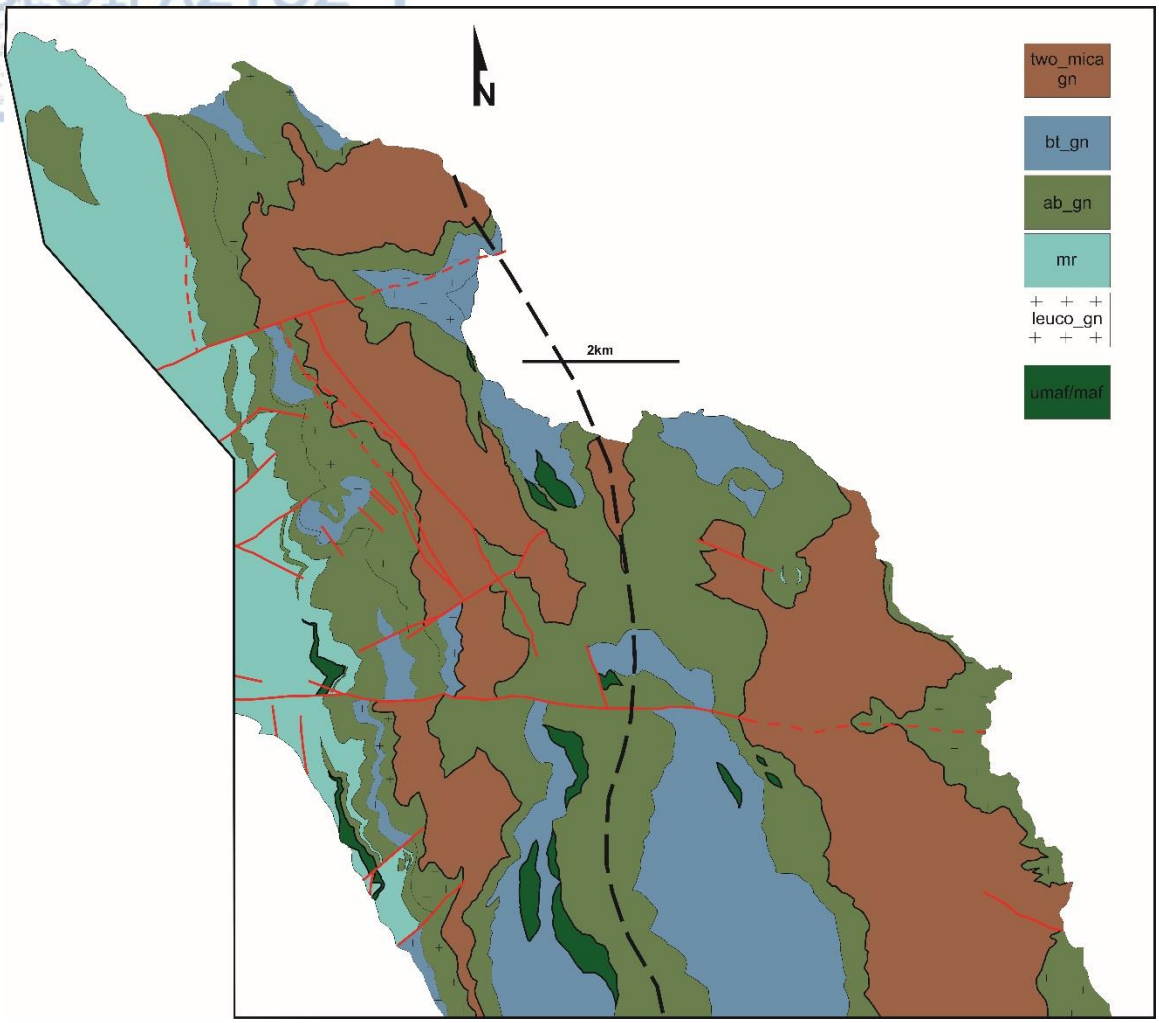

Fig. 3.20. N-S trending symmetry axis (dashed line), bilaterally of which the map units structurally repeat themselves, separating the study area in a western and eastern segment respectively, for the S3 structural correlation with the F3 folding event.

b) In most cases a horizontal-to-sub-horizontal isoclinal-to-tight folding can be concluded, from the two most prominent S3 concentrations which can be distinguished. These f-axes generally coincide with the direction of the afore-mentioned symmetry axes. The latter also points towards the predominance of NNW-SSE trending, isoclinal to tight folds in the western segment of the subdivision we have followed and the predominance of NNE-SSW trending, isoclinal to tight folds in the eastern segment. Finally, wherever two main, uneven concentrations can be distinguished, they were interpreted as limbs of mega-scopic S-Z parasitic folds, in the sense that the highest concentration represents the most frequently recorded longer limb of such a fold and the lower concentration the

shorter limb (Fig. 3.21, e.g. a NNW-SSE trending, Z fold in the western segment-belonging marbles unit or a NNE-SSW, trending S fold in the western segment-belonging two-mica gneiss map unit). The characterization of these folds as S or Z parasitic folds was carried out, based on the observation along the plane parallel to the best-fit great circles and normal to the extrapolated f-axis. Such an extrapolation could be useful when trying to decipher later on the large-scale structure governing the study area.

c) Discrepancies between successive map units concerning the trend of the observed symmetry axis, as is the case of the two-mica gneiss being in discordance with the amphibolite and biotite gneiss map units, in some localitites, advocates towards contacts of tectonic nature.

WESTERN SEGMENT

UPPER_AB_BT_W

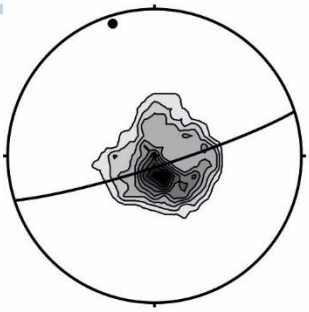

TWO_MICA_GN_W

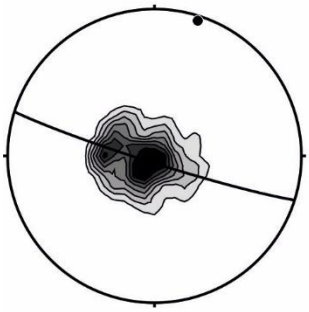

LOWER_AB_BT_W

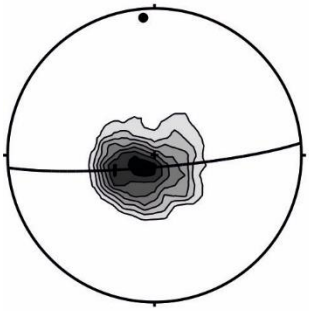

MR_W

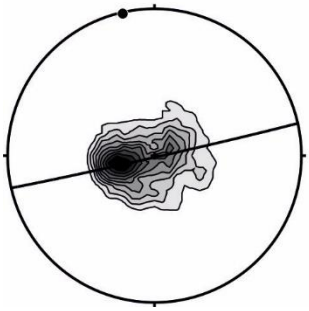

EASTERN SEGMENT

UPPER_AB_BT_E

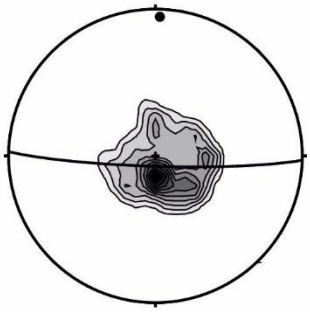

TWO_MICA_GN_E

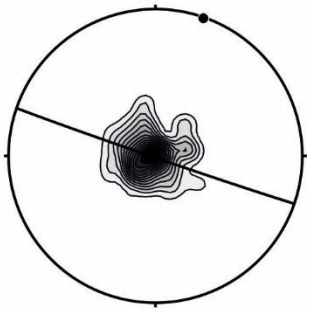

LOWER_AB_BT_E

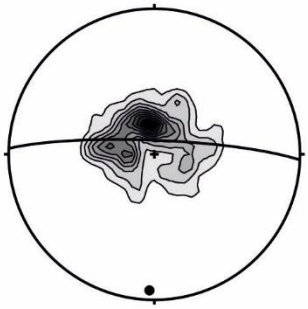

Fig. 3.21. Structural analysis on the S3 dataset, subdivided according to the structural position of the map units and their bilateral repetition along a N-S symmetry axis. The distribution of the best-fit great circles suggests in each case an either NNW-SSE trending or NNE-SSW trending isoclinal folding.

Considering the very gentle dip angles of the map units, an effort was made to ensure the afore-mentioned structural conclusions and for this reason, the whole study area was further sub-divided in 5 ENE-WSW to E-W trending domains, normal to the main boundaries (Fig. 3.22). The afore-mentioned structural analysis was followed for these domains. The results of this further more detailed analysis are (Figs 3.23-3.27):

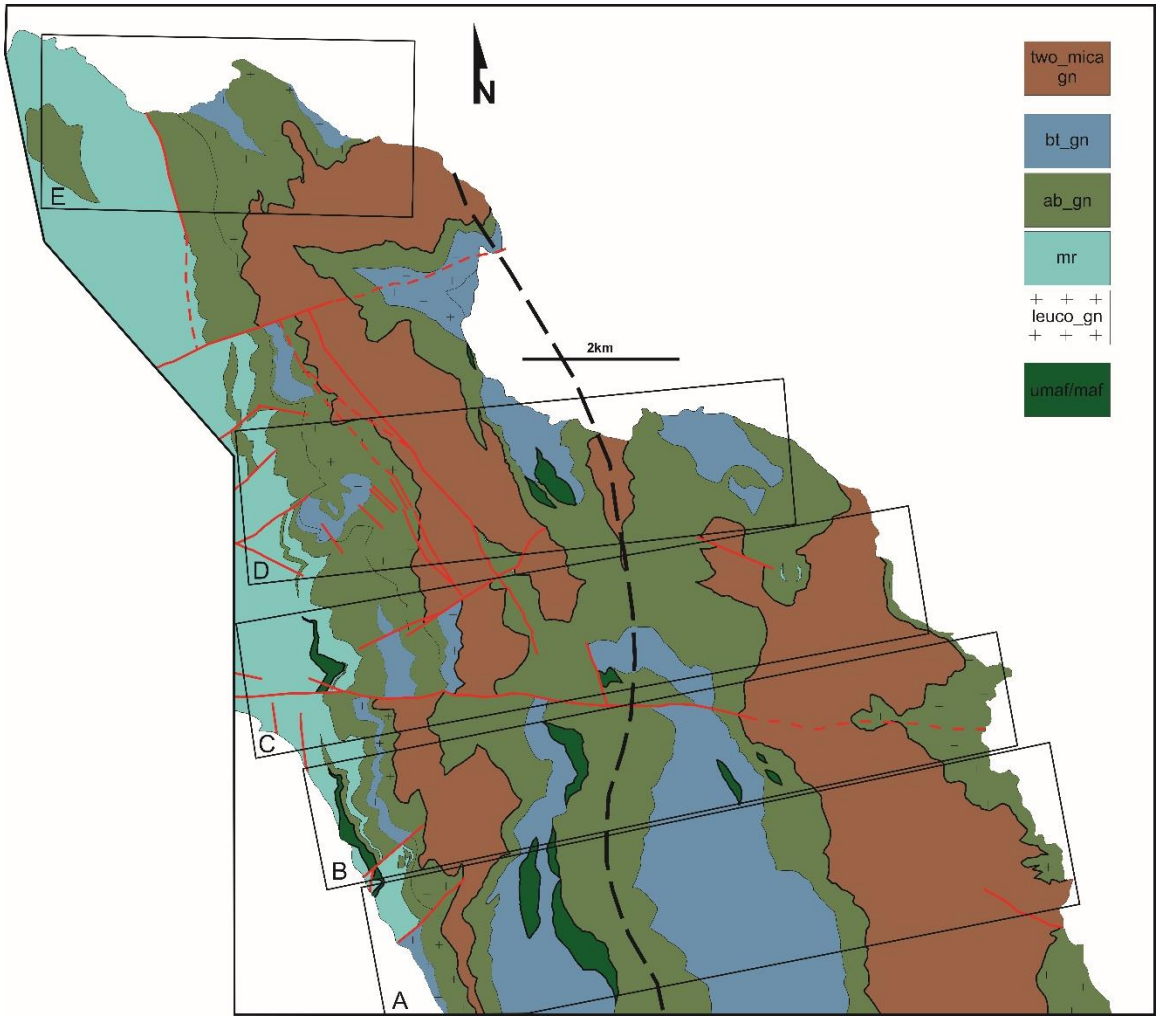

Fig. 3.22. Subdivision of the study area in structural domains A-E for the S3 analysis and correlation with the F3 folding event.

a) Both NNW-SSE and NNE-SSW symmetries insist, as shown from the geometrical distribution of the best-fit great circles. More precisely, the ENE-WSW striking best-fit

great circles, revealing a NNW-SSE symmetry axis, prevail as a whole in the western part of the study area, whereas the ESE-WNW striking best-fit great circles, revealing a NNE-SSW symmetry axis, prevail in the eastern part of it.

b) Wherever the stereo-diagrams allowed it, and two dominant concentrations of S3 measurements could be distinguished, the corresponding folds where also extrapolated. Following the same rationale, as in the previous analysis concerning the map units as a whole, most of these folds were also interpreted as being parasitic and therefore kinematic indicators and parts of a larger structure. The f-axes of these folds were identified as the poles of the afore-mentioned best-fit great circles. As a whole, the analysis outlines and verifies horizontal to sub-horizontal, tight to isoclinal folds, with recumbent to gently-dipping axial surfaces, trending, as mentioned, from the NNW-SSE to the NNE-SSW. As far as their characterization as parasitic folds is concerned, Z folds were found to co-exist but structurally prevail over S folds in the western segment, as well as generally NNW-SSE trending folds over their symmetric counterpart, whereas S-folds are the dominant parasitic structure at the eastern segment and generally NNE-SSW trending folds clearly prevail on their symmetric counterpart.

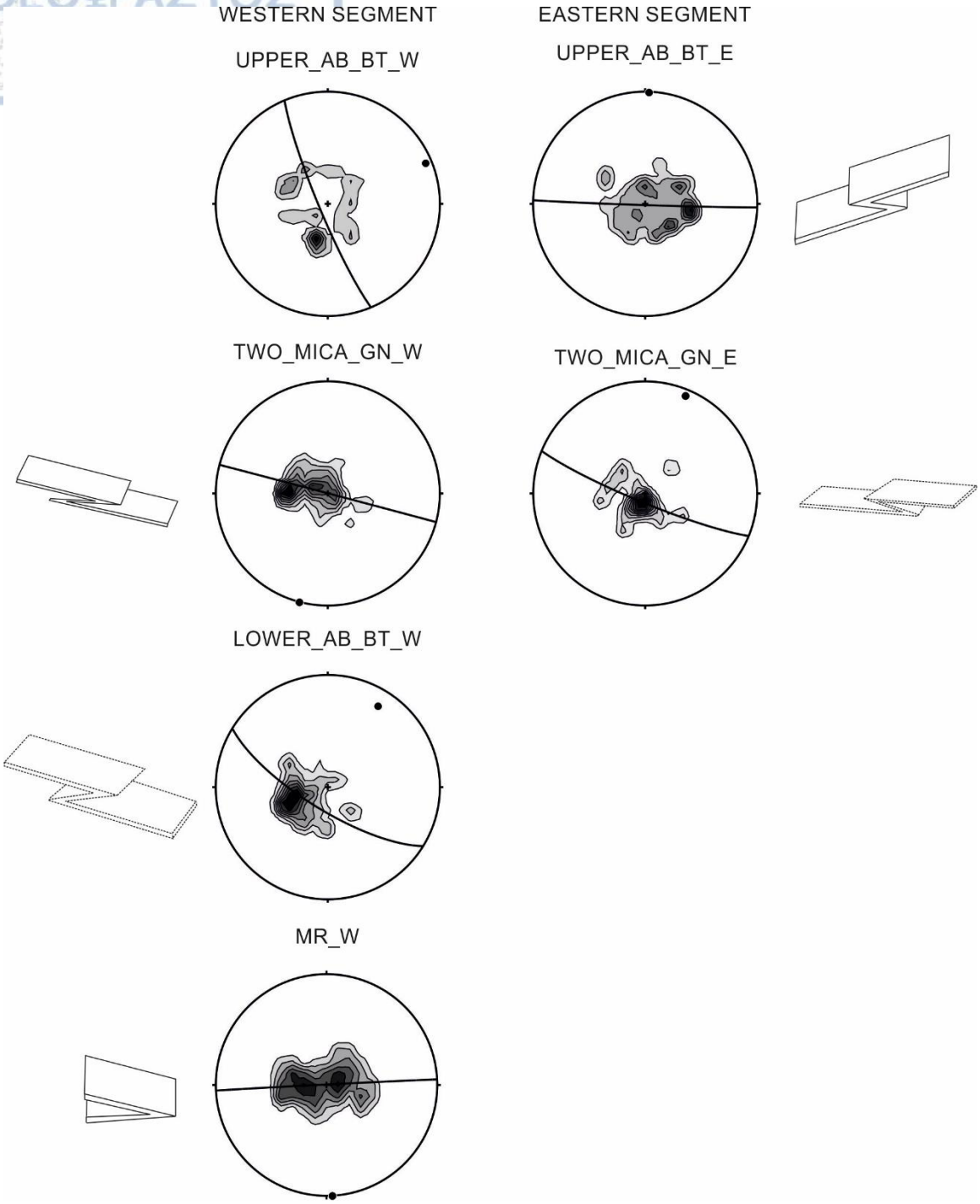

Fig. 3.23. Structural analysis of the S3 foliation at the A domain and correlation of the latter with the F3 isoclinal to tight folding and the respective megascopic parasitic folds.

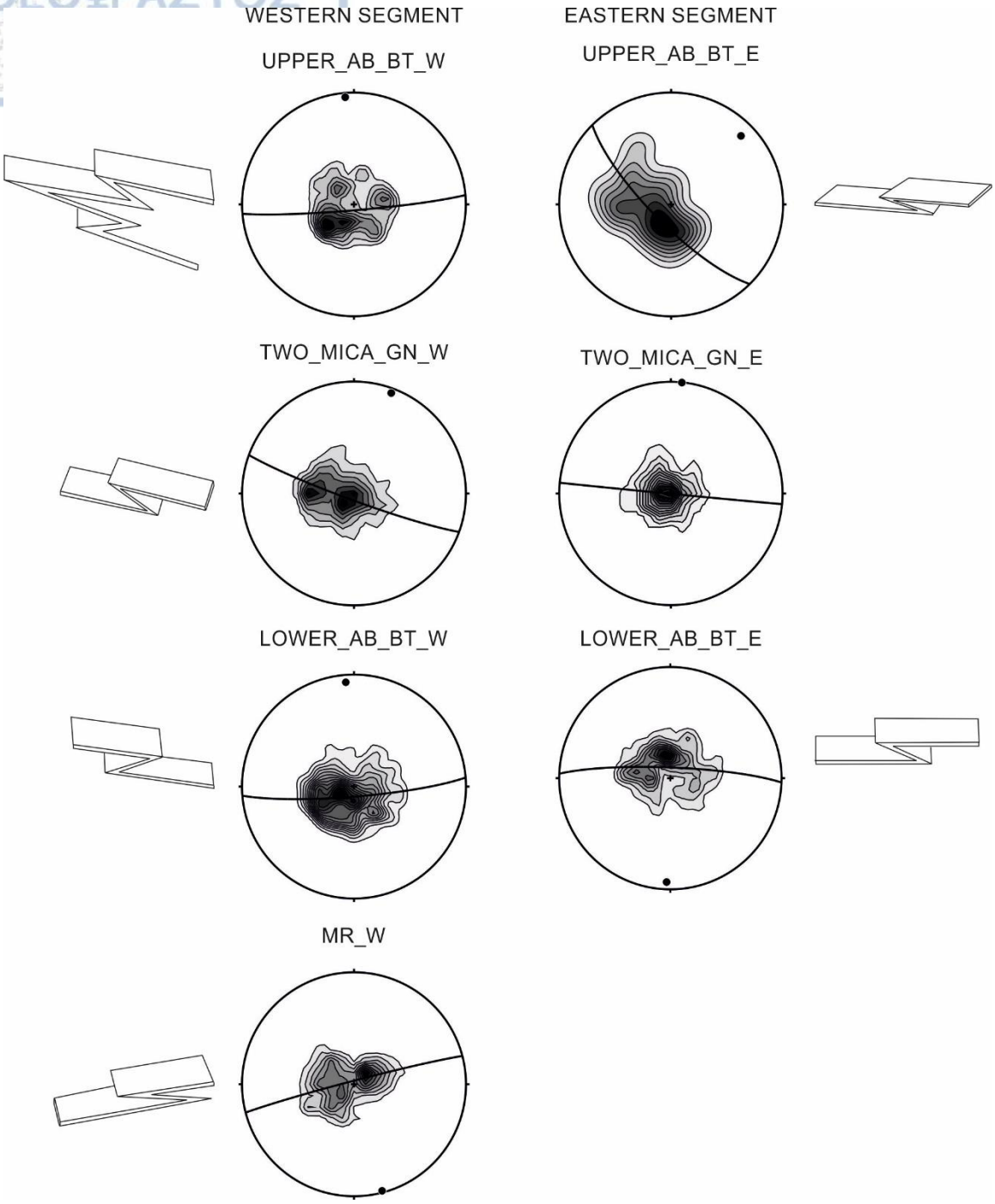

Fig. 3.24. Structural analysis of the S3 foliation at the B domain and correlation of the latter with the F3 isoclinal to tight folding and the respective megascopic parasitic folds.

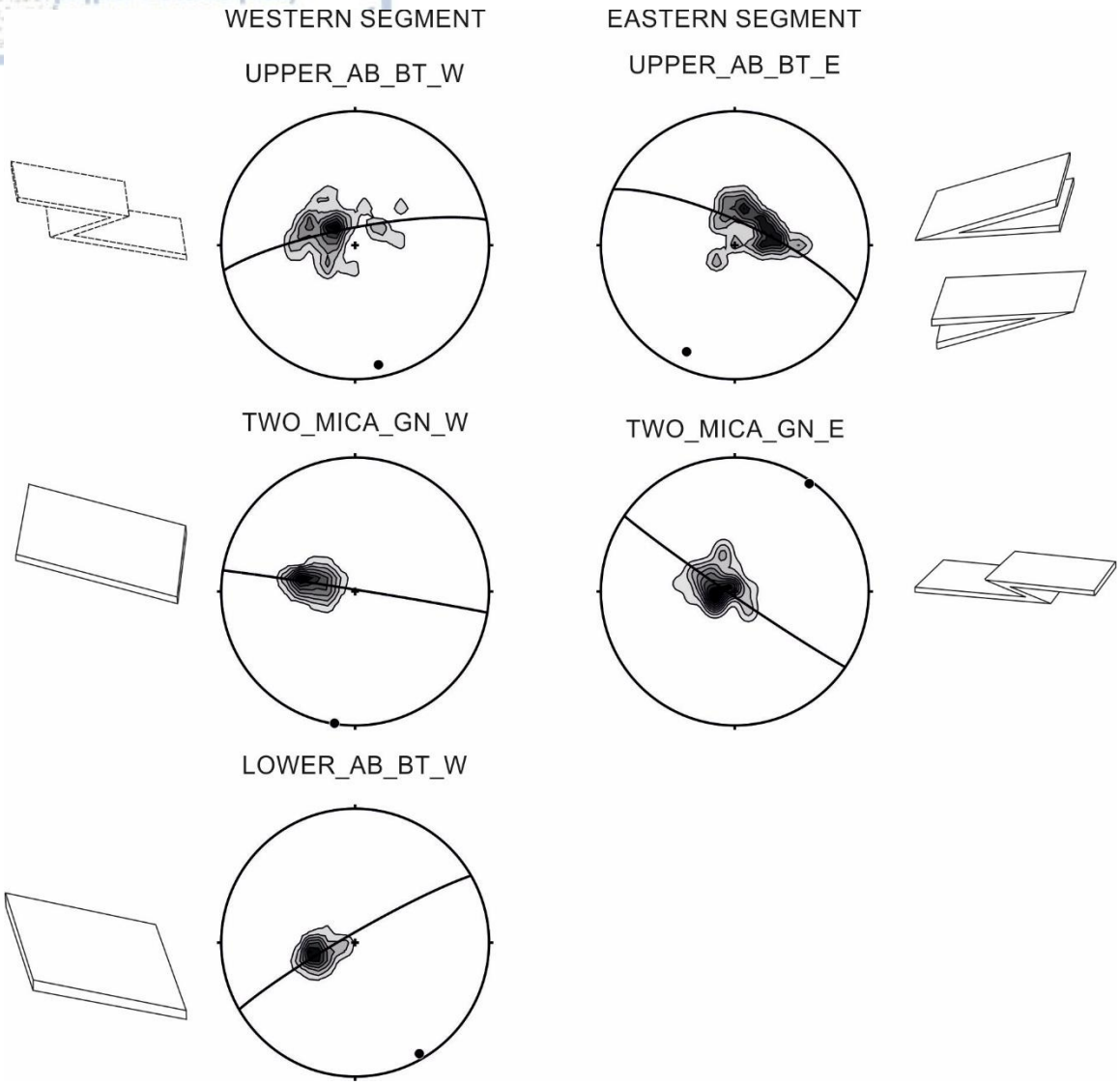

Fig. 3.25. Structural analysis of the S3 foliation at the C domain and correlation of the latter with the F3 isoclinal to tight folding and the respective megascopic parasitic folds.

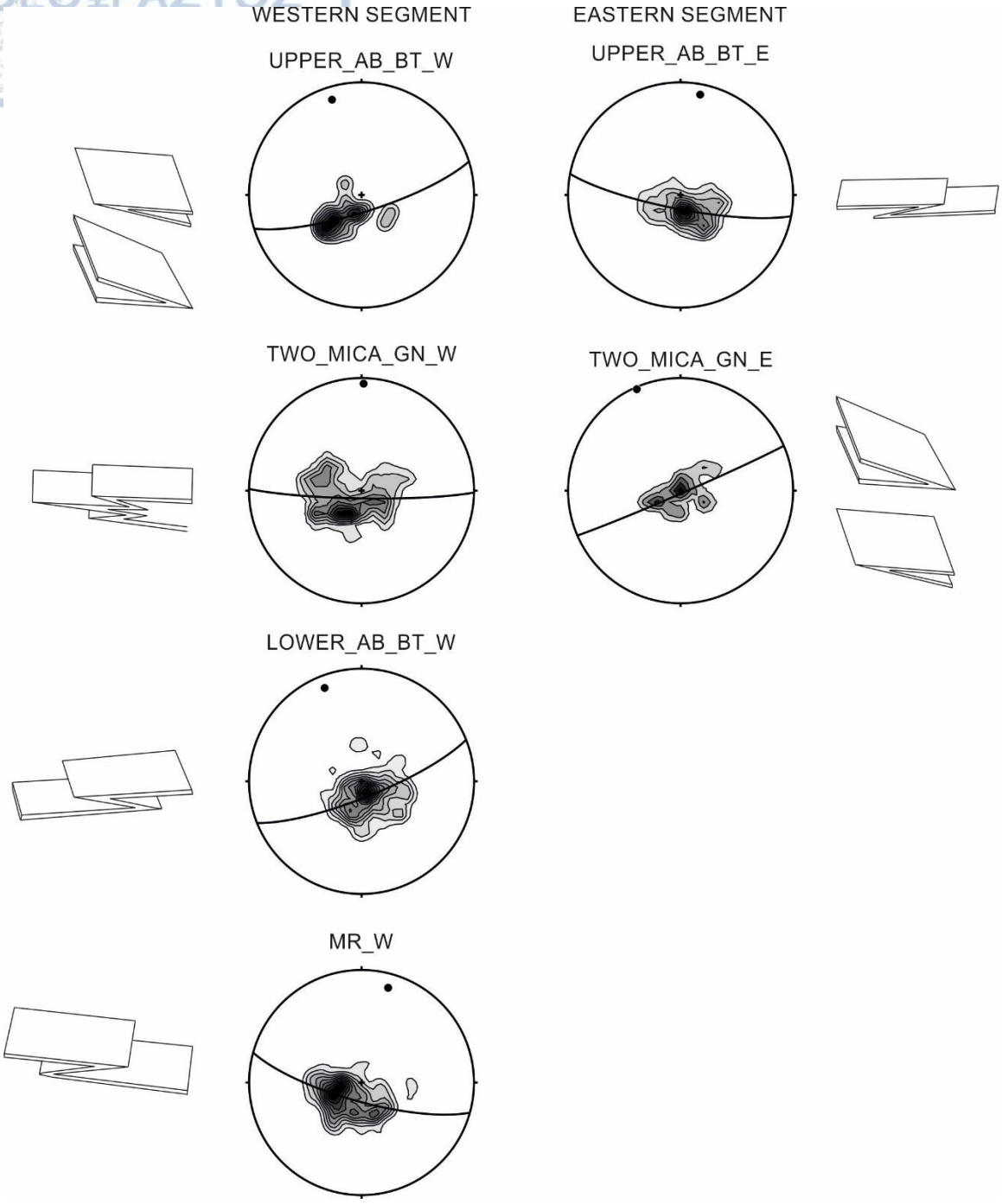

Fig. 3.26. Structural analysis of the S3 foliation at the D domain and correlation of the latter with the F3 isoclinal to tight folding and the respective megascopic parasitic folds.

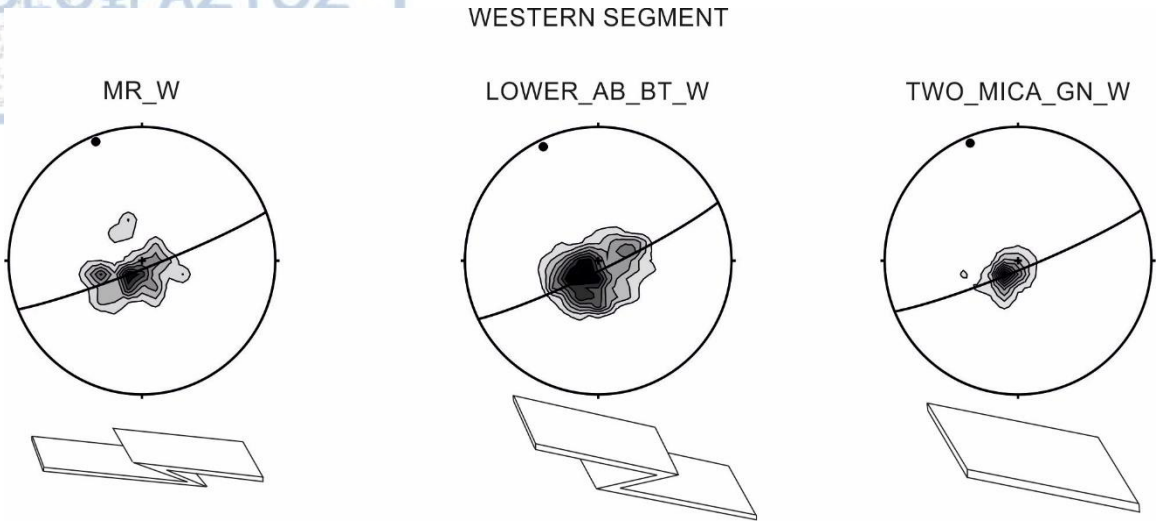

Fig. 3.27. Structural analysis of the S3 foliation at the E domain and correlation of the latter with the F3 isoclinal to tight folding and the respective megascopic parasitic folds.

The recorded mesoscopic parasitic folds (Fig. 3.28) are in agreement with the megascopic parasitic folds extrapolated from the detailed, above S3 analysis. These mesoscopic, parasitic, isoclinal to tight folds also show a distinct preference to a specific geometry, meaning that there are locations where S or Z parasitic folds prevail one over the other. In particular, mesoscopic Z folds were found to prevail in the western segment of the lower amphibolite/biotite gneiss map units, whereas S folds were found to predominate in the eastern segment of the two mica gneiss map unit, especially towards its upper boundary with the upper amphibolite map unit (Fig. 3.29 and 3.23-3.27). M folds were bitterly seen within the two-mica gneiss map unit and in the middle to eastern part of region.

Fig. 3.28. F3 parasitic folds in some of the map units of the study area: a) S-folds facing N, in marbles WSW of Konstamonitou monastery. b) Z-folds facing N from the previous location. Notice that S and Z parasitic folds co-exist at the same outcrop, pointing towards the existence of sheath folds. c) Z-folds facing N, in

marbles map unit S of Zografou monastery. d) S-folds in marbles map unit, S of Zografou monastery. e) S-folds facing N, in the biotite gneiss map unit N of Dohiarion monastery. f) Z-folds facing N in biotite gneiss map unit, E of Zografou monastery. g) Z-folds facing N, in the biotite gneiss map unit, E of Zografou monastery. h) M-folds in the two-mica gneiss map unit, E of Pantokratoros monastery.

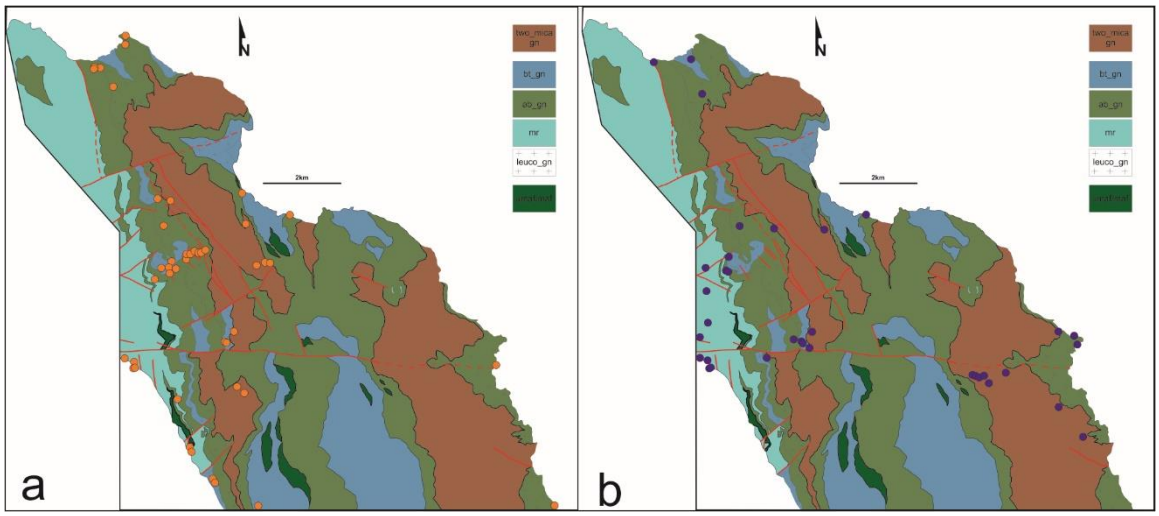

Fig. 3.29. Spatial distribution of the mesoscopic parasitic F3 folds in the study area: a) Z-folds (orange-colored bullets, b) S-folds (purple-colored bullets).

In many locations, S and Z mesoscopic, parasitic folds exist altogether without having in between any M-shape folds. The most characteristic location of S/Z co-existence is within the marbles exposed WSW of Konstamonitou monastery and the marbles exposed WNW of Esfigmenou monastery. In both cases these folds are associated by an intense S3 mylonitic foliation. This co-existence of S and Z folds along S3 surfaces, without an isoclinal M-fold hinge interrupting these geometries, at an E-W trending observational plane, could represent transport-parallel neutral verging (M) open folds, associated with the development of sheath folds (Alsop and Holsworth, 2004) and in the case of the study area, N-S trending sheath folds, which were also observed as meso-scopic structures in the field (Fig. 3.30 and 3.31). This structural scenario of a large-scale sheath fold will be discussed later on.

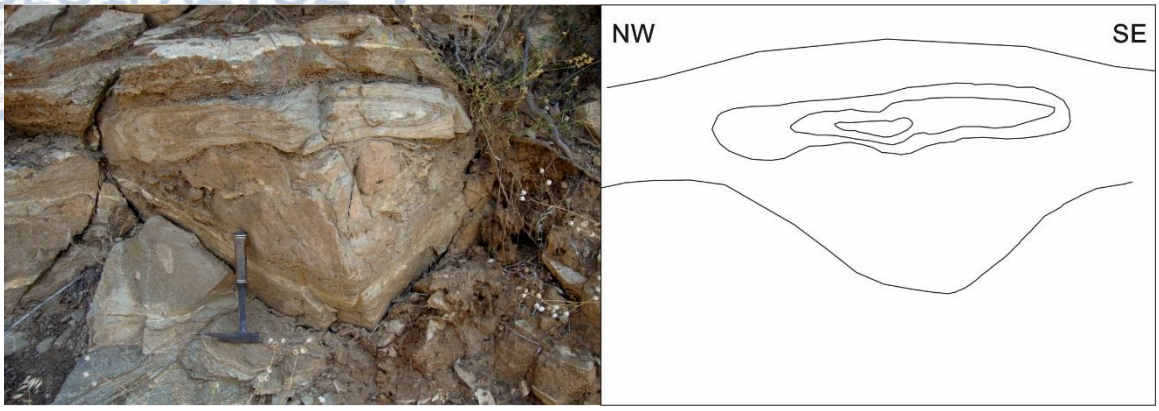

Fig. 3.30. Sheath fold within the lower biotite-hornblende gneiss map unit, E of Dohiarion monastery.

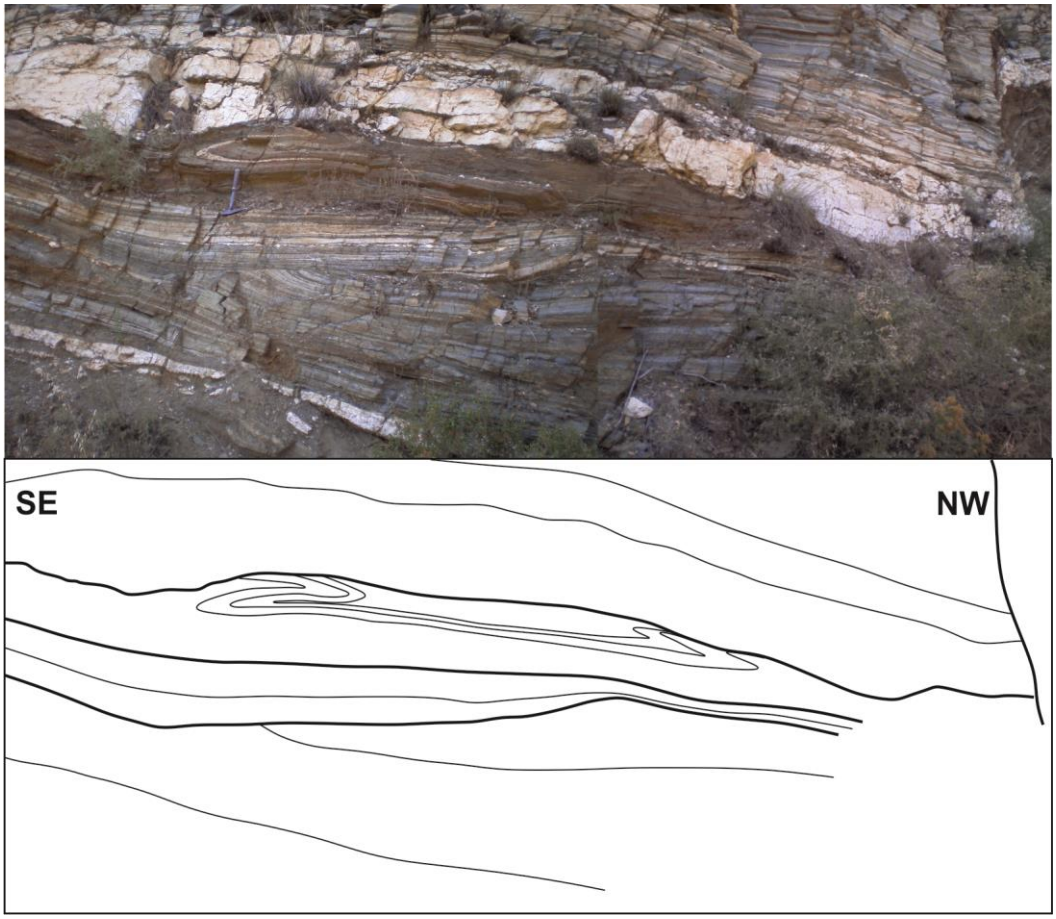

Fig. 3.31. Neutral verging (M) sheath fold, within the migmatitic amphibolite gneiss underlying the two mca gneiss, truncated by narrow shear zones, E of Esfigmenou monastery

Further structural analysis was also performed on the L3 dataset, in an attempt to correlate its distribution with the F3 isoclinal folding and consequently the overall geometry of the study area, via its correlation with the S3 planes on which the L3 was

recorded at each site. The L3 distribution in two main concentrations trending NNE-SSW and NNW-SSE respectively (Figs 3.12 and Fig. 3.32) shows that in each case an isoclinal to tight folding is suggested by the corresponding S3 planes (Fig. 3.32). More specifically, the S3 referring to the NNE-SSW L3 concentration dips with low angles either towards the E to ESE and to a much lesser extent towards the WNW, representing either a NNE-SSW trending, recumbent isoclinal fold or a tight again NNE-SSW trending fold (Fig. 3.32a). In any case the best-fit great circle resulting from the S3 data suggests a NNE-SSW trending geometrical axis. As far as the NNW-SSE L3 concentration is concerned, the S3 primarily dips with low angles towards the ENE and secondary concentrations represent shallow dipping planes towards the WSW, representing a NNW-SSE trending tight fold, again parallel to the L3 trend (Fig. 3.32b). The best-fit great circle resulting from the S3 data suggests a NNW-SSE trending geometrical axis.

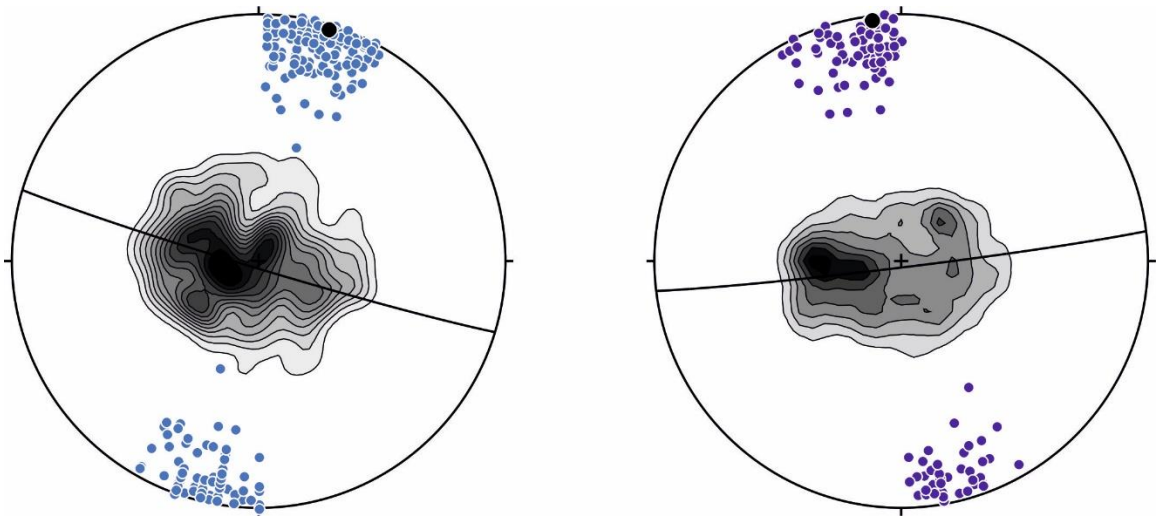

Fig. 3.32. Correlation of the L3 lineation with the corresponding S3 planes: a) for the NNE-SSW L3 concentration, and b) for the NNEW-SSE concentration. In both cases a respective NNE and NNW, horizontal F3 fold axis is suggested by the analysis of the S3 planes, verifying a bilateral geometry, about a N-S axis.

The afore-mentioned analysis, which was applied on the L3, took place for the F3 axes as well: the dataset was sub-divided into two sub-sets, one for the NNW-SSE concentration and one for the NNE-SSW concentration, and the S3 measurements were analyzed, belonging to the sites of the corresponding F3 data. A similar structural pattern

was also revealed during this analysis (Fig. 3.33): a) a NNW-SSE symmetry axis was outlined for the respective F3 concentration, giving insight to two possible sets of NNW-SSE trending, isoclinal to tight, horizontal, recumbent folds, with shallow-dipping limbs either to the WSW or the ESE (Fig. 3.33b), b) a NNE-SSW symmetry axis was outlined for the respective F3 concentration, suggesting a NNE-SSW trending, tight, horizontal recumbent fold, with shallow-dipping limbs towards the ESE and WNW (Fig. 3.33a). The structural pattern of a bilateral geometry trending both NNW-SSE and NNE-SSW repeats itself in the F3 fold-axis as well, as already described in the S3 and L3 analysis, thus verifying the dominant isoclinal folding structure governing the study area and leading to a structural combination of all these elements under the same deformational event.

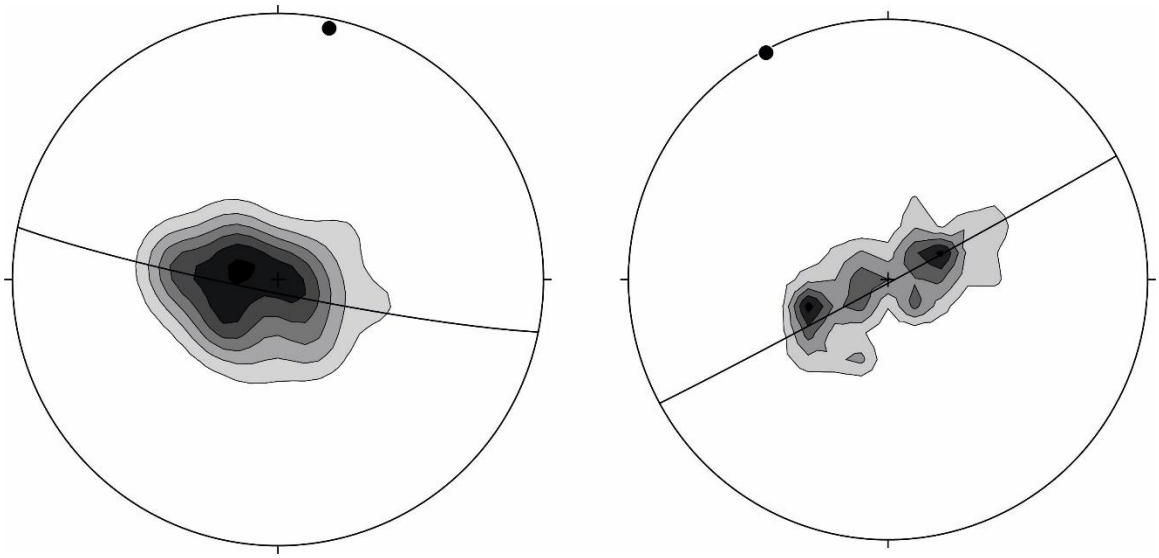

Fig. 3.33. Correlation of the S3 planes recorded at sites with the F3 fold axes: a) trending NNE-SSW to N-S and corresponsing to the according F3 axes concentration from Fig. 3.18, b) trending NNW-SSE to N-S and corresponsing to the according F3 axes concentration from Fig. 3.18. The S3 foliation follows a parallel geometry in both cases, with best-fit great circles striking ESE-WNW and ENE-WSW respectively. An isoclinal to tight folding can be concluded from both stereo-diagrams, trending in each case parallel to sub-parallel to the respective F3 axis concentration.

In overall, the fact that the L3 stretching lineation has been documented in this study to be parallel to the f-axes of the F3 isoclinal to tight folds, the axial planes of which partly constitute the S3 foliation, has sought its explanation in a large-scale sheath fold

geometry. Mesoscopic isoclinal folds and parasitic folds, as well as the large-scale parasitic folds (indicated by the S3 analysis), trending both NNW-SSE and NNE-SSW could be describing isolated parts of a larger-scale sheath fold, and constitute domes or basins, where fold hinges converge or diverge respectively, when taking into account the transport direction and kinematics of the large-scale shear zone in question. The fewer in number recorded fold axes of isoclinal folds, trending NW-SE to WNW-ESE and NE-SW to ENE-WSW, could represent the conical parts of the megascopic sheath folds. In addition, the two main best–fit great circles defined by the F3 axis generally trend about an E-W axis (Fig. 3.33), thus indicating a transport direction normal to this trend and towards either the N or to the S (Alsop et al. 2004). The former arcs of these best-fit great circles represent the Y axis of the bulk finite strain ellipsoid and their normal trend, coinciding with the L3 and the F3 axes represent the X-axis of the bulk finite strain ellipsoid (Alsop et al. 2004) (Fig. 3.12, 3.18). Bearing in mind that the isoclinal fold geometry is contemporaneous with the L3 stretching lineation, which represents a general transport direction trending N-S, so do the bilaterally dispersed NNW-SSE and NNE-SSW fold axes represent the general orientation of dome and basin closures of sheath folds, as well as the large-scale kinematics of a corresponding shear zone (Fig. 3.34). Whether the spatial combination of this bilateral geometry represents domal or basinal sheath folds depends on whether the transport direction of the overall shearing is top-to-the-N or top-to-the-S, an issue that will be discussed and clarified in the description and kinematic analysis of the deformational events that affected the study area. Moreover, judging from the small apical angle between the stretching lineation L3 and the isoclinal axes F3 (Fig. 3.12, 3.18 and 3.33), an increased hinge curvilinearity is concluded, which also suggests an increased axial planar rotation of these generally recumbent isoclinal folds. In this sense, the shear zones leading to the afore-mentioned structures should be parallel or sub-parallel to the axial planes of the F3 folds. This inferred, increased curvilinearity and axial planar rotation is also an indicator of a mature/well-developed sheath fold geometry (Alsop and Holsworth, 2004; 2006).

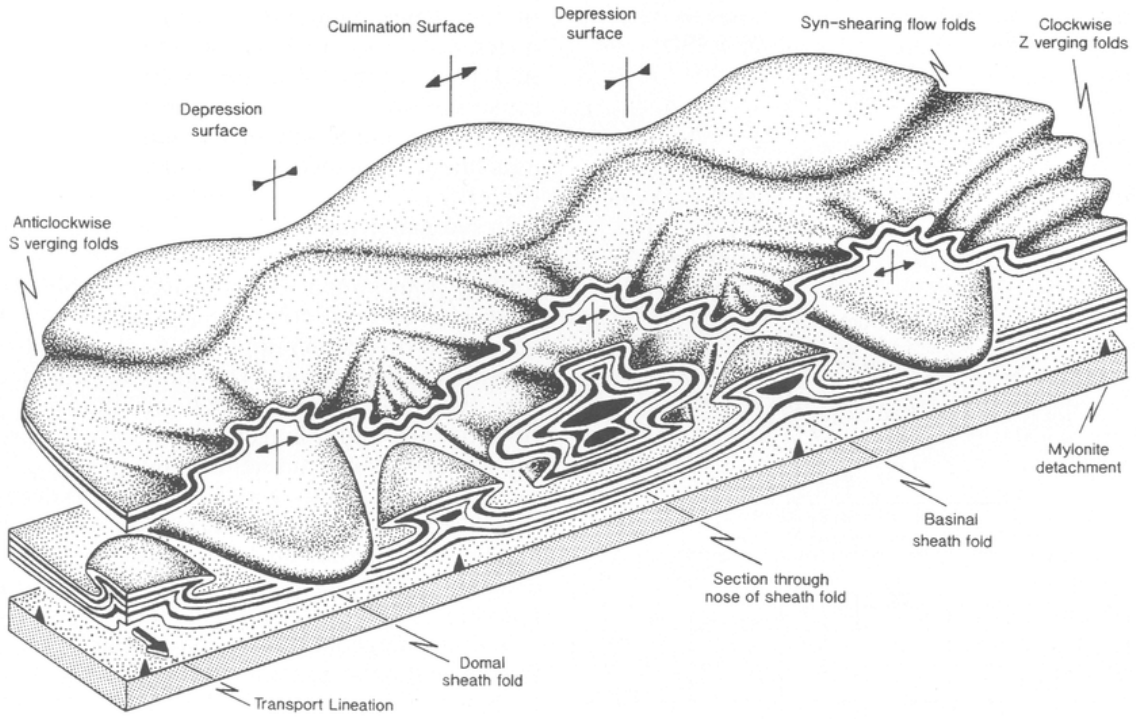

Fig. 3.34. Schematic 3D cartoon illustrating the sheath fold geometry and orientation of synshearing flow folds together with sheath folds associated with transport-parallel culmination and depression surfaces. Increasing deformation towards the underlying detachment surface (marked by barbs) results in pronounced attenuation of the lower limb and reduction in the apical angle of the sheath fold from tongue folds on the upper limb to tubular folds on the lower limb. Culmination and depression surfaces are associated with transport-parallel neutral verging (M) open folds with steeply dipping axial planes. They separate regions of synshearing flow folds with S folds trending anticlockwise of transport fromZ folds developed clockwise of transport. From Alsop and Holsworth, 2004.

3.3.4. F4 folds

F4 folds are NNW-SSE to N-S trending (Fig. 3.35) generally horizontal to subhorizontal, steeply-inclined, and asymmetric to overturned verging mainly towards the WSW (Fig. 3.36-3.43). Sometimes they also appear as upright folds. The characteristic micro-crenulation folds observed in various localities and associated genetically with the formation of the afore-mentioned S4 crenulation cleavage, also belong to this F4 group. F4 folds were recorded to have affected all the map units in the study area.

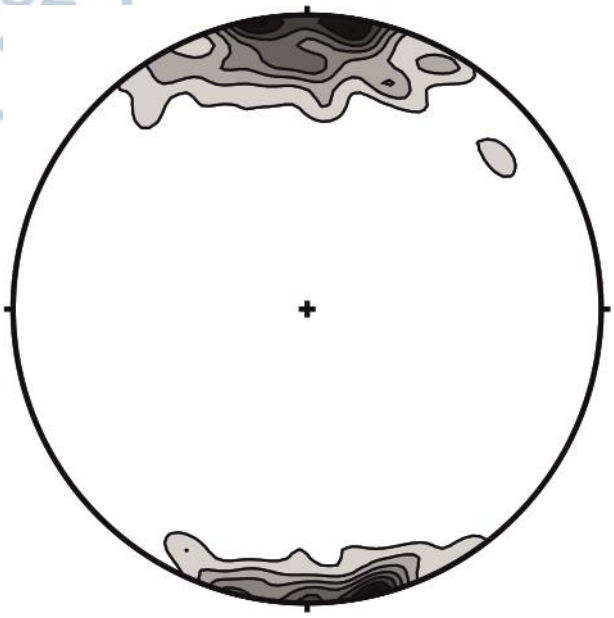

Fig. 3.35. Structural analysis of the F4 axes trending NNW-SSE to N-S.

Fig. 3.36. F4 asymmetric, sub-horizontal S-plunging folds, within the marbles map unit, NNW of Xenofontos monastery, verging towards the W.

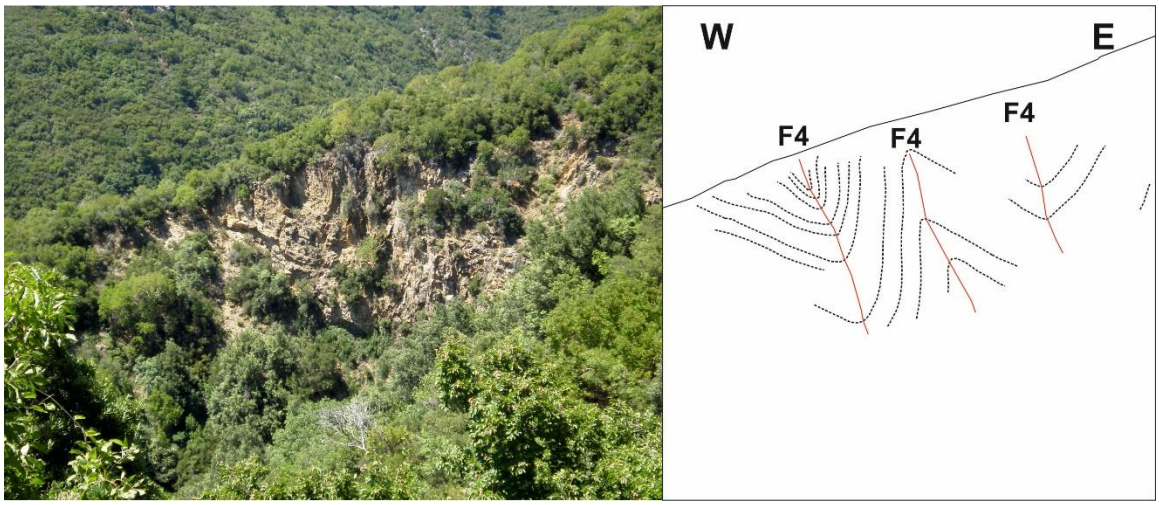

Fig. 3.37. F4, asymmetric, steeply inclined, N-S trending folds, within the marbles map unit, WSW of Konstamonitou monastery, verging towards the W.

Even though they mainly appear as asymmetric close folds verging mainly towards the WSW to W, but occasionally also towards the ENE to E, they vary in inter-limb angle as well as in their axial plane dip angle from site to site. That is why at some locations overturned, close folds are observed and at other locations we document nearly upright, open folds. The distribution of the limbs of isolated F4 folds varies, representing different combinations of the fold types constituting the F4 group (Fig. 3.38). Nonetheless, the limbs of the F4 folds define a general fold axis plunging towards the NNW, verifying the geometry mentioned for the isolated F4 axes as well. Moreover, a main vergence towards the WSW can also be concluded from this afore-mentioned F4 limbs distribution (Fig. 3.38); the asymmetry of the two main concentrations suggests a relatively shallower, ENE dipping limb, which has been more frequently recorded, and a slightly more steeply, WSW dipping limb, which has been less frequently recorded, conclusively outlining an F4 asymmetric, steeply-inclined fold, verging towards the WSW.

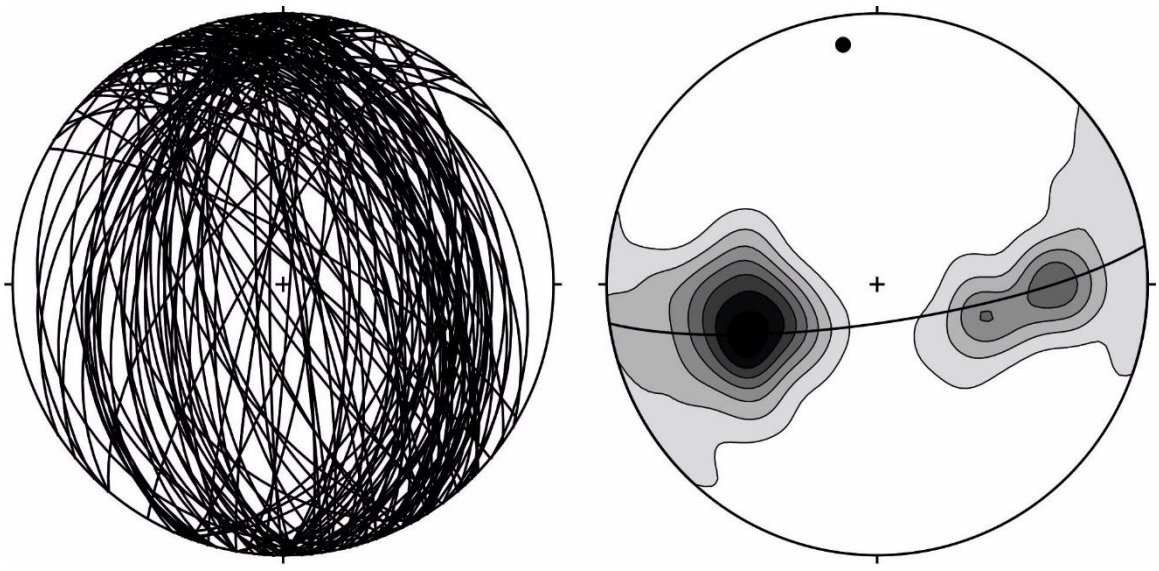

Fig. 3.38. Structural analysis of the recorded F4 fold limbs: a) Planes of the F4 fold limbs; b) The distribution of the F4 limbs suggests a general subhorizontal, NNW-plunging F4 axis, with a main vergence towards the WSW. Equal area, lower hemisphere projection.

Another noteworthy fact is that these F4 folds have been found to overprint pre-existing F3 folds in various locations (Figs 3.39-3.43) and, where evident, F2 folds as well (Fig. 3.40. and 3.43). Isoclinal previously recumbent folds have been refolded, by F4 folds having as a result F3 axial planes to obtain, at places steeply inclined to vertical orientations. Taking into account the fact that F4 folds mainly trend NNW-SSE to N-S and that F3 axes were originally oriented parallel or sub-parallel to the afore-mentioned F4 folds (Figs 3.18, 3.35 and 3.40), the two fold patterns interfere co-axially, with the F4 pattern superimposing the F3 geometry (Type III of Ramsay fold interference patterns, Ramsey, 1967).

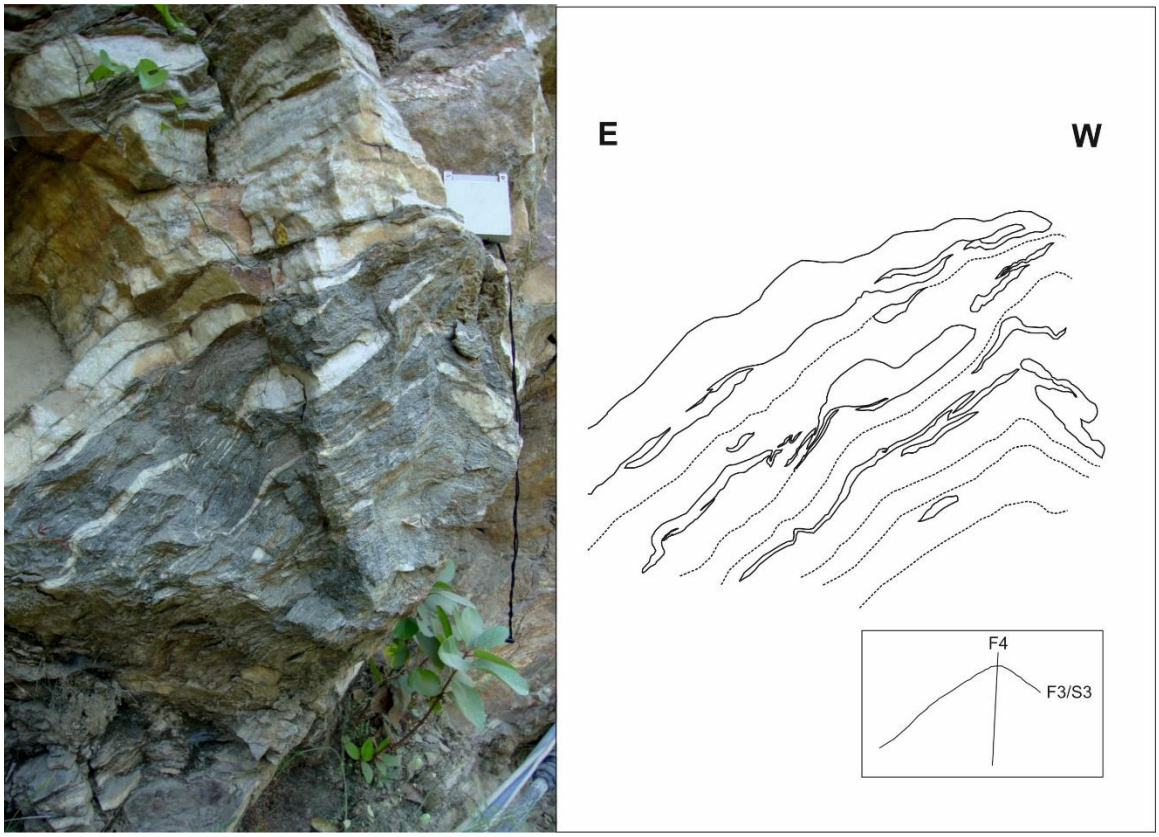

Fig. 3.39. Isoclinal parasitic F3 folds and S3 foliation fabric being refolded by a steeply-inclined to upright N-S trending F4 fold, within the marbles map unit, N of Dohiarion monastery.

Fig. 3.40. Upright to overturned limb of F4 asymmetric fold in marbles, S of Hiliandariou monastery. Notice how pre-existing N-S trending, F3 isoclinal folds have been "co-axially" refolded by F4 parasitic folds. The interference pattern within the isoclinal folds also bears witness of F2 isocinal folds being refolded by F3 folds.

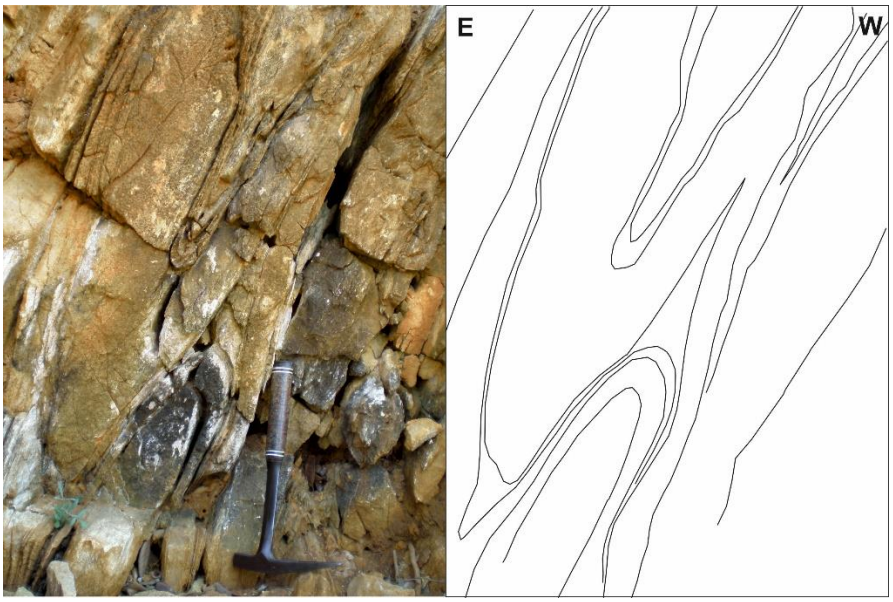

Fig. 3.41. Isoclinal, N-S trending, F3 fold, constituting part of an overturned limb belonging to an also N-S trending, overturned F4 fold, verging towards the W, within the marbles, E of Esfigmenou monastery.

Fig. 3.42. Isoclinal F3 fold, being refolded by gentle-open F4 fold, in the two-mica gneiss map unit, E of Konstamonitou monastery.

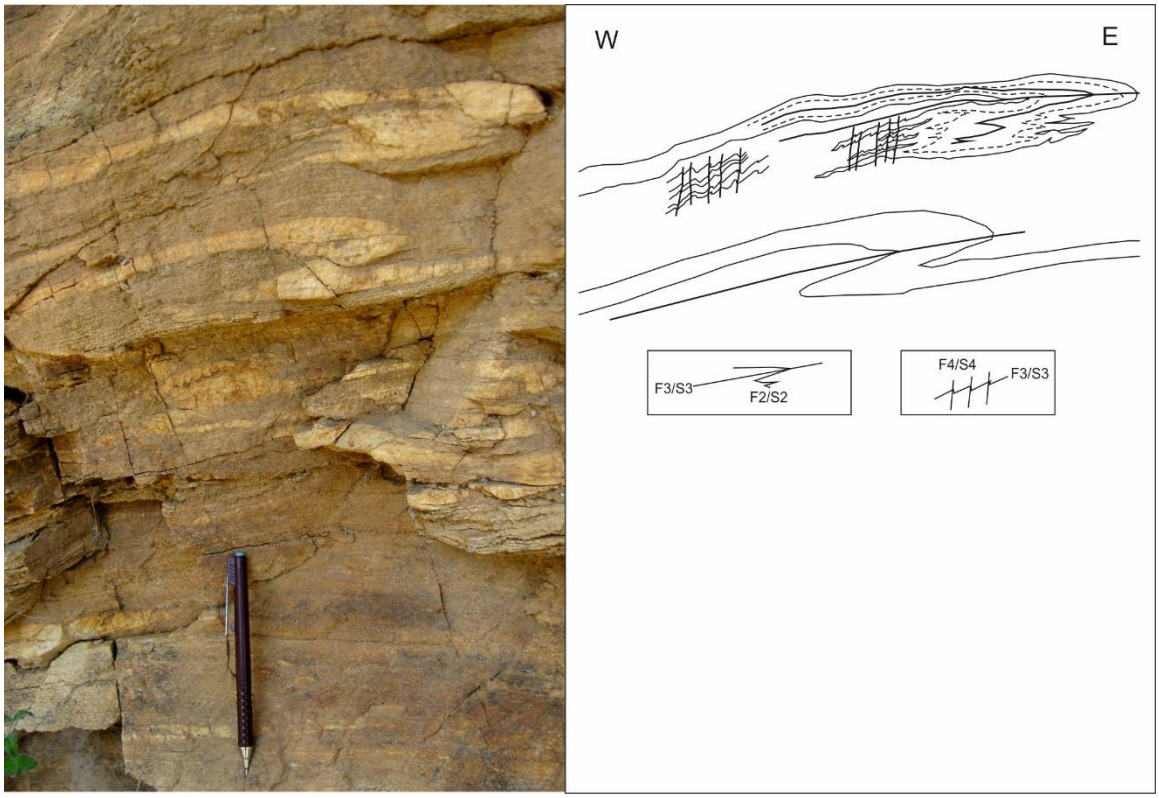

Fig. 3.43. Overprinting relationships of 3 distinct generations of folds and planar fabrics, within the two-mica gneiss map unit WNW of Vatopedi monastery. Pre-existing isoclinal F2 folds being isoclinally

refolded by F3 folds and both structures, subsequently, crenulated by "co-axial", N-S trending, F4 crenulation folds.

3.3.5. F5 folds

The last recognized folding event includes mainly gentle to open, upright, sub-horizontal F5 folds, trending ENE-WSW to ESE-WNW, about an E-W axis (Fig. 3.44), and in few cases kink folds of according orientation (Fig. 3.10). They constitute the least imprinted folding pattern on the map units of the study area and their documentation meso-scopically in the field was restricted only in scarce locations.

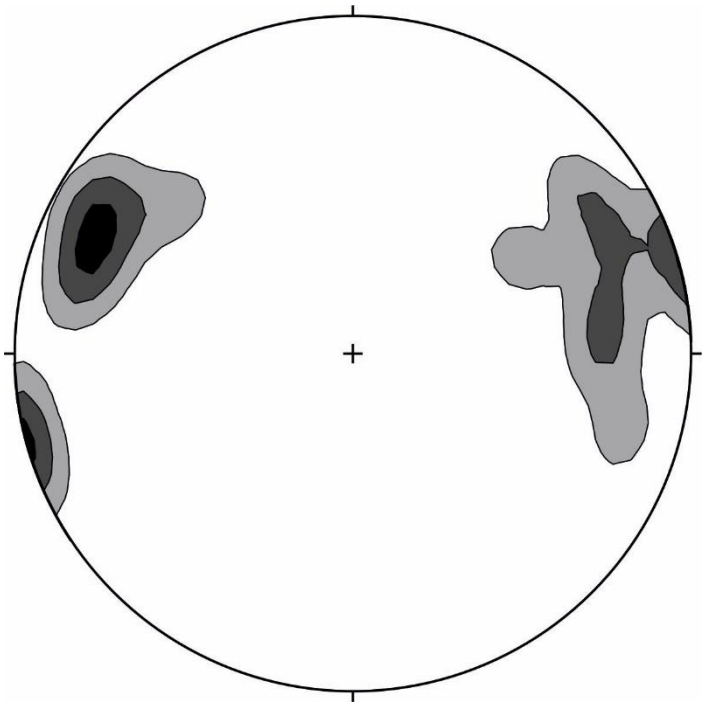

Fig. 3.44. Distribution of F5 fold axes trending about an E-W axis.

Chapter 4. Micro-structural analysis

4.1. Microscopic shear sense indicators in mylonites

As it has already been outlined the whole study area is characterized by an overall ductile deformation diffused in all the map units and expressed via numerous shear zones, throughout the whole body rock. This ductile deformation and its apparent high-strain has been imprinted in these ductile shear zones, in the form of mylonites, including various fabric elements, which have recorded this shearing. In some cases, the sense of shear can be concluded for these mylonitic shear zones, through the proper kinematic analysis of these fabric elements, which are called shear sense indicators. Therefore thin-sections of various rock samples from the majority of the map units were examined. They are always cut parallel to the stretching lineation of minerals and aggregates, normal to the mylonitic foliation in order for the observation plane to coincide with the XZ-plane of the strain ellipsoid. As already mentioned the collection of samples for preparing and analyzing thin sections was primarily focused on specific locations where the primary contact of the lower amphibolite gneiss and two-mica gneiss map units could be micro-structurally examined. Therefore, the majority of the thin-sections come from this specific structural horizon (Fig. 4.1). However, additionally to the microscopic observation of thin sections, observations concerning the afore-mentioned kinematic fabric elements were also carried out in the field, throughout the whole study area. During this overall examination the following microscopic shear sense indicators were recorded in thin-sections:

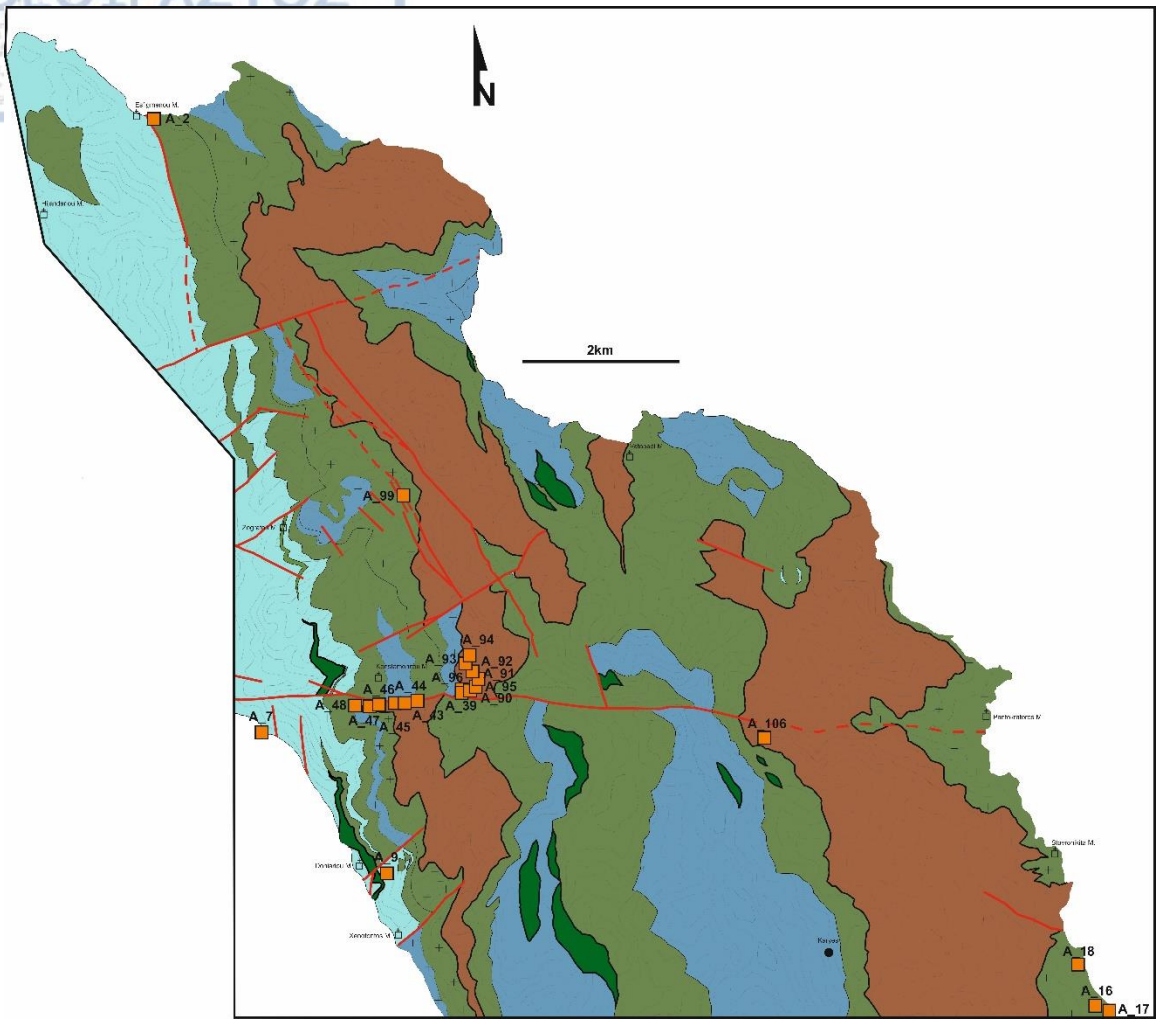

Fig 4.1. Location of the samples and respective thin sections used in the micro-structural analysis.

- **Porphyroclasts**. They are defined as mineral grains that were more resistant and remained as remnants in a matrix that is characterized by a relatively smaller grain size (Passchier and Trouw, 2005). The planar fabric of the matrix wraps around the porphyroclasts, which develop due to a difference between the rheological behavior of the porphyroclasts themselves and the minerals constituting the less resistant matrix (Passchier and Trouw, 2005). Quite frequently porhyroclasts are surrounded by a mantle formed by the same recrystallized mineral (mantled porphyroclasts) or a rim of different composition than the porphyroclast (strain shadow porphyroclasts), which in both cases forms wings. According to the geometry and symmetry of these wings, the porphyroclasts can be distinguished into: ϕ -type, σ –type (which can also extend their geometry and

interpretation to sigmoid aggregates), δ -type, and complex mantled clasts (Hanmer 1984b; Passchier and Simpson 1986; Hooper and Hatcher 1988).

The porphyroclasts, found in abundance in most of the thin–sections, belong in their majority to porphyroclasts with strain shadows, usually comprised of quartz, plagioclase and K-feldspar clasts, in a quartzofeldspathic and micaceous matrix. Porphyroclast systems were recorded in thin-sections from the two-mica gneiss map unit (samples A_39, A_41, A_43, A_44, A_45, A_46, A_92, A_93, A_94, A_96, E of Konstamonitou monastery and A_16, W of Iviron monastery), the leucocratic counterparts of the migmatitic amphibolite gneiss map unit (sample A_99), the biotite gneiss map unit (A_2) and its leucogneissic bands (A_47) and the marbles map unit (A_7). In their vast majority they indicate a top-to-the-S sense of shear (Fig. 4.2).

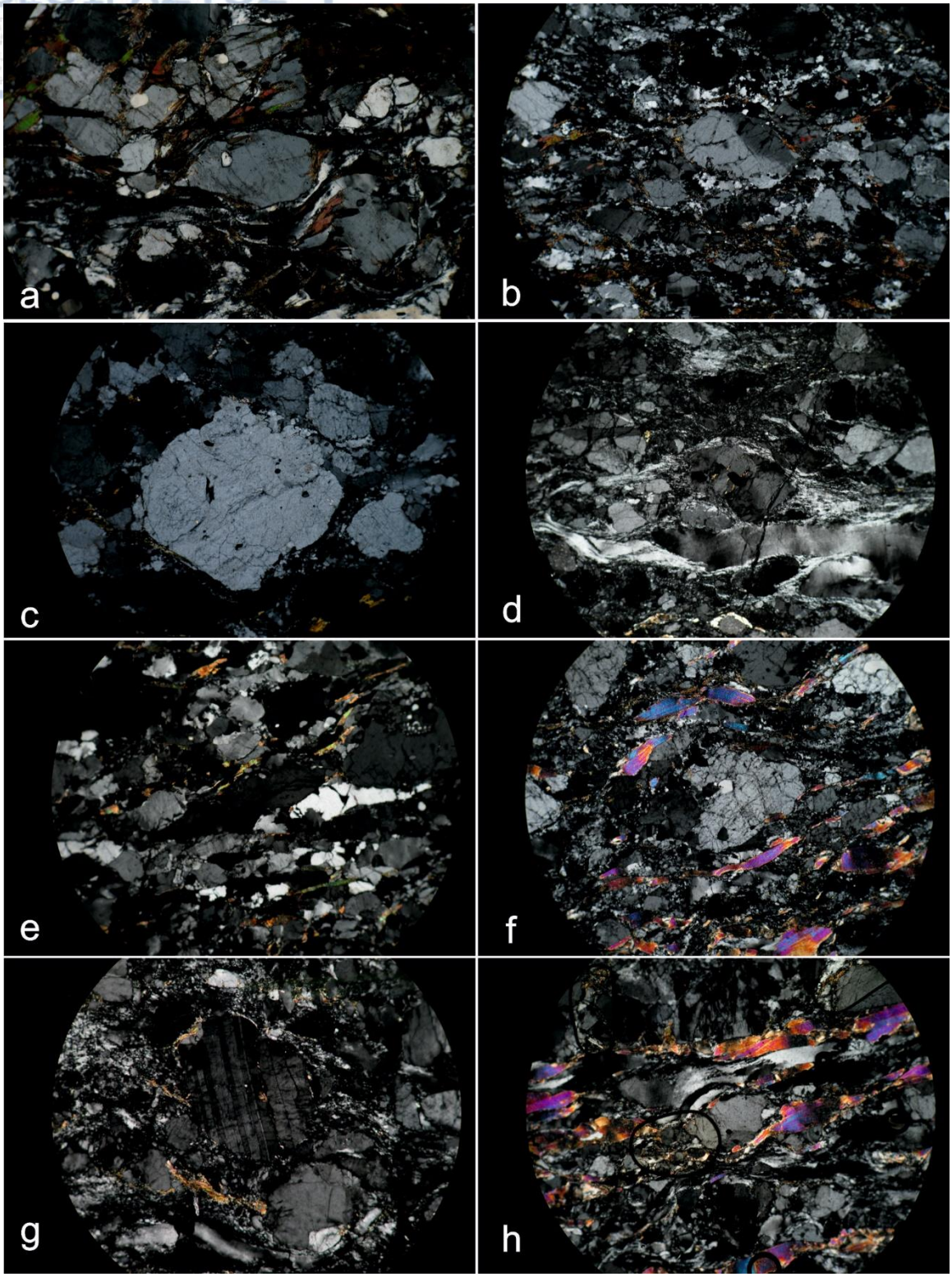

Fig. 4.2. Porphyroclasts with strain shadows, from thin sections: a) σ-clast, within the biotite gneiss map unit, indicating a dextral sense of shear (top-to-the-S). Sample A_2; b) σ-clast, within the two mica-gneiss gneiss map unit, indicating a dextral sense of shear (top-to-the-S). Sample A_43; c) σ-clast, within the two

mica-gneiss gneiss map unit, indicating a dextral sense of shear (top-to-the-S). Sample A_43; d) σ-clast, within the two mica-gneiss gneiss map unit, indicating a sinistral sense of shear (top-to-the-S). Sample A_90; e) σ-clast, within the two mica-gneiss gneiss map unit, indicating a dextral sense of shear (top-to-the-S). Sample A_92; f) σ-clast, within the two mica-gneiss gneiss map unit, indicating a dextral sense of shear (top-to-the-S). Sample A_93; g) σ-clast, within the two mica-gneiss gneiss map unit, indicating a sinistral sense of shear (top-to-the-N). Sample A_93; g) σ-clast, with mica quarter mats (Hanmer and Passchier, 1991) within the two mica-gneiss gneiss map unit, indicating a dextral sense of shear (top-to-the-S). Sample A_96.

- **C and C′ type shear bands**. C-type shear bands or shear band cleavage (Passchier and Trouw, 2005), constitute part of a C/S fabric. In this fabric the S planes are transected by the C-type shear bands (Berthé et al. 1979a,b; Vernon et al. 1983; Lister and Snoke 1984; Krohe 1990; Toyoshima 1998), the latter being parallel to the shear zone boundaries and considered generally straight and continuous. C′-type shear band cleavage, on the other hand is oblique to the shear zone boundaries (with an angle ranging from 15-35° between the C′-type shear band and the shear zone boundary, Dennis and Secor, 1987; Passchier, 1991b; Blenkinsop and Treloar, 1995), it is frequently short and wavy, with a tendency to appear in more micaceous rocks and can overprint the C-S fabric (Berthé et al. 1979b, Passchier and Trouw, 2005).

C-S fabric and the according C-type shear band cleavage was also quite frequent in many of the samples collected in this study, belonging to the two-mica gneiss map unit (samples A_16, W of Iviron monastery, and A_43, A_44, A_46 and A_93 E of Konstamonitou monastery), the biotite gneiss map unit (samples A_2, E of Esfigmenou monastery and A_17, SSE of Iviron monastery), the leucogneiss inlayers within the biotite gneiss (sample A_90, E of Konstamonitou monastery) and the marbles map unit as well (sample A_7, W of Konstamonitou monastery) (Fig. 4.3).

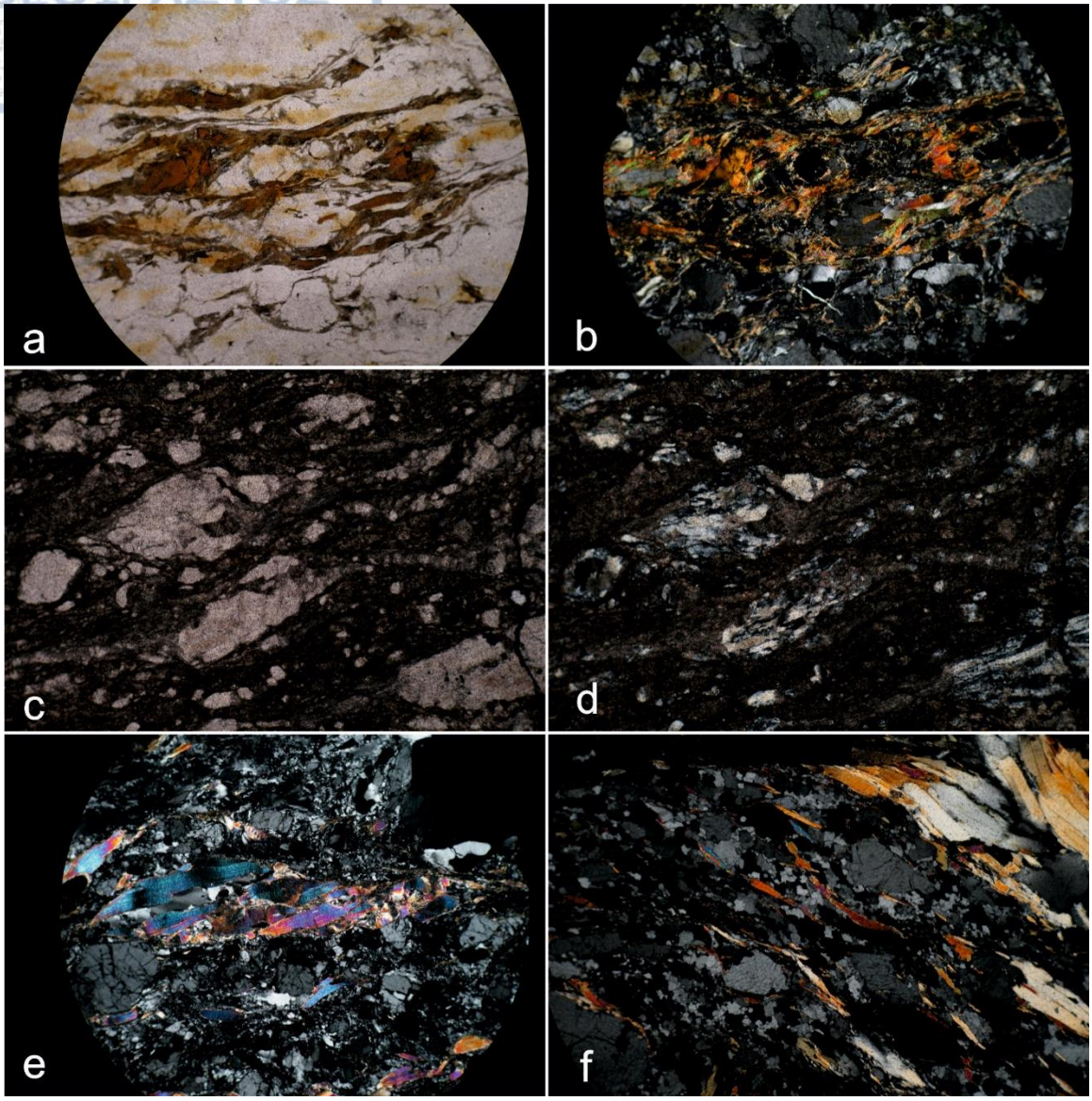

Fig 4.3. C-S fabric and C-type shear bands in thin-sections: a) C-S fabric and C-type shear bands, within the biotite gneiss map unit, indicating a dextral sense of shear (top-to-the-S). Sample A_2; b) C-S fabric and C-type shear bands, within the biotite gneiss map unit, indicating a dextral sense of shear (top-to-the-S). Crossed polarizers, sample A_2; c) C-S fabric and C-type shear bands, within the marbles, indicating a dextral sense of shear (top-to-the-S). Sample A_7; d) C-S fabric and C-type shear bands, within the marbles, indicating a dextral sense of shear (top-to-the-S). Crossed polarizers, sample A_7; e) C-S fabric and C-type shear bands, within the two mica gneiss map unit, indicating a dextral sense of shear (top-to-the-S). Sample A_93; f) C-S fabric and C-type shear bands, within the two mica gneiss map unit, indicating a sinistral sense of shear (top-to-the-S). Sample A_46.

Most of the C′-type shear band cleavage micro-structures were recorded in two-mica gneiss thin-sections, (samples A_39, A_44, A_48 and A_96, E of the Konstamonitou monastery), but also within the amphibolite gneiss, from its leucocratic counterparts, where it becomes migmatitic and the biotite gneiss map unit (samples A_2 and A_47 from the biotite gneiss map unit, E of Esfigmenou monastery and E of Konstamonitou monastery respectively, and sample A_99 from the amphibolite gneiss map unit, E of Zografou monastery) (Fig. 4.4). Both C- and C′-type shear bands indicate in their vast majority a top-to-the-S sense of shear.

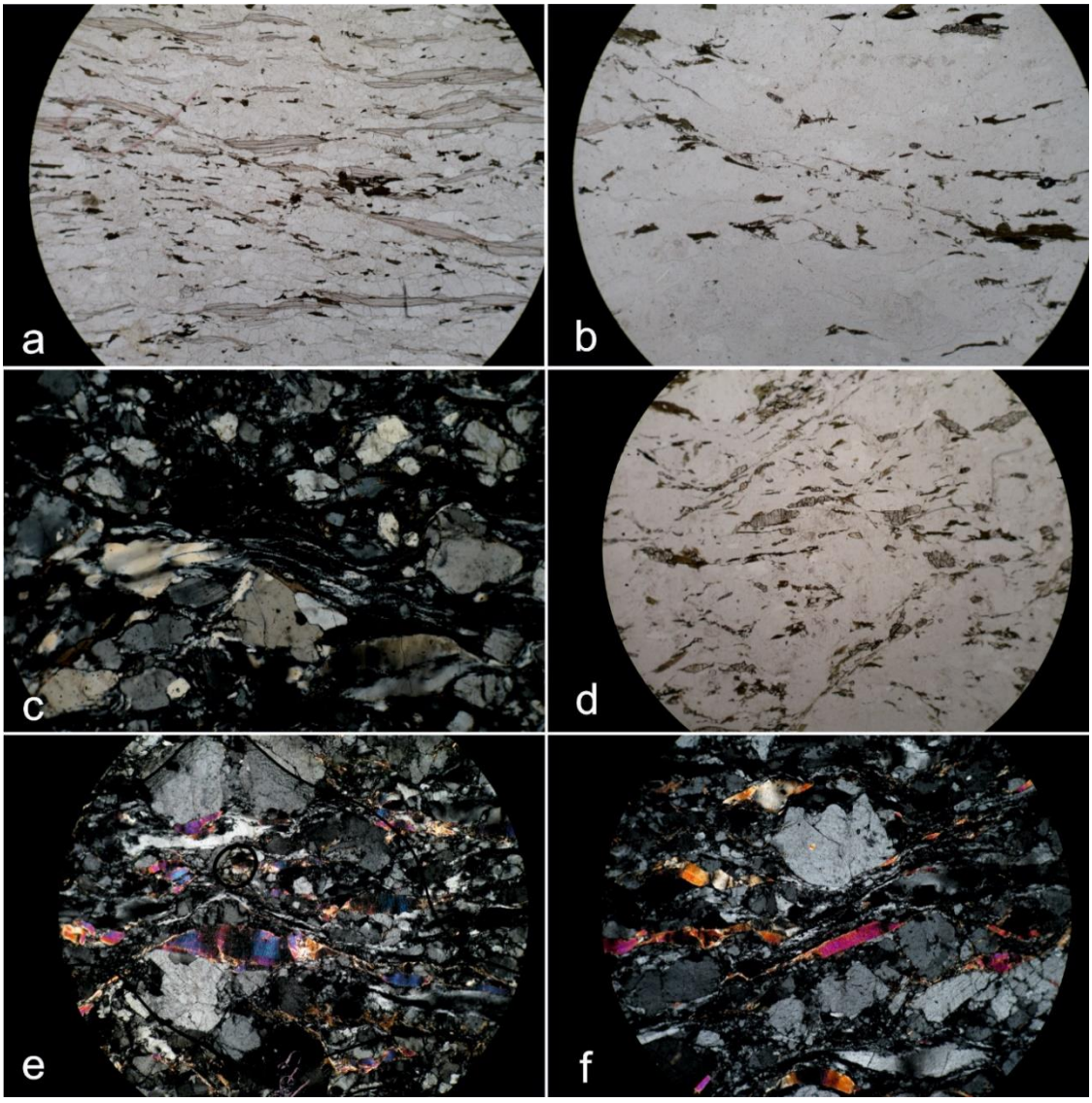

Fig. 4.4. C′-type shear bands in thin-sections: a) C′-type shear band, within the two mica-gneiss map unit, indicating a dextral sense of shear (top-to-the-S). Sample A_48; b) C′-type shear band, within the two

mica-gneiss map unit, indicating a dextral sense of shear (top-to-the-S). Sample A_44; c) C′-type shear band, also developing within its boundaries an oblique foliation, within the biotite gneiss map unit, indicating a dextral sense of shear (top-to-the-S). Sample A_2; d) C′-type shear band, within leucogneiss inlayers from the amphibolite gneiss, indicating a sinistral sense of shear (top-to-the-S). Sample A_99; e) C′-type shear band, also developing within its boundaries an oblique foliation, from the two mica-gneiss map unit, indicating a dextral sense of shear (top-to-the-S). Sample A_96; f) C′-type shear band, also developing within its boundaries an oblique foliation, from the two mica-gneiss map unit, indicating a sinistral sense of shear (top-to-the-S). Sample A_39.

-**Mineral fish.** Mineral fish is characterized by their typical elongate shape, their strong preference towards an orientation parallel to the mylonitic foliation and their lack of evidence of rotation (Passchier and Trouw, 2005). It has been experimentally shown that once a mineral fish obtains an elongate lozenge shape, and on the condition the mineral fish has poor bonding with the matrix, it can remain in a stable position in any non-coaxial flow, even in simple shear (Grotenhuis et al., 2002, Mancktelow et al., 2002, and Ceriani et al., 2003, Passhier and Trouw, 2005). The most common mineral fish found in mylonitic zones is the mica fish, which is also the most common mineral fish observed in the samples of the study area as well, even though few biotite-fish were also recorded.

Mica fish was recorded within the two-mica gneiss map unit (samples A_39, A_44, A_46, A_93, A_94, A_95, A_96, E of Konstamonitou monastery), the leucogneiss inlayers within the amphibolite gneiss map unit (sample A_106, N of Pantokratoros monastery) and the the biotite gneiss map unit (sample A_48, E of Konstamonitou monastery), also recording the highest strain intensity represented by the structure's extremely elongate, lozenge shape, and the marbles map unit (sample A_9). They overall indicate a top-to-the S sense of shear, with a few exceptions, indicating the opposite sense of shear (Fig. 4.5).

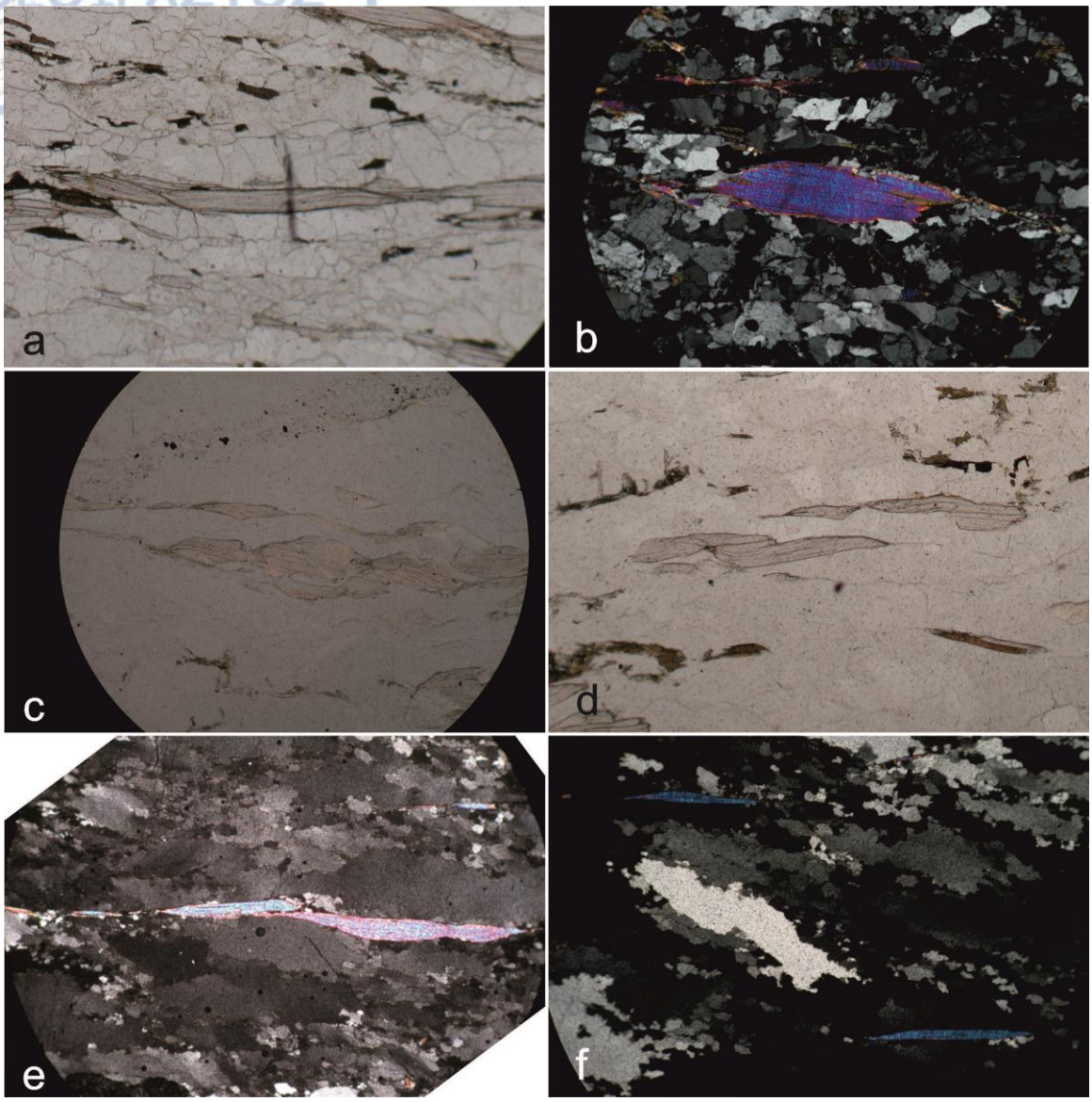

Fig. 4.5. Mica fish in thin-sections: a) Mica fish developed along with C′-type shear bands, within the leucogneiss, indicating a dextral sense of shear (top-to-the-S). Sample A_48; b) Mica fish, within the two mica-gneiss map unit, indicating a dextral sense of shear (top-to-the-S). Sample A_44; c) Mica fish within the two mica-gneiss map unit, indicating a sinistral sense of shear (top-to-the-N). Sample A_94; d) Mica fish within the two mica-gneiss map unit, indicating a sinistral sense of shear (top-to-the-S). Sample A_95; e) Mica fish within a leucogneiss inlayer from the amphibolite gneiss map unit, indicating a sinistral sense of shear (top-to-the-N). Sample A_106; f) Mica fish within a leucogneiss inlayer from the amphibolite gneiss map unit, indicating a sinistral sense of shear (top-to-the-N). Sample A_106.

- **Oblique foliation**. Oblique foliation is a type of foliation observed in mylonites, it is located within monomineralic domains, which in turn are usually subject to dynamic recrystallization, and it is characterized by a grain shape preferred orientation (Passchier and Trouw, 2005). The recrystallized grains constituting this oblique foliation can be characterized by an overall elongate shape (Means, 1981; Lister and Snoke, 1984), and its orientation is usually oblique to the compositional layering of a mylonite. Oblique foliations have been reported for quartz (Brunel, 1980; Law et al., 1984; Law, 1998; Knipe and Law, 1987; Lister and Snoke, 1984; Dell'Angelo and Tullis, 1989), among other minerals, and these were the monomineralic domains where oblique foliations were observed in this study, whereas Sub-Grain Rotation (SGR) was recognized as the dynamic recrystallization mechanism that led to the specific mylonite-related fabric elements (Fig. 4.6).

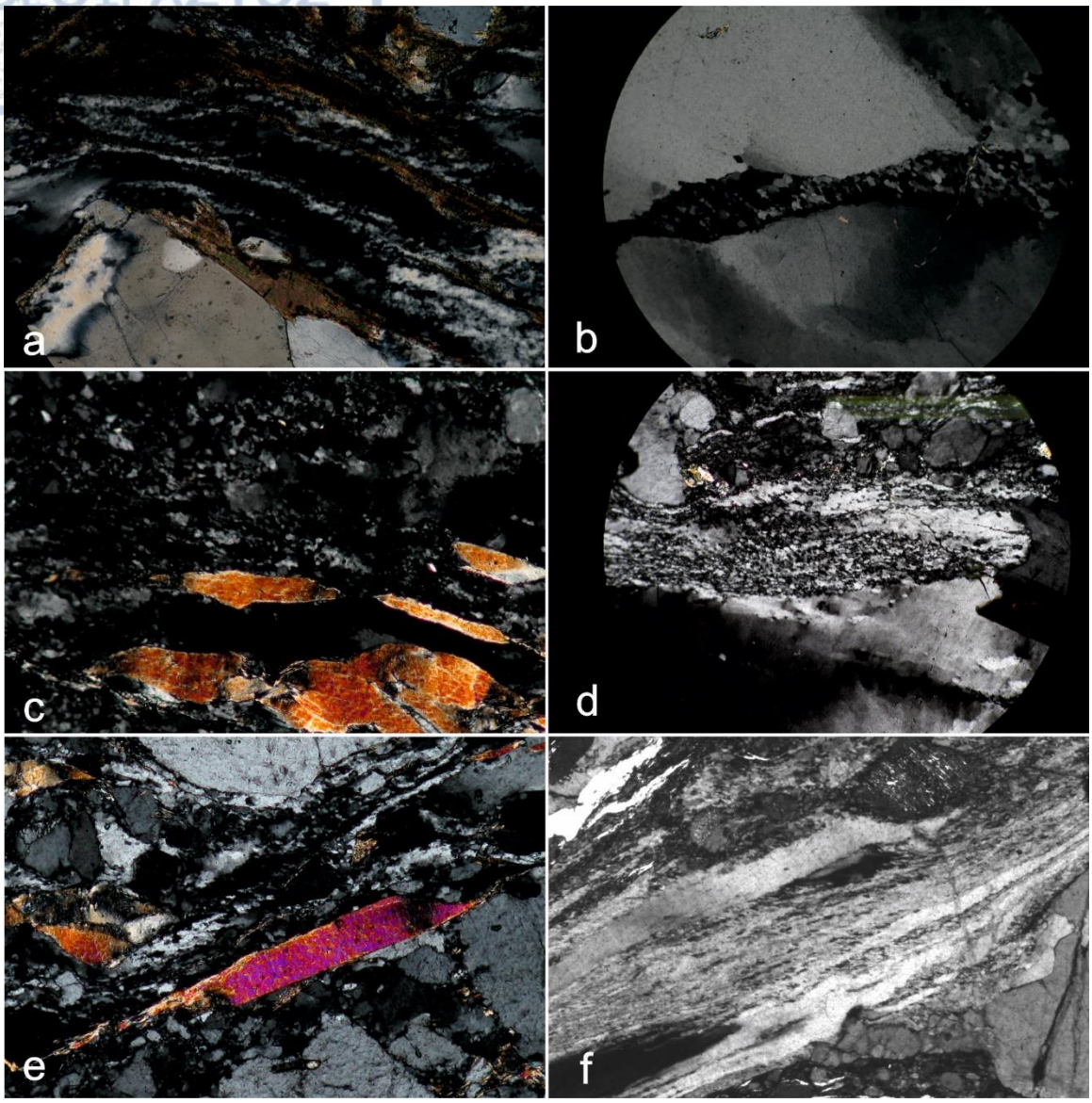

Fig. 4.6. Oblique foliation dominated by SGR as a dynamic recrystallization mechanism: a) Oblique foliation within a C'-type shear band, defined by elongate quartz ribbons, recrystallized by SGR, and mica domains, overall inclined to the horizontal S3 main foliation. The oblique foliation along with the shear band indicate a dextral sense of shear (top-to-the-S). Sample A2, biotite gneiss, E of Esfigmenou monastery; b) Oblique foliation within a quartz ribbon recrystallized by SGR, between two larger quartz crystals, indicating a sinistral sense of shear (top-to-the-S). Sample A44, two mica gneiss, E of Konstamonitou monastery; c) Oblique foliation within quartz-rich domains, separated by mica crystals and defining the S part of an overall C-S fabric, indicating an overall sinistral sense of shear (top-to-the-S). Sample A46, two mica gneiss, E of Konstamonitou monastery; d) Oblique foliation in quartz layers, indicating a sinistral sense of shear (top-to-the-S). Sample A_39, two mica gneiss, E of Konstamonitou monastery; e) Oblique foliation within a C'-type shear band, defined by elongate quartz ribbons,

recrystallized by SGR, and mica domains, overall inclined to the horizontal S3 main foliation. The oblique foliation along with the shear band indicate a sinistral sense of shear (top-to-the-S). Sample A39, two-mica gneiss gneiss, E of Esfigmenou monastery; f) Oblique foliation within and with respect to the boundaries of a C'-type shear band, developed in former quartz ribbons by SGR. Sample A_90, two mica gneiss, E of Konstamonitou monastery.

-Porphyroblasts. Porphyroblasts are single crystals, of a considerably larger size than their surrounding finer matrix and form by metamorphic growth (Passchier and Trouw, 2005). They constitute a valuable source of information, when it comes to the interpretation of the tectonic and metamorphic evolution of a study area, as their inclusion patterns can mimic the structure of rock, at the time of their growth (Passchier and Trouw, 2005). Thus, a relative timing of mineral growth can be achieved, providing insight to the metamorphic condition and the deformational history of the rock in question. Porphyroblasts, when referring to their inclusion pattern, have been classified by Zwart (1960, 1962) as: pre-, syn-, inter- and post-tectonic.

Garnet porphyroblasts have been recognized in various samples and map units both mesoscopically and microscopically but they were safely considered as a shear sense indicator only in sample A_18, coming from the biotite gneiss map unit and its leucogneissic inlayers, SSE of Stavronikita monastery, where strain shadows were prominent and in some porphyroblasts a syn-tectonic, spiral inclusion pattern could be inferred (Fig. 4.7).

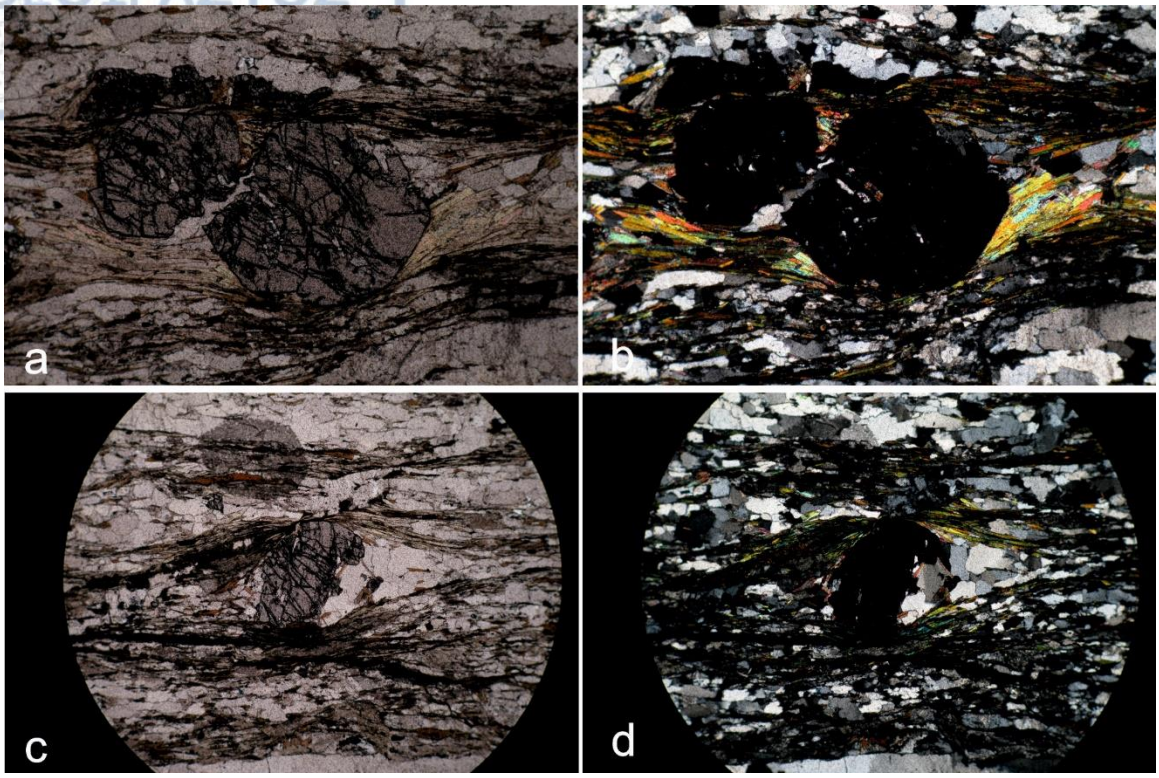

Fig. 4.7. Garnet porphyroblasts in the leucogneiss inlayers from the biotite gneiss map unit. Spiral inclusion patterns and stair-stepping from the quartz-rich strain shadows suggest a syn-tectonic temporal relationship with the formation of the dominant fabric imprinted on these rocks as well as with a dextral sense of shear (top-to-the S), SSE of Stavronikita monastery.

As already mentioned, shear sense indicators and markers were also recorded in the field, always following the same rationale of identifying fabric elements at an observational XZ-plane, parallel to the stretching lineation (Figs 4.8 and 4.9).

Fig. 4.8. Mesoscopic shear sense markers recorded throughout the study area: a) Sigmoidal quartzo-feldspathic aggregate in the migmatitic biotite-horneblende gneiss map unit, indicating a dextral sense of shear (top-to-the-S), SSE of Xenofontos monastery, b) Feldspar σ-clast in the migmatitic biotite gneiss

map unit, indicating a dextral sense of shear (top-to-the-S), SSE of Xenofontos monastery, c) Feldspar δ-clast, in the migmatitic biotite gneiss map unit, indicating a sinistral sense of shear (top-to-the-N), SSE of Dohiarion monastery, d) Garnet porphyroblasts with quartz strain shadows, in the amphibolite gneiss map unit, indicating a dextral sense of shear (top-to-the-N), E of Esfigmenou monastery, e) Sigmoidal feldspar and quartzo-feldspathic augens and C'-type shear bands, in the migmatitic, biotite gneiss map unit, indicating a sinistral sense of shear (top-to-the-S), E of Zografou monastery, f) Sigmoidal epidote-rich aggregate, with biotite-rich tails, within within an ultramafic sliver, tectonically emplaced within the amphibolite gneiss, indicating a sinistral sense of shear (top-to-the-S), E of Karyes, g) Sigmoidal bodies of mafic tectonic lenses and quartzo-feldspathic aggregates within the amphibolite gneiss map unit, indicating a dextral sense of shear (top-to-the-S), SSE of Zografou monastery, h) Domino structure of antithetic C'-type shear bands in the migmatitic, biotite gneiss map unit, indicating a dextral sense of shear (top-to-the-S), at Xenofontos monastery.

Fig. 4.9. Mesoscopic shear sense markers recorded throughout the study area: a) C-type shear bands forming an S-C fabric within a cm-thick shear zone, in the marbles map unit, indicating a dextral sense of shear (top-to-the-S), S of Zografou monastery, b) C-type shear bands forming an S-C fabric in the

leucogneiss, close to the amphibolite gneiss' boundary with the overlying the two-mica gneiss map unit, indicating a sinistral sense of shear (top-to-the-S), SSE of Iviron monastery,c) C-type shear bands forming an S-C fabric in altered ultramafic map unit, indicating a dextral sense of shear (top-to-the-S), ESE of Dohiarion monastery, d) C'-type shear bands in the biotite augen-gneiss, indicating a sinistral sense of shear (top-to-the-S) ESE of Zografou monastery, e) C'-type shear band in a leucogneiss inlayer, concordantly emplaced within the biotite gneiss map unit, indicating a sinistral sense of shear (top-to-the-S), E of Konstamonitou monastery, f) C-type shear bands forming an S-C fabric in leucogneiss layer, within the amphibolite gneiss map unit and its upper boundary with the two-mica gneiss map unit, indicating a dextral sense of shear (top-to-the-S), NNW of Pantokratoros monastery, g) C'-type shear band in a leucogneiss layer, concordantly emplaced within the biotite gneiss map unit, indicating a sinistral sense of shear (top-to-the-N), E of Esfigmenou monastery, h) Pematoid vein in the biotite gneiss map unit, boudinaged and sheared by the S3 mylonitic foliation into sigmoid beads, indicating a sinistral sense of shear (top-to-the-S), W of Karyes.

The above observations suggest that: a) A mylonitic fabric resulting from an intense shearing is the dominant fabric in all metamorphic rocks throughout the the study area. b) A dominant top-to-the-S sense of shear can be concluded for the thin-sections, as only 3 out of 24 samples indicated a top-to-the-N sense of shear. Even though the collection of samples was aimed at the structural horizon of the lower amphibolite gneiss and two-mica gneiss map units, shear sense indicators and markers were recorded throughout the study area and this dominant top-to-the-S sense of shear was also verified (Fig. 4.10), with a few exceptions at specific localitites, as is the case of the upper boundary of the two mica gneiss with the overlying amphibolite gneiss, in the form of a top-to-the-N mylonitic shear zone, W of Pantokratoros monastery. c) A non-coaxial, general to simple shear ductile deformation can be inferred for the study area, concerning the main deformational event which dominated in the ductile flow regime.

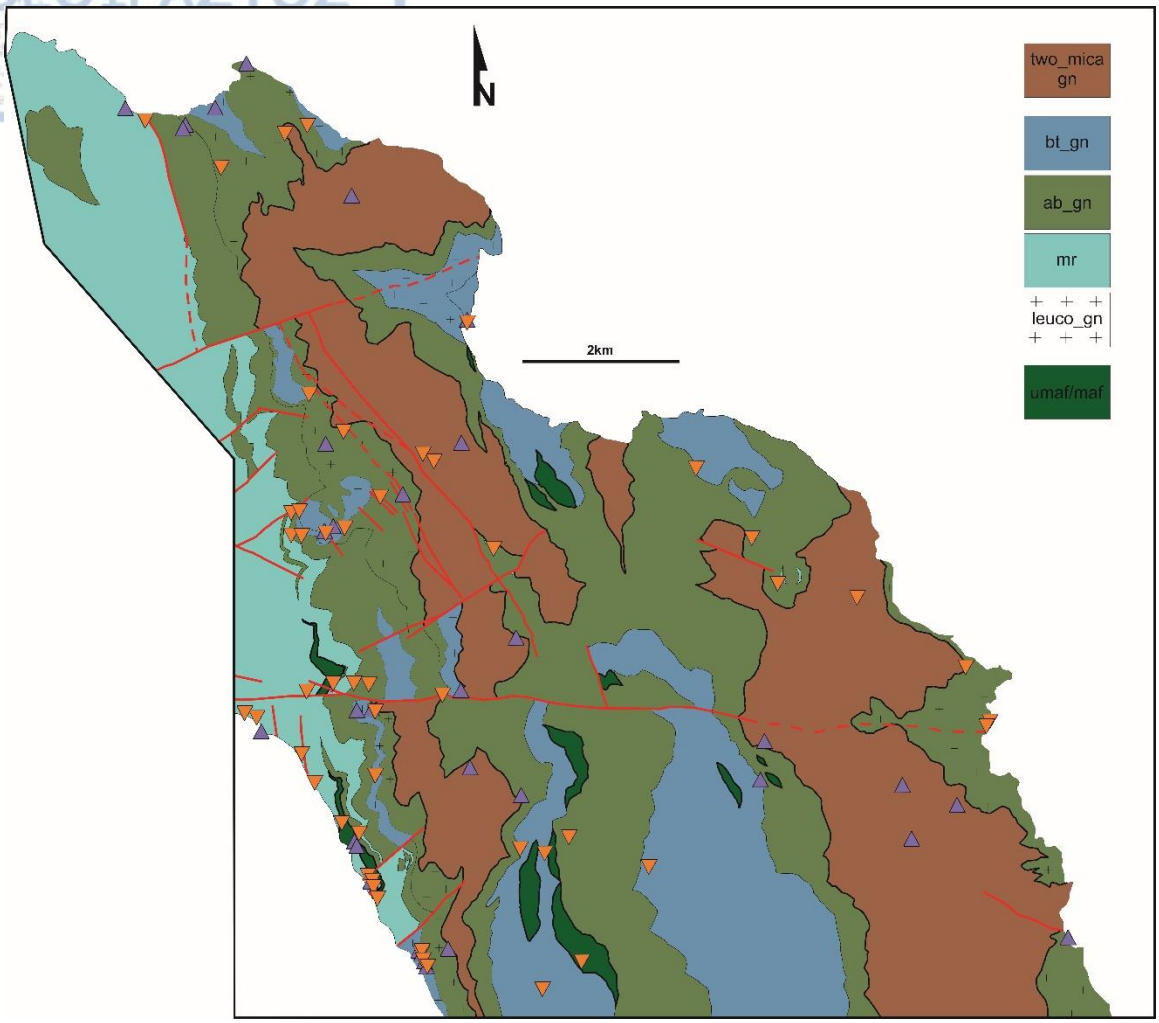

Fig. 4.10. Spatial distribution of mesoscopic kinematic indicators in the study area revealing an overall shearing throughout the whole body rock and a predominance of top-to-the-S (orange triangles) sense of shear.

Chapter 5. Analysis of crystallographic textures

Crystallographic textures have been used in the past to study and document the evolution of tectonic contacts (Stipp et al., 2002, Marti et al., 2013). Such an attempt takes place in this dissertation as well by applying the CIP analysis on samples taken across the tectonic contact of the Vertiskos and Kerdyllion units in the study area. The primary aim of this analysis is to study the potential variations of deformational fabrics with respect to the afore-mentioned contact, to verify whether c-axis pole figures can be used to infer shear sense in the study area and, should the inferred shear senses exist, whether they support shear senses inferred from field data already described in the previous chapters.

5.1. Structural background of selected samples

The collection of samples for the application of the CIP analysis on the study area was based on the rational of examining the contact of the two-mica gneiss, belonging to the Vertiskos Unit and the amphibolite and biotite gneiss, belonging to the Kerdyllion Unit, which has been mesoscopically identified at the western part of the study area as a shear zone with an overall top-to-the-S sense of shear. Therefore samples A39, A40, A43, A44, A45, A46, A47 and A48 were collected along an E-W trending transect, E of Konstamonitou monastery, in an attempt to verify the mesoscopic shear sense observations and also to document whether a deformational fabric is developed or intensifies with respect to the distance from the afore-mentioned contact. Samples A39, A40, A43, A44, A45 and A46 are, generally speaking, fine-to-medium grained, tightly foliated two-mica gneisses. A44 sample lithologically deviates from the rest of the samples, in the sense that it acquires an intense augen texture, with feldspar porphyroclasts ranging from a mm-to even-cm scale, whereas A46 has an increased participation of white mica in its overall compostition. Samples A47 and A48 come from leucogneissic concordantly emplaced bodies within the underlying amphibolite and biotite gneiss. They resemble, fine-grained, white mica (primarily) leucogneisses, also tightly foliated.

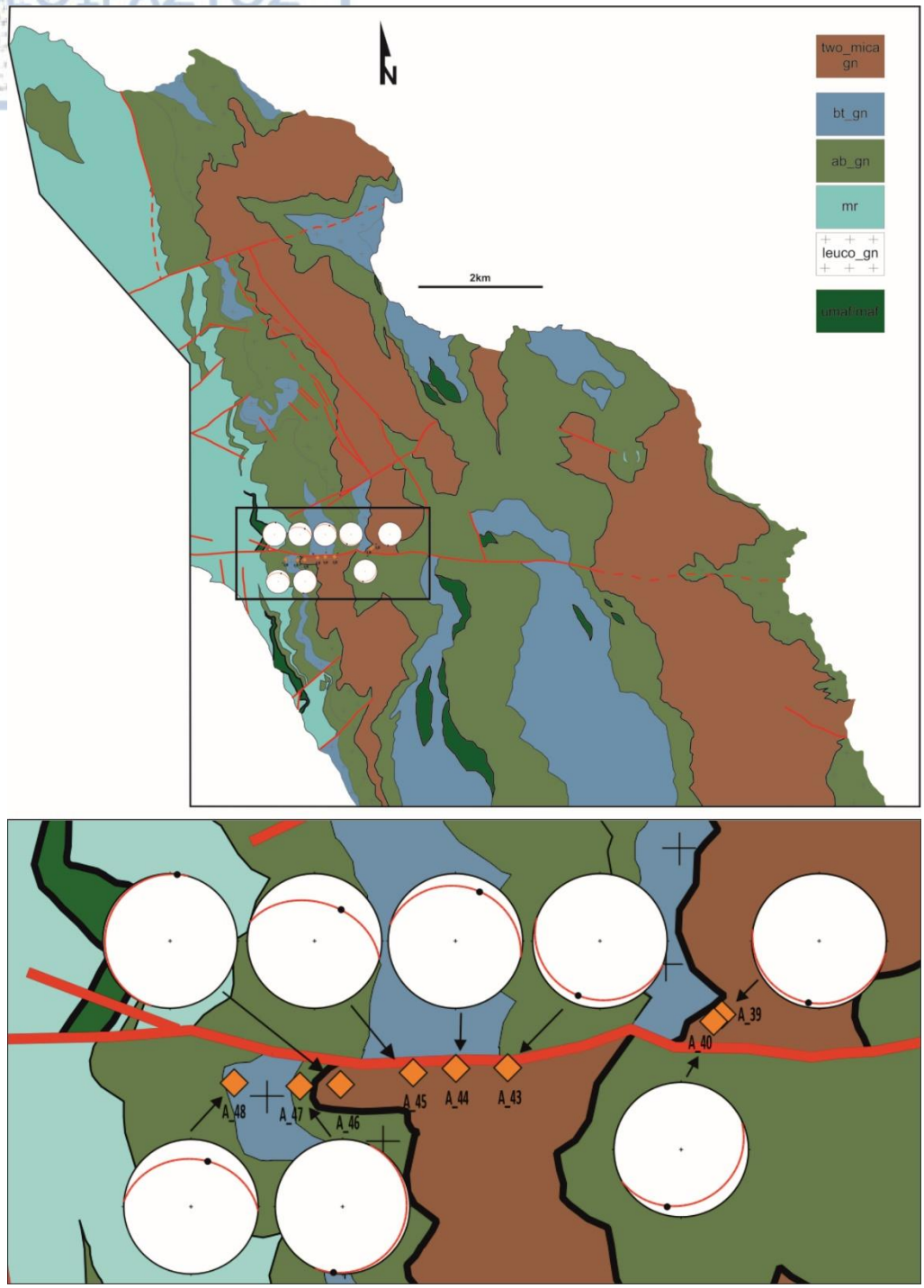

Fig. 5.1. Geological map of the study area with the sampling area also indicated. Detailed map showing the exact location of the CIP samples analyzed in this dissertation. For each sample the main S3 foliation and the stretching lineation L3 is provided.

The samples are spatially divided as belonging to a northern and a southern block, with respect to the large-scale E-W trending normal fault truncating and displacing the

contact under investigation (Fig. 5.1). The main foliation S3 and the stretching lineation L3 is also indicated for each sample. The vertical distance from the contact was also calculated for each sample in order to be able to examine the initial assumption of the development and growing intensity of a deformational fabric (Fig. 5.2). The thin sections were cut at a xz plane, each time parallel to the stretching lineation and vertical to the foliation. Since thin sections were cut both N-S and also S-N directed, a reference frame of structural and geometrical coordinates is provided in order to avoid misinterpretations (Fig. 5.3).

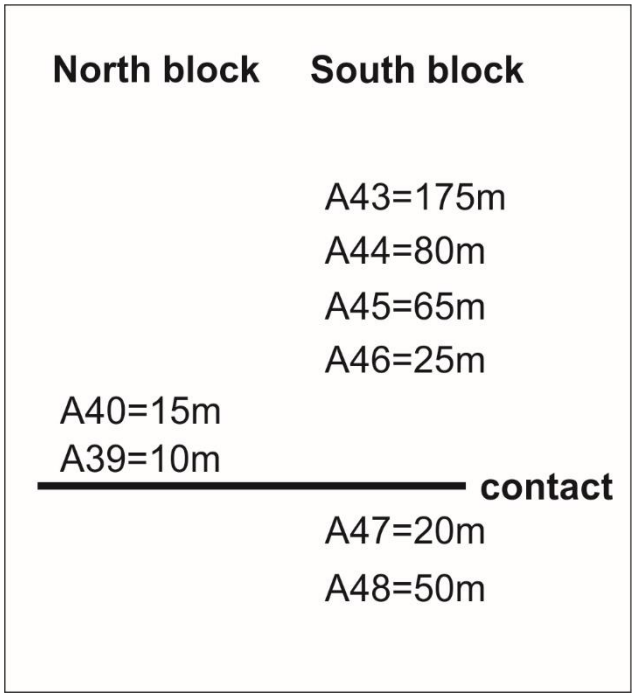

Fig. 5.2. Structural position of each sample analyzed with CIP, with respect to the studied contact.

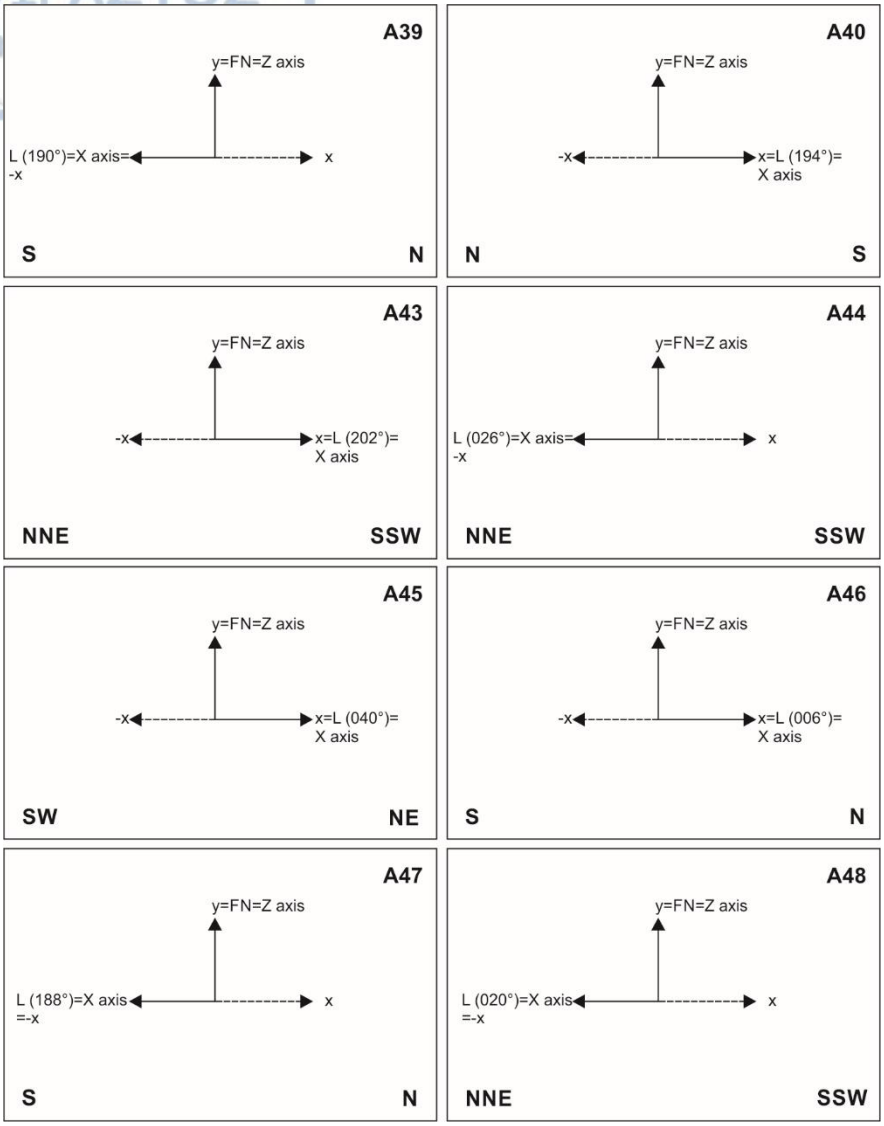

Fig. 5.3. Structural and geographical coordinates for each thin section analyzed with CIP. FN=foliation normal, L=stretching lineation (azimuth), X= structural axis, Z=structural axis, x,-x,y=Cartesian coordinates.

5.2. Method of analysis and procedure

5.2.1. ACF analysis

The thin sections prepared for the CIP analysis (thickness ~25μm, polished, uncovered) were initially scanned, once under parallel polarizer and once under crossed polarizer conditions (see Appendix). By outlining the quartz aggregates, quartz maps were produced (see Appendix & Fig. 5.4). These served as a basis for shape analysis by the

autocorrelation function (ACF). The thin sections were scanned with a resolution of 3000 LPI, the scans and quartz maps cover an area of approximately 30 · 17 mm, their pixel size is 3500 · 2200 (Fig. 5.4).

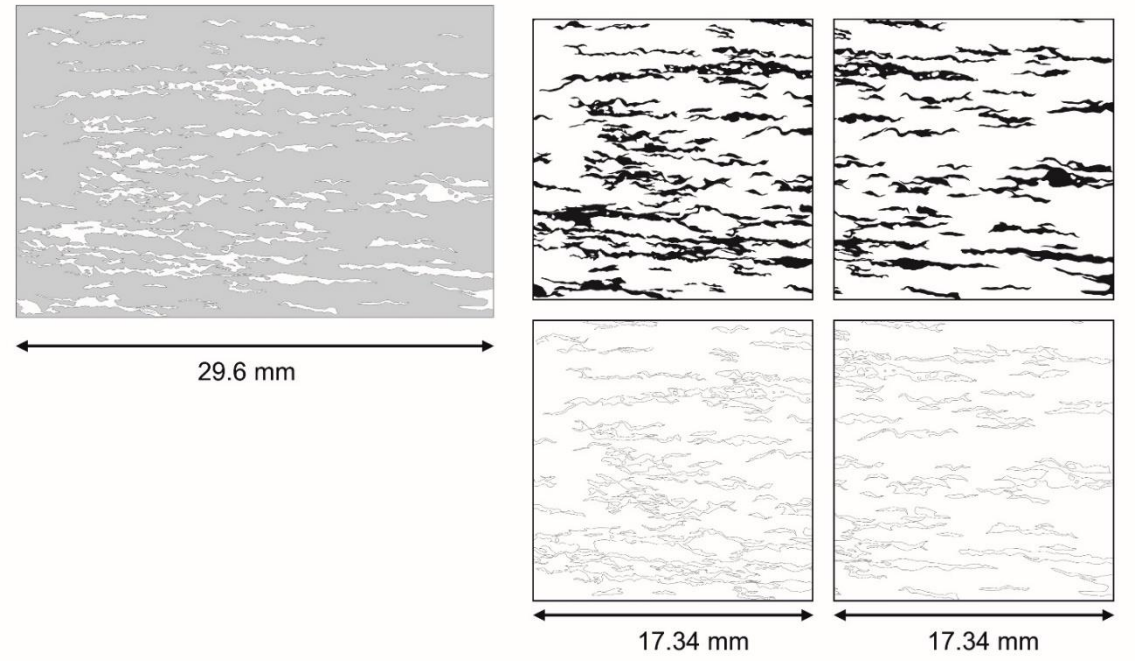

Fig. 5.4. The quartz map on which shape analysis by ACF was based and its segmentation into two separate 'phases maps', for both the PAROR and the SURFOR method.

On these maps, the matrix, the outlines and the quartz are represented by grey, black or white pixels, respectively (Fig. 5.4). The maps were segmented to produce two separate 'phases maps' each: a 'qtz-map' consisting of the quartz (including the boundary pixels), and an 'outline-map' consisting of the outline only. The ACF of a qtz-map - corresponds roughly to the shape analysis of the quartz aggregates, as obtained by the PAROR method while the ACF of the outlines is the equivalent of the analysis of the surface fabric by the SURFOR method. For methods see, Heilbronner & Barrett (2014).

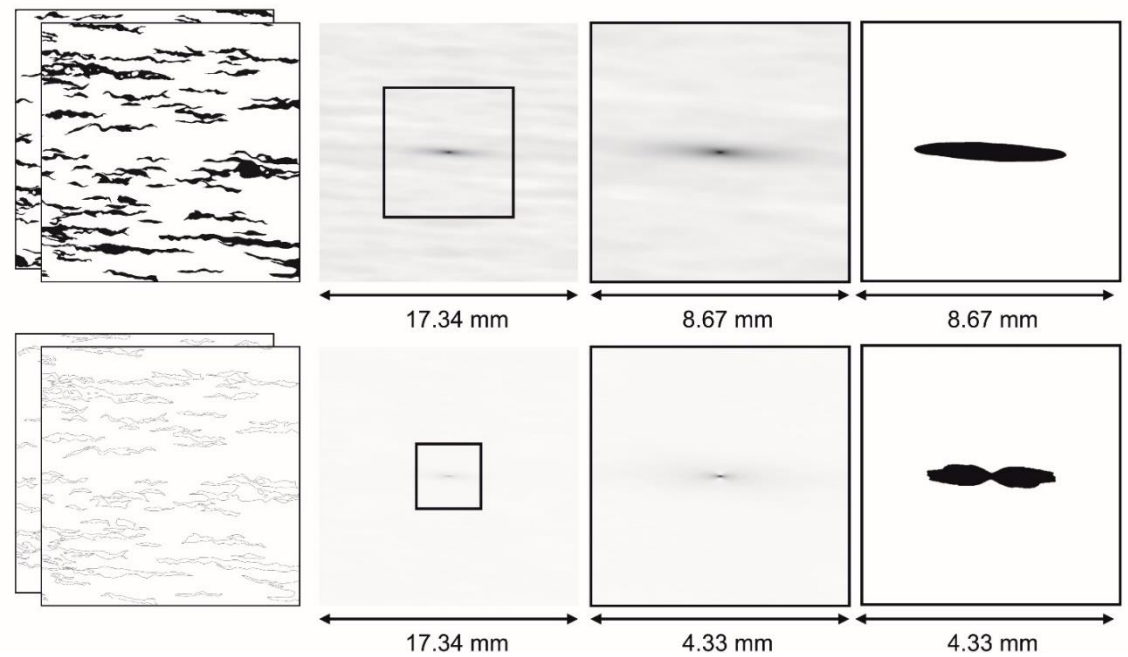

Fig. 5.5. ACF analysis steps for the PAROR and the SURFOR method applied on the qtz-maps.

On each qtz-map, two squares of 2048 · 2048 size were selected, one on the left and one on the right side of the thin section, creating some overlap in the center, and the ACF of each was calculated. The ACFs were then averaged to produce one ACF representing the entire thin section (for validity of this method, see Heilbronner (2002) (Fig. 5.5). Due to the size of the thin section, only one ACF was calculated in the center of sample A48. For better visualization, the ACFs were cropped to the center half (1024 · 1024). These results will be referred to as the paror-ACFs.

Each 'outline-map' was enlarged by a factor of 2, and the outlines were dilated. Again, two squares were selected and ACFs were calculated on the left and the right size, and the average ACF was determined (Fig. 5.5). And again, for A48, only one ACF was calculated. Here, the ACF size is 4096 · 4096, and for presentation, the center quarter (1024 · 1024) is used. These results will be referred to as the surfor-ACFs.

5.2.2. CIP analysis

Basic Concepts

The Computer-Integrated Polarization microscopy method is aimed at deriving c-axis orientations from optical micrographs and presenting the results in the form of pole-figures and orientation images, originally developed by Panozzo Heillbronner and Pauli (1993) (Heillbronner and Barret, 2014). By using the relation between interference colors of uni-axial minerals in thin sections, when viewed under a polarization microscope, the optical texture can be analyzed and an optical orientation imaging can be performed (Heillbronner and Barret, 2014). When mineral grains rotate under a polarization microscope their interference colors change and this change and variation in color can uniquely define the azimuth and the orientation of the c-axis (Fig. 5.6). Since the method is based on the interference colors of mineral grains, much attention has to be paid to the thickness of the thin section, so that the mineral in question each time appears in first-order interference colors, according to the Michel-Levy chart (Heillbronner and Barret, 2014). In the case of quartz, which is the mineral studied in this dissertation via the CIP method, thin sections must be prepared with a 25μm thickness.

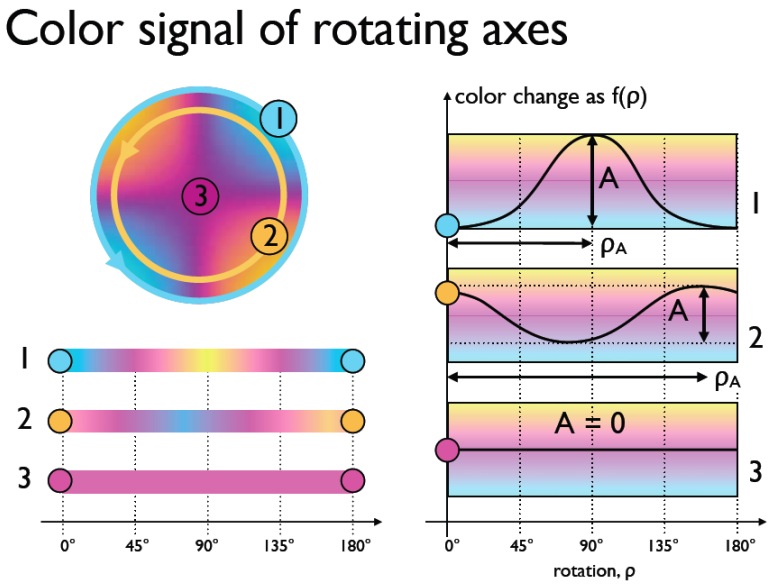

Fig. 5.6. Interference colors for three rotating c-axes with starting orientation of grains: 1) ϕ=45°, θ=90°, 2) ϕ=300°, θ=70°, 3) θ=0°. From the amplitude and phase angle of the rotation signal a primary inclination

(0°<θ<90°) and the full azimuth (0°<ϕ<180°) can be derived with the application of the CIP analysis. From Heilbronner and Barrett, 2014.

As far as the technical prerequisites for the application of the method are concerned they consist of: an optical microscope equipped for polarization, two extra polarizers introduced both below and above the thin section, a full wave plate and two quarter-wave plates, in order to achieve circular polarization, a narrow band interference filter, transmitting a 660-700 μm wavelength and finally a monochrome digital camera to capture the images.

The steps and actions needed to perform the CIP analysis on a set of micrographs, as described by Heillbronner and Barrett (2014), include the acquisition of a micrograph stack, which will be later on processed with the CIP software, its preparation with appropriate image processing software and the application of the CIP software, to derive the c-axis orientation at every single pixel of the image. From then on a number of tasks can be performed, such as preparing pole figures, corresponding to the c-axis orientation, derive misorientations and orientation gradients, generate color-coded orientation images and perform texture-based image analysis.

In order to better illustrate the application of the CIP method on actual field data stemming from thin sections of studied rocks, a sample and the corresponding thin section from the study area will be used. The illustrated example is from sample A39 and the CIP site used is A39_i (Table 5.1).

sample	site	version A	version P	name of COI2	scale (m/px)	image width (px)	image height (px)	% masked A	% masked P	name of polfig A	max of polfig A	max contour A	name of polfig P	max of polfig P	max contour P
A39	a		F1_Ncalib, F1_4	A39_a_F4_COI2.tif	1.6447	1580	1180	29,000	29,000				A39_a.POLFIG2_15.0_of_10, A39_a.POLFIG2	15.0	16.0
A39	b	F6	F4	A39_2.5x_b.COI2.tif	1.6447	1600	1200	34,000	31,000	A39_2.5x_PN_b.POLFIG2_07.0_of_0	07.0	0...	A39_2.5x_PN_b.POLFIG2_17.0_of_1	17.0	1..
A39	c	F5_amp notindex	F4	A39_2.5x_c.COI2.tif	1.6447	1600	1200	45,000	45,000	A39_2.5x_PN_c.POLFIG2_10.1_of_0	10.1	0...	A39_2.5x_PN_c.POLFIG2_22.0_of_1	22.0	1...
A39	d	amp6.123	F1	A39_2.5x_d.COI2.tif	1.6447	1600	1200	22,000	22,000	A39_2.5x_PN_d.POLFIG2_15.0_of_1	15.0	1...	A39_d.POLFIG2_21.0_of_14	21.0	14.0
A39	e	F6	F1	A39_2.5x_e.COI2.tif	1.6447	1600	1200	34,000	29,000	A39_2.5x_PN_e.POLFIG2_12.7_of_0	12.7	0...	A39_e.POLFIG2_19.0_of_12	19.0	12.0
A39	f	F6	F4	A39_10x_PN_f.COI2.tif	0.4386	1560	1180	46,000	58,000	A39_10x_PN_f.POLFIG2_08.0_of_05	08.0	05.0	A39_10x_PN_f.POLFIG2_14.4_of_10	14.4	10.0
A39	g	F2	F1	A39_10x_PN_g.COI2.tif	0.4386	1560	1180	72,000	72,000	A39_10x_PN_g.POLFIG2_11.2_of_08	11.2	08.0	A39_g.POLFIG2_21.0_of_14	21.0	14.0
A39	h	mask1amp2	mask1_pol	A_39_h.COI2.tif	0.4386	1540	1110	44,000	44,000	A_39_h.POLFIG2_11.0_of_07	11.0	07.0	A_39_h.POLFIG2_10.0_of_07	10.0	07.0
A39	i	mask1_amp1	mask1_cirpol	A_39_i.COI2.tif	0.4386	1540	1110	77,000	77,000	A_39_i.POLFIG2_10.0_of_06	10.0	06.0	A_39_i.POLFIG2_11.4_of_07	11.4	07.0
A39	j	mask1_amp1	mask1_cirpol	A39_j.COI2.tif	0.4386	1540	1100	59,000	59,000	A39_j.POLFIG2_14.0_of_10	14.0	10.0	A39_j.POLFIG2_09.5_of_06	09.5	06.0
A39	k	mask1_amp1	mask1_cirpol	A39_k.COI2.tif	0.4386	1540	1100	60,000	60,000	A39_k.POLFIG2_08.4_of_06	08.4	06.0	A39_k.POLFIG2_08.0_of_05	08.0	05.0
A39	l	mask1_amp1	mask1_cirpol	A39_l.COI2.tif	0.4386	1540	1100	56,000	56,000	A39_l.POLFIG2_12.0_of_08	12.0	08.0	A39_l.POLFIG2_18.0_of_12	18.0	12.0
A39	m	mask1_amp1	mask1_cirpol	A39_m.COI2.tif	0.4386	1540	1100	50,000	50,000	A39_m.POLFIG2_11.8_of_08	11.8	08.0	A39_m.POLFIG2_10.4_of_06	10.4	06.0
A39	n	mask1_amp1	mask1_cirpol	A39_n.COI2.tif	0.4386	1540	1100	85,000	85,000	A39_n.POLFIG2_11.3_of_08	11.3	08.0	A39_n.POLFIG2_12.5_of_08	12.5	08.0
A39	o	amp2_crop	F2T4e	A39_o.COI2.tif	0.4386	1540	1100	81,000	81,000	A39_o.POLFIG2_07.1_of_05	07.1	05.0	A39_o.POLFIG2_12.9_of_08	12.9	08.0
A39	p	ampl	cirpol	A39_p.COI2.tif	0.4386	1540	1100	83,000	83,000	A39_p.POLFIG2_09.6_of_06	09.6	06.0	A39_p.POLFIG2_12.9_of_08	12.9	08.0
A39	q	ampl	cirpol	A39_q.COI2.tif	0.4386	1550	1100	70,000	70,000	A39_q.POLFIG2_08.8_of_06	08.8	06.0	A39_q.POLFIG2_19.5_of_12	19.5	12.0
A40	a	m2_amp1	cirpol	A40_2.5x_PN_a.COI2.tif	1.6447	1600	1200	39,000	39,000	A40_2.5x_PN_a.POLFIG2_11.7_of_0	11.7	0...	A40_2.5x_PN_a.POLFIG2_20.5_of_1	20.5	1...
A40	b	m2_amp1	cirpol(47,284)	A40_b.COI2.tif	1.6447	1580	1180	28,000	28,000	A40_b.POLFIG2_18.4_of_12b	18.4	12.0	A40_b.POLFIG2_22.0_of_14	22.0	14.0
A40	c	amp2_cropped	cirpol(49,246)	A40_2.5x_PN_c.COI2.tif	1.6447	1600	1200	34,000	34,000	A40_2.5x_PN_c.POLFIG2_08.2_of_0	08.2	0...	A40_2.5x_PN_c.POLFIG2_23.1_of_1	23.1	1...
A40	d	amp1	cirpol()	A40_2.5x_PN_d.COI2.tif	1.6447	1600	1200	46,000	46,000	A40_2.5x_PN_d.POLFIG2_18.0_of_1	18.0	1...	A40_2.5x_PN_d.POLFIG2_33.2_of_2	33.2	2...
A40	e	amp1	cirpol()	A_40_2.5x_PN_e.COI2.tif	1.6447	1600	1200	23,000	23,000	A_40_2.5x_PN_e.POLFIG2_08.3_of_	08.3	...	A_40_2.5x_PN_e.POLFIG2_14.9_of_	14.9	...
A40	f	amp1	cirpol()	A40_f.COI2.tif	0.8734	1550	1150	56,000	56,000	A40_f.POLFIG2_08.5_of_06	08.5	06.0	A40_f.POLFIG2_12.0_of_08	12.0	08.0
A40	g	amp1	cirpol(20,249)	A40_g.COI2.tif	0.8734	1550	1150	43,000	43,000	A40_g.POLFIG2_10.0_of_07	10.0	07.0	A40_g.POLFIG2_15.4_of_10	15.4	10.0
A40	h	amp2crop	cirpol(21,249)	A40_h.COI2.tif	0.8734	1550	1150	87,000	87,000	A40_h.POLFIG2_12.7_of_08	12.7	08.0	A40_h.POLFIG2_12.4_of_08	12.4	08.0
A43	a	amp1	cirpol()	A_43_10x_PN_a.COI2.tif	0.4386	1560	1180	53,000	53,000	A_43_a.POLFIG2_09.0_of_06b	09.0	06.0	A_43_10x_PN_a.POLFIG2_33.9_of_2	33.9	2...
A43	b	amp1	cirpol()	A43_10x_PN_b.COI2.tif	0.4386	1560	1180	76,000	76,000	A43_10x_PN_b.POLFIG2_09.8_of_06	09.8	06.0	A43_10x_PN_b.POLFIG2_28.4_of_19	28.4	19.0
A43	c	amp(2-99)	cirpol()	A43_c.COI2.tif	0.8734	1580	1180	42,000	42,000	A43_c.POLFIG2_06.5_of_04	06.5	04.0	A43_c.POLFIG2_12.7_of_08	12.7	08.0
A43	d	amp(2-99)	cirpol()	A43_d_col2	0.4386	1550	1150	52,000	52,000	A43_d.POLFIG2_17.7_of_12	17.7	12.0	A43_d.POLFIG2_11.9_of_08	11.9	08.0
A43	e	amp(2-99)	cirpol()	A43_e.COI2.tif	0.4386	1550	1150	60,000	60,000	A43_e.POLFIG2_09.0_of_06	09.0	06.0	A43_e.POLFIG2_15.5_of_10	15.5	10.0
A43	f	amp(2-98)	cirpol()	A43_f_COI2	0.4386	1550	1150	38,000	38,000	A43_f.POLFIG2_10.8_of_07	10.8	07.0	A43_f.POLFIG2_17.0_of_12	17.0	12.0
A43	g	amp(2-98)	cirpol()	A43_g.COI2.tif	0.4386	1550	1150	70,000	70,000	A43_g.POLFIG2_07.2_of_05	07.2	05.0	A43_g.POLFIG2_18.5_of_12	18.5	12.0
A44	b	amp()	cirpol(68-245)	A44_b.COI2.tif	1.6447	1600	1200	75,000	75,000	A44_b.POLFIG2_21.8_of_14	21.8	14.0	A44_b.POLFIG2_15.4_of_10	15.4	10.0
A44	c	amp()	F1_2	A44_d_COI2	1.6447	1600	1200	58,000	50,000	A44_c.POLFIG2_12.1_of_08	12.1	08.0	A44_c.POLFIG2_21.0_of_14	21.0	14.0
A44	d	amp(2-98)	cirpol()	A44_d.COI2.tif	1.6447	1600	1200	77,000	77,000	A44_d.POLFIG2_13.7_of_09	13.7	09.0	A44_d.POLFIG2_26.1_of_18	26.1	18.0
A44	e	amp(2-98)TXA4d	cirpol()	A44_e.COI2.tif	0.8734	1600	1200	81,000	81,000	A44_e.POLFIG2_27.4_of_18	27.4	18.0	A44_e.POLFIG2_26.3_of_18	26.3	18.0
A44	f	amp(5-95)	cirpol()	A44_f.COI2.tif	0.4386	1550	1150	94,000	94,000	A44_f.POLFIG2_41.5_of_28	41.5	28.0	A44_f.POLFIG2_57.3_of_38	57.3	38.0
A44	g	amp(2-99)	cirpol()	A44_g.COI2.tif	0.4386	1550	1150	91,000	91,000	A44_g.POLFIG2_12.5_of_08	12.5	08.0	A44_g.POLFIG2_17.5_of_12	17.5	12.0
A44	h	amp(2-98)	cirpol()	A44_h.COI2.tif	0.4386	1550	1150	35,000	35,000	A44_h.POLFIG2_22.2_of_14	22.2	14.0	A44_h.POLFIG2_12.2_of_08	12.2	08.0
A44	i	amp(2-98)	cirpol()	A44_i.COI2.tif	0.4386	1550	1150	58,000	58,000	A44_i.POLFIG2_24.1_of_16	24.1	16.0	A44_i.POLFIG2_29.5_of_20	29.5	20.0
A45	a	amp(5-98)	cirpol()	A45_a.COI2.tif	1.6447	1600	1200	45,000	45,000	A45_a.POLFIG2_10.2_of_07	10.2	07.0	A45_a.POLFIG2_18.6_of_12	18.6	12.0
A45	b	amp(2-99)	cirpol()	A45_b.COI2.tif	0.8734	1580	1180	46,000	46,000	A45_b.POLFIG2_11.1_of_07	11.1	07.0	A45_b.POLFIG2_25.3_of_16	25.3	16.0
A45	c	amp(2-98)	cirpol()	A45_5x_c.COI2.tif	0.8734	1550	1150	28,000	28,000	A45_5x_c.POLFIG2_10.3_of_07	10.3	07.0	A45_5x_c.POLFIG2_12.1_of_08	12.1	08.0
A45	d	amp(2-98)	cirpol()	A45_d.COI2.tif	0.8734	1580	1180	42,000	42,000	A45_d.POLFIG2_06.2_of_04	06.2	04.0	A45_d.POLFIG2_13.5_of_09	13.5	09.0
A45	e	amp(2-98)	cirpol()	A45_e.COI2.tif	0.4386	1550	1150	66,000	66,000	A45_e.POLFIG2_11.1_of_07	11.1	07.0	A45_e.POLFIG2_18.3_of_12	18.3	12.0
A45	f	amp(2-98)	cirpol()	A45_f.COI2.tif	0.4386	1550	1150	65,000	65,000	A45_f.POLFIG2_08.4_of_06	08.4	06.0	A45_f.POLFIG2_15.8_of_10	15.8	10.0
A46	a	amp1	F1_2	A46_2.5x_PN_a.COI2.tif	1.6447	1600	1200	37,000	55,000	A46_2.5x_PN_a.POLFIG2_05.0_of_0	05.0	0...	A46_a.POLFIG2_10.0_of_06	10.0	06.0
A46	b	amp1	cirpol()	A46_2.5x_PN_b.COI2.tif	1.6447	1600	1200	45,000	45,000	A46_2.5x_PN_b.POLFIG2_04.6_of_0	04.6	0...	A46_2.5x_PN_b.POLFIG2_13.0_of_0	13.0	0...
A46	c	mask2_amp1	cirpol()	A46_2.5x_PN_c.COI2.tif	1.6447	1600	1200	72,000	72,000	A46_PN_c.POLFIG2_05.4_of_b	05.4	0...	A46_2.5x_PN_c.POLFIG2_14.4_of_1	14.4	1...
A46	d	mask2_amp1	cirpol()	A46_5x_PN_d.COI2.tif	0.8734	1580	1180	84,000	84,000	A46_5x_PN_d.POLFIG2_13.3_of_09	13.3	09.0	A46_5x_PN_d.POLFIG2_18.5_of_12	18.5	12.0
A47	a	amp(2-99)	cirpol()	A47_5x_PN_a.COI2.tif	0.8734	1580	1180	28,000	28,000	A47_5x_PN_a.POLFIG2_17.8_of_12	17.8	12.0	A47_5x_PN_a.POLFIG2_12.1_of_08	12.1	08.0
A47	b	amp(5-98)	cirpol()	A47_5x_PN_b.COI2.tif	0.8734	1580	1180	47,000	47,000	A47_5x_PN_b.POLFIG2_08.3_of_05	08.3	05.0	A47_5x_PN_b.POLFIG2_08.8_of_06	08.8	06.0
A47	c	amp(2-98)	cirpol()	A47_5x_PN_c.COI2.tif	0.8734	1580	1180	19,000	19,000	A47_5x_PN_c.POLFIG2_07.8_of_05	07.8	05.0	A47_5x_PN_c.POLFIG2_19.9_of_13	19.9	13.0
A47	d	amp(2-99)	cirpol()	A47_5x_PN_d.COI2.tif	0.8734	1580	1180	21,000	21,000				A47_5x_PN_d.POLFIG2_17.2_of_11	17.2	11.0
A47	e	amp(2-98)	cirpol()	A47_5x_PN_e.COI2.tif	0.8734	1580	1180	23,000	23,000	A47_5x_PN_e.POLFIG2_14.9_of_10	14.9	10.0	A47_5x_PN_e.POLFIG2_11.6_of_08	11.6	08.0
A47	f	amp(2-99)	cirpol()	A47_5x_PN_f.COI2.tif	0.8734	1580	1180	36,000	36,000	A47_5x_PN_f.POLFIG2_09.9_of_07	09.0	07.0	A47_5x_PN_f.POLFIG2_22.8_of_15	22.8	15.0
A48	a	amp(2-99)	cirpol()	A48_5x_PN_a.COI2.tif	0.8734	1580	1180	45,000	45,000	A48_5x_PN_a.POLFIG2_11.8_of_08	11.8	08.0	A48_5x_PN_a.POLFIG2_12.6_of_08b	12.6	08.0
A48	b	amp(2-99)	cirpol()	A48_5x_PN_b.COI2.tif	0.8734	1580	1180	37,000	37,000	A48_5x_PN_b.POLFIG2_08.6_of_05	08.6	05.0	A48_5x_PN_b.POLFIG2_20.1_of_14	20.1	14.0
A48	c	amp(5-98)	cirpol()	A48_c.COI2.tif	0.8734	1580	1180	29,000	29,000	A48_c.POLFIG2_15.9_of_10	15.9	10.0	A48_c.POLFIG2_09.3_of_06	09.3	06.0
A48	d	amp(5-98)	cirpol()	A48_d.COI2.tif	0.8734	1580	1180	37,000	37,000	A48_d.POLFIG2_13.0_of_08b	13.0	08.0	A48_d.POLFIG2_12.6_of_08b	12.6	08.0
A48	e	amp()	cirpol(43,247)	A48_e.COI2.tif	0.8734	1550	1100	51,000	51,000	A48_e.POLFIG2_08.5_of_06	08.5	06.0	A48_e.POLFIG2_07.9_of_05	07.9	05.0
A48	h	amp()	cirpol(36,250)	A48_h.COI2.tif	0.4386	1550	1150	35,000	35,000	A48_h.POLFIG2_06.5_of_04	06.5	04.0	A48_h.POLFIG2_05.8_of_04	05.8	04.0

Table 5.1. List of all the information concerning all the CIP site micrographs analyzed with CIP and the produced results.

Image Acquisition

The first basic step is to acquire a micrograph stack, which will be later on processed with the CIP software. The equipment used for the acquisition of the micrograph stack from all the studied thin sections was a Zeiss AXIO-Scope polar microscope, two extra polarizers introduced both below and above the thin section, a full wave plate and two quarter-wave plates, in order to achieve circular polarization, a narrow band interference filter, transmitting a 660-700 μm wavelength, an additional x-y stage, mounted on the microscope stage, in order to keep the thin section in place and a Basler monochrome camera. Prior to the acquisition of the micrograph stack one should make sure that the thin section coordinates (x=Foliation trace=Lineation=X structural axis and y=Foliation normal=Z structural axis) are perpendicular to the microscope cross, as well as the frame of the monochrome camera, so that all the images taken and processed are aligned to a specific structural frame. Moreover, the thin section should be placed under the microscope, rotated 180°, so that the actual way-up is pointing down and the image seen through the microscope lens and taken by the monochrome camera matches the actual orientation of the thin section. Since the samples and corresponding thin sections studied in this dissertation do not constitute quartzites, but polyphase rocks, the sites of the thin sections which were processed with the CIP method were selected basically according to the qtz content and the crystallographic texture. Different magnifications were used (2.5x, 5x and 10x magnifying microscope lenses) depending on the afore-mentioned criteria. In the case of A39_i CIP site a 10x magnification was used.

Assembling the Image Stack

The micrograph stack, needed for the application of the CIP software and acquired for the A39_i CIP site, consists of 24 micrographs in total:

1) One CIRPOL image, which is acquired by inserting the crossed polarizers and the two quarter-wavelength plated, inserted at 45° angle with respect to the polarizers, thus achieving circular polarization (Fig. 5.7). Full light intensity was also used, whereas the intake of light from the outer source was also shut. Moreover, the

exposure time of the captured image was selected in such a way through the image-capturing software that no over- or under-saturation took place and to make sure that the widest range of gray values was achieved. This rational was applied on the capturing of the NOPOL and the ROT images as well.

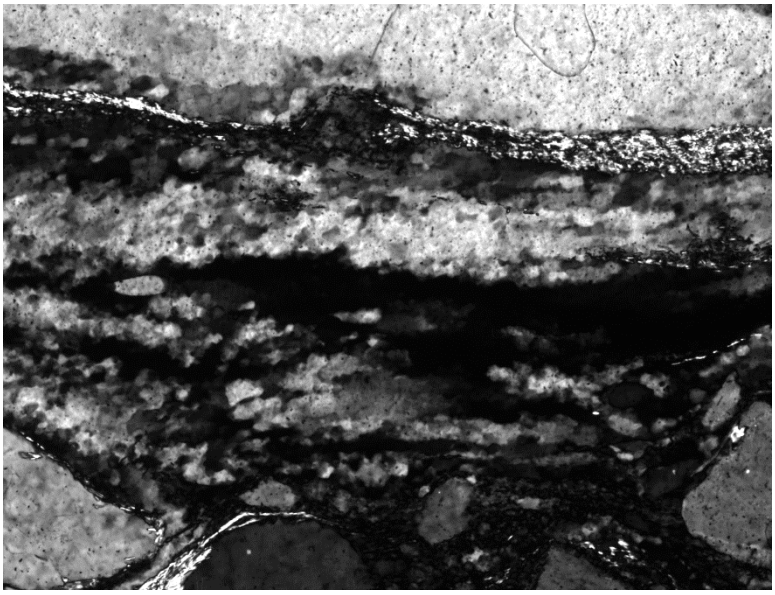

Fig. 5.7. CIRPOL image taken for the A39_i CIP site.

2) One NOPOL image, which is obtained by removing the quarter-wave plate and retracting the lower polarizer, thus achieving plane polarized light (Fig. 5.8). Again, the illumination and corresponding exposure was adjusted through the capturing software in order to avoid over- or under-saturating the final image.

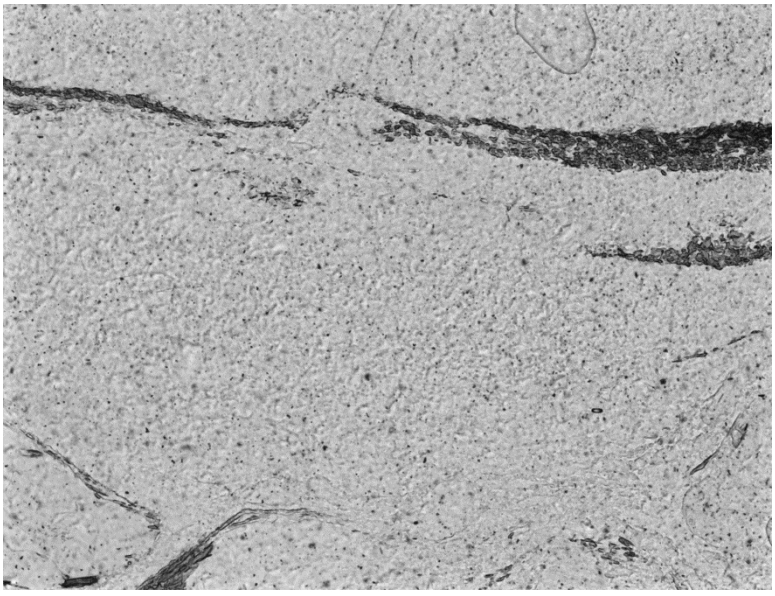

Fig. 5.8. NOPOL image taken for the A39_i CIP site.

3) The ROT images, 19 in total and acquired with the lower polarizer in position and the quarter-wave plate inserted anew. The 19 rotation images are acquired either by counter-clockwise rotating the microscope stage every 10°, from 0° to 180°, or by clockwise rotating both the polarizers and the quarter-wave plate (Fig. 5.9). In the case of the A39_i CIP site, as well as the rest of the studied sites, the microscope used for the acquisition of the images was equipped with rotating polarizers as well as rotating quarter-wave plates, so clockwise rotation was applied. Exposure time of the captured images, once decided prior to the 0° ROT image was not modified during rotation and acquisition of the whole ROT sub-stack of images.

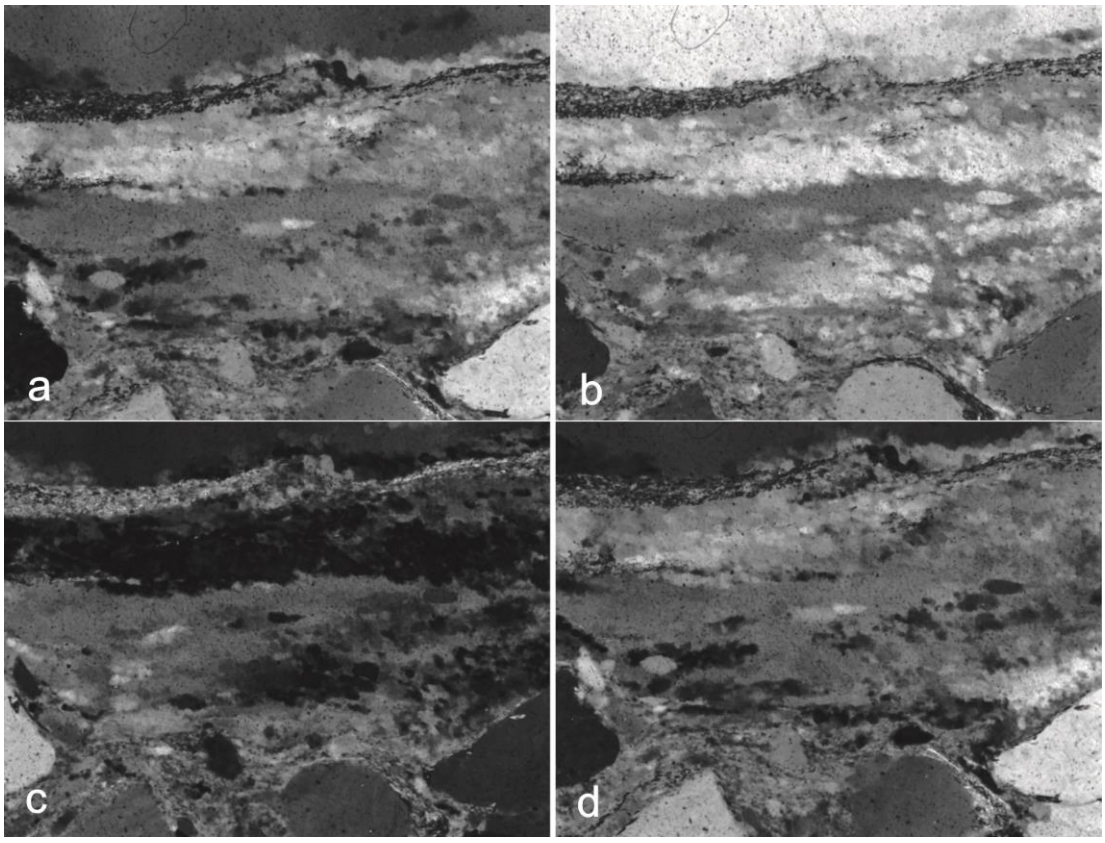

Fig. 5.9. ROT images taken for A39_i CIP site at: a) 0°, b) 40°, c) 120° and d) 180°.

4) Four TILT images, which were acquired by physically tilting the thin section with a specially designed tilting stage and the insertion of a mm-thick wedge underneath the right edge (the EUP image), the bottom edge (the SUP image), the left edge (the WUP image) and the top edge (the NUP image) of the thin section. Since the thin section is tilted, 2 to 4 images need to be taken for each tilted image, focused each time to different segments of the tilted cross sections. The number of re-focused

images covering the whole range of the thin section naturally depends on the magnification used. Since the A39_i micrographs were taken with a 10x magnification, 4 images were captured in order to achieve a fully focused tilted image each time (Fig. 5.10). These 4 micrographs were later on, in the preparation stage, combined in one image, via additional software (Image SXM).

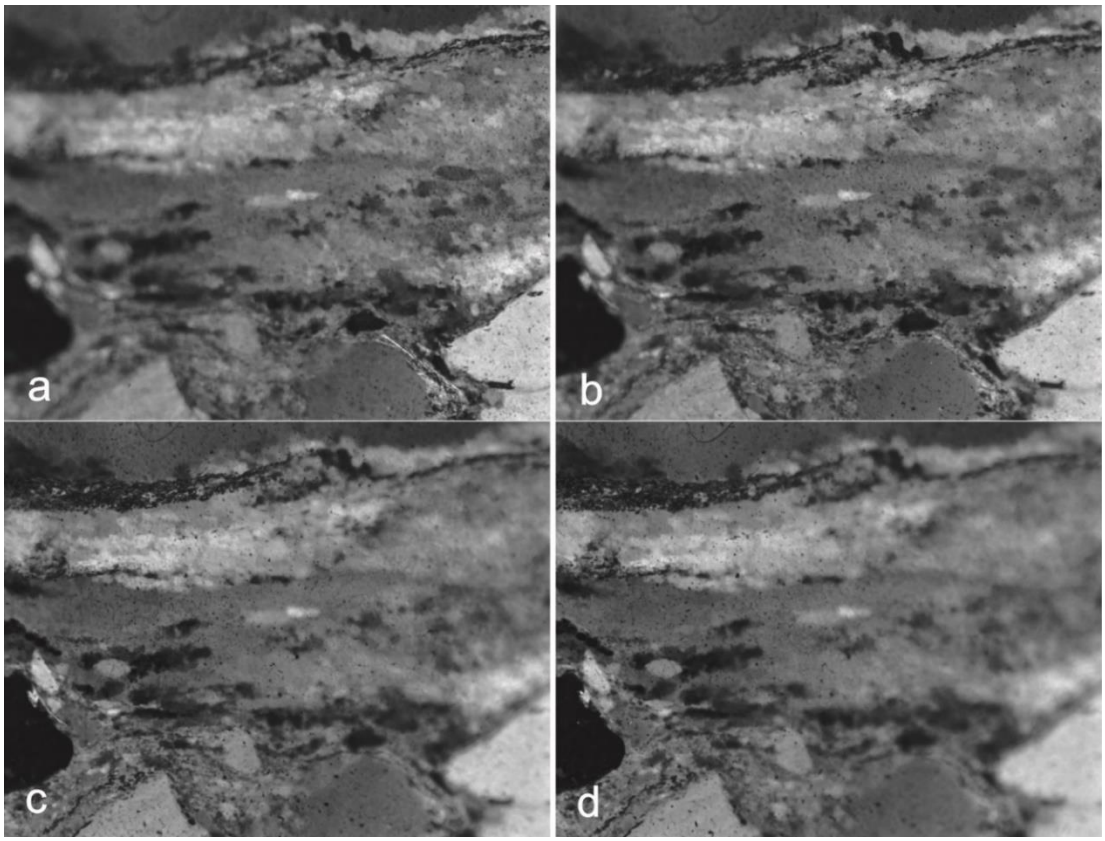

Fig. 5.10. Four successive images a-d, taken for the compilation of the final EUP image. Each image is focused on a different region of the CIP site since the thin section has been previously physically tilted by inserting a mm-thick wedge underneath its right side.

5) One or two BACK images, which are actually taken by leaving the polarizers and wave plate in place and removing the thin section from the microscope stage. This is done in order to numerically remove later on any systematic inhomogeneities, caused by a number of reasons, such as aged polarizers or unnoticed smudges etc. In our case two BACK images were captured for the A39_i CIP site, the first corresponding to the tilted images (backT image) and the second, after having re-inserted the thin section, focused and then removed again, for the flat images (backF image) (Fig. 5.11).

(a)

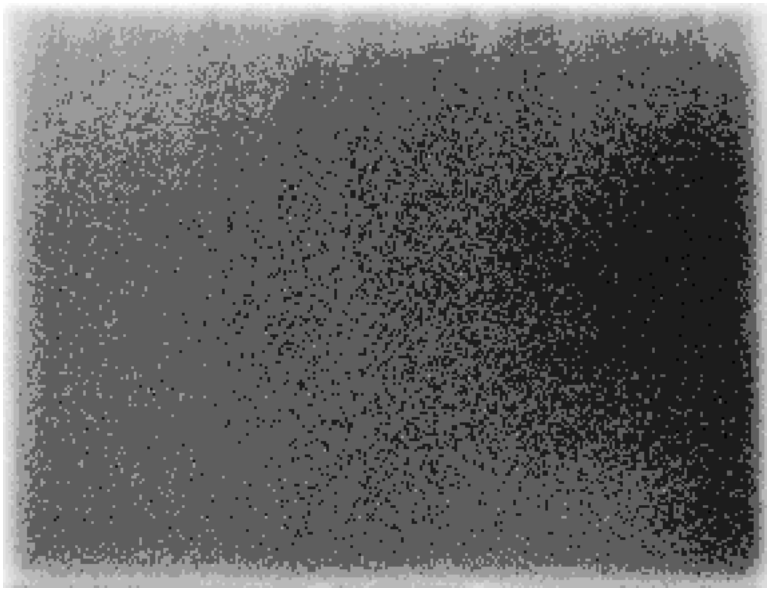

(b)

Fig. 5.11. BACK-F image taken for the A39_i CIP site. (a) original (b) same with enhanced contrast to show unevenness of illumination

The next step concerns the preparation of the acquired images, in order for them to be ready for the CIP processing. The micrograph stack described above was initially imported as an 8-bit Gray scale image sequence to Fiji software and exported. This image sequence was then opened with Image SXM software and the Lazy Prepstack Macros were loaded to the software, necessary for the preparation of the acquired micrographs. Initially, four substacks were created concerning the four groups of TILT images, e.g. the four images comprising the EUP tilt were sub-stacked and merged into one fully focused EUP image (Fig. 5.12), so that in the end, after the 19 ROT images

only four images follow, corresponding to EUP, SUP, WUP and NUP fully focused micrographs. Then a fifth sub-stack was created, comprised of 23 images (Fig. 5.13): the 19 rotated ones and the 4 tilted ones. This substack of images was then opened again with Fiji software and was registered, aligned and perfectly matched.

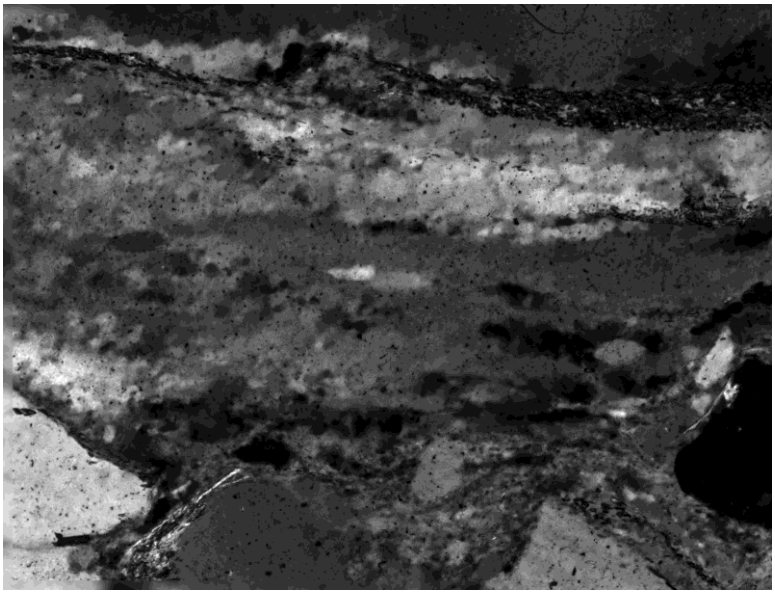

Fig. 5.12. Merged EUP image in Image SXM, of the previously described four partially focused EUP images, illustrated in Fig 5.10.

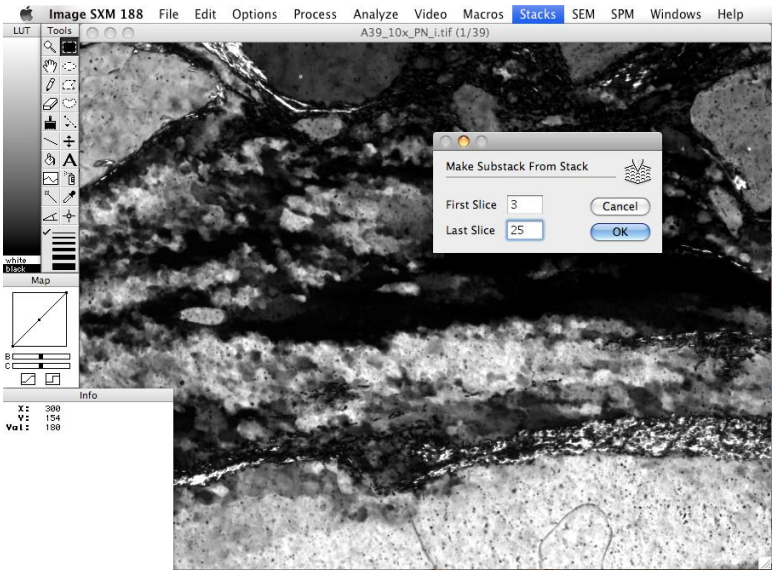

Fig. 5.13. Creation of sub.stack containing the 19 ROT and 4 merged TILT images in Image SXM.

Proceeding with the preparation stage of the micrograph stack, this “matched” sub-stack was then re-opened in Image SXM software and 2 slices were inserted, 2 in

the beginning and two at the end of the stack. The first two were assigned to the CIRPOL and the NOPOL images and the last two to the BACK-T and the BACK-F images. The CIRPOL and NOPOL images were then perfectly matched with the rest of the stack and the whole image sequence was cropped and the cropping dimensions were recorded (1540 · 1110, Table 5.1). The gray values of the four TILT images were also matched to the ones of the last rotated image, by applying the respective Macros from the Lazy Prepstack, in Image SXM. Then, the stack was exported in the form of the final 27 files, corresponding to the circular polarized, parallel polarized, rotated, tilted and background image files, which comprised the input stack for the CIP analysis (Fig. 5.14, 5.15).

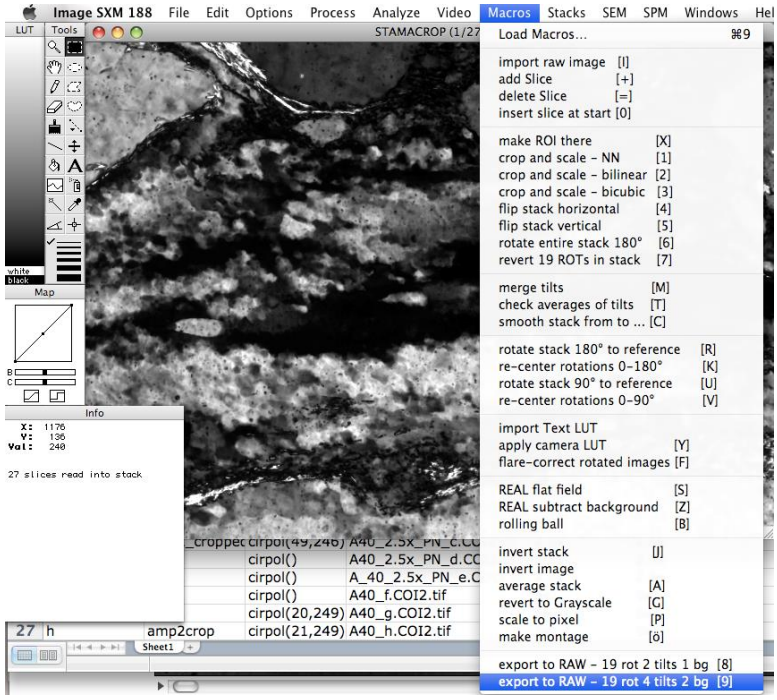

Fig. 5.14. Application of the Lazy Prepstack macro in Image SXM to create the 27 raw images that are used as input for the CIP program.

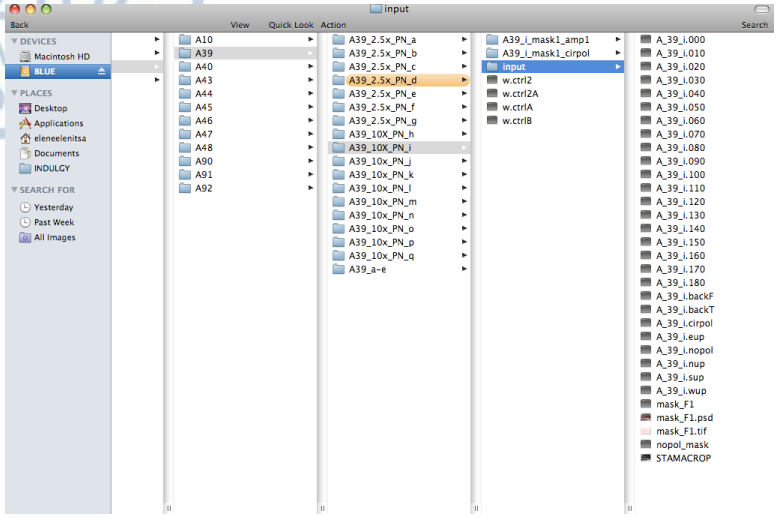

Fig. 5.15. Content of input folder and control files for the CIP program.

As a last preparation step, before applying the CIP software to analyze the stack, a mask was produced in order to define which part of the micrograph was going to be processed and analyzed. The reason for this was the fact that the micrographs analyzed are not monomineralic and various minerals occupy parts of the micrographs, which the method does not apply to. For instance, the mineral analyzed in this dissertation with the CIP method was quartz and the vast majority of the thin sections did not come from monomineralic quartzites, but from quartzofeldspathic mainly bands within the map units of the study area. Naturally, in some micrographs additional non-uniaxial, minerals, such as feldspars and mica or biotite occasionally occupied some parts of the micrographs and needed to be masked out, in order not to be included in the analysis. For this reason an initial mask was created by using the NOPOL exported image file. It was imported to Image SXM software and processed by subtracting its background, thresholded and inverted (Fig. 5.16a). Such a preliminary mask can be useful for masking out phases like micas. This mask was then used as a basis and, after masking out other non-qtz phases such as feldspar porphyroclasts, participating in the mineral assemblage at the A39_i CIP site, the final mask was exported as an image file (Fig. 5.16b), which was applied later on during the application of the CIP software.

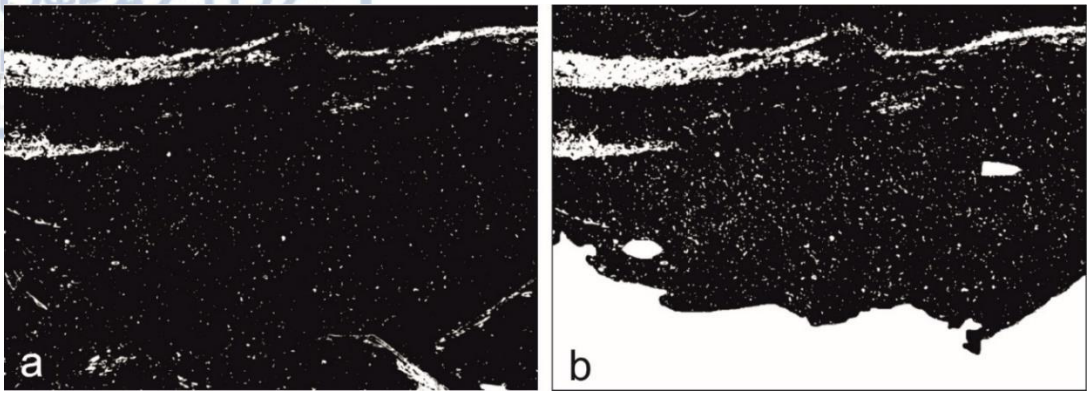

Fig 5.16. Preparation of the mask used in CIP2 process: a) an initial mask is produced from the NOPOL image and b) the final mask, as a combination of the NOPOL mask and the manual masking-out of non-quartz phases.

Once the input stack has been prepared we can proceed to apply the CIP routines (CIP1a, CIP1b and CIP2) on our data, which constitute a Fortran software package. This means that the according control files (w.ctrlA, w.ctrlB & w.ctrl2) need to be prepared for each CIP site, indicating the image size (cropping dimensions), the input and calibration files, as well as the expected results each time (Fig. 5.17).

w.ctrlB

```
cip---------INPUT----------
1) Title of problem
A_39_i 10x
2a) x- and y dimension (max width = 3000)
1540,1110
3) azi image:
CIP1A/A_39_i.AZI
4) incp image (0-90):
CIP1A/A_39_i.INCP
5) T-index file (255 if flipped):
CIP1A/A_39_i.TXP
6) inca image (0-90):
CIP1A/A_39_i.INCA
7) T-index file (255 if flipped):
CIP1A/A_39_i.TXA
8) Calibration of inclination - MUST be same as for cip1a
../../../calib/sine2-lin-256.LUT
9) Stereographic Colour Lookup Table
../../../clut/CIP-P-standard.CLUT
cip---------CIP1results----------
1) Final result file INC cirpol
CIP1B/A_39_i.INCP
1) Final result file INC amplitude
CIP1B/A_39_i.INCA
2) c-axis orientation image (NON-INTERLEAVED)
CIP1B/A_39_i.COIP.raw
3) c-axis orientation image (NON-INTERLEAVED)
CIP1B/A_39_i.COIA.raw
4) filename for CPF (MENTEX format) and pole figures
CIP1B/A_39_i.CPF
```

Fig. 5.17. Example of the CIP1b control file, prepared for the A39_i CIP site.

The first CIP routine is CIP1a which performs the following operations:

- determination of the rotation signal J(ρ) and the phase angle ρA.

- AZI: conversion of the phase angle of the rotation signal to azimuth
- INCA: conversion of the amplitude of the rotation signal to primary inclination
- INCP: conversion of the amplitude of the circular polarization image to primary inclination
- TINDEX: derivation of the tilt index from the tilt images
- INC: determination of the full inclination
- Cropping of the inclination histogram
- ERR: derivation of the quality index from curve fit errors.

When running the CIP1a, the input stack that has been prepared is used (Fig. 5.18). The first variants needed to be inserted, when running CIP1a, are the coordinates of the brightest and darkest pixels from the CIRPOL image.

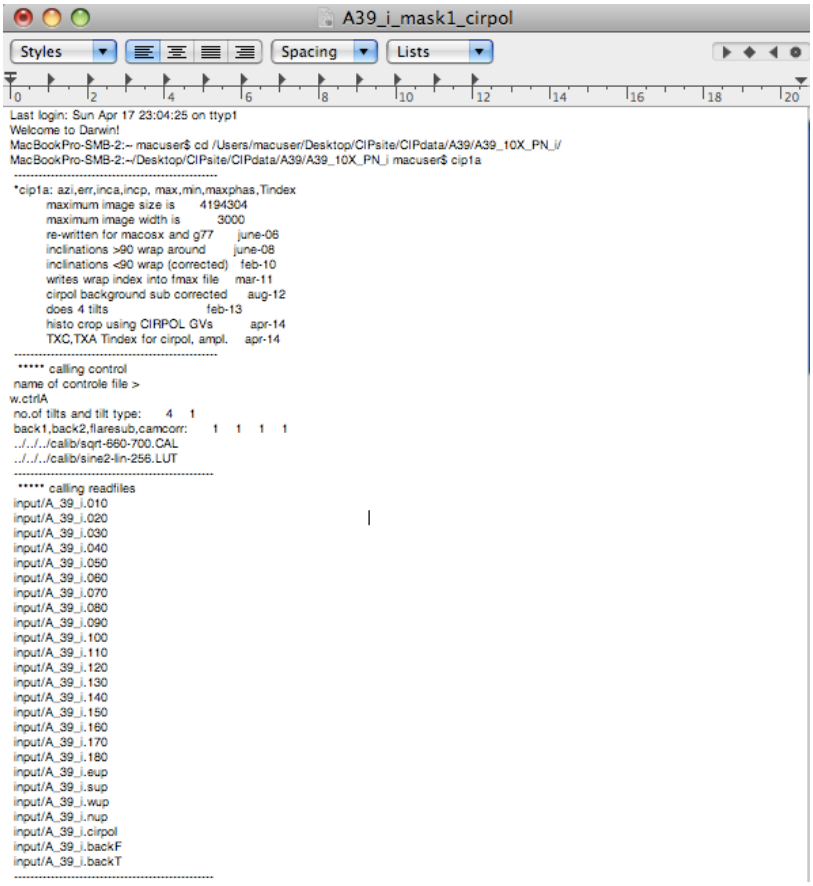

Fig. 5.18. Log file of the initial part of the CIP1a process, listing the input files for CIP site A39_i.

This is done by re-opening the final cropped stack, created during the preparation stage and thresholding the first CIRPOL image, so that the x, y coordinates of the brightest and darkest pixels or gray values, in a 1540 x 1110 cropping frame concerning the A39_i CIP stack, can be chosen (Fig. 5.19).

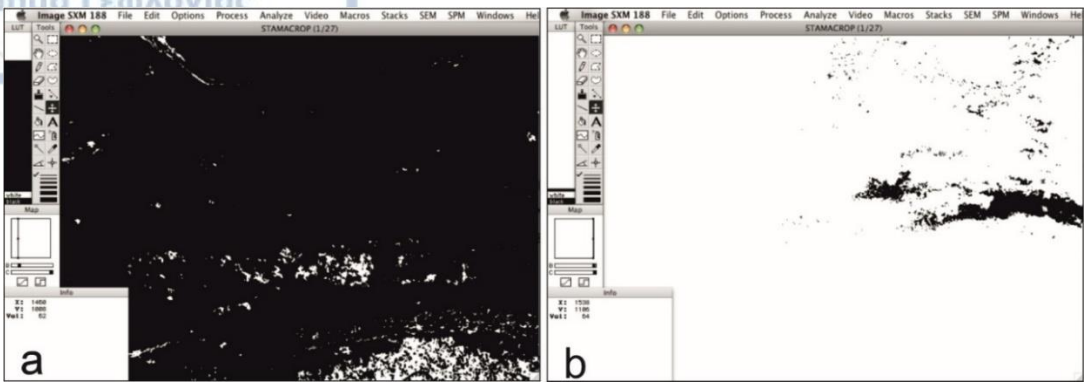

Fig. 5.19. Thresholding process of the CIRPOL image in order to define the x, y coordinates for a) the brightest and b) the darkest gray values, corresponding to quartz grains.

Much attention needs to be given during this stage so that the x, y coordinates firstly actually belong to qtz grains, as it has already been discussed the studied samples are polyphase and e.g. the brightest pixels chosen for the results could belong to the mica phase, misleading the process to erroneous results. Then two histograms are presented by the software, one for the inclination calculated from the amplitude (inca in Fig. 5.20) and one for the inclination calculated from the circular polarization image file (incp in Fig. 5.20).

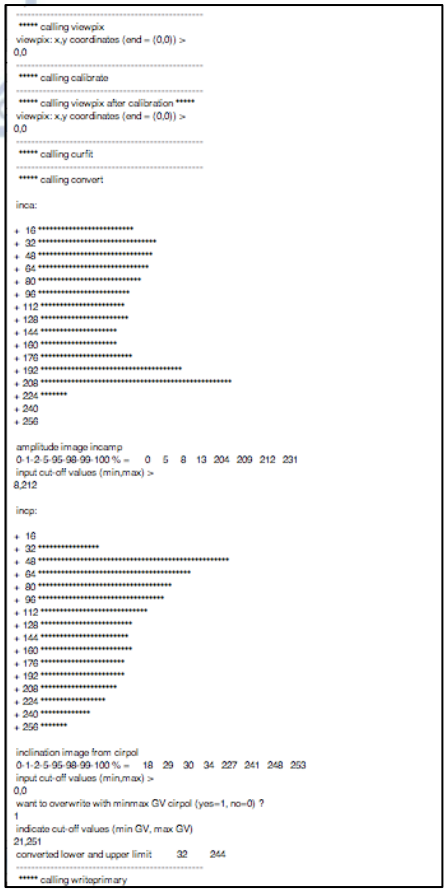

Fig. 5.20. Second part of the CIP1a log file, documenting the cropping of the inca and incp histograms.

The inca histogram was cut-off, in most cases, at the gray values corresponding to the 2% and 98% of the histogram curve, whereas the incp histogram was cut-off based on the darkest and brightest gray values (21, 251 gray values) derived from the CIRPOL thresholded image file. Using a cropped range of gray values in both cases is of utter importance so that the C- axis Orientation Images and pole figures to be produced correspond to the real distribution of c-axis and does not cause artifacts where halos or empty centers ("doughnut" textures) are present in the pole figures. The results are exported by the program in the form of image files as well and correspond to the operations described above (Fig. 5.21).

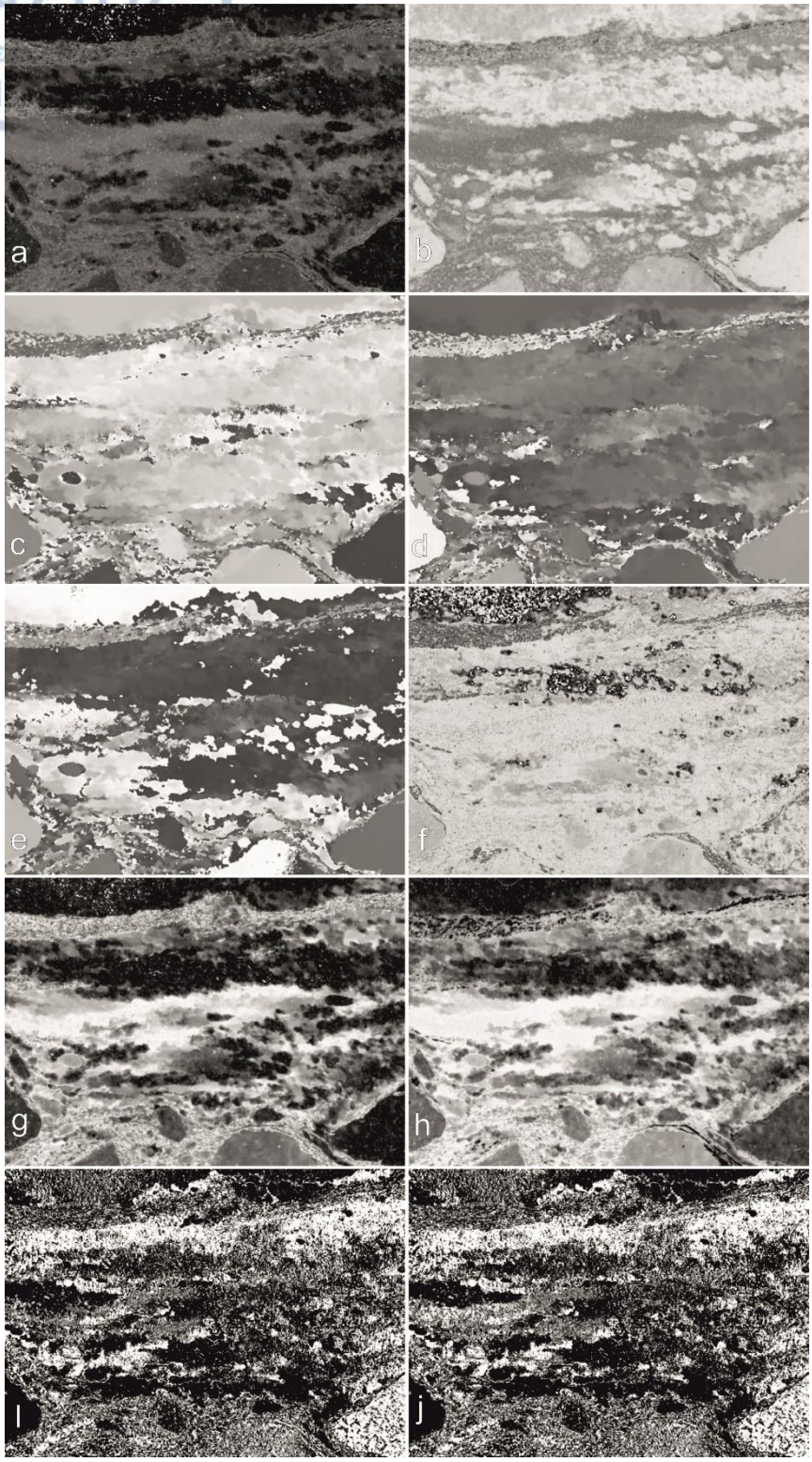

Fig. 5.21. Resulting image files after the application of CIP1a on the input stack: a) MAX image of maximum amplitude, A, intensity; b) MIN image of minimum amplitude, A, intensity; c) FMAX image of maximum phase angle, ρA; d) FMIN image of minimum phase angle, ρA΄; e) AZI image of the azimuth calculated from the FMAX and FMIN image files; f) ERR image, used to produce a quality index of the results; g) INCA image of the 0°-90° inclination, calculated from the MAX, MIN image

files, based on the inca cut off values; h) INCP image of the 0°-90° inclination, calculated from the MAX, MIN image files, based on the incp cut off values; i) TXA image, which will be used by CIP1b process to convert the primary INCA inclination file to full inclination; j) TXP image, which will be used by CIP1b process to convert the primary INCP inclination file to full inclination.

The second CIP routine applied on the A39_i input stack was CIP1b (Fig. 5.22) which primarily aims at producing C-axis Orientation Images (COI) of the studied site, based on the full inclination (0°-180°) of each individual pixel and the mineral grains under investigation respectively (CIP1a calculations refered to partial c-axis orientation images, as they represented half the inclination 0°-90°). The input files consist of the .AZI, .INCA, .INCP, .TXA, .TXP files produced via CIP1a and the output consists of full inclination image files, histograms, polefigures and COIs for both amplitude-based and circular polarization-based calculations (Fig. 5.23).

```
-------------------------------------------------------
MacBookPro-SMB-2:~/Desktop/CIPsite/CIPdata/A39/A39_10X_PN_i macuser$ cip1b
-------------------------------------------------------
*cip1b: azi/inc  from  azi/inc/tindex
      maximum image size is     4194304
      re-written for macosx and g77     june-06
      calculates COI for ampl and cirpol
      calculates polfigA, polfigB
      last update                april-14
-------------------------------------------------------
 ***** calling control
name of controle file >
w.ctrlB
-------------------------------------------------------
 ***** calling readfiles
CIP1A/A_39_i.AZI
CIP1A/A_39_i.INCP
CIP1A/A_39_i.TXP
CIP1A/A_39_i.INCA
CIP1A/A_39_i.TXA
-------------------------------------------------------
 ***** calling convert2
-------------------------------------------------------
 ***** calling writefiles
-------------------------------------------------------
 ***** calling polefigure
CIP1B/A_39_ip.polfig
-> maximum of polefigure is at (18,20):    10.41110
 CIP1B/A_39_ia.polfig
-> maximum of polefigure is at (17, 2):    7.22566
-------------------------------------------------------
 ***** calling ava
../../../clut/CIP-P-standard.CLUT
-------------------------------------------------------
```

Fig. 5.22. Log file of the CIP1b process, listing the input and output files and the calculated pole figure maxima for CIP site A39_i.

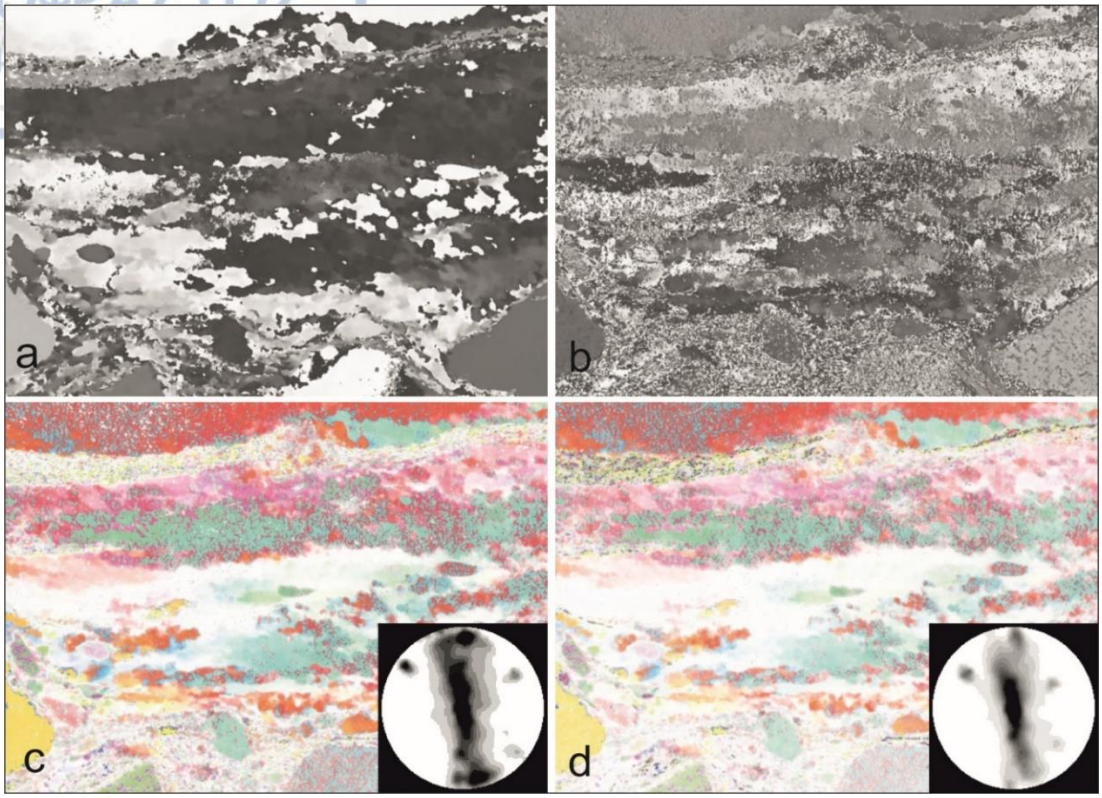

Fig. 5.23. Resulting image files after the application of CIP1b on the input stack: a) Azimuth image; b) INCP image of the 0°-180° full inclination, based on the incp cut off values; c) COIA image derived from the INCA values and corresponding pole figure; d) COIP image derived from the INCP values (as shown in b) and corresponding pole figure.

The last CIP routine applied on A39_i input stack and generally on all the studied samples was CIP2 (Fig. 5.24). The input comprises of the .AZI file, produced by CIP1a process, the .INC file produced by CIP1b process (whether it is INCA or INCP) and finally the mask that has been created to exclude non-qtz phases and was described in the preparation stage. The output primarily used in this study was the COI2 images and the resulting pole figure files calculated with the mask prepared and used in the final analysis (Fig. 5.25).

```
MacBookPro-SMB-2:~/Desktop/CIPsite/CIPdata/A39/A39_10X_PN_i macuser$ cip2
-------------------------------------------------------------
 cip2:  coi/mis/edg  from  azi/inc/mask
        maximum image size is      10000000
        maximum image width is      3000       oct-13
        re-written for macosx and g77          apr-04
  >>>   reads square (CLUT) and stereo (POL)
 edg2s  sum of difference with 2 neighbours (0-180)
 edg4a  2*av of difference with 4 neighbours (0-180)
        last update (polfig correction)     march-07
        last update (edges)                 august-07
 +MASK  considers mask in misor and edge     june-08
-------------------------------------------------------------
*calling control
name of controle file :
w.ctrl2
-------------------------------------------------------------
*calling readfiles
*calling readfiles: azi
CIP1A/A_39_i.AZI
*calling readfiles: inc
CIP1B/A_39_i.INCP
*calling readfiles: mask
input/mask_F1
*   xdim*ydim=itot         1540       1110     1709400
-------------------------------------------------------------
*calling segment
-------------------------------------------------------------
*calling writefiles
CIP2/A_39_i.EDG2s
CIP2/A_39_i.EDG4a
CIP2/A_39_i.MISN2
CIP2/A_39_i.MISE2
CIP2/A_39_i.MISH2
CIP2/A_39_i.MIS-45-90
-------------------------------------------------------------
*calling polefigure using mask
*   imask =              1  (0=no,1=yes)
*   polcorr =            1  (option 1-5)
--> maximum of polefigure is at (18,20):     11.40150
-------------------------------------------------------------
*calling ava
../../../clut/CIP-P-spectrum.CLUT
```

Fig. 5.24. Log file of the CIP2 process, listing the input and output files for CIP site A39_i and the maximum of pole figures (these values are not automatically saved but need to be recorded).

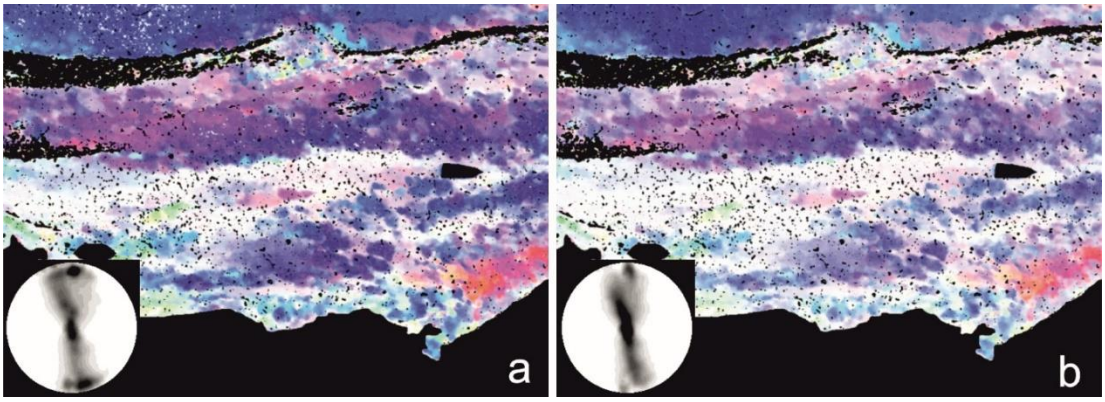

Fig. 5.25. Resulting image files after the application of CIP2: a) COI2 image based on the CIP1b INCA image file, the applied mask and the corresponding c-axis pole figure; b) COI2 image based on the CIP1b INCP image file, the applied mask and the corresponding c-axis pole figure.

The final pole figures and generally all pole figures produced by the CIP routines are the result of the respective CIP files' process in Image SXM. The Lazy pole Macros are firstly loaded on the program and then the .polfig file is opened as a 36 x 36 pixel size image and the Macro: make 180*180 CIP pole figure is selected. The pole figure maximum calculated by CIP2 needs to be inserted, as well as the contour maximum for the produced pole figure. However, the CIP2 also produces misorientation images, with respect to the CIP coordinates (misE, misH, misN, mis45/90), where the relative orientation of the derived c-axis is considered with respect to these fixed directions

(Fig. 5.26). These output files can be later used by CIP4 routine to produce grain boundary and sub-grain boundary maps. CIP4 was, however, not applied in the present analysis.

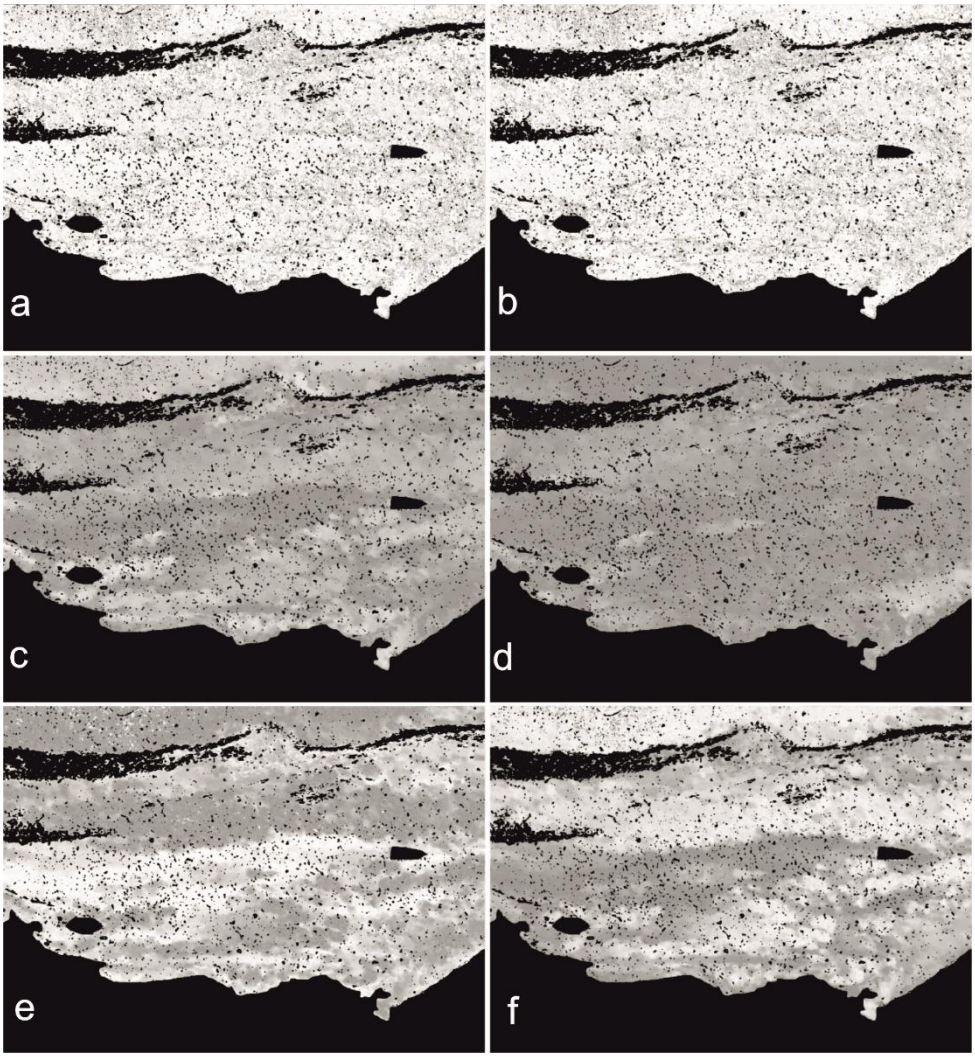

Fig. 5.26. Resulting image files after the application of the CIP2 process to produce grain boundary maps: a) EDG2s image; b) EDG4a image; and misorientation images c) MIS-45-90 image; d) MISE2 image; e) MISH2 image and f) MISN2 image.

The procedure and analysis described above for A39_i CIP site was applied on all samples and respective CIP sites listed in Table 5.1, whereas the final c-axis orientation images (COI2), their respective pole figures (corresponding to both amplitude-based and circular polarization-based calculations) and the representative CIRPOL image are presented in the Appendix and will be discussed further on.

Finally, it was attempted to derive a 'bulk pole figure' for each sample. To this end, only the pole figures derived from 2.5x magnifications can be used because higher

magnification COIs do not represent enough area of the thin section. Moreover, wherever possible, 2.5x CIP sites and respective pole figures were selected that minimized the influence of localised strain, as is the case in the direct vicinity of large feldspar porpyroclasts, where deforming quartz crystals around them record a respective texture orientation non-representative of the “bulk” texture under study. As a rough, first estimate, the pole figures were used as is, i.e. without re-contouring or normalization. With the exception of A43 and A47, between 1 and 6 pole figures were available for each sample. The pole figures were copied into an image stack (using Image SXM) and averaged. The pole figures derived from INCA and INCP inclinations were evaluated separately. The resulting pole figures are shown in Fig. 5.27 and Fig. 5.28, respectively.

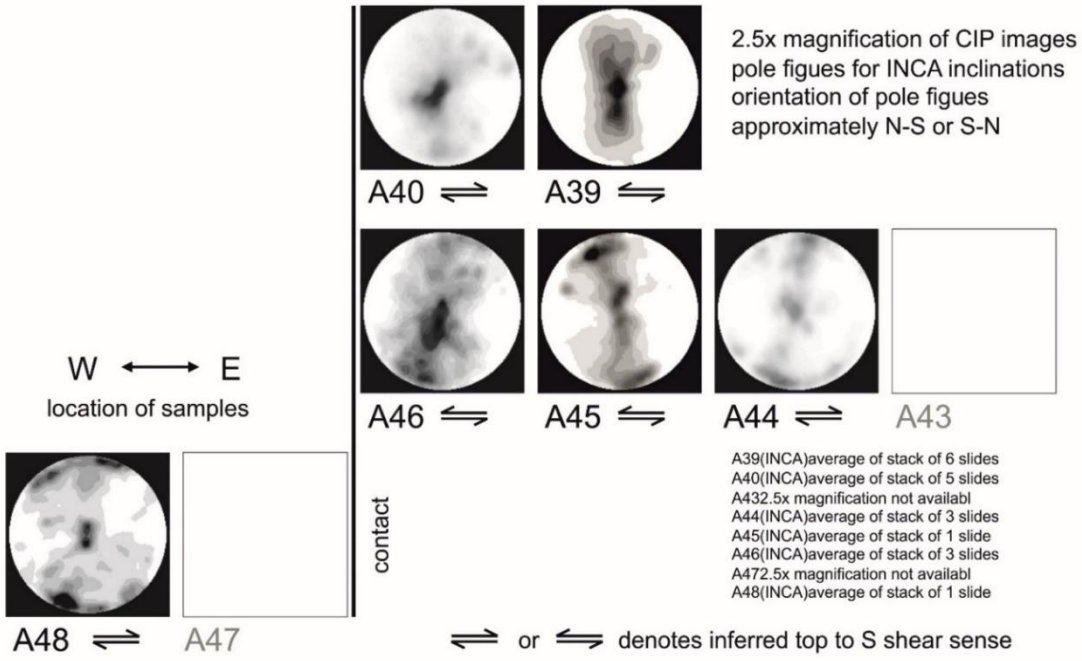

Fig. 5.27. ‘Bulk’ pole figures selected for the interpretation of the CIP analysis for INCA inclinations.

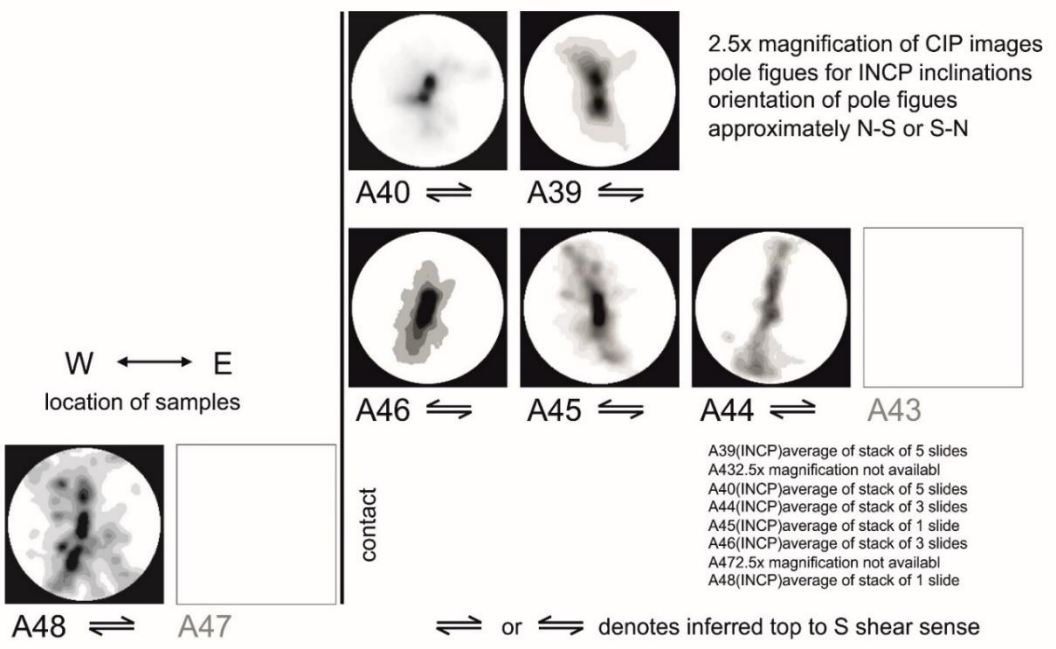

Fig. 5.28. 'Bulk' pole figures selected for the interpretation of the CIP analysis for INCP inclinations.

5.3. Discussion of results

The present analysis constitutes a first overview of the study of crystallographic textures in the study area.

A quick evaluation of the quartz content was achieved by evaluating the area of the qtz-maps (Table 5.2). Errors, however, may be quite large because the area of the qtz-maps is usually larger than the evaluated area, and hence the quartz content may be underestimated significantly. The matrix, referred to in Table 5.2, is mainly composed of plagioclase, K-feldspars, white mica and biotite.

Sample	Matrix (%)	Quartz (%)
A39	83	17
A40	85	15
A43	92	8
A44	83	17
A45*	80	20
A46*	76	24
A47	93	7
A48*	94	6

Note:
Matrix and Quartz percentages may have large errors
* denotes that qtz map was cropped for matrix and qtz %

Table 5.2. A rough evaluation of the quartz content for the samples analysed, based on the produced qtz-maps.

To derive a sense of shear from the shape of the quartz aggregates, the paror-ACFs of the qtz-maps (thresholded ACFs, right column of Fig. 5.29) and the surfor ACFs of the outline maps (representation of ACFs, center column of Figure 5.30) are considered. The inferred shear senses are listed in Table 5.3 and 5.4). For a consistent top-to-the South shear sense as inferred from the shear sense indicators (previous chapter), it appears that the surface-ACF analysis reproduces these results more reliably than the paror-ACF analysis.

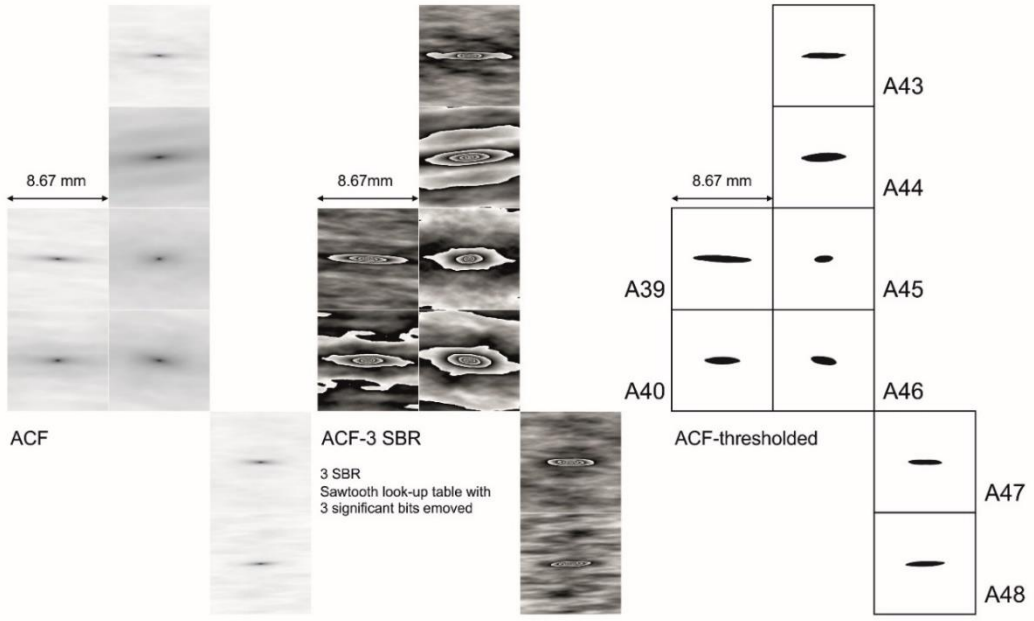

Fig. 5.29. PAROR-ACFs used to infer the sense of shear in each sample.

Sample	Area	Major	Minor	a/b	Angle(°)	Shear sense in image	South in image
A39	32819	597.51	69.934	8.54	177	sin	left
A40	21903	356.69	78.184	4.56	180	(-)	right
A43	21289	440.58	61.524	7.16	1	dex	right
A44	31441	446.81	89.596	4.99	3	dex	right
A45	10665	191.25	71.003	2.69	5	dex	left
A46	17907	266.38	85.592	3.11	171	sin	left
A47	15077	351.57	54.603	6.44	179	sin	left
A48	17313	397.92	55.397	7.18	2	dex	right

Note:
(dip of foliation denotes shear sense, S-C interpretation)
A40 no shear sense, symmetrical
A43 only 1° off horizontal
A45 opposite to top to South
A47 only 1° off horizontal

Table 5.3. Sense of shear inferred from the PAROR ACFs.

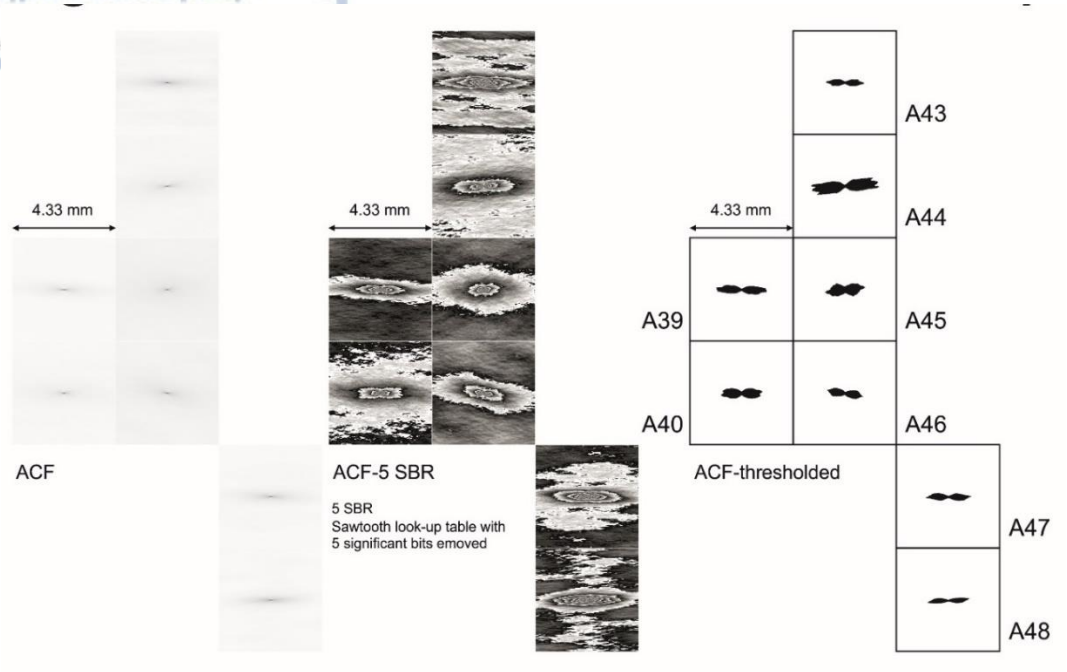

Fig. 5.30. SURFOR-ACFs used to infer the sense of shear in each sample.

Sample	Symmetry	Shear sense in image	South in image
A39	monoclinic	sinistral	left
A40	orthorhombic	-	right
A43	slighly monoclinic	(dextral)	right
A44	inclined orthorhombic	dextral	right
A45	Small: orthorhombic, Large: monoclinic	dextral, sinistral	left
A46	monoclinic	sinistral	left
A47	orthorhombic	-	left
A48	monoclinic	dextral	right

Note:
Interpretation by visual inspection
A45 Small / Large refers to small / large correlation distances (small / large contours in ACF)

Table 5.4. Sense of shear inferred from the SURFOR ACFs.

From the skeletons of the 'bulk pole figures' of six samples (Figs 5.27 and 5.28), shear senses can be inferred. In order to do so, the skeleton type was determined (see Table 5.5). In two cases (A39 and A48), no sense of shear could be determined, in one case (A46), the inferred sense of shear is opposite to the top-to-the-S shear sense, inferred from the shear sense indicators (previous chapter). Moreover, the girdles outlined by the majority of the sites indicate a plane strain flow regime with a strong

simple shear component, with the exception of A48 pole figures (based on amplitude calculations) and maybe A47 pole figure as well, which outline type I cross girdles and point towards a stronger constrictional component, according to the Flinn diagram (Schmid and Casey, 1986).

Sample	Skeleton of average INCA pole figue 2.5x	Skeleton of average INCP pole figue 2.5x	Inferred shear sense	South in image
A39	vertical girdle	type I cross girdle ?	none	left
A40	Y max - dex?	Y max	(dex?)	right
A43	-	-	-	right
A44	dextral girdle, peri maxes	dextral girdle, (peri maxes?)	dex	right
A45*	sinistral girdle, peri maxes	sinistral kinked girdle, Y max	sin	left
A46*	dextral girdle	dextral girlde, Y max	dex	left
A47	-	-	-	left
A48*	type II cross girdle GBM	type I cross girdle GBM	none	right

Note:
A39 no shear sense, symmetrical
A46 opposite to top to South
A48 symmetrical cross girdle

Table 5.5. Inferred sense of shear from the bulk pole figures.

5.4. Conclusions and outlook

5.4.1. Shear sense

Taking the ACF and CIP analysis and results into consideration, a shear sense has been inferred in most cases. As far as the ACF analysis is concerned, all samples indicated a top-to-the-S sense of shear, expcept for sample A40, where no sense of shear could be inferred and sample A45, where the opposite sense of shear, top-to-the-N, was inferred. As far as the CIP analysis is concerned, the interpretation of the sense of shear was primarily based on the representative 2.5x pole figures chosen for each samples (Table 5.). Samples A40, A44 and A45 indicated a top-to-the-S sense of shear. The 2.5x pole figure for sample A39 presents a vertical girdle, thus leading to no inferred sense of shear. The majority of the A39 CIP sites, however, and their respective pole figures (Appendix) indicate a sinistral sense of shear and thus a top-to-the-S sense of shear as well. For samples A43 and A47, no 2.5x magnification was available. However, from the pole figures produced for other magnifications (see Appendix), a top-to-the-S sense of shear can also be inferred, even though the area analysed is not sufficient for the extrapolation of a “bulk” texture. Finally, sample A46

pole figure indicated an opposite to the overall sense of shear with kinematics of top-to-the-N.

Judging from the results of the two analyses it is concluded that there is a general agreement, as far as the sense of shear is concerned, since both methods have led to an overall top-to-the-S sense of shear. The latter also agrees with field observations as already indicated in chapter 4, where the bulk sense of shear is top-to-the-S throughout the whole study area and especially along the contact of the two mica gneiss overlying the amphibolite and biotite gneiss, both in the western and the eastern part of the study area, and points towards the compatibility of the ACF/CIP results with field data.

5.4.2. Deformation mechanisms

While examining, processing and analysing the studied samples the deformation mechanisms recognized in quartz grains, when observing the microstructures (see Appendix) were, primarily, the recrystallization mechanisms of Bulging (BLG), Subgrain Rotation (SGR) and Grain Boundary Migration (GBM). In the Tonale outcrops, these mechanisms are dominant from 280-400°C, 400-500°C and 500°C to about 700°C (Stipp et al., 2002). In other words, increasing T conditions can be expected from BLG to SGR to GBM.

BLG recrystallization was identified in samples A43, A44, A45, whereas sample A40 also exhibited co-existence of BLG and SGR recrystallization. SGR recrystallization was the dominant deformation mechanism identified in the quartz ribbons of A39 sample, frequently leading to the formation of an oblique foliation, and in sample A46, where SGR grains constituted the S counterpart of a dominant C-S fabric in this specific rock sample. GBM recrystallization was evident in samples A47 and A48. As far as the two mica gneiss is concerned the samples being most proximal to the contact A39, A40 and A46, all exhibit SGR as a deformation mechanism, whereas from the multitude of their pole figures a Y-max can be inferred. On the other hand, by increasing the distance from the contact BLG takes over as a quartz deformation mechanism, indicating lower temperatures, whereas peripheral maxes are much more evident in the skeletal fabric of their pole figures. This could point towards a rising temperature

(due to the cross-over from BLG to SGR) as well as increasing strain, despite of the higher T (due to the dominance of Y maxes in the skeletal fabric of the respective pole figures (Heilbronner and Tullis, 2006)), as we approach the contact. As far as the underlying amphibolite and biotite gneiss map units and their leucogneissic bodies are concerned, GBM points to higher T and it is noteworthy that this recrystallization mechanism manifests itself more distinctively in sample A48, which is structurally further away from the contact. The observation of decreasing T as we move from the structurally lower to the structurally upper units could point towards the existence of a thermal body beneath the contact, with the relatively «hotter» amphibolite and biotite gneiss coming in contact with the «colder» two mica gneiss. Anatexis has already been suggested within the amphibolite and biotite gneisses, expressed via the existence of these leucogneissic, anatexitic bodies, assigned to the D2 event (see next chapter), whereas the development of the shear zone, has been assigned to the D3 event (see next chapter). Taking into account the alternative of the D2 and D3 events constituting progressive stages of a Mesozoic deformational event, the above observations seem to favour such a scenario as well.

Since this is a preliminary version of an analysis of crystallographic textures in the study area, there is certainly room for future work. First of all, more CIP sites could be chosen and analysed for each sample, preferably covering continuous quartz domains, so that the CIP results refer to wider areas and are more representative. Samples A90-A98, collected from the north block of the sampling area and continuing the sampling transect to the E, from within the two mica gneisses should be also processed with the CIP method, since the micrographs have already been taken, a multitude of CIP stacks has already been prepared for a number of them and they all need to be processed with the CIP software. Moreover, more samples should be collected from the underlying amphibolite and biotite gneisses, in order to have a much clearer view of how textures evolve in the underlying units as well, also with respect to their distance from the contact under study. Collection of CIP samples could be extended to the eastern part of the study area, W of Pantokratoros monastery and the shear zone between the underlying two mica gneiss and the overlying amphibolite gneiss,

in order to examine if the mesoscopic observations of a top-to-the-N sense of shear are verified by the crystallographic microstructures and possible shed more light on how this «sandwiched» megascopic structure developed.

Chapter 6. Deformational events

6.1. D1 event

The D1 deformational event has been related with an S1 foliation, identified in discordant pegmatoid veins and truncated by later metamorphic and deformational fabrics. It has also been associated with the presence and co-existence of titanite and rutile in thin sections from the amphibolite gneiss. Such a mineralogic relationship has been related with relic eclogite phases in amphibolites resulting from tholeitic basalts, according to Hellman and Green (1979). Therefore, this D1 event could be assigned an eclogite metamorphic grade.

6.2. D2 event

The D2 deformational event is characterized by a ductile fabric, which was recognized in all rocks, except the mafic/ultramafic rocks of the study area. The S2 foliation is assigned to this deformational event, occurring as an older, transposed, relict, planar fabric, constituted by minerals indicating an amphibolite-facies metamorphic grade (having as a strong indicator a 1st generation of hornblende porphyroclasts preserved within the later S3 planar fabric of the amphibolite gneiss). It is characterized by rootless, intrafolial, isoclinal folds, which along with the according L2 lineation were overprinted and rotated into parallelism with later D3-assigned structures and could not be geometrically and kinematically distinguished from them. Moreover, relics of the D2 fabric were also found within the leucogneiss inlayers of the amphibolite and biotite gneiss, a rock which signifies a round of anatexitic phenomena, the latter gaving rise to the migmatization within the amphibolite and biotite gneiss. Lastly, the pegmatoid veins, associated with the D1 event, have been found, at places, to be isoclinally folded by F2 folds, thus setting a relevant time limit to the D2 definitely later than the appearance of these frequently discordant to the D2/D3 fabrics pegmatoid veins.

6.3. D3 event

The D3 event constitutes the dominant ductile deformational event and gives rise to the main deformational and metamorphic fabric of the study area, imprinted on all the map units. Its most prominent feature is the S3 planar fabric gently dipping, in an

undulating fashion, mainly towards the ENE. This S3 planar fabric is constituted by an amphibolite facies mineral assemblage and in many locations appears as a mylonitic foliation. It is noteworthy that ductile deformation during this D3 event was not localized only in specific shear zones along major tectono-stratigraphic contacts but was partitioned throughout the whole body rock of the study area, accommodated by numerous shear zones from microscopic to map scale. That is why structures traditionally attributed to shear zones and mylonites, such as shear bands, porphyroclast systems, Lattice Preferred Orientation fabrics, S-C fabric, mica-fish structures and sheath folds have been documented almost throughout the whole body rock of the study area (Fig. 4.1-8 and 4.9). It is during this deformational event that F3 isoclinal folding takes place along with the creation of an L3 stretching lineation, which both follow a bilateral geometry along a NNW-SSE and a NNE-SSW trending axis. This parallelism of isoclinal and according parasitic fold axes with the stretching lineation has been attributed to a large-scale sheath folding pattern and the incorporation of the whole study area to a multi-scale shear zone.

There is a combination of structural information to be taken into account in order to better visualize this multi-scale sheath folding pattern depicted in meso-scale sheath folds, as well as map-scale highly-curvilinear, sheath folds. First of all the isoclinal fold axes spatially converge and diverge in specific locations throughout the study area, suggesting the formation and existence of dome and basin domains of a relatively acute apical angle (<30°). Moreover, when analyzing at places the S3 foliation bilaterally of the XZ-plane in the body of these dome and basin sheath folds, an overall high ellipticity is concluded, as far as the yz observation plane is concerned. This relatively high ellipticity is verified by meso-scale observations in various outcrops, where elliptical closures have been documented, commonly referred to as “eye folds” (Alsop and Holsworth, 2004; 2006), representing YZ-cross-sections of sheath folds. When taking into account the ellipticity ratio between outer and inner elliptical rings in these meso-scale sheath folds cross-sections, a “cat eye” fold pattern is concluded (Fig. 3.30 and 3.31), according to the classification set by Alsop and Holsworth (2006). Cat-eye folds have been linked to sheath folds formed primarily by simple shear deformation and general shear as well, with higher ellipticities pointing

towards higher deformation intensity and a higher simple shear component (Alsop and Holsworth, 2006). The fact that the sandwiched two-mica gneiss map unit fades out at the SW part of the study area, whereas it seems to gain thickness at the eastern part, suggests that, in the structural context of a large-scale sheath fold, the whole study area would actually comprise, with its smaller scale basinal and domal domains, the left half of the cat's eye, constituting a large scale dome structure verging towards the S.

The kinematics, verified via kinematic indicators throughout the whole study area, governing the shearing, have been found to be top-to-the-S directed, even though there were cases where the opposite, top-to-the-N, sense of shear was documented. This opposite sense of transport direction could either be attributed to counter-rotating kinematic indicators, under a deformational framework of general shear or areas where basin sheath folds are forming. In such areas the combination of isoclinal folds axes rotating and counter-rotating in respect with the stretching lineation indicate a convergence of F3 axes towards the N and thus the formation of basin folds. Moreover, it is necessary to take into account the fact that during sheath folding flow perturbation takes place and dome sheath folds experience an acceleration of flow (surging flow), whereas basin sheath folds experience a deceleration of flow (slackening flow), thus leading to a differential flow when crossing from one domain to another. This slackening flow could lead to an opposite sense of shear when one is situated in basin domains. Accordingly parasitic fold axes would converge towards the opposite direction, with respect to the main transport direction of a major shear zone, and kinematic indicators could point towards the opposite direction as well.

It is during this D3 event, with the overall top-to-the S sense of shear governing its kinematics and this multi-scale sheath folding event taking place that the main contacts among the tectonostratigraphic units, observed today were formed either in the form of pre-existing tectonostratigraphic contacts that were isoclinally folded or in the form of low angle shear zones.

This D3 deformational event has already been characterized as a ductile deformational event, which obviously must have taken place at a considerable depth within the crust. Taking into account mylonitic fabrics associated with this D3 event, a

low-to-medium grade is assigned to the related mylonites. Especially regarding quartz, participating in the S3 fabric, and its deformation within mylonitic zones, it is concluded that intra-crystalline deformation has taken place and more specifically crystal-plastic deformation by means of a dislocation creep mechanism. The dominant recrystallization process taking place seems to be Sub-Grain Rotation (SGR) mechanism, which in turn leads us to indicative temperatures of 400-500 °C (Hirth and Tullis, 1992; Stipp et al. 2002). Moreover, the fact that, in some microscopic samples, an oblique foliation is apparent, constituted by SGR recrystallized quartz grains, could point to even slightly higher temperatures, as the development of this oblique foliation is assigned to a combined SGR and Grain Boundary Migration (GBM) recrystallization regime (Passchier and Trouw, 2005). These temperatures, which constitute the deformational framework of shearing, seem to be in agreement with the lower-middle amphibolite metamorphic conditions suggested by the mineral assemblage constituting this S3 planar fabric in amphibolites (hornblende + plagioclase(an 20-40) + epidote + biotite). It is possible that the development of this multi-scale shear zone took place during the later stages of this lower-middle amphibolite facies metamorphism and shearing. In particular, it seems that the mylonitization took place progressively with intrafolial shear zones and these shear zones were also progressively folded with isoclinal and sheath folds. Later the deformation became more localized along distinct shear zones, which cross-cut and transposed the afore-mentioned sheath folds.

6.4. D4 event

The D4 deformational event corresponds mainly to an outcrop to map-scale asymmetric folding event characterized by a vergence primarily towards the WSW to W as well as the ENE to E. The associated S4 foliation, manifested either as a crenulation cleavage, fanning out at places, or an axial planar spaced cleavage, is attributed to this folding event and the interaction of this foliation with the pre-existing S3 has led to the development of an L4 lineation in the form of either an intersection lineation or a crenulation lineation. The minerals usually participating in the formation of this S4 crenulation cleavage are micas, suggesting a lower-grade

metamorphic grade for the D4 event. The afore-mentioned structures related with this D4 event, even though they have been recorded in all the rocks and found to have overprinted previous D3 structures, they are not present throughout the whole study area, but can be mostly observed at specific locations, which represent map-scale F4 folds.

This deformational event exhibits semi-ductile/semi-brittle characteristics, with scarce S-C type structures, displaying mainly a top-to-the-WSW to SW sense of shear, or low-angle thrust faults, often exhibiting foliation dragging and verging towards the WSW (Fig. 6.1). This semi-brittle character and the low-grade metamorphic conditions assigned to the D4 event, suggest that it must have taken place in the upper crust and can be correlated with a greenschist facies metamorphism. Finally, based mainly on the NNW-SSE to N-S trending F4 fold axes recorded and verified by our structural analysis, it can be concluded that the main structures related with this deformational event were a result of an ENE-WSW oriented compression.

Fig. 6.1. Fold limb of an asymmetric F4 fold truncated by low-angle thrust faults, exhibiting foliation dragging and indicating a top-to-the-WSW sense of shear, within the marbles map unit, S of Konstamonitou monastery.

6.5. D5 event

The D5 event is characterized by gentle to open folds, trending about an E-W axis and kink bands associated with an S5 foliation at scarce locations, whereas S5 foliation occurs as a crenulation cleavage or spaced cleavage along the fold axial surfaces. The presence of chlorite in most of the rock mineral assemblages must be attributed to this deformational event, which is characterized by a lower greenschist facies metamorphism. It constitutes the least imprinted deformational event on all the formations' fabric and can be associated with a general N-S oriented compression.

6.6. Age of deformational events

Since no absolute geochronological data was collected throughout this dissertation no absolute aging of the deformational events can take place. The relative geochronological order of the 5 deformational events defined in this study has been carried out by observing and documenting overprinting relationships among their respective textures and structures. However, their ages have been assigned by interrelating them with similar rocks from the wider area to which published ages exist.

D1 event has not been thoroughly documented in this dissertation and therefore its assignment to an age is quite dubious. The co-existence of rutile and titanite in thin sections from the amphibolite gneiss has been related with a relict eclogite facies metamorphism, also mentioned by Sakellariou (1989) for rocks belonging to the Kerdyllion and Vertiskos Units. Eclogite facies metamorphism has been documented in other parts of the Serbo-Macedonian massif and it has been attributed pre-Mesozoic ages (Sakellariou, 1989; Kostopoulos, 2000), even though a relict eclogite facies within garnet was also documented in Mesozoic meta-sediments, of respective Alpine age and located within the Chalkidiki peninsula, by Kydonakis et al. (2015). Additionally, Himmerkus et al. (2011) documented a Permo-Carboniferous age as the protolith age of the biotite gneisses, setting a further time constraint for the dating of the consequent syn-metamorphic deformational events concerning the study area.

Following this rationale a **pre-Mesozoic** age is assigned to this poorly defined D1 event.

D2 event was primarily dated based on the recognition of relict forms of S2 within a first generation of pre-D3 hornblende porphyroclasts from the amphibolite gneisses. This early amphibolite grade metamorphism, correlated with the D2 event, has been also documented by Sakellariou (1989) in the Vertiskos and Kerdyllion Units and has been asssigned by the same author an upper amphibolite grade and an either Late-Paleozoic age (related with the Hercynian orogeny (Borsi et al., 1985)) or an age related to the Cimmeric orogenic processes, during the Early and Middle Mesozoic. Taking the above into account, we conclude that this D2 event took place by the end of the Cimmeric orogenic cycle, **prior to the Late Jurassic**. Moreover, the migmatization, which is evident within the amphibolite and biotite gneiss map units, and the anatexis signified by the concordant leucogneissic bodies, could have initiated during this event and progressively deformed under the lower-to-medium grade amphibolite facies of the following D3 event.

The D3 event represents the main deformation event of the study area resulting in the main tectonic fabric of the metamorphic rocks of the study area. It is associated with the metamorphism of the rocks to lower and medium amphibolite facies. Rocks belonging to the Kerdyllion and Vertiskos Units have also recorded the same syn-tectonic metamorphic grade, characterizing the main fabric of these two units, in other part of the Serbo-Macedonian massif. Its dating varies and spans within the Mesozoic, since dates of Middle-Late Jurassic to Early Cretaceous or Middle-Late Cretaceous are assigned to this event from different researchers. In particular, the former age is assigned by Harre et al. (1968), Zervas (1980, 1984), Papadopoulos (1982) and De Wet et al. (1989) based on radiometric dating of hornblende and micas, whereas the latter is assigned to mid-late Cretaceous also based on radiometric data from hornblende, mica and biotite by Papadopoulos and Kilias, 1985; Kilias et al., 1999. Moreover, a time limit of a post-Early-Mid Triassic age or a post-Late Jurassic age for this S3 syn-metamorphic planar fabric and the D3 event conclusively is set, since these are the two calculated protolith ages for the Arnaea granite (Vital, 1987;

Himmekrus et al., 2009 for the first Triassic age group, and Kockel et al., 1977; Dixon and Dimitriadis, 1984; Papadopoulos & Kilias, 1985; De Wet et al., 1989; Ricou et al., 1998; Lips et al., 2000, for the second Late Jurassic age group), intruding the Vertiskos Unit. This plutonic body has also been imprinted by an analogous, dominant planar fabric of lower to medium syn-metamorphic grade, documented by Sakellariou (1989). Moreover, Himmerkus et al., (2011) calculated a Late Jurassic age for a magmatic event based on zircon dating from biotite gneisses of the study area. Bearing also in mind that the amphibolite gneiss and the biotite gneiss exhibit a pronounced migmatitic layering, whereas the leucogneiss concordant bodies, following and defining at places the S3 geometry, lithologically refer to anatexitic bodies, which could have originated during the previous Cimmeric orogenic cycle, it is concluded that this D3 event is of **Late Jurassic-to-Early Cretaceous age.** It was accompanied by a syn-metamorphic lower to middle amphibolite grade and appears as a progressive stage of the D2 event, which is characterized by a parallel geometry and a slightly higher metamorphic grade.

The D4 event, as already described in the previous chapters, gave rise to a characteristic NNW-SSE tending folding event associated with S4 foliation. Such a deformation event, charactrized by similar structures, has been documented by Sakellariou (1989), in the central eastern part of Chalkidiki peninsula, to affect the rocks of both Vertiskos and Kerdyllion Units. Moreover, Sakellariou (1989), based on mica ages (Harre et al., 1968; Papadopoulos, 1982; De Wet and Miller, 1987), assigns to this event, which is associated with a greenschist to upper-greenschist grade metamorphism, an Early Cretaceous age. Because the metamorphic grade and the afore-mentioned deformational pattern and style fit well the D4 structures and metamorphism exhibited by the rocks in the present study area, an **Early Cretaceous** age for the D4 event is initially suggested. On the other hand, the Tertiary Alpine contraction gave rise to NNW-SSE striking thrusts directed towards WSW and asymmetric folds with vergence towards WSW, similar to folds included in the D4 deformation event. The Alpine contraction has affected the Internal Hellenides, as has been recognized in the Circum Rhodope Belt Thrust System (Tranos et al. 1999), but, more importantly, similar ENE-WSW kinematics has resulted from a deformation that

took place before and simultaneously with the Sithonia granitoid emplacement (Tranos et al. 1993), thus dating the D4 event to outlast the **Eocene**.

Finally, the D5 event was identified in this study as an ESE-WNW to ENE-WSW trending folding event caused by a general N-S oriented shortening. It gave rise to a general E-W trending S5 foliation, mainly in the form of a crenulation cleavage made up of the presence of chlorite mineral in various samples from the study area. It was, therefore, associated with a syn-tectonic, retrograde, lower greenschist facies metamorphism. Analogous geometry folds have been recorded by Sakellariou (1989) in the central eastern part of Chalkidiki peninsula, within the Vertiskos and Kerdyllion Units, and were also correlated and documented as part of an Eocene, syn-tectonic, lower greenschist metamorphic event, fitting well with mica ages by Harre et al. (1968), and Marakis (1968). In addition Tranos et al. (1993) documented the Sithonia granite as an Eocene, syn-kinematic intrusion, which underwent during the Eocene-Oligocene a late stage of NNW-SSE to NNE-SSW oriented shortening, which also fits well with the structural data of the D5 event. Therefore an **Eocene-Oligocene** age is attributed to the D5 event. Should we accept an Eocene age for the D4 event as well, then D4 and D5 could be regarded as progressive stages of an Eocene-Oligocene, retrograde, greenschist facies event, as is the case in Tranos et al. (1993) for the Sithonia pluton.

Based on the structural analysis and interpretation of the deformational events recognized in the study area, this dissertation comes as an additional proof to previous studies that the innermost part of the Internal Hellenides, formely known as Hellenic Hinterland, part of which is comprised by the Vertiskos and Kerdyllion Units, may have a Paleozoic protolith age, but its main fabric and overall structure was acquired during Mesozoic Alpine reworking processes, which stretched in time until the Early Tertiary. A first crucial hint for the unravelling of the geotectonic evolution of the study area is the dating of granitic bodies within both the Vertiskos and the Kerdyllion Unit. The Vertiskos Unit, apart from the Silurian orthogneiss protolith ages documented by Himmerkus et al. (2008), is characterized by the intrusion of the Arnea granite, attributed both a Triassic age (Vital, 1987; Himmerkus et al., 2009) and a Late Jurassic age (Kockel et al., 1977; Dixon and Dimitriadis, 1984; Papadopoulos & Kilias, 1985; De Wet et al., 1989; Ricou et al., 1998; Lips et al., 2000), whereas the Kerdyllion Unit has been associated with Permo-Carboniferous and Late Jurassic magmatic arc-related intrusions (Himmerkus et al. 2007; 2011). Eocene granites intrude both units. Therefore these two units, based on the above geochronological data, could not have come in contact prior to the Late Jurassic, which is also the time limit for the D3 event in this disseration.

Another crucial structural feature for the unravelling of the geotectonic evolution of the study area are the tectonic slivers of the ultra-mafic/mafic map unit located mainly along the boundary of the Kerdyllion-related amphibolite and biotite gneiss map units, and close to their respective boundary with the Vertiskos-related two-mica gneiss map unit. These ultra-mafic/mafic slivers follow the geometry of the main deformational fabric outlined by the S3, as the main foliation in the study, and are secondarily rotated along with the S3 by the successive, “co-axial” D4 event to more upright positions. The presence of these slivers therefore along these D3 shear zones structurally and genetically bind their emplacement along the Vertiskos-Kerdyllion contact in the study area with the D3 event, which has been temporally constrained in the Late Jurassic-Early Cretaceous, in this dissertation.

Analogous mafic and ultra-mafic rocks have been documented close to the Kerdyllion-Vertiskos boundary, as already mentioned, and grouped under the Therma-Volvi-Gomati ophiolite complex. Various interpretations have been suggested, such as being part of an ophiolitic suture of the Paleo Tethys (Papadopoulos, 1980; Sengor et al., 1984) or in-situ, rift-related rocks attributed to a Mesozoic opening, oceanic crust (Dixon and Dimitriadis, 1984).

Taking into account our discussion so far, the Vertiskos and Kerdyllion Units in the study area must have come in contact, during this Late Jurassic-to Early Cretaceous D3 event. The presence of “ophiolitic” slivers close to their boundary also advocates towards the scenario of these two lithologically distinct Units being separate segments of one or multiple pre-Mesozoic continental crusts. Whether a pre-Mesozoic Paleo Tethys oceanic crust existed and a subduction occurred or a rifting event took place with the opening of a juvenile Mid-Jurassic ocean, which did not further develop and convergence was activated, the Vertiskos and Kerdyllion continental crusts collided during the Late Jurassic-to-Early Cretaceous, with one Unit underplating the other.

Taking into account the fact that:

a) the triple magmatic pulse documented for the Kerdyllion Unit in the study area has led to its juxtaposition and correlation with analogous Rhodope Units, such as the Sidironero Unit. It can be therefore be concluded that Kerdyllion Unit was situated relatively to the S and the Vertiskos Unit to the N, the latter constituting an exotic terrane of Gondwanan origin already accreted to Laurasia, during Late Paleozoic (von Raumer and Stampfli 2008; Spiess et al. 2010)

b) throughout the Serbo-Macedonian massif the Vertiskos Unit has been found to overlie the Kerdyllion Unit, whereas the Vertiskos Unit (two-mica gneiss map unit) has been found to be “sandwiched” by the Kerdyllion Unit (marbles, amphibolite and biotite gneisses) in the study area,

c) the kinematic analysis of the D3 event, suggesting an overall top-to-the S sense of shearing, as well as a progressive deformational pattern where D3 shear zones and structures are refolded and sheared anew, and

d) a resulting sheath fold geometry with the afore-mentioned characteristics, with parallel isoclinal F3-axes and L3 stretching lineation,

it is concluded that during this Jurassic convergence and consequent collision the Kerdyllion Unit collided and underplated the Vertiskos Unit, forming an initial ductile shear zone which, during the D3 event, was progressively sheared anew by an intense S3 mylonitic foliation and was isoclinally folded into a large-scale sheath fold. The study area constitutes a basin/dome domain of this afore-mentioned large-scale sheath fold, with the initially underlying Kerdyllion Unit surrounding the Vertiskos Unit. This underplating process, which might have initiated already by the Early to Middle Mesozoic (D2 event), must have initially led the Kerdyllion Unit to deeper crustal levels, which in turn could have given rise to the synchronous intense migmatization processes of the amphibolite and biotite gneiss and the anatexis signified by the leucogneiss, concordantly emplaced within the afore-mentioned map units. Considering the possibility of a progressive character for D2 and D3, this whole D3-related, dominant structure of the study area could have resulted during extrusion processes, following the initial D2 path of the Units to deeper crustal levels.

Concerning the D4 event and its dual temporal juxtaposition with either an Early Cretaceous or an Eocene-Oligocene time the following can be presented. The D4 event has been described in this study as an ENE-WSW oriented shortening event, under semi-brittle conditions, with the production of generally asymmetric to upright steeply inclined, NNW-SSE to N-S trending folds, verging mainly towards the WSW, and the appearance of semi-brittle fault zones with an overall top-to-the WSW sense of shear. As already mentioned the Kerdyllion Unit has been correlated with Rhodope Units of according metamorphic grade and more specifically the Sidironero Unit (Burg, 2012 and references therein). The Sidironero Unit presents a significant shear zone at its lower boundary, which has been named Nestos thrust or Nestos shear zone and has been attributed a top-to-the SW shear sense in the regional context of an analogous shortening, during Late Eocene times (Dinter, 1998; Krohe and Mposkos, 2002). The orientation, kinematics and timing of the Nestos shear zone seems to fit well with the according features of the D4 event recognized and defined in the study area, providing further constraining criteria, concerning the dating of this event favorably in Late Eocene-Early Oligocene times. The fact that the Nestos shear zone bears signs of a more ductile nature, when compared with the D4 structures, could be

attributed to its contemporary occurrence at deeper crustal levels with respect to its westernmost counterpart, the Kerdyllion Unit.

The present thesis, in its attempt to analyze, decipher and unfold the overall structure and the processes which led to this structure in the study area, has reached the following conclusions:

1) The marbles, the amphibolite gneiss, formerly independent amphibolites by Kockel et al. (1977), the biotite gneiss, assigned in the study area to Vertiskos Unit by Kockel et al. 1977, and the anatexitic leucogneiss bodies, considered also by Kockel et al. (1977) as initial melts of the Plagioclase-microcline gneiss Unit, belong to the Kerdyllion Unit, whereas the Vertiskos Unit is represented by the two-mica gneiss. The ultra-mafic rocks are considered to represent oceanic-derived material, assigned to the Therma-Volvi-Gomati complex (Dimitriadis, 1980) and belonging most probably to a Mesozoic rift-related in-situ ocean, according to Dixon and Dimitriadis (1984). The presence of theses mafic-ultramafic rocks, in the form of tectonic slivers, within the Kerdyllion Unit, permits us to consider the Kerdyllion Unit as of being in closer relationship with the oceanic crust, possibly representing a deep submarine environment.

2) The overall structure of the study area is represented by the map units successively gently dipping mainly to the ENE, and repeatedly outcropping, in most cases, both at the western and the eastern part of the study area. The marbles dip underneath the amphibolite gneiss, incorporating a biotite gneiss horizon at the western part of the study area. The amphibolite gneiss and biotite gneiss both underlie and overlie the, slightly discordant at places, two-mica gneiss map unit, both at the western and eastern part of the study area. The two-mica gneiss, in turn, appears structurally sandwiched between the amphibolite and biotite gneiss. The only map unit which does not repeat itself to the E is the marbles map unit.

3) The contact, however, between the Vertiskos and Kerdyllion Units is not a normal contact, as mapped by Kockel et al. (1977) in the central-eastern part of the Chalkidiki peninsula, but a tectonic contact, as already indicated in other parts of the Serbo-Macedonian massif (i.e., Sakellariou, 1989; Burg, 1995; 1996; Plougarlis and Tranos, 2014), and more precisely a large mylonitic shear zone with an overall top-to-

the-S sense of shear. Nonetheless, the tectonic contact between the Vertiskos and Kerdyllion Units is more complicated since it is locally inverted. As a result, an opposite top-to-the-N sense-of-shear occasionaly occurs, and the two-mica gneisses appear sandwiched between the rocks of the Kerdyllion Unit, due to simultaneous shearing and isoclinal folding that prevails the deformation. This verifies the complexity of the tectono-metamorphic evolution of the study area, in the ductile flow regime, and indicates the need for future research, combining geochronological and P-T data.

4) Through the overall structural analysis performed on the data collected from the study area, five deformational events were concluded:

D1 event was poorly documented in this study. It was correlated with the co-existence of titanite and rutile found in the amphibolite gneisses of the study area and also related with the discordant, to the dominant S3, pegmatoid veins, documented mainly within the upper biotite gneiss map unit. This event was assigned a pre-Mesozoic age.

D2 event was considered syn-metamorphic with a higher to middle amphibolite grade facies and related with isoclinal, rootless folds, as parts of this D2-belonging fabric, which was intensely transpositioned by the subsequent D3 event. Such structures were identified both in the Kerdyllion-assigned map units and the Vertiskos-assigned map units, which, according to our analysis did not come in contact until Late-Jurassic times, when the afore-mentioned overprinting took place and D2 fabrics in both Units were forced into parallelism with the dominant D3 fabric. D2 is also related to the initial stages of the anatexis signified by the leucogneiss bodies and the procounced migmatization of the amphibolite and the biotite gneiss. An early to middle Mesozoic age was assigned to the D2 event. The case of D2 being an early progressive stage of the D3 event, due to the metamorphic grade affinity, the parallel geometries and the successive age attribtute to the two deformational events, is considered highly possible.

D3 event, which gave rise to the dominant structure of the study area, was related with a lower amphibolite grade metamorphic grade, the formation of an S3 pervasive foliation, quite frequently considered as mylonitic, and a distinct parallelism of NNW-

SSE and NNE-SSW trending F3 isoclinal fold axes and L3 stretching lineation. This parallelism and the overall deduced top-to-the S sense of shear, were attributed to a large-scale shear zone and an also large-scale sheath fold geometry, which led to the structural repetition of Kerdyllion-related, lower and upper amphibolite gneisses and biotite gneisses around the Vertiskos-related two-mica gneiss map unit. Their boundary consists of an isoclinally folded, initial D3 shear zone, progressively deformed by younger shear zones, developed during the late stages of this deformational event. The age which was assigned to the D3 event was Late Jurassic-to-Early Cretaceous and it was related with the accretion of the Kerdyllion Unit underneath the Vertiskos Unit, involving as a geotectonic process the destruction of an either Mesozoic in-situ, rift-related oceanic crust (Dixon and Dimitriadis, 1984), or a part of the Paleo-Tethys (Sengor et al., 1984). In both cases this oceanic-derived material is represented in the study area by the tectonic slivers of the ultra-mafic map units found mainly close to the boundary between the upper amphibolite gneisses/biotite gneisses and the two-mica gneiss map units. The present study suggests a northward subduction and subsequent underplating of the Kerdyllion Unit, located relatively-to-the S, underneath the Vertiskos Unit, located relatively-to-the N.

D4 event which gave rise to the second most imprinted fabric and structures in the study area, was related with a greenschist metamorphic grade, generally WSW-verging asymmetric folds, an S4 crenulation cleavage/axial foliation, an L4 intersection lineation and semi-brittle faults, indicating altogether a WSW-ENE directed compression. In many cases it was documented to overprint previous structures and was assigned an Eocene age, mainly due to equivalent structures documented in neighboring syn-tectonic, granitic bodies, such as the Sithonia pluton (Tranos et al., 1993). It was considered to represent the Late-Alpine processes which led to the accretion of the Apulia to the Eurasian plate.

Finally the D5 event, was related with a lower greenschist metamorphism, generally E-W trending kink and gentle folds, a weak S5 crenulation cleavage and an L5 intersection lineation, produced by the interference of pre-existing S3 and S5 surfaces. It was therefore related with a N-S directed compression, which has also

been documented in the wider area (Tranos et al., 1993). It was considered as part of the late-orogenic processes that affected the whole study area, during this afore-mentioned Late-Alpine event.

5) Concerning the existing geological map of Kockel et al. (1977) and the geological map at scale 1:50.000 (IGME), we can argue that: (a) the boundary between the Vertiskos and Kerdyllion Unit, needs a thorough revision, b) the biotite gneisses, which were only referred to as alternations with the two-mica gneisses, are not actually in alternations with the two-mica gneisses, but with the amphibolite gneisses. Therefore, they do not belong to the Vertiskos, but the Kerdyllion Unit, c) the two-mica gneisses, which were initially mapped to cover the largest part of the study area, seem to be of much more limited extent.

In summary, our work strongly suggests that the overall structure and tectono-stratigraphy concerning the Vertiskos and Kerdyllion Units is much more complicated than the view provided by the existing geological maps, and the contact between these units does not necessarily coincide with the roof of the uppermost marbles of the Kerdyllion Unit. Finally, the deformation events, concluded in this dissertation declare the Alpine reworking of the crystalline rocks of the Athos peninsula that was previously considered as part of the stable Hellenic hinterland.

Abstract

The Athos peninsula occupies the south-eastern part of the wider Chalkidiki peninsula in Central Macedonia, Greece. It is mainly built up by crystalline rocks belonging to the Serbo-Macedonian massif, traditionally constituting, along with the Rhodope massif, the Hellenic hinterland. The northern part of the Athos peninsula is mainly composed of marbles, initially grouped into the Kerdyllion Unit and biotite gneisses and two-mica gneisses, grouped into the Vertiskos Unit, both units belonging to the Serbo-Macedonian massif, whereas their contact was initially considered as a normal contact. However, amphibolites and ultramafic rocks exist along with the rocks mentioned above, making the geology and relationship between the two units much more complicated.

This dissertation reports the results of a detailed mapping and structural analysis of the Serbo-Macedonian massif on the Athos Peninsula. It also includes a complementary study on crystallographic fabrics of mylonites at the contact between the Vertiskos and the Kerdyllion Units. In light of the structural analysis, a number of units are re-interpreted. More precisely, the following map units have been defined: marbles, amphibolite gneisses, biotite gneisses and two-mica gneisses. The marbles, amphibolite gneisses, and biotite gneisses have been grouped in the Kerdyllion Unit, whereas only the two-mica gneisses belong to the Vertiskos Unit. Anatexitic leucogneiss bodies have been found within the rocks of the Kerdyllion Unit, but not in the two-mica gneisses of the Vertiskos Unit, and can be correlated with either the Anatexites of the Kerdyllion Unit or the anatexites-granitic gneisses of the Ammouliani Unit. Ultramafic/mafic rocks exposed in the area are considered as parts of the Therma-Volvi-Gomati complex, belonging to a Mesozoic oceanic crust. Five deformation events D1 through D5 were extrapolated by the structural analysis and its interrelation with previous works, spanning from the pre-Mesozoic to the Late-Eocene. D1 and D2 are hardly seen in the area, due to their thourough overprinting by the dominant fabric that characterizes the rocks of the study area and which is attributed to a Late-Jurassic to Early Cretaceous syn-metamorphic D3 event of amphibolite facies. D3 is associated with isoclinal folding and intense shearing with an overall top-to-the-S sense of shear, which resulted in a mylonitic shear zone at the

contact between the Kerdyllion and Vertiskos Units, with the Vertiskos Unit sandwiched between the rocks of the Kerdyllion Unit and the development of a large-scale sheath fold geometry. This event dominated during the Alpine reworking of the Serbo-Macedonian massif in the study area. This Alpine reworking continues during Eocene times with an ENE-WSW compression D4 event, giving rise to asymmetric to inverted folds, co-axially refolding pre-existing fabrics and structures, whereas D5 describes a N-S compression and belongs to the late-Alpine orogenic processes. Additionally, based on the geological mapping carried out herein, it seems clear that the long-standing view of the contact between the Vertiskos and Kerdyllion Units being at the roof of the uppermost marbles of the Kerdyllion Unit cannot be further considered as a tectono-stratigraphic fact. In summary, our work strongly suggests that the overall structure and tectono-stratigraphy concerning the Vertiskos and Kerdyllion Units is much more complicated than the view provided by the previous geological maps.

Περίληψη

Η χερσόνησος του Άθω αποτελεί το νότιο-ανατολικό τμήμα της ευρύτερης χερσονήσου της Χαλκιδικής στην Κεντρική Μακεδονία, Ελλάδα. Αποτελείται κυρίως από κρυσταλλικά πετρώματα της Σερβο-Μακεδονικής μάζας, η οποία, μαζί με τη μάζα της Ροδόπης, συνιστούν την Ελληνική Ενδοχώρα. Το βόρειο τμήμα της χερσονήσου του Άθω αποτελείται κυρίως από μάρμαρα, τα οποία αρχικά τοποθετήθηκαν στην Ενότητα των Κερδυλλίων και βιοτιτικούς και διμαρμαρυγιακούς γνευσίους, οι οποίοι επίσης αρχικά θεωρήθηκαν τμήμα της Ενότητας του Βερτίσκου. Και οι δύο ενότητες ανήκουν στη Σέρβο-Μακεδονική μάζα, ενώ η επαφή τους αρχικά θεωρήθηκε ως κανονική. Παρόλα αυτά, αμφιβολίτες και υπερβασικά πετρώματα συνυπάρχουν με τα προαναφερθέντα πετρώματα, καθιστώντας τη γεωλογία της περιοχής και τη σχέση των δύο ενοτήτων πολύ πιο περίπλοκη.

Η παρούσα διδακτορική διατριβή παρουσιάζει τα αποτελέσματα μιας λεπτομερούς χαρτογράφησης και τεκτονικής ανάλυσης της Σέρβο-Μακεδονικής μάζας στη χερσόνησο του Άθω. Εμπεριέχει, επίσης, μια συμπληρωματική μελέτη του κρυσταλλογραφικού ιστού μυλονιτικών ζωνών στην επαφή των ενοτήτων του

Βερτίσκου και των Κερδυλλίων. Μέσω αυτής της μελέτης, κάποιες χαρτογραφικές μονάδες αναθεωρούνται και ερμηνεύονται εκ νέου. Πιο συγκεκριμένα, καθορίστηκαν οι ακόλουθες χαρτογραφικές μονάδες: μάρμαρα, αμφιβολιτικοί γνεύσιοι, βιοτιτικοί γνεύσιοι και διμαρμαρυγιακοί γνεύσιοι. Τα μάρμαρα, οι αμφιβολιτικοί γνεύσιοι και οι βιοτιτικοί γνεύσιοι αποτελούν μέρος της Ενότητας των Κερδυλλίων ενώ οι διμαρμαρυγιακοί γνεύσιοι ανήκουν στην Ενότητα του Βερτίσκου. Ανατηκτικά, λευκογνευσιακά σώματα βρέθηκαν εντός της Ενότητας των Κερδυλλίων, ενώ απουσιάζουν από την Ενότητα του Βερτίσκου, και μπορούν να συσχετιστούν είτε με τους Ανατηξίτες της Ενότητας Κερδυλλίων είτε με τους ανατηξίτες/γρανιτικούς γνευσίους της Ενότητας της Αμμουλιανής. Τα υπερβασικά/βασικά πετρώματα που εκτίθενται στην περιοχή μελέτης θεωρούνται μέρος του Θέρμα-Βόλβη-Γομάτι συμπλέγματος, το οποίο με τη σειρά του αποτελεί τμήμα ενός Μεσοζωικού ωκεάνιου φλοιού. Από την τεκτονική ανάλυση και τη συσχέτιση με προηγούμενες έρευνες, προέκυψαν πέντε παραμορφωτικά γεγονότα, D1 ως D5, , τα οποία χρονικά εκτείνονται από το προ-Μεσοζωικό ως και το Ανώτερο Ηώκαινο. Τα D1 και D2 τεκμηριώθηκαν μετά δυσκολίας, λόγω της εκτεταμένης επικάλυψης τους από τον κύριο παραμορφωτικό ιστό που χαρακτηρίζει τα πετρώματα της περιοχής μελέτης και αποδίδεται σε ένα συμμεταμορφικό D3 γεγονός, αμφιβολιτικής φάσης, κατά το Άνω Ιουρασικό-Κάτω Κρητιδικό. Το D3 γεγονός σχετίζεται με μια ισοκλινή πτύχωση και μια έντονη διάτμηση με κίνηση προς Ν, η οποία οδήγησε στη γένεση μιας μυλωνιτικής διατμητικής ζώνης στης επαφή των Ενοτήτων Βερτίσκου και Κερδυλλίων και την δημιουργία, παράλληλα, της γεωμετρίας μιας sheath μεγα-πτυχής. Αποτέλεσε το κυρίαρχο παραμορφωτικό γεγονός κατά τον Αλπικό ορογενετικό κύκλο. Αυτός ο Αλπικός ορογενετικός κύκλος συνεχίζεται στην περιοχή μελέτης με το D4 γενονός κατά το Ηώκαινο και σχετίζεται με μια συμπίεση ΑΒΑ-ΔΝΔ διεύθυνσης, δημιουργώντας ασύμμετρες ως ανεστραμμένες πτυχές, οι οποίες επανα-πτυχώνουν ομοαξονικά τους προϋπάρχοντες παραμορφωτικούς ιστούς και τις αντίστοιχες δομές. Το D5 γεγονός περιγράφει μια συμπίεση διεύθυνσης Β-Ν και ανήκει στις ύστερο-Αλπικές ορογενετικές διεργασίες. Επιπλέον, βασισμένοι στην παρούσα χαρτογράφηση και μελέτη γίνεται ξεκάθαρο ότι η προϋπάρχουσα άποψη της ύπαρξης της επαφής των Ενοτήτων Κερδυλλίων και Βερτίσκου στη οροφή του

ανώτερου ορίζοντα των μαρμάρων δεν μπορεί να θεωρείται πλέον δεδομένη, όσον αφορά την τεκτονο-στρωματογραφία της Σέρβο-Μακεδονικής μάζας. Συνοψίζοντας, η παρούσα μελέτη προτείνει μια πολύ πιο περίπλοκη συνολική δομή και τεκτονο-στρωματογραφική διάρθρωση για τη περιοχή, από αυτήν που υποδείκνυαν προηγούμενοι γεωλογικοί χάρτες.

References

Alsop G. & Holdsworth R., 2004. Shear zone folds: Records of flow perturbation or structural inheritance?. Geological Society, London, Special Publications. 224. 177-199. 10.1144/GSL.SP.2004.224.01.12.

Alsop, G.I., Holdsworth, R.E., 2004b. The geometry and topology of natural sheath folds: a new tool for structural analysis. Journal of Structural Geology 26, 1561e1589.

Alsop, G.I., Holdsworth, R.E., 2006. Sheath folds as discriminators of bulk strain type. Journal of Structural Geology 28, 1588e1606.

Bauer, C., Rubatto, D., Krenn, K., Proyer, A., Hoinkes, G., 2007. A zircon study from the Rhodope metamorphic complex, N-Greece: time record of a multistage evolution. Lithos 99, 207-228.

Berthé D., Choukroune P., Jegouzo P., 1979a. Orthogneiss, mylonite and non-coaxial deformation of granites: the example of the South Armoricain shear zone. J Struct Geol 1:31–42

Blenkinsop T.G., Treloar P.J., 1995. Geometry, classification and kinematics of S-C fabrics. J Struct Geol 17:397–408

Borsi, S., Ferrara, G., Mercier, J., 1965. Détermination de l'âge des séries métamorphiques du Massif Serbomacédonien au Nord-Est de Thessalonique (grèce) par les methodes Rb/Sr et K/Ar. Ann. Soc. Géol. Nord 84, 223–225.

Brun J.-P., and Sokoutis D., 2004. North Aegean extension: from the Rhodope core complex to Neogene basins, paper presented at 5th International Symposium of Eastern Mediterranean Geology, Thessaloniki, Greece. 49-52.

Brun, J.-P., Sokoutis, D., 2007. Kinematics of the Southern Rhodope Core Complex (NorthGreece). International Journal of Earth Sciences 96, 1079–1099.

Brunel M., 1980. Quartz fabrics in shear zone mylonites: evidence for a major imprint due to late strain increments. Tectonophysics 64:T33–T44

Burg, J.-P., Ivanov, Z., Ricou, L.-E., Dimor, D., Klain, L., 1990. Implications of shear-sense criteria for the tectonic evolution of the Central Rhodope massif, southern Bulgaria. Geology 18, 451–454.

Burg, J.P., Godfriaux, I., Ricou, L.E., 1995. Extension of the Mesozoic Rhodope thrust units in the Vertiskos-Kerdilion Massifs (northern Greece). Comptes Rendus de l' Académie des sciences, Paris 320, 889–896.

Burg, J.-P., Ricou, L.-E., Ivanov, Z., Godfriaux, I., Dimov, D., Klain, L., 1996. Syn-metamorphic nappe complex in the Rhodope Massif. Structure and kinematics. Terra Nova 8, 6–15.

Burg, J.-P., 2012. Rhodope: From Mesozoic convergence to Cenozoic extension. Review of petro-structural data in the geochronological frame, J. Virtual Explorer, 42(1), doi:10.3809/jvirtex.2011.00270.

Ceriani S., Mancktelow N. S., Pennacchioni G., 2003. Analogue modelling of the influence of shape and particle/matrix interface lubrication on the rotational behaviour of rigid particles in simple shear. J Struct Geol 25:2005–2021

Chatzidimitriadis, E., Kilias, A., Staikopoulos, G., 1985. Nouvi aspetti petrologici e tettonici del massiccio Serbomacedonne e delle regioni adiacenti, della Grecia del Nortd. Boll Soc Geol It 104 :515–526

Christofides, G., D'Amico, C., Del Moro, A., Eleftheriadis, G., Kyriakopoulos, C., 1990. Rb-Sr-geochronology and geochemical characters of the Sithonia plutonic complex (Greece). Eur J Mineral 2:79–87

Christofides, G., Koroneos, A., Pe-Piper, G., Katirtzoglou, K., Catzikirkou, A., 1999. Pre-Tertiary A-Type magmatism in the Serbo-macedonian massif (N. Greece): Kerkini granitic complex. Bulletin of the Geological Society, Greece 33, 131–48.

Christofides G., Koroneos A., Soldatos, T., Eleftheriadis G., Kilias A., 2001. Eocene Magmatism (Sithonia and Elatia plutons) in the Internal Hellenides and Implications for Eocene-Miocene-Geological Evolution of the Rhodope Massif (Northern Greece). Acta Vulcanologica. 13. 73-89.

Christofides, G., Koroneos, A., Liati, A., Kral, J., 2007. The A-type Kerkini granitic complex in North Greece: geochronology and geodynamic implications. Bull. Geol. Soc. Greece XXXX, 700–711.

Cornelius, N., 2008. UHP metamorphic rocks of the Eastern Rhodope Massif, NE Greece: new constraints from petrology, geochemistry and zircon ages. Dissertation, Universitat Mainz, 164 pp.

Dell'Angelo L. N., Tullis J., 1989. Fabric development in experimentally sheared quartzites. Tectonophysics 169:1–21

Del Moro A., Kyriakopoulos K., Pezzino A., Atzori P., Lo Giudice A., 1990. The metamorphic complex associated to the Kavala plutonites: An Rb-Sr geochronological, petrological and structural study, Geol. Rhodop., 2,

143-152.

Dennis A. J., Secor D. T., 1987. A model for the development of crenulations in shear zones with applications from the Southern Appalachian Piedmont. J Struct Geol 9:809–817

Dercourt, J., Ricou, L.E., Vrielynck, B., 1993. Atlas Tethys Palaeoenvironmental Maps. Gauthier-Villars, Paris.

DeWet, A.P., Miller, J.A., Bickle, M.J., Chapman, H.J., 1989. Geology and geochronology of the Arnea, Sithonia and Ouranoupolis intrusions, Chalkidiki peninsula, Northern Greece. Tectonophysics 161, 65–79.

Dimitriadis, S., 1974. Petrological study of the migmatitic gneisses and amphibolites of Rentina-Asprovalta-Stavros-Olympias: unpubl. Thesis, Univ. of Thessaloniki, 231pp.

Dimitriadis S., 1980. A possible palaeomargin evolution of the southern-most part of Serbo-Macedonian Massif: Abstr. Proc. 26th Int. Geol. Congr. 1, 335.

Dimitriadis S., Godelitsas A., 1991. Evidence for high pressure metamorphism in the Vertiskos group of the Serbo-macedonian Massif: the eclogite of Nea Roda, Chalkidiki. Bulletin of the Geological Society of Greece XXV/2:67–80

Dimitrievic, M. D., 1966. Der tektonische Bau des Serbo-Mazedonischen Massivs. Geotektonika, 5: 32—41, 1 Taf.;Moskau.

Dimitrievic, M. D., 1974. Sur l'äge du metamorphismeet des plissementsdans la masse serbo-macedonienne. Bull. VI Congr. Assoc. Geol. Carpato-Balkanique, 1 (3): 339—347, 1 Abb.; Warschau.

Dinter D. A., Macfarlane A., Hames W., Isachsen C., Bowring S., and Royden L., 1995. U-Pb and 40Ar/39Ar geochronology of the Symvolon granodiorite: Implications for the thermal and structural evolution of the Rhodope metamorphic complex, northeastern Greece, Tectonics, 14, 886–908, doi:10.1029/95TC00926.

Dinter D. A., and Royden L., 1993. Late Cenozoic extension in northeastern Greece: Strymon Valley detachment system and Rhodope metamorphic core complex, Geology, 21(1), 45-48. 10.1130/0091-7613(1993)021<0045:LCEING>2.3.CO;2

Dixon, J.E., Dimitriadis, S., 1984. Metamorphosed ophiolitic rocks from the Serbo-Macedonian Massif, near lake Volvi, North-east Greece. In: Dixon, J.E., Robertson, A.H.F. (Eds.), The Geological Evolution of the eastern Mediterranean. Geol. Soc. London Special Publ., vol.17, pp. 603–618.

Eleftheriadis, G., Frank, W., Petrakakis, K., 2001. 40Ar–39Ar dating and cooling history of the Pangeon granitoids, Rhodope Massif (Eastern Macedonia, Greece). Bulletin of the Geological Society of Greece 34 (3), 911–916.

Gebauer, D., Liati, A., 1997. Geochronological evidence for mesozoic rifting and oceanization followed by Eocene subduction in the Rhodope complex (Northern Greece). Terra Nova 9 (Suppl. 1), 10.

Hanmer S., 1984b. The potential use of planar and elliptical structures as indicators of strain regime and kinematics of tectonic flow. Geol Surv Can Pap 84:133–142

Harre W., F. Kockel, H. Kreuzer, H. Lenz, P. Müller, and H. W. Walther (1968), Über Rejuvenationen im Serbo-Mazedonischen Massiv (Deutung radiometrischer Altersbestimmungen). Paper presented at 23rd International Geological Congress, Prague. 223-236.

Heillbronner R., 2002. Analysis of bulk fabrics and microstructure variations using tessellations of autocorrelation functions. Comput Geosci 28:447-455

Heilbronner R., Barrett S., 2006. Evolution of c-axis pole figures and grain size during dynamic recrystallization: results from experimentally sheared quartzite. J Geophys Res 111:B10202

Heilbronner and Barrett, 2014. Image Analysis in earth Sciences. Springer, Berlin.

Hellman, P.L., Green, T. H., 1979. The role of sphene as an accessory phase in the high pressure partial melting of hydrous mafic compositions. Earth planet. Sci. Lett., 42: 191-201, California.

Himmerkus, F., Zachariadis, P., Reischmann, T., Kostopoulos, D.K., 2005. The mafic complexes of the Athos-Volvi-Zone—a suture zone between the Serbo-Macedonian Massif and the Rhodope Massif. Geophys Res Abstr 7:10240

Himmerkus, F., Reischmann, T., Kostopoulos, D.K., 2006. Late Proterozoic and Silurian basement units within the Serbo-Macedonian Massif, northern Greece: the significance of terrane accretion in the Hellenides. In: Robertson, A.H.F., Mountrakis, D. (Eds.), Tectonic Development of the Eastern Mediterranean Region. Geol. Soc. London Special Publ., vol. 260, pp. 35–50.

Himmerkus F., Reischmann T., Kostopoulos D.K., 2009a. Serbo-Macedonian revisited: a Silurian basement terrane from northern Gondwana in the internal Hellenides, Greece. Tectonophysics. doi:10.1016/j.tecto.2008.10.016

Himmerkus F., Zachariadis P., Reischmann T., Kostopoulos D., 2011. The basement of the Mount Athos peninsula, northern Greece: Insights from geochemistry and zircon ages, Int. J. Earth Sci. (Geol Rundsch), 101(6), 1467–1485, doi:10.1007/s00531-011-0644-4.

Hirth G, Tullis J., 1992. Dislocation creep regimes in quartz aggregates. J Struct Geol 14:145–159

Hooper R.J., Hatcher R.D., 1988. Mylonites from the Towaliga fault zone, central Georgia: products of heterogeneous non-coaxial deformation. Tectonophysics 152:1–17

Ivanov, Z., 1988. Aperçu général sur l'évolution géologique et structurale du massif des Rhodopes dans le cadre des Balkanides. Bulletin de la Société Géologique de France 4, 227-240.

Κασώλη-Φουρναράκη, Α., 1981. Συμβολή στην ορυκτολογική και πετρολογική μελέτη των αμφιβολιτικών πετρωμάτων της Σερβομακεδονικής μάζας. Διδ. Διατρ., 231 σελ., Θεσσαλονίκη.

Kassoli-Fournaraki, A., 1981. Contribution to the mineralogical and petrological study of amphibolitic rocks from the Serbo-macedonian massif. PhD thesis, Univ Thessaloniki, 231 pp (in Greek).

Kilias, A., Falalakis, G., Mountrakis, D., 1997. Alpine tectonometamorphic history of the Serbo-macedonian metamorphic rocks: implication for the tertiary unroofing of the Serbo-macedonian-Rhodope metamorphic complexes (Makedonia, Greece). ΟρυκτόςΠλούτος 105, 32–50.

Kilias, A.A., Mountrakis, D.M., 1998. Tertiary extension of the Rhodope massif associated with granite emplacement (Northern Greece). Acta Volcanologica 10 (2), 331–337.

Kilias, A., Falalakis, G., Mountrakis, D., 1999. Cretaceous-Tertiary structures and kinematics of the Serbomacedonian metamorphic rocks and their relation to the

exhumation of the Hellenic hinterland (Macedonia, Greece), Int. J. Earth. Sci., 88(3), 513–531. 10.1007/s005310050282.

Knipe R.J., Law R.D., 1987. The influence of crystallographic orientation and grain boundary migration on microstructural and textural development in a S-C mylonite. Tectonophysics 135: 155–169

Kober, L., 1928. Der Bau der Erde. Gebrüder Borntraeger, Berlin.

Kockel, F. & Walther, H. W. 1965: Die Strimonlinie als Grenzezwischen Serbo-Mazedoni-schem und Rila-Rhodope-Massiv in Ost-Mazedonien. — Geol. Jb., 83: 575—602, 7 Abb., 1 Tab., 1 Taf.; Hannover.

Kockel, F., Mollat, H., Walther, H.W., 1971. Geologie der Serbo-Mazedonischen Massivs und seines mesozoischen Rahmens (Nord griechenland).Geologisches Jahrbuch 89, 529–551.

Kockel, F., Mollat, H., Walther, H.W., 1977. Erlauterungenzur Geologischen Karte der Chalkidiki und angrenzender Gebiete 1:100000 (Nord-Griechenland). Bundesanstalt fur Geowisseschaften und Rohstoffe, Hannover, 119 pp.

Kostopoulos, D., Ioannidis, N. M., and Sklavounos, S. A., 2000. A new occurrence of ultrahigh-pressure metamorphism, central Macedonia, northern Greece: Evidence from graphitized diamonds? Int. Geol. Rev., 42(6), 545-554.10.1080/00206810009465098

Koukouvelas I., and Doutsos T., 1990. Tectonic stages along a traverse cross cutting the Rhodopian zone (Greece), Geol. Rundsch., 79(3), 753-776. 10.1007/BF01879213

Krenn K., Bauer C., Proyer A., Mposkos E., and Hoinkes G. 2008. Fluid entrapment and reequilibration during subduction and exhumation: A case study from the high-grade Nestos Shear Zone, central Rhodope, Greece, Lithos, 104, 33–53, doi:10.1016/j.lithos.2007.11.005.

Krenn, K., Bauer, C., Proyer, A., Klotzli, U., Hoinkes, G., 2010. Tectonometamorphic evolution of the Rhodope orogen. Tectonics 29, TC4001, doi: 10.1029/2009TC002513.

Krohe A., 1990. Local variations in quartz (c)-axis orientations in non-coaxial regimes and their significance for the mechanics of S-C fabrics. J Struct Geol 12:995–1004

Krohe A., and Mposkos E., 2002. Multiple generations of extensional detachments in the Rhodope Mountains (northern Greece): evidence of episodic exhumation of high-pressure rocks, in The timing and location of major ore deposits in an evolving orogen, edited by Blundell, D. J., Neubauer, F. and Von Quadt, A., pp. 151-178, Geological Society, Special Publication 204, London. 10.1144/GSL.SP.2002.204.01.10

Kronberg P., Meyer W., and Pilger A., 1970. Geologie der Rila- Rhodope-Masse zwischen Strimon und Nestos (Nordgriechenland), Beihefte Geologisches Jahrbuch, 88, 133-180.

Kydonakis, K., Moulas, E., Chatzitheodoridis, E., Brun, J.-P., Kostopoulos, D., 2015b. First report on Mesozoic eclogite-facies metamorphism preceding Barrovian overprint from the western Rhodope (Chalkidiki, northern Greece). Lithos 220–223, 147–163.

Law R.D., 1998. Oblique grain-shape fabrics in a mylonitic quartz vein. In: Snoke A, Tullis J, Todd VR (eds) Fault related rocks – a photographic atlas. Princeton University Press, New Jersey, pp 264–265

Law R.D., Knipe R.J., Dayan H. 1984. Strain path partitioning within thrust sheets: microstructural and petrofabric evidence from the Moine Thrust zone at Loch Eriboll, northwest Scotland. J Struct Geol 6:477–497

Liati A., Seidel E., 1996. Metamorphic evolution and geochemistry of kyanite eclogites in central Rhodope, N. Greece. Contrib. Mineral. Petrol. 123, 293307.

Liati A., Gebauer D., 1999. Constraining the prograde and retrograde P–T–t path of Eocene HP-rocks by SHRIMP dating of different zircon domains: inferred rates of heating, burial, cooling and exhumation for central Rhodope, northern Greece. Contrib Mineral Petrol 135:340–354.

Liati A., Gebauer D., 2001. Alpine UHP rocks in the Rhodope zone (N. Greece): evidence from exsolution textures in garnet-rich rocks. 6th International Eclogite Conference, Abstract Volume, 7677.

Liati A., Gebauer D., Wysoczanski R., 2002. U–Pb SHRIMP-dating of zircon domains from UHP mafic rocks in the Rhodope zone (N' Greece); evidence for Early Cretaceous crystallization and Late Cretaceous metamorphism. Chem Geol 184:281–300.

Liati A., 2005. Identification of repeated Alpine (ultra) high pressure metamorphic events by UPb SHRIMP geochronology and REE geochemistry of zircon: the Rhodope zone of northern Greece. Contrib. Mineral. Petrol. 150, 608630.

Liati A., Fanning, C. M., 2005. Eclogites and their country rock orthogneisses in East Rhodope representing Upper Permian gabbros and Upper Carboniferous granitoids: Geochronological constraints. Mitt Oesterr Mineral Ges 150:88

Liati A., Gebauer, D., Fanning, C. M., 2011. Geochronology of the Alpine UHP Rhodope Zone: A Review of Isotopic Ages and Constraints on the Geodynamic Evolution, Editor(s): Larissa F. Dobrzhinetskaya, Shah Wali Faryad, Simon Wallis, Simon Cuthbert, Ultrahigh-Pressure Metamorphism, Elsevier, 2011, Pages 295-324, ISBN 9780123851444

Liati A., Gebauer D., Fanning C. M., 2011. Geochronology of the Alpine UHP Rhodope Zone: a review of isotopic ages and constraints on the geodynamic evolution, in Ultrahigh- Pressure metamorphism: 25 years after the discovery of coesite and diamond, edited by Dobrzhinetskaya, L., Faryad, S. W., Wallis, S. and Cuthbert, S., pp. 295-324, Elsevier, Amsterdam.

Lips, A. L. W., White, S. H., Wijbrans, J. R., 2000. Middle-Late Alpine thermostatic evolution of the southern Rhodope Massif, Greece. Geodinamica Acta 13, 281–92.

Lister G.S., Snoke A.W., 1984. S-C Mylonites. J Struct Geol 6:617–638

Mancktelow N.S., Arbaret L., Pennacchioni G., 2002. Experimental observations on the effect of interface slip on rotation and stabilisation of rigid particles in simple shear and a comparison with natural mylonites. J Struct Geol 24:567–585

Marakis G., 1968. Geochronology studies of some granites from Macedonia. – Ann. Geol. Pays Hell., 21: 121-152, Athens.

Means W.D., 1981. The concept of steady – state foliation. Tectonophysics 78:179–199

Meyer W., Pilger A., Birk F., Jordan H., 1963. Zur Geologie des Gebietes zwischen Strymon und Nestos (Rhodopen- Massiv) in Griechisch-Makedonien, N. Jb. Geol. Paläont. Abh., 118(3), 272-280.

Meyer W., 1969. Die Faltenachsen im Rhodopen-Kristallin östlich des Strimon (Nordost-Griechenland), Geotekt. Forsch., 31, 86-96.

Mposkos E., 1989. High-pressure metamorphism in gneisses and pelitic schists in East Rhodope zone (N Greece). Mineral. Petrol. 41, 337-351.

Mposkos E., 1998. Cretaceous and tertiary tectonometamorphic events in Rhodope zone (Greece). Petrological and geochronological evidences. Bull Geol Soc Greece 32(3):59–67

Mposkos, E., Krohe, A., 2000. Petrological and structural evolution of continental high pressure (HP) metamorphic rocks in the Alpine Rhodope Domain (N. Greece). In:

Proceedings of the Third International Conference on the Geology of the Eastern Mediterranean, pp. 221–232.

Mposkos, E., Krohe, A., 2006. Pressuretemperaturedeformation paths of closely associated ultra-high-pressure (diamond-bearing) crustal and mantle rocks of the Kimi complex: implications for the tectonic history of the Rhodope Mountains, northern Greece. Can. J. Earth Sci. 43, 17551776.

Mposkos, E., Kostopoulos, D., 2001. Diamond, former coesite and supersilicic garnet in metasedimentary rocks from the Greek Rhodope: a new ultrahigh-pressure province established. Earth Planet. Sci. Lett. 192, 497506.

Panozzo Heillbronner R., Pauli C., 1993. Integrated spatial and orientation analysis of quartz c-axes by computer-aided microscopy. J Struct Geol 15(3-5):369-382.

Papadopoulos C., Kilias A., 1985. Altersbeziehungen zwischen Metamorphose und Deformation imzentralen Teil des Serbo-mazedonischen Massivs (Vertiskos Gebirge, Nord-Griechen-land). GeolRundsch 74 : 77–85

Papanikolaou D., Panagopoulos A., 1981. On the structural style of southern Rhodope, Greece, Geologica Balcanica, 11(3), 13-22.

Passchier C.W., 1991b. Geometric constraints on the development ofshear bands in rocks. Geol Mijnb 70:203–211

Passchier C.W., Simpson C., 1986. Porphyroclast systems as kinematic indicators. J Struct Geol 8:831–844

Passchier C. W., and Trouw R. A. J., 2005. Microtectonics. Springer, Berlin.

Piazolo S., Passchier C. W., 2002b. Experimental modelling of viscous inclusions in a circular high-strain rig: implications for the interpretation of shape fabrics and deformed enclaves. J Geophys Res 107, B10, 2242, ETG 11:1–15

Patras D., Kilias A., Chatzidimitriadis E., Mountrakis D., 1989. Study of the deformation phases of the Internal Hellenides in Northern Greece. Bull. Geol. Soc. Greece, 20 (1), 139-158.

Peytcheva, I., von Quadt, A., 1995. U–Pb zircon dating of metagranites from Byala Reka region in the East Rhodopes, Bulgaria. Geol Soc Greece Sp Publ., No. 4, 2:637–642

Plougarlis, A.P., Tranos, M.D., 2014. Geological map of Ammouliani Island (Northern Greece). Implications for the tectono-magmatic evolution of the Serbo-Macedonian Massif. Journal of Maps, 11, 4, 552-560, doi: 10.1080/17445647.2014.948504.

Ramsey, J. G., 1967. Foliding and Fracturing of Rocks. International Series in the Earth and Planetary Sciences. New York, 568 p.

Ramsey, J. G., Huber M. I., 1987. The Techniques of Modern Structural Geology, vol. 2, 700 pp., Academic, London.

Reischmann, T., Kostopoulos, D., 2002. Timing of UHPM in metasediments of the Rhodope Massif, N. Greece. Geochim. Cosmochim. Acta 66, A633.

Ricou, L.-E., Burg, J.-P., Godfriaux, I., Ivanov, Z., 1998. Rhodope and Vardar: the metamorphic and the olistostromic paired belts related to the Cretaceous subduction under Europe. Geodin. Acta 11, 285–309.

Sakellariou D., 1989. The geology of the Serbo-macedonian massif in the northeastern Chalkidiki peninsula, North Greece. Deformation and metamorphism. PhD thesis, Univ Mainz, 177 pp.

Sapountzis E., Kassoli-Fournaraki A., Christofides G., 1990. Amphibolites from the Serbo-Macedonian Massif (Northern Greece), Geologica Balcanica, 20(4), 3-17.

Sengör, A. M. C., Yilmaz, Y., Sungurlu, O., 1984. Tectonics of the Mediterranean Cimmerides: nature and evolution of the western termination of Paleo-Tethys. Geol Soc Lond Spec Publ 17 :77–112

Sidiropoulos, N., 1991. Lithology, geochemistry, tectonics and metamorphism of the Northwestern part of the Vertiskos Group, The area of the Disoro (Krousia) Mountain, North of Kilkis. PhD Thesis, School of Geology, Aristotle University of Thessaloniki, Greece, 592 p.

Soldatos, T., Koroneos, A., Christofides, G., Del Moro, A., 2001. Geochronology and origin of the Elatia plutonite (Hellenic Rhodope massif, N. Greece) constrained by new Sr isotopic data. Neues Jahrbuch für Mineralogie Abhandlungen 176, 179–209.

Sokoutis D., Brun J.-P., Van Den Driessche J., Pavlides S., 1993. A major Oligo-Miocene detachment in southern Rhodope controlling north Aegean extension, J. Geol. Soc. London, 150(2), 243-246. 10.1144/gsjgs.150.2.0243

Spiess R., Cesare B., Mazzoli C., Sassi R., Sassi F.P., 2010. The crystalline basement of the Adria microplate in the eastern Alps: a review of the palaeostructural evolution from the Neoproterozoic to the Cenozoic. Rend Fis Acc Lincei 21(Suppl 1):S31– S50. doi:10.1007/s12210-010-0100-6

Stais A., & Ferriere J., 1991. Nouvelles donnees sur la paleogeographie Mesozoique du domain Vardarien: Les bassins d' Almopias et de Peonias (Macedonie, Hellenides internes septentrionales). Bull. Geol. Soc. Greece. 25. 491-507.

Stampfli, G., Borel, G., 2002. A plate tectonic model for the Paleozoic and Mesozoic constrained by dynamic plate boundaries and restored synthetic oceanic isochrons. Earth Planet. Sci. Lett. 196 (1–2), 17–33.

Stipp M., Stunitz H., Heilbronner R., Schmid S. M., 2002. The eastern Tonale fault zone: a natural laboratory for crystal plastic deformation of quartz over a temperature range from 250°C to 700°C. J struct Geol 24:1861-1884

Stipp M, Tullis J., 2003. The recrystallized grain size piezometer for quartz. Geophys Res Lett 30:2088 doi:10.1029/2003GL018444

ten Grotenhuis S.M., Passchier C.W., Bons P.D., 2002. The influence of strain localisation on the rotation behaviour of rigid objects in experimental shear zones. J Struct Geol 24:485–501

Toyoshima T., 1998. Gabbro mylonite developed along a crustal-scale decollement. In: Snoke A, Tullis J, Todd VR (eds) Fault related rocks – a photographic atlas. Princeton University Press, New Jersey, pp 426–427

Tranos, M. D., Kilias, A. A., Mountrakis, M. D., 1993. Emplacement and deformation of the Sithonia granitoid pluton (Macedonia, Greece). Bulletin of Geological Society of Greece, 28(1), 195–211.

Tranos, M.D., Kilias, A.A., Mountrakis, D.M., 1999. Geometry and kinematics of the Tertiary post-metamorphic Circum Rhodope Belt Thrust System (CRBTS) North- ern Greece. Bulletin of Geological Society of Greece 33, 5–16.

Tranos, M.D., Kilias, A.A., Mountrakis, D.M., 1999. Geometry and kinematics of the Tertiary post-metamorphic Circum Rhodope Belt Thrust System (CRBTS) Northern Greece. Bulletin of Geological Society of Greece 33, 5–16.

Tranos, M.D., Lacombe, O., 2014. Late Cenozoic faulting in SW Bulgaria: Fault geometry, kinematics and driving stress regimes. Implications for late orogenic processes in the Hellenic hinterland. Journal of Geodynamics, 74, 32-55, doi: 10.1016/j.jog.2013.12.001.

Turpaud, P., Reischmann, T., 2010. Characterisation of igneous terranes by zircon dating: implications for UHP occurrences and suture identification in the Central Rhodope, northern Greece. Int J Earth Sci (Geol Rundsch). doi:10.1007/s00531-008-0409-x

Vernon R.H., Williams V.A., D'Arcy W.F., 1983. Grain-size reduction and foliation development in a deformed granitoid batholith. Tectonophysics 92:123–145

Vital, C., 1987. Mineralogical and Petrographical investigations of the area between Arnea and Megali Panagia Chalkidiki Peninsula (Northern Greece). – Diploma Thesis, ETH Zurich

von Braun E., 1993. The Rhodope question viewed from Eastern Greece, Z. dt. Geol. Ges., 144, 406-418.

von Raumer J.F., Stampfli G.M., 2008. The birth of the Rheic Ocean— Early Palaeozoic subsidence patterns and subsequent tectonic plate scenarios. Tectonophysics 461:9–20

Wawrzenitz N., 1997. Mikrostrukturell unterstutzte Datierung von Deformation sinkrementen in Myloniten: Dauer der Exhumierung und Aufdomung des metamorphen Kernkomplexes der Insel Thassos (Sud-Rhodope, Nordgriechenland). Dissertation, Universitat Erlangen, pp 192.

Wawrzenitz N., Baumann A., Nollau G., 1994. Miocene uplift of Mid-Crustal rocks in the Rhodope metamorphic core complex, caused by Late Alpine extension of previously thickened crust (Thassos island, Pangaeon complex, N. Greece). Δελτ. Ελλ. Γεωλ. Εταιρ. 30/1, 147-157.

Wawrzenitz N., Mposkos E., 1997. First evidence for Lower Cretaceous HP/HT metamorphism in the Eastern Rhodope, North Aegean Region, North-East Greece. Eur. J. Mineral. 9, 659-664.

Zervas S., 1980. Age determination by the Rb-Sr method of some pegmatites in the area of Lagada (Macedonia, Greece). Ann. Geol. Pays Hell., 30: 143-153, Athens.

Zervas S., 1984. Les isotopes Rb-Sr comee traceurs des phenomenes geologiques et petrologiques. Application de cette notion sur la Massif Serbo-Macedonien (Grece). Habil. Thesis, 181 p., Univ. of Athens.

Zwart H.J., 1960. The chronological succession of folding and metamorphism in the central Pyrenees. Geol Rdsch 50:203–218

Zwart H.J, 1962. On the determination of polymetamorphic mineral associations, and its application to the Bosost area (central Pyrenees). Geol Rdsch 52:38–65

SCANNED IMAGES OF THIN SECTIONS WITH PARALLEL POLARIZERS AND UNDER CIRCULAR POLARIZATION WITH THE CIP SITES INDICATED

A39

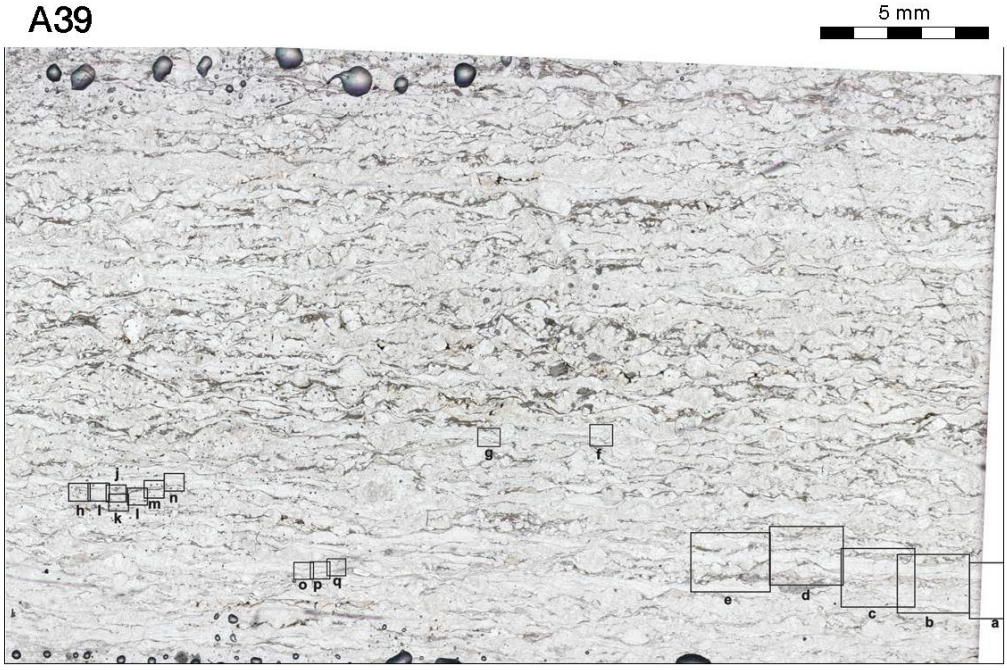

A39

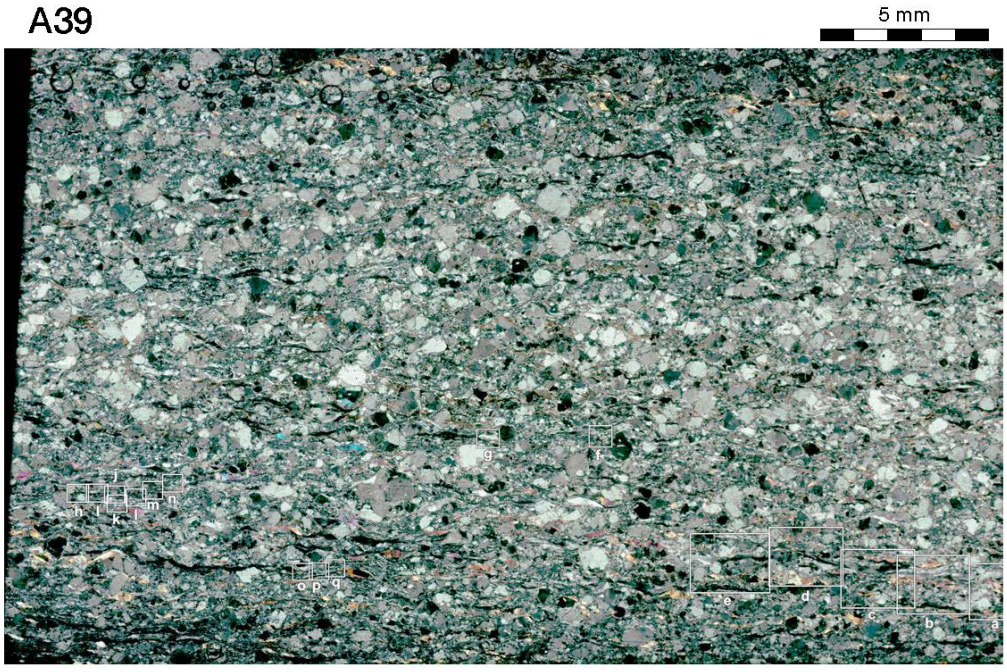

A40

5 mm

A40

5 mm

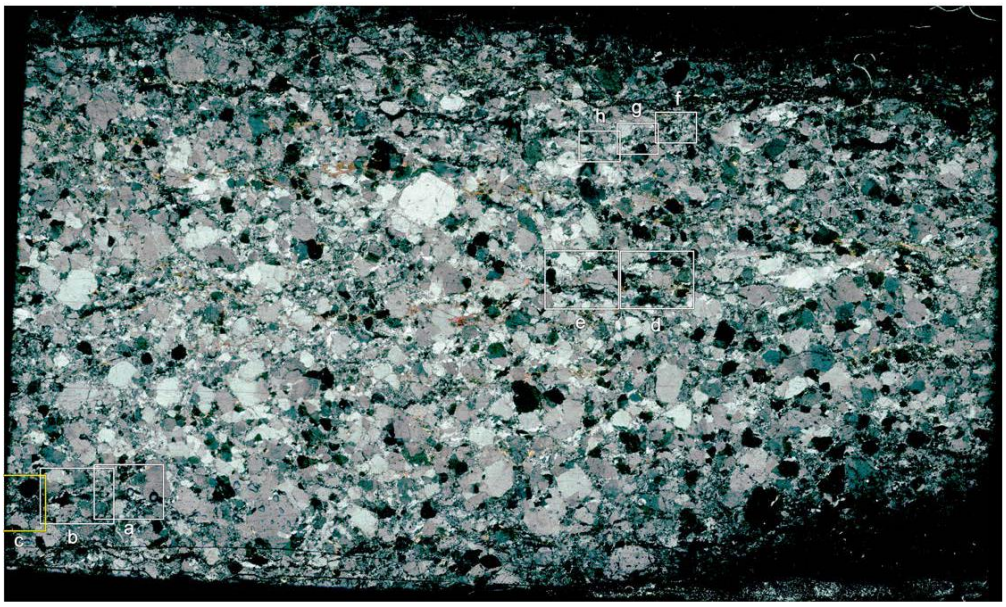

A43

5 mm

A43

5 mm

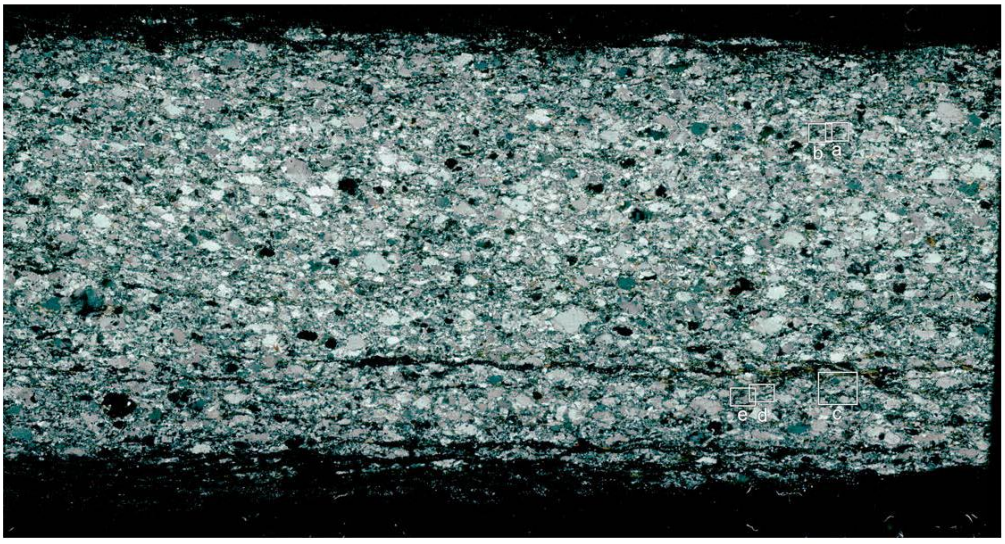

A44

5 mm

A44

5 mm

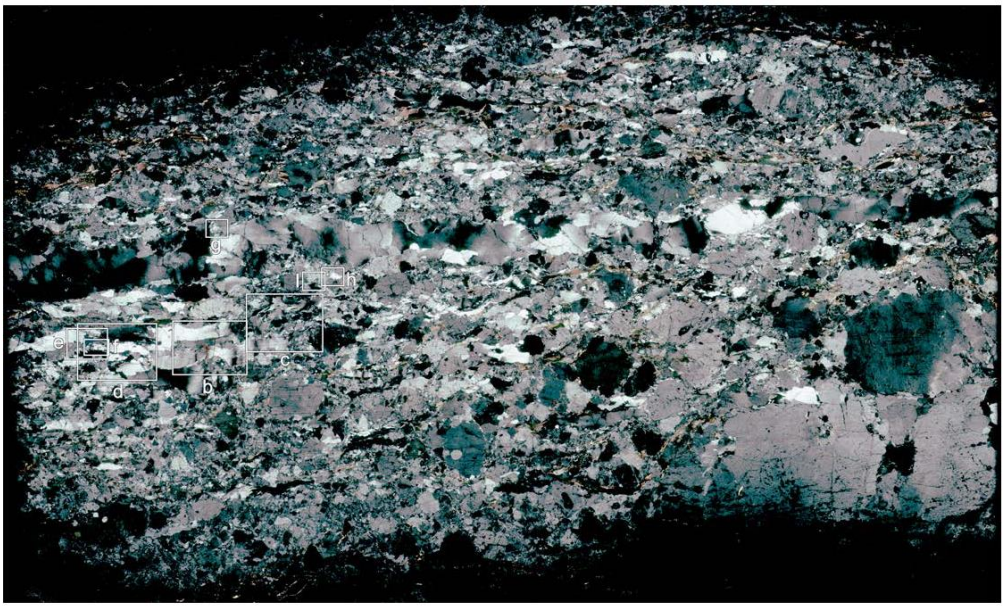

A45

A45

A46

5 mm

A46

5 mm

A47

5 mm

A47

5 mm

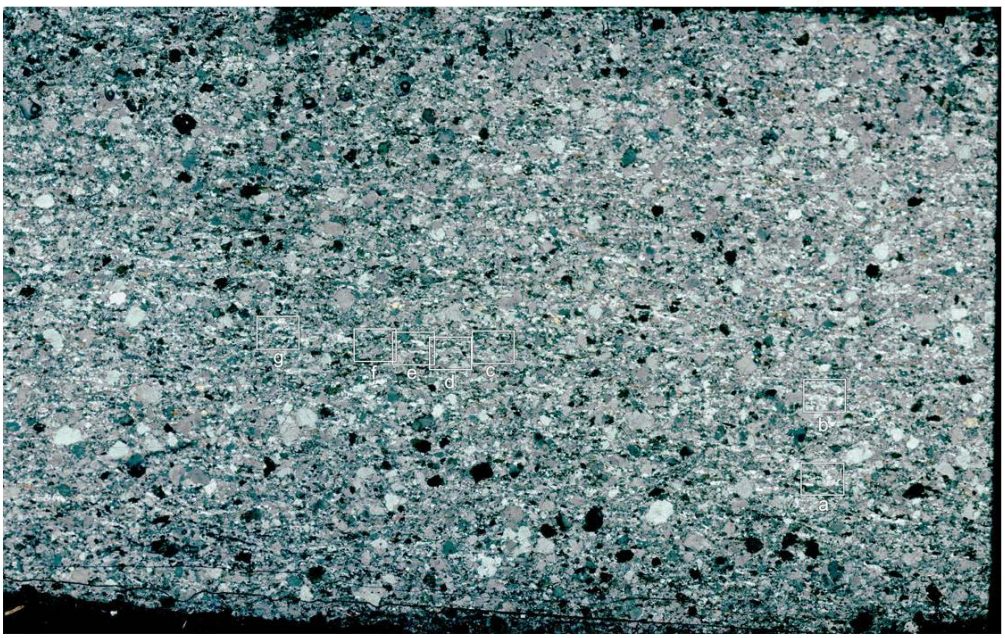

A48

5 mm

A48

5 mm

INITIAL QTZ-MAPS PRODUCED FOR THE ACF ANALYSIS WITH THE CIP SITES INDICATED

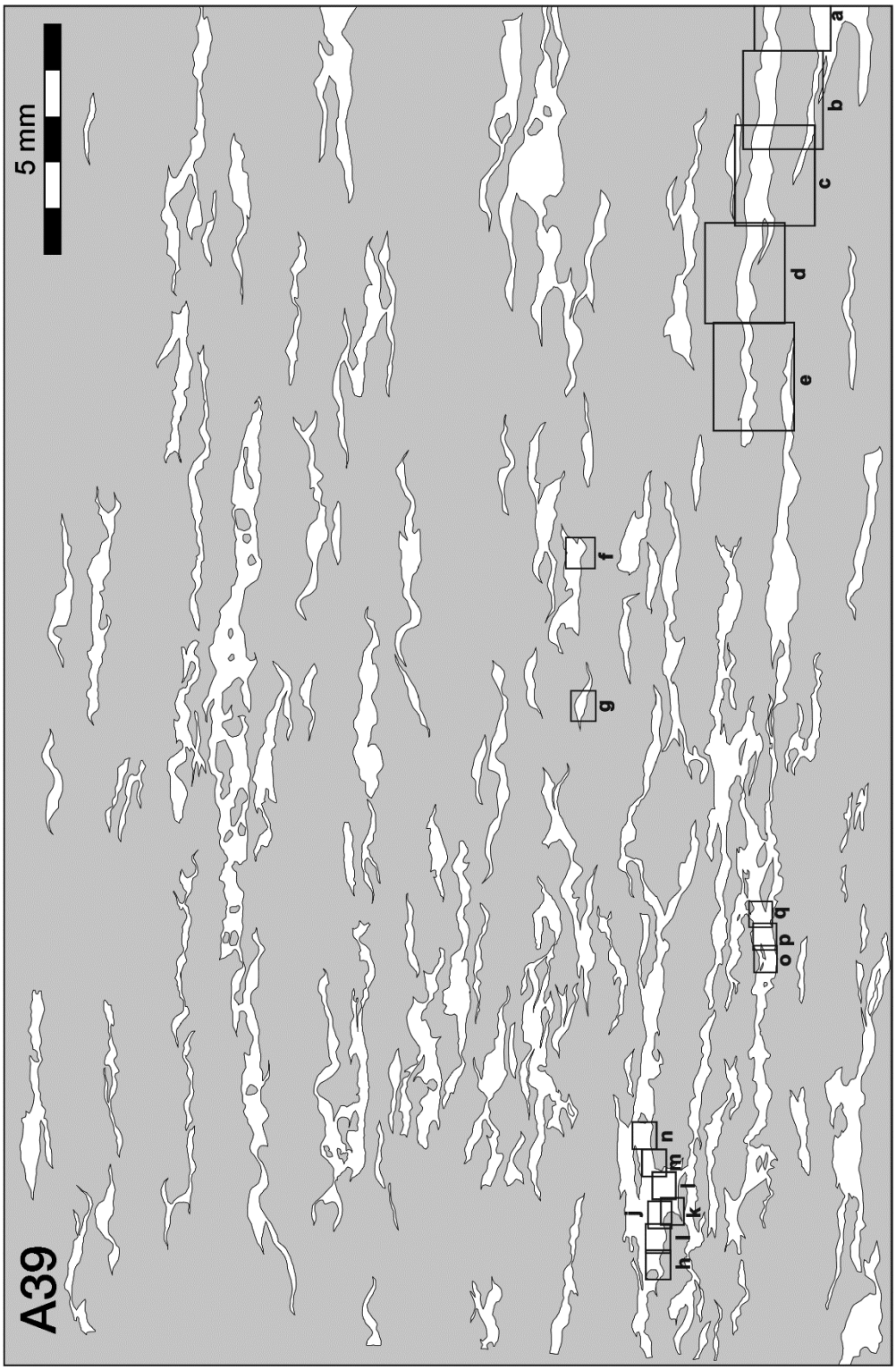

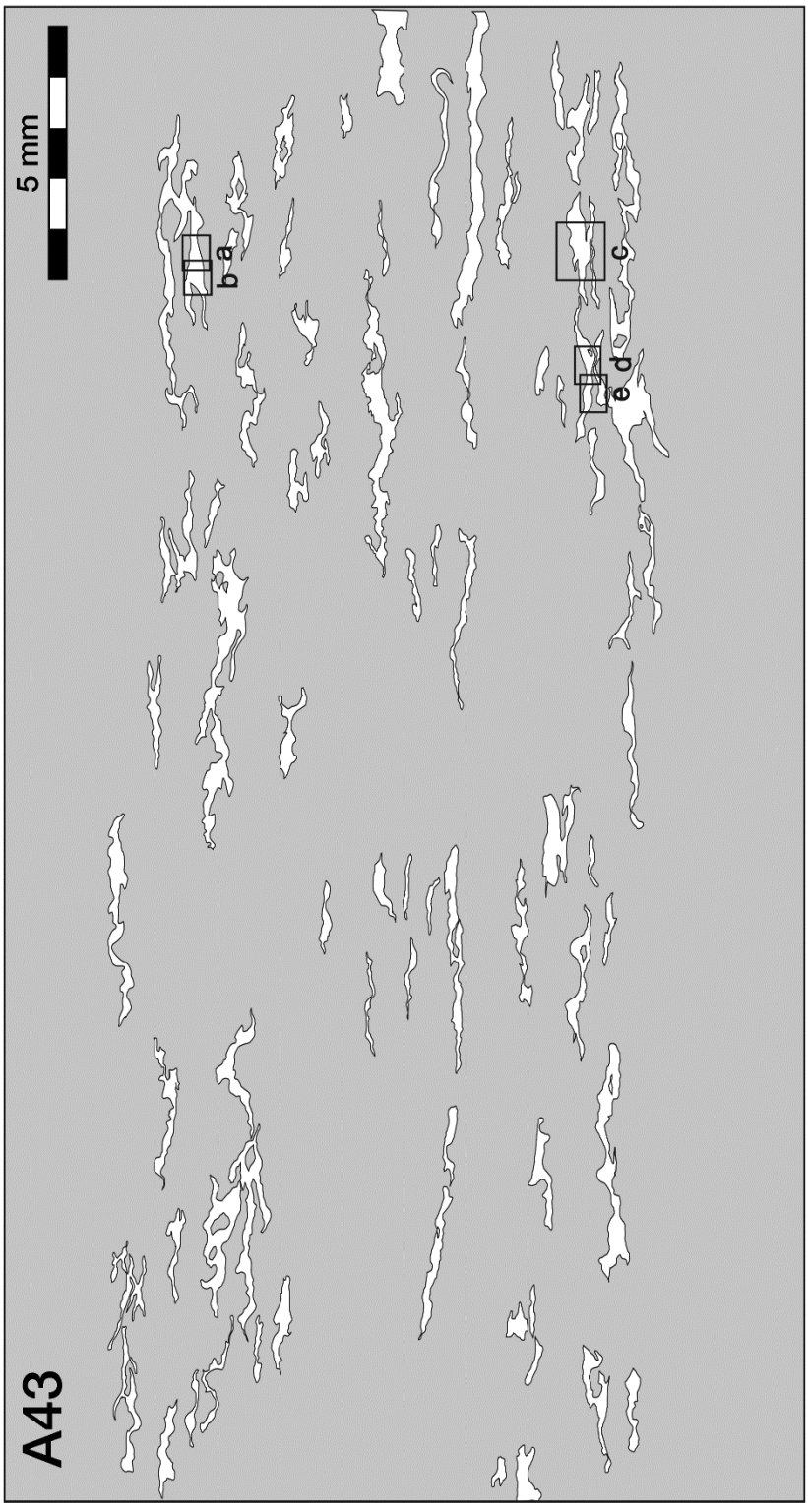

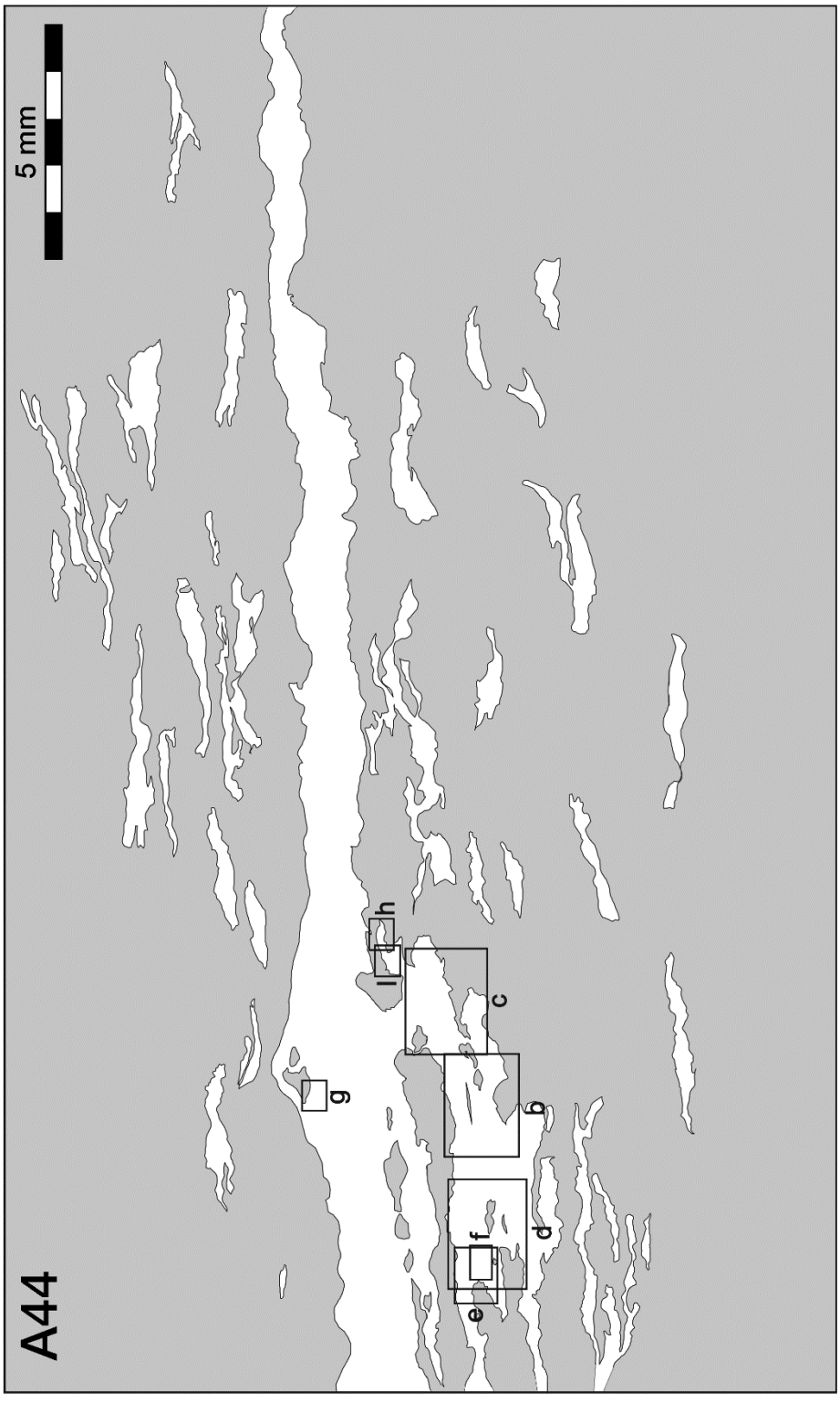

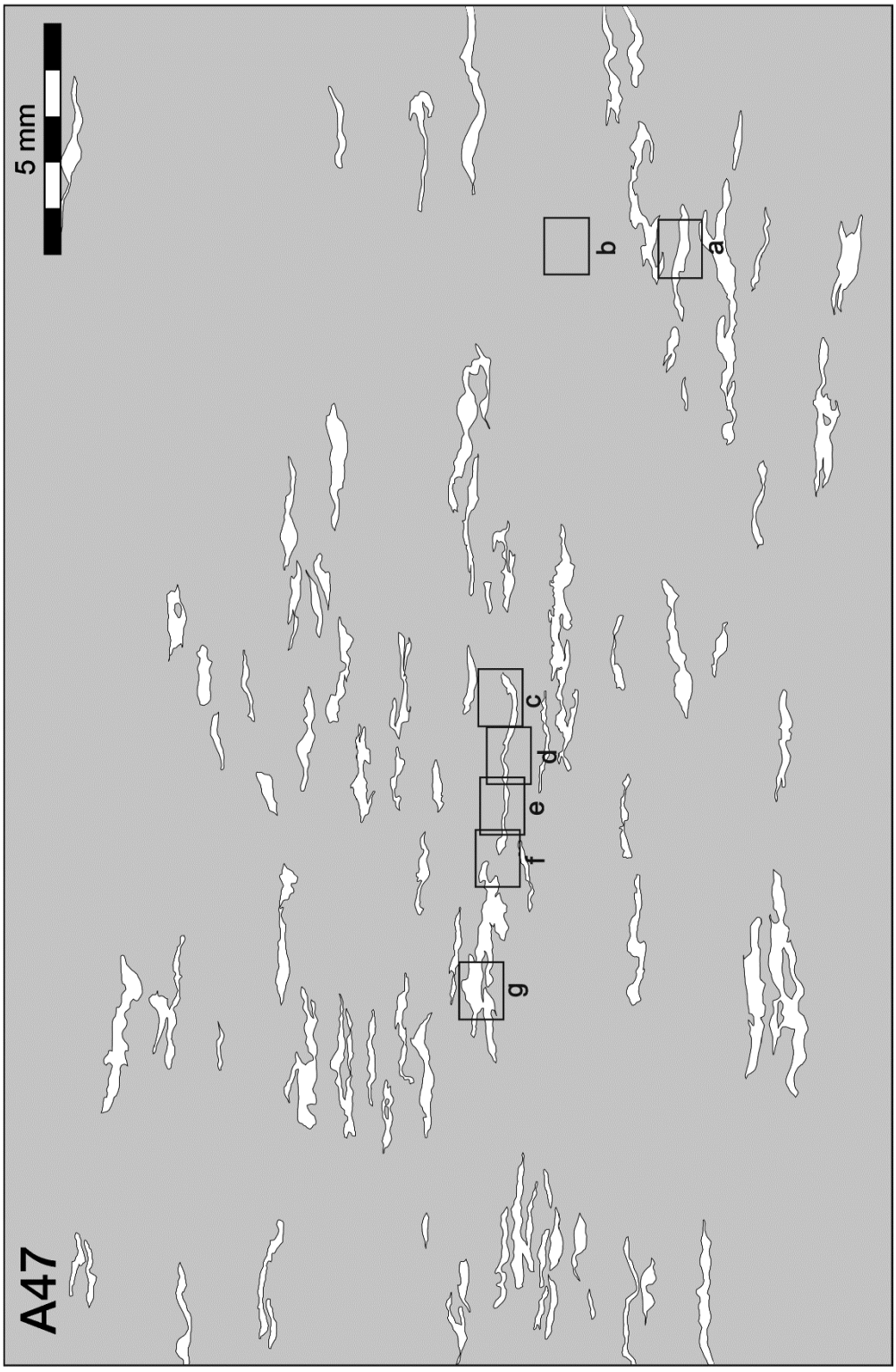

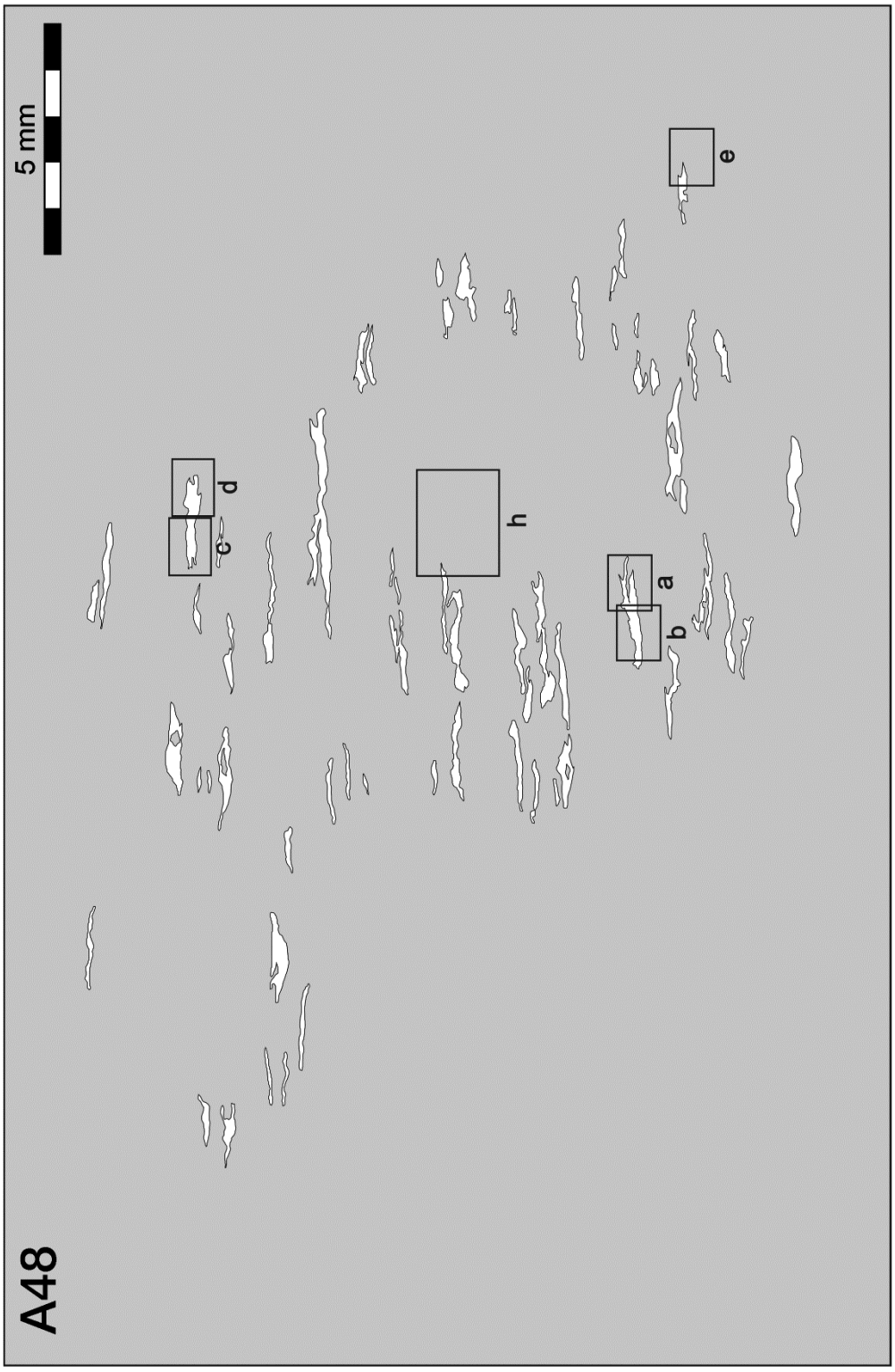

CIRPOL, C-AXIS ORIENTATION IMAGE AND RESPECTIVE C-AXIS POLE FIGURE CALCULATED WITH CIP ANALYSIS FOR EACH SAMPLE AND CIP SITE

A39

A39_a_2.5x

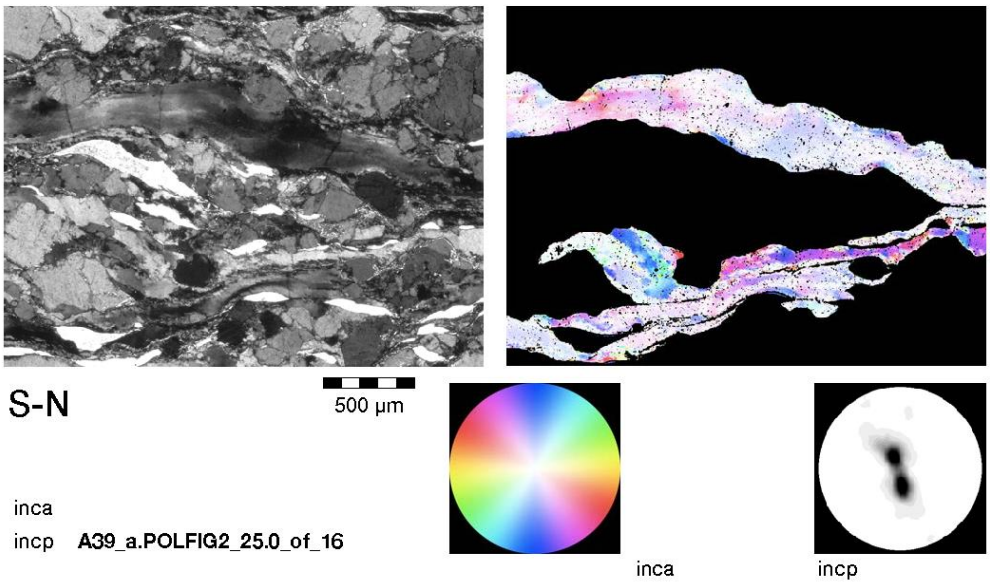

A39_b_2.5x

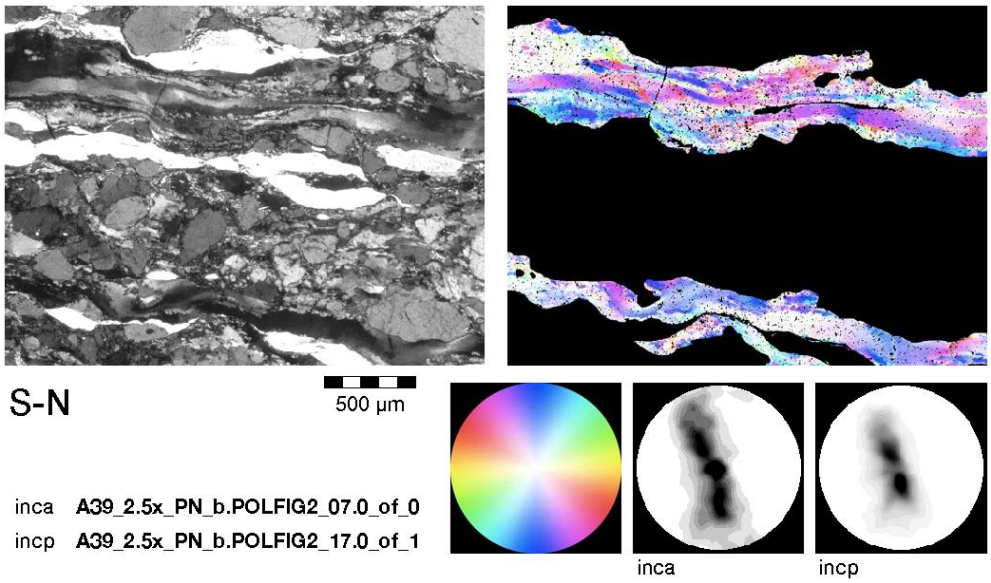

inca **A39_2.5x_PN_b.POLFIG2_07.0_of_0**
incp **A39_2.5x_PN_b.POLFIG2_17.0_of_1**

A39_c_2.5x

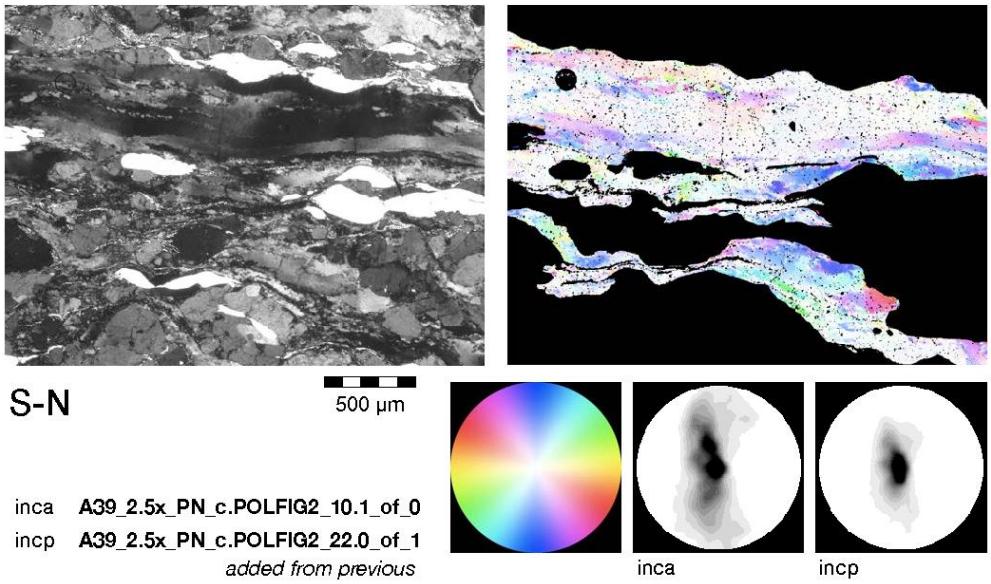

inca **A39_2.5x_PN_c.POLFIG2_10.1_of_0**
incp **A39_2.5x_PN_c.POLFIG2_22.0_of_1**
added from previous

A39_d_2.5x

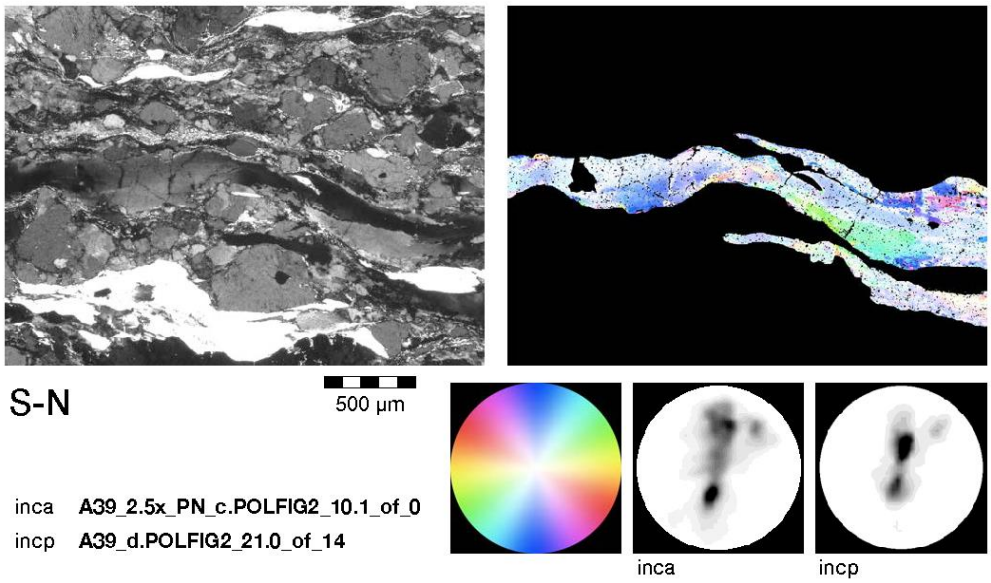

inca A39_2.5x_PN_c.POLFIG2_10.1_of_0
incp A39_d.POLFIG2_21.0_of_14

A39_e_2.5x

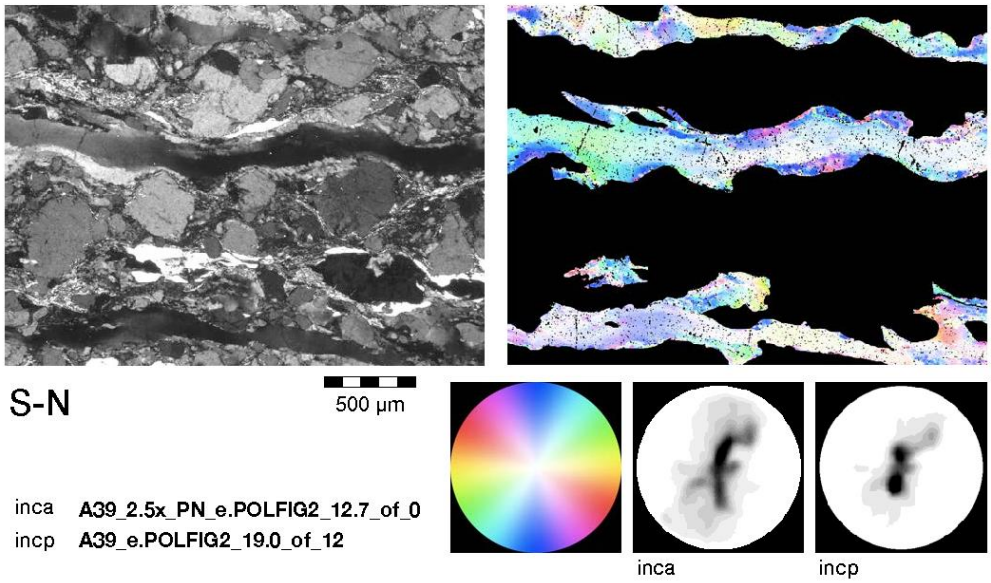

inca A39_2.5x_PN_e.POLFIG2_12.7_of_0
incp A39_e.POLFIG2_19.0_of_12

A39_f_10x

in fig

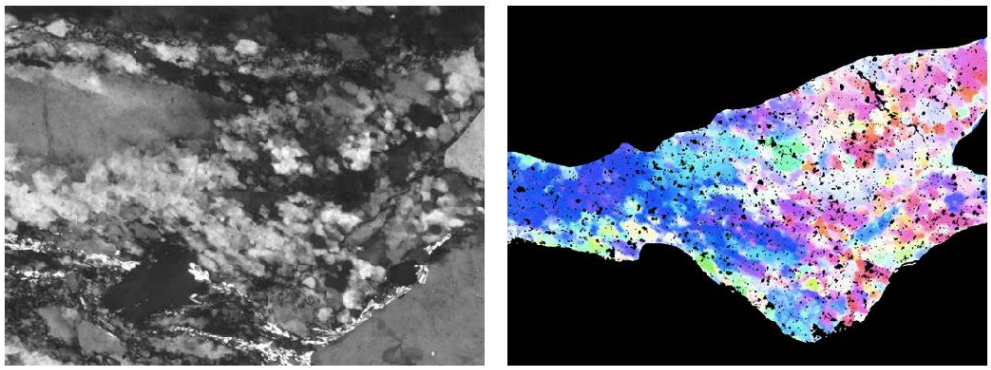

S-N

200 µm

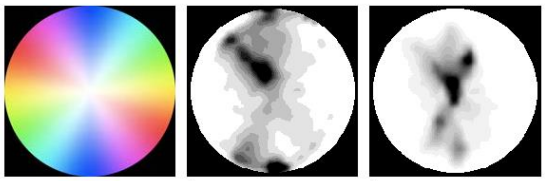

inca

incp

inca A39_10x_PN_f.POLFIG2_08.0_of_05
incp A39_10x_PN_f.POLFIG2_14.4_of_10

A39_g_10x

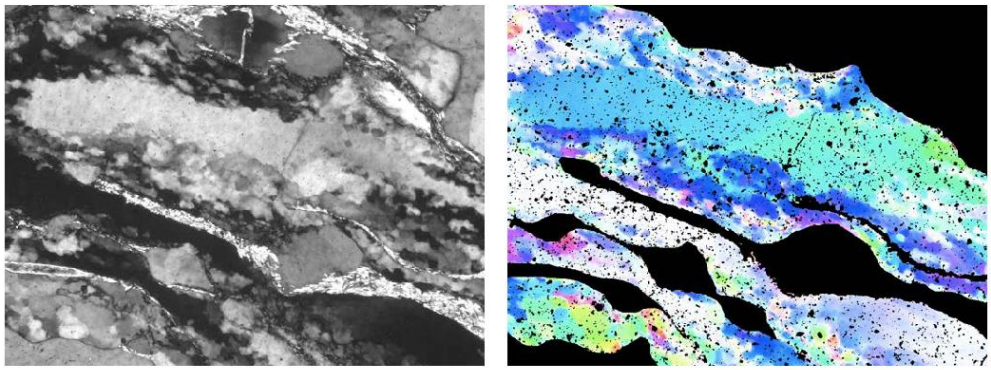

S-N

200 µm

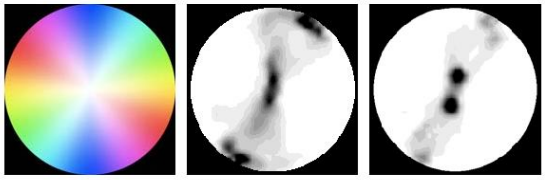

inca

incp

inca A39_10x_PN_g.POLFIG2_11.2_of_08
incp A39_g.POLFIG2_21.0_of_14

A39_h_10x

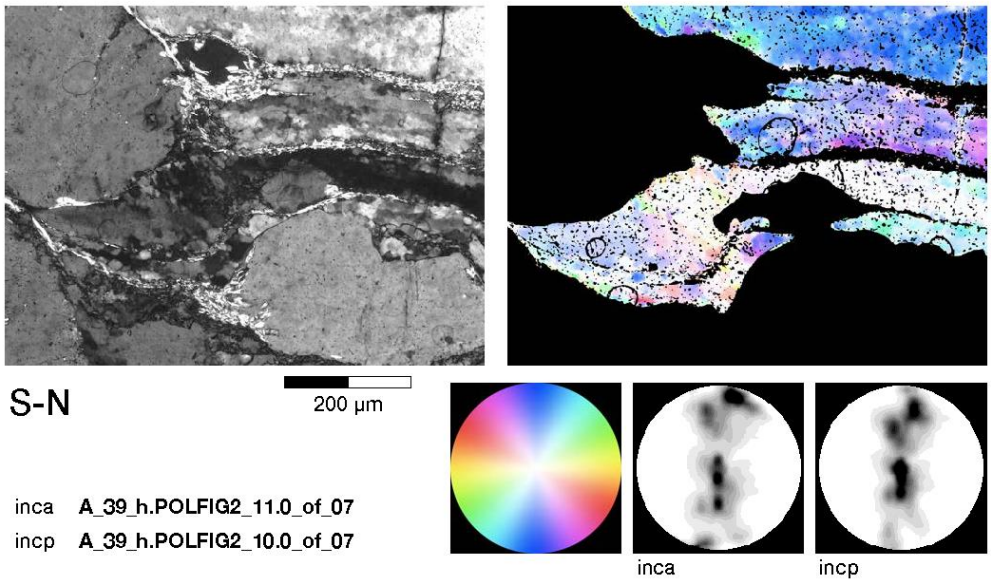

inca A_39_h.POLFIG2_11.0_of_07
incp A_39_h.POLFIG2_10.0_of_07

A39_i_10x

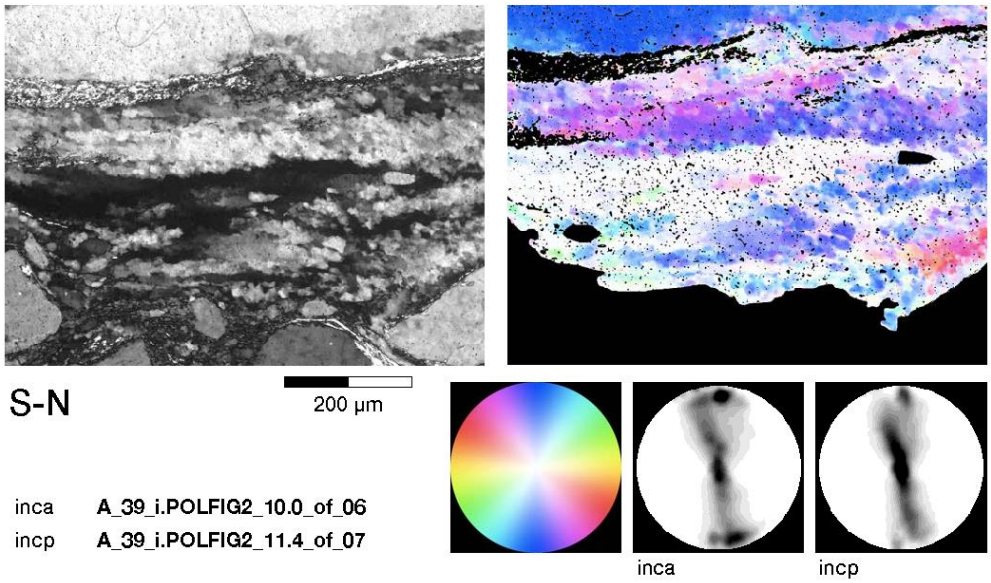

inca A_39_i.POLFIG2_10.0_of_06
incp A_39_i.POLFIG2_11.4_of_07

A39_j_10x

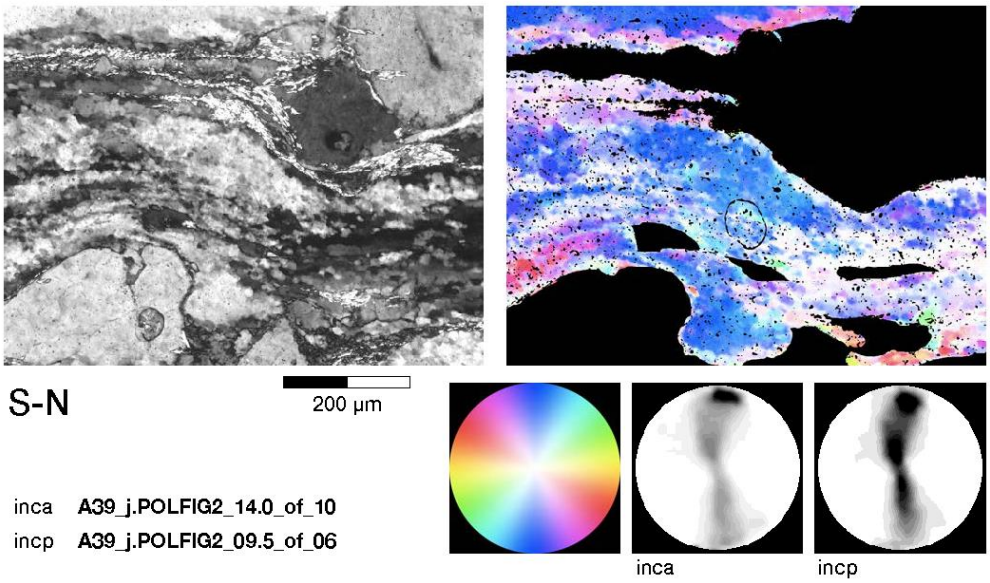

inca **A39_j.POLFIG2_14.0_of_10**
incp **A39_j.POLFIG2_09.5_of_06**

A39_k_10x

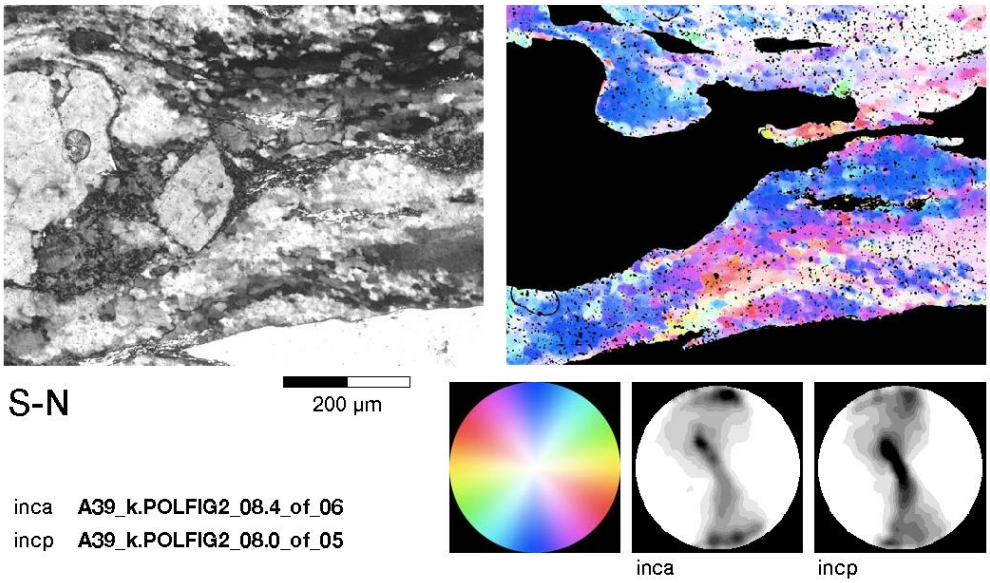

inca **A39_k.POLFIG2_08.4_of_06**
incp **A39_k.POLFIG2_08.0_of_05**

A39_l_10x

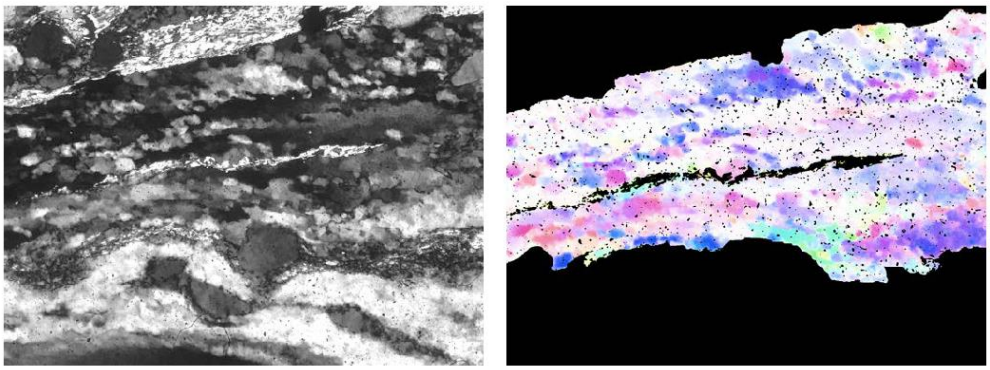

S-N

200 µm

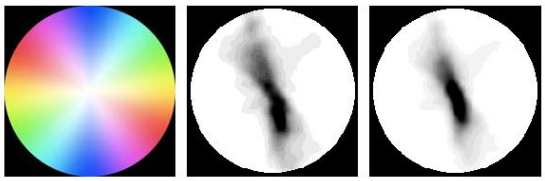

inca

incp

inca A39_l.POLFIG2_12.0_of_08

incp A39_l.POLFIG2_18.0_of_12

A39_m_10x

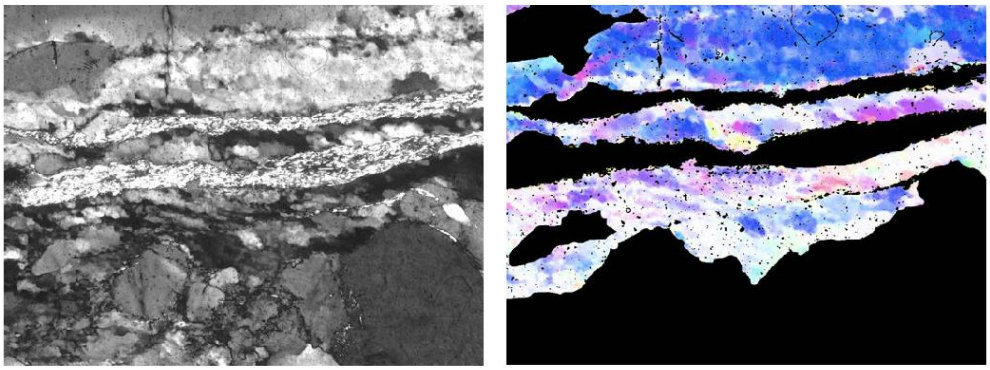

S-N

200 µm

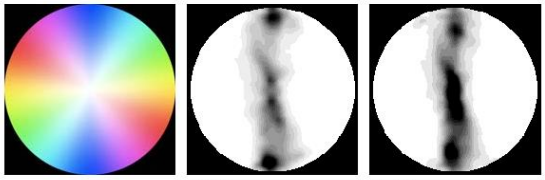

inca

incp

inca A39_m.POLFIG2_11.8_of_08

incp A39_m.POLFIG2_10.4_of_06

A39_n_10x

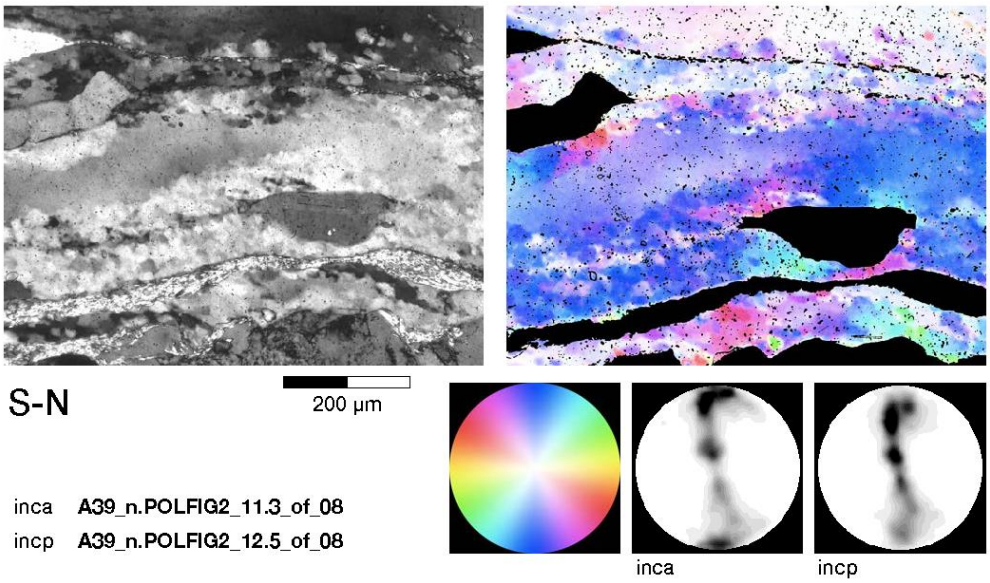

inca A39_n.POLFIG2_11.3_of_08
incp A39_n.POLFIG2_12.5_of_08

A39_o_10x

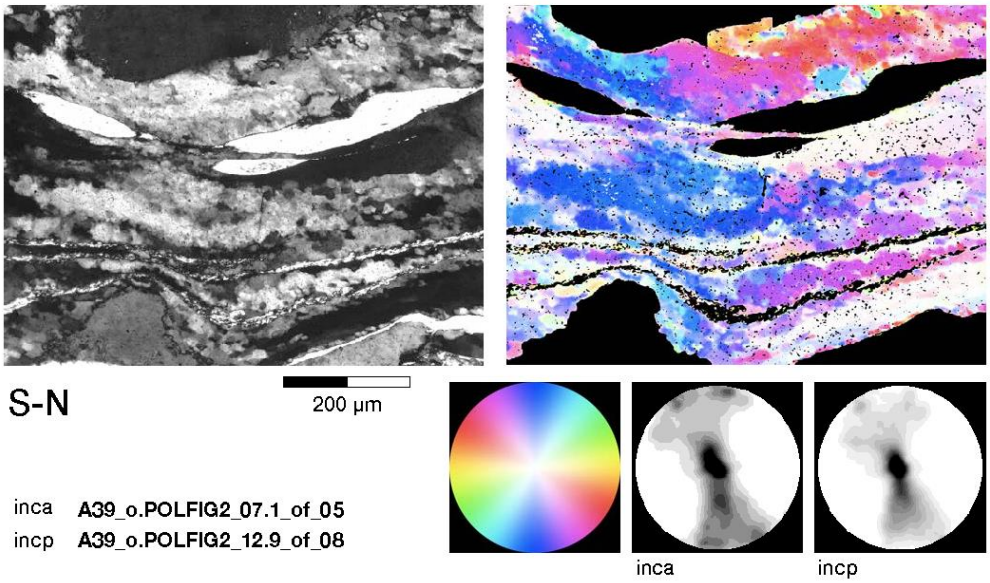

inca A39_o.POLFIG2_07.1_of_05
incp A39_o.POLFIG2_12.9_of_08

A39_p_10x

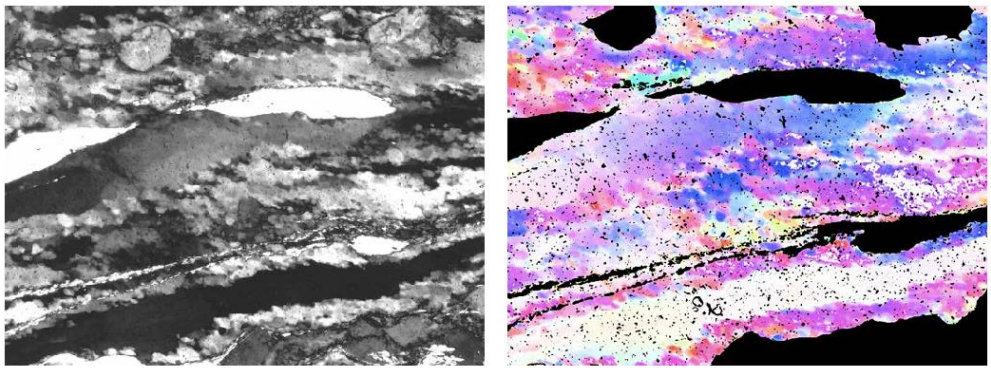

S-N

200 μm

inca A39_p.POLFIG2_09.6_of_06
incp A39_p.POLFIG2_12.9_of_08

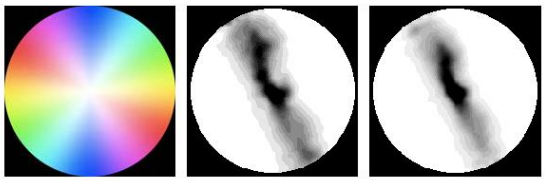

inca incp

A39_q_10x

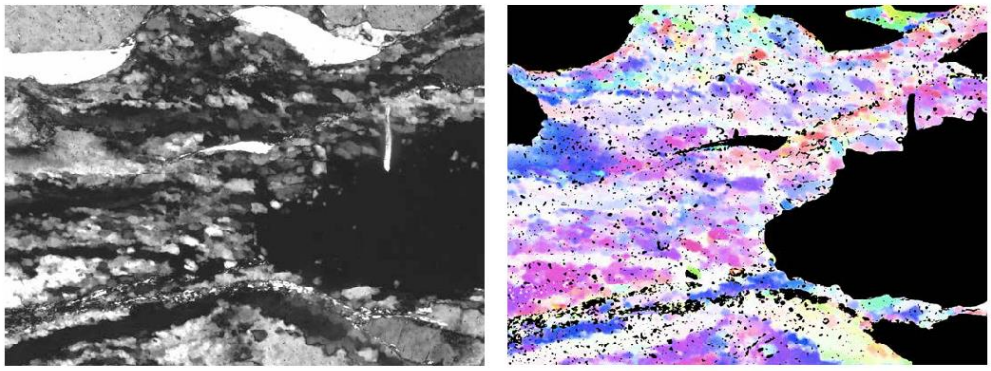

S-N

200 μm

inca A39_q.POLFIG2_08.8_of_06
incp A39_q.POLFIG2_19.5_of_12

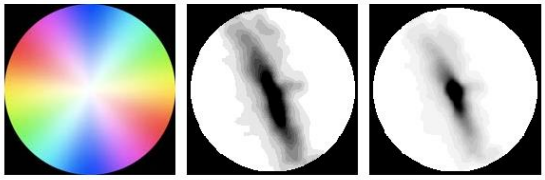

inca incp

A40

A40_2.5X_a

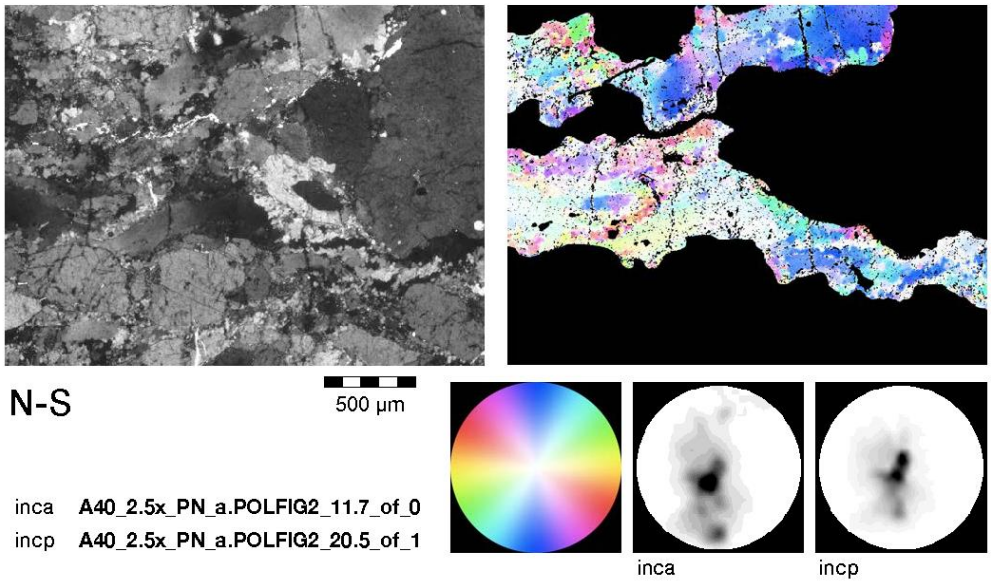

A40_2.5X_b

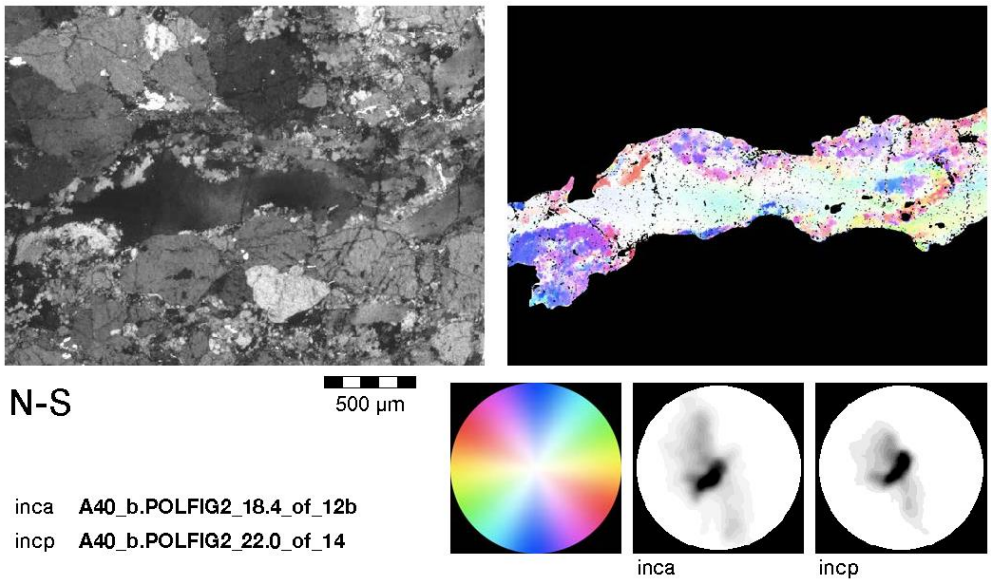

inca **A40_b.POLFIG2_18.4_of_12b**
incp **A40_b.POLFIG2_22.0_of_14**

A40_2.5X_c

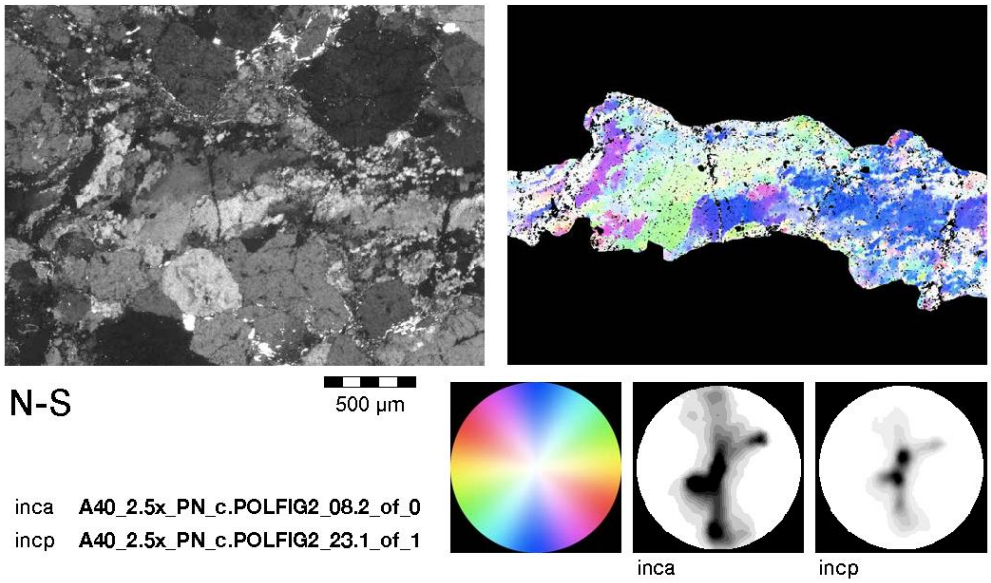

inca **A40_2.5x_PN_c.POLFIG2_08.2_of_0**
incp **A40_2.5x_PN_c.POLFIG2_23.1_of_1**

A40_2.5X_d

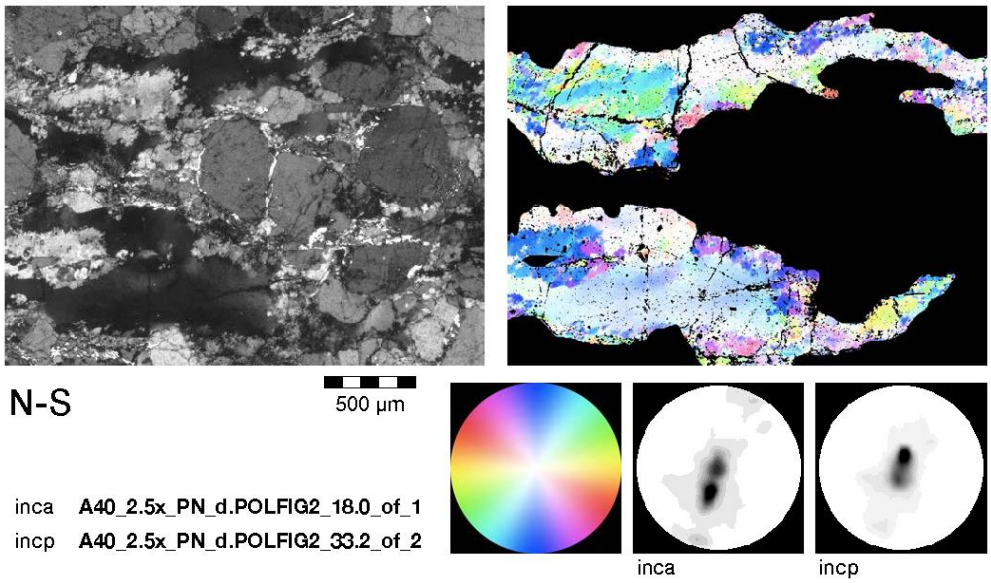

inca **A40_2.5x_PN_d.POLFIG2_18.0_of_1**
incp **A40_2.5x_PN_d.POLFIG2_33.2_of_2**

A40_2.5X_e

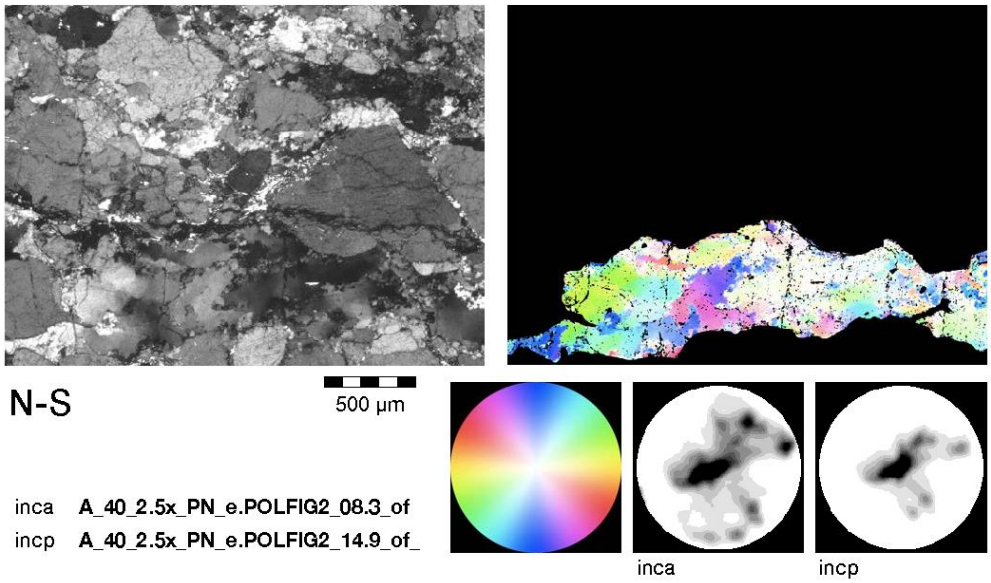

inca **A_40_2.5x_PN_e.POLFIG2_08.3_of**
incp **A_40_2.5x_PN_e.POLFIG2_14.9_of_**

A40_5X_f

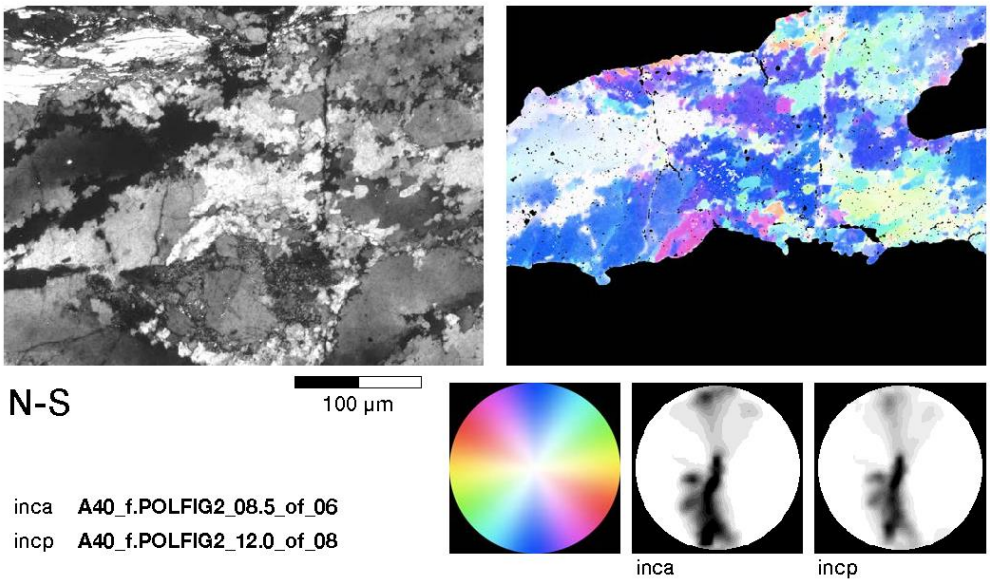

inca **A40_f.POLFIG2_08.5_of_06**
incp **A40_f.POLFIG2_12.0_of_08**

A40_5X_g

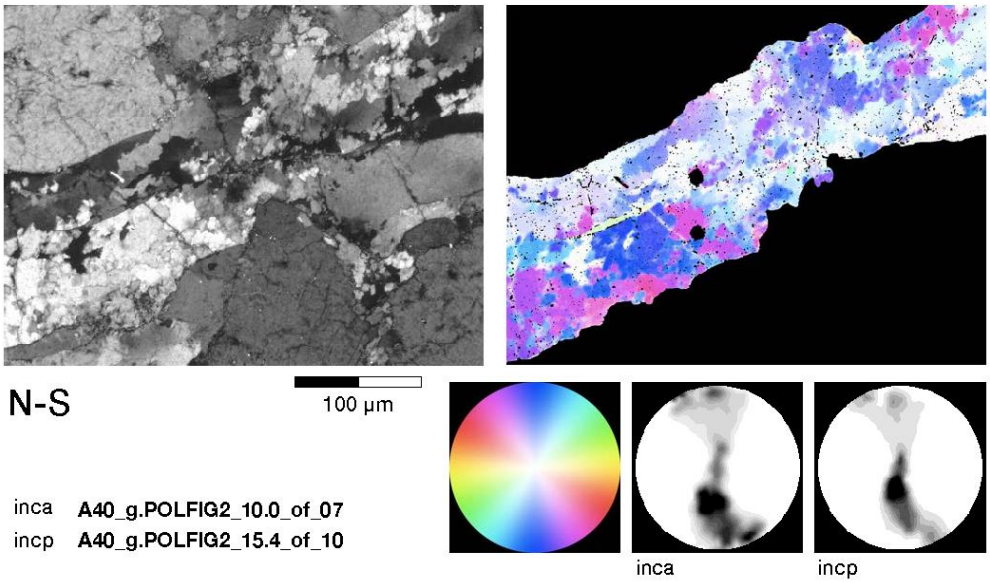

inca **A40_g.POLFIG2_10.0_of_07**
incp **A40_g.POLFIG2_15.4_of_10**

A40_5X_h

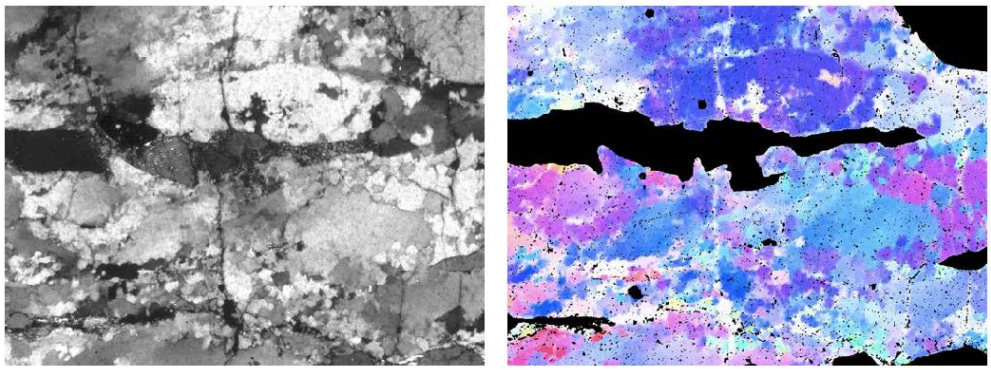

N-S

100 μm

inca A40_h.POLFIG2_12.7_of_08
incp A40_h.POLFIG2_12.4_of_08

inca incp

A43

A43_10x_a

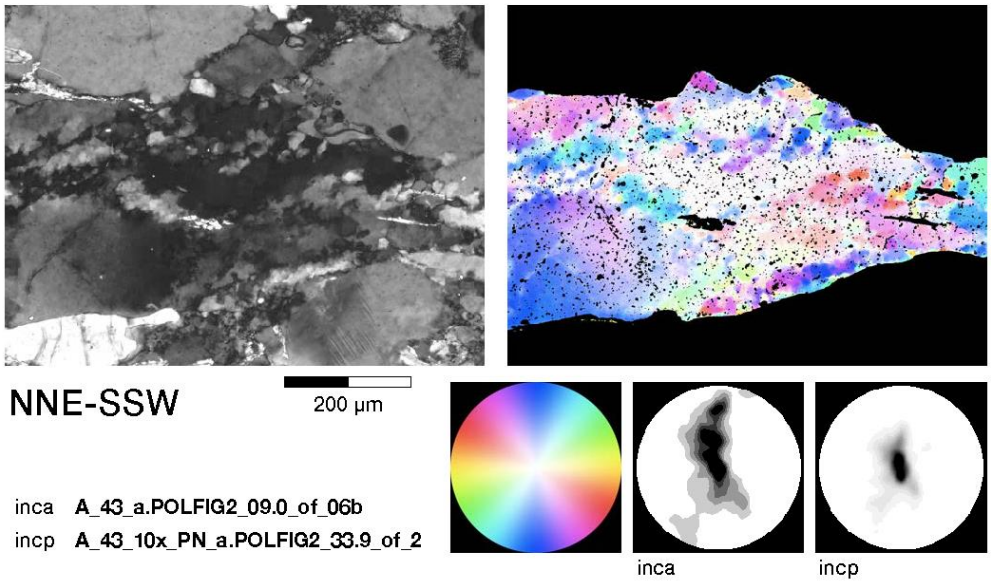

A43_10x_b

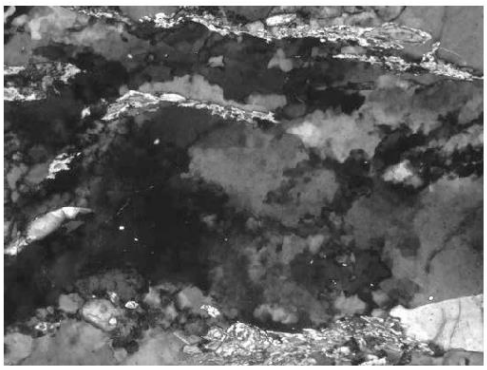

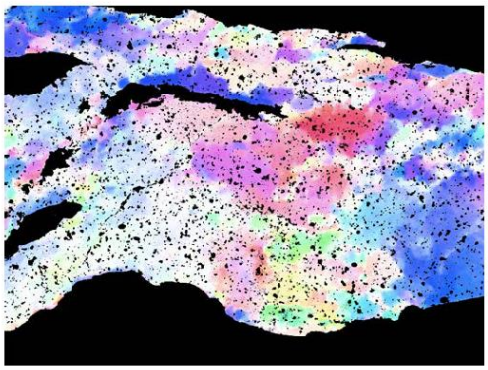

NNE-SSW

200 µm

inca A43_10x_PN_b.POLFIG2_09.8_of_06
incp A43_10x_PN_b.POLFIG2_28.4_of_19

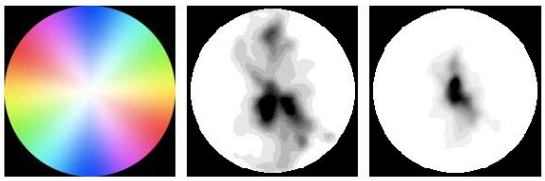

inca incp

A43_5x_c

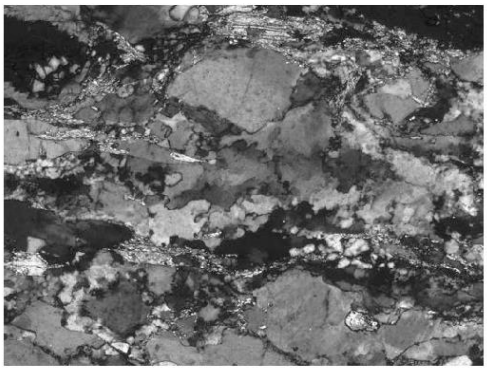

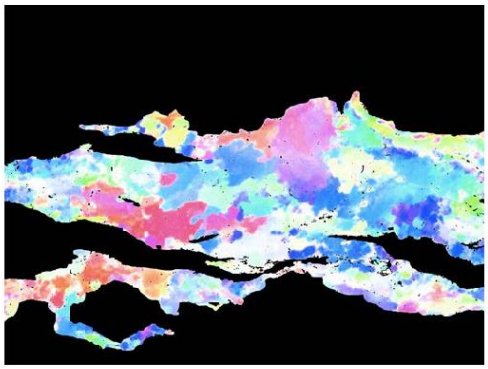

NNE-SSW

100 µm

inca A43_c.POLFIG2_06.5_of_04
incp A43_c.POLFIG2_12.7_of_08

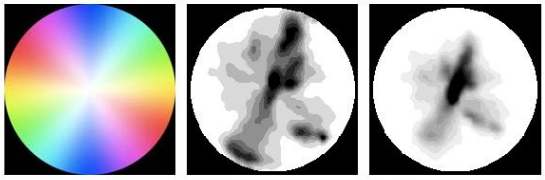

inca incp

A43_10x_d

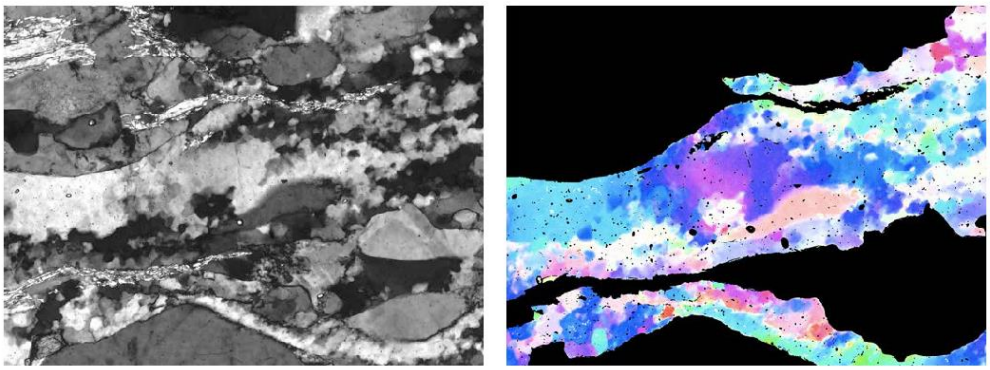

NNE-SSW

200 µm

inca A43_d.POLFIG2_17.7_of_12
incp A43_d.POLFIG2_11.9_of_08

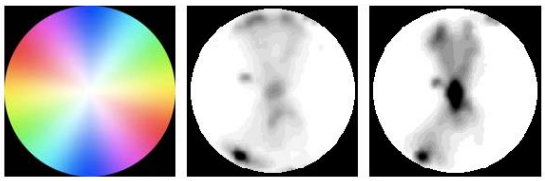

inca incp

A43_10x_e

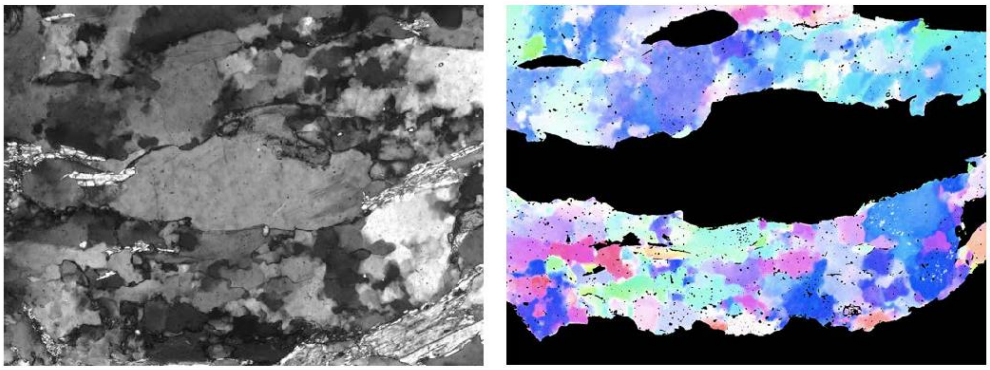

NNE-SSW

200 µm

inca A43_e.POLFIG2_09.0_of_06
incp A43_e.POLFIG2_15.5_of_10

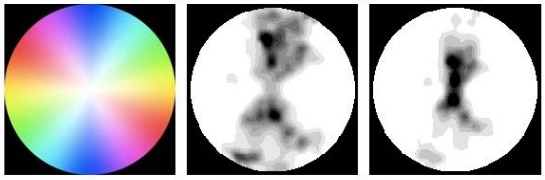

inca incp

A43_10x_f

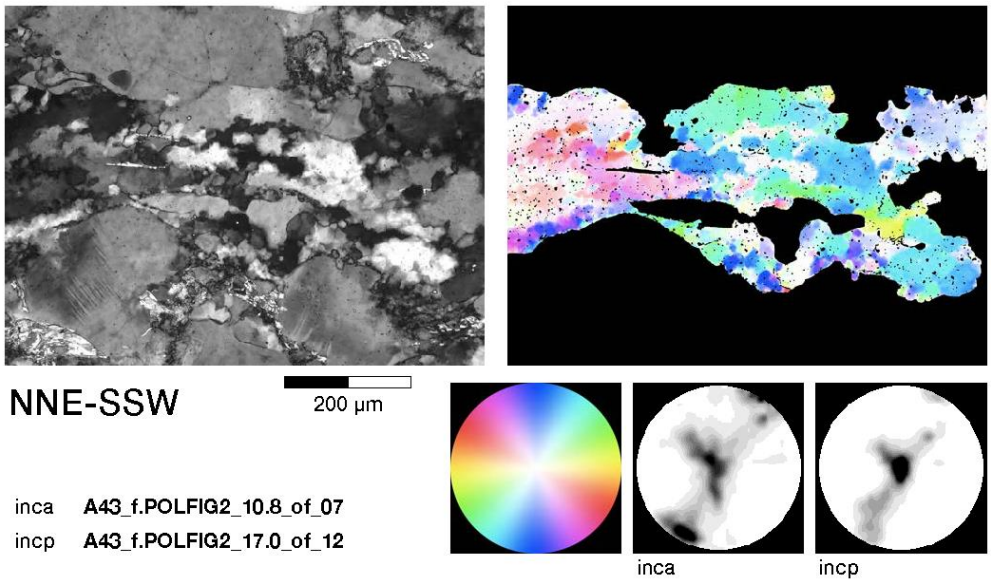

inca **A43_f.POLFIG2_10.8_of_07**
incp **A43_f.POLFIG2_17.0_of_12**

A43_10x_g

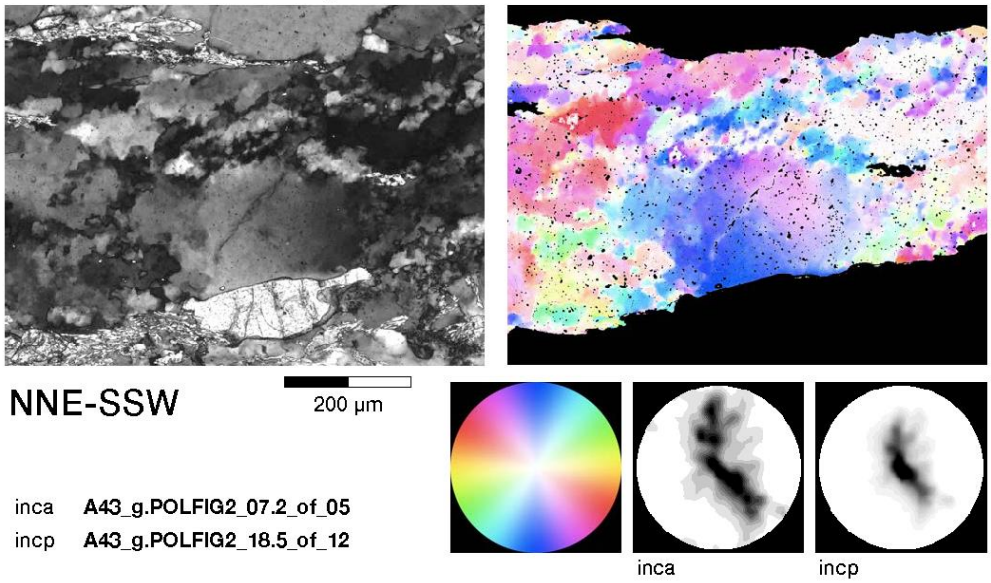

inca **A43_g.POLFIG2_07.2_of_05**
incp **A43_g.POLFIG2_18.5_of_12**

A44

A44_2.5x_b

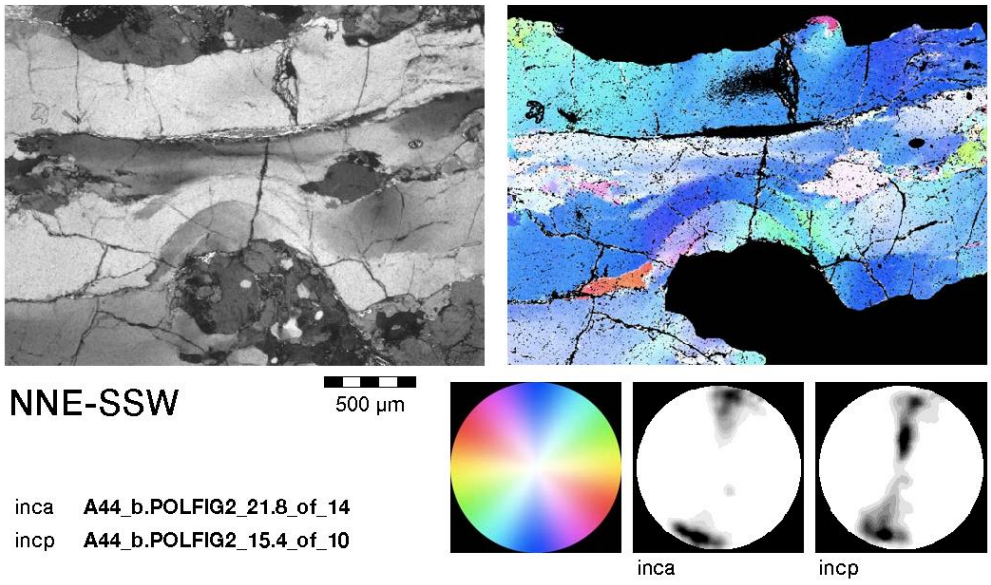

A44_2.5x_c

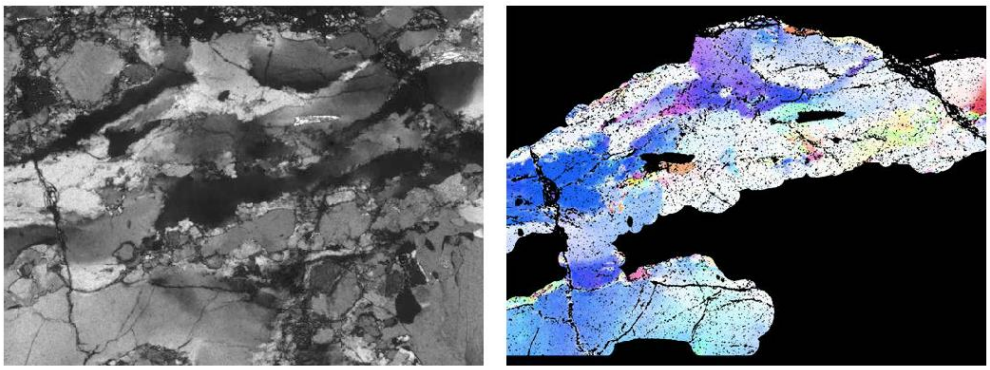

NNE-SSW

500 µm

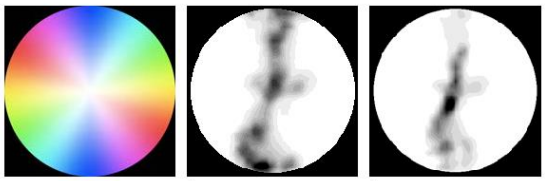

inca

incp

inca A44_c.POLFIG2_12.1_of_08

incp A44_c.POLFIG2_21.0_of_14

A44_2.5x_d

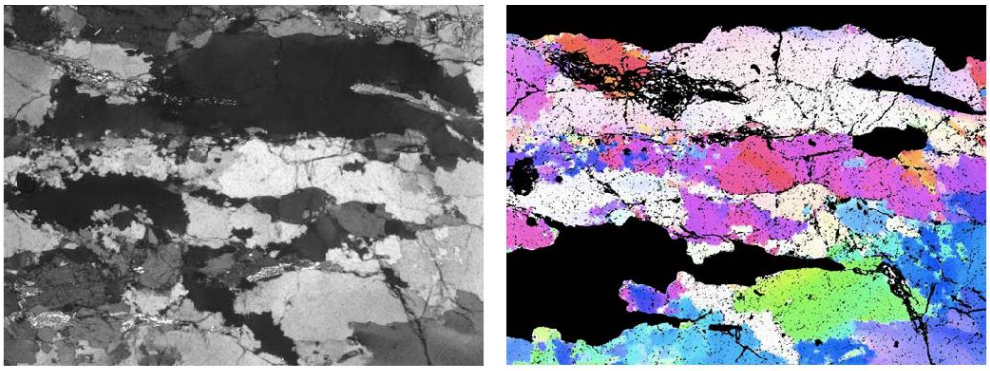

NNE-SSW

500 µm

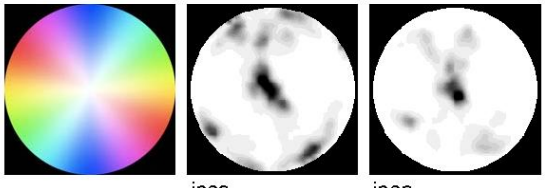

inca

incp

inca A44_d.POLFIG2_13.7_of_09

incp A44_d.POLFIG2_26.1_of_18

A44_5x_e

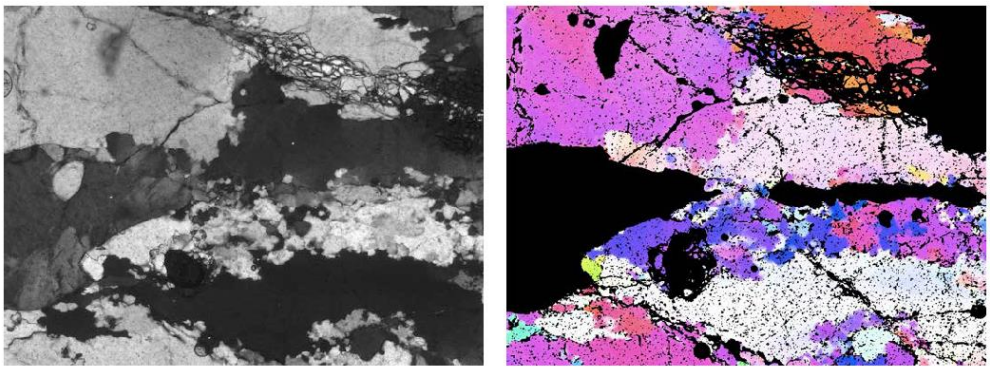

NNE-SSW

100 µm

inca A44_e.POLFIG2_27.4_of_18
incp A44_e.POLFIG2_26.3_of_18

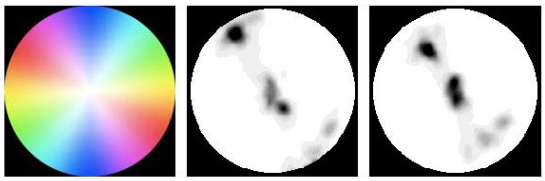

A44_10x_f

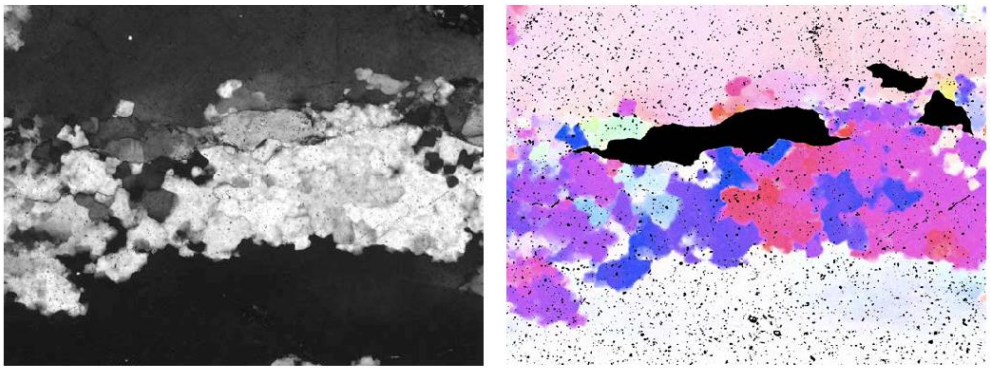

NNE-SSW

200 µm

inca A44_f.POLFIG2_41.5_of_28
incp A44_f.POLFIG2_57.3_of_38

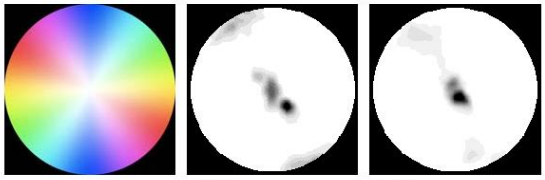

A44_10x_g

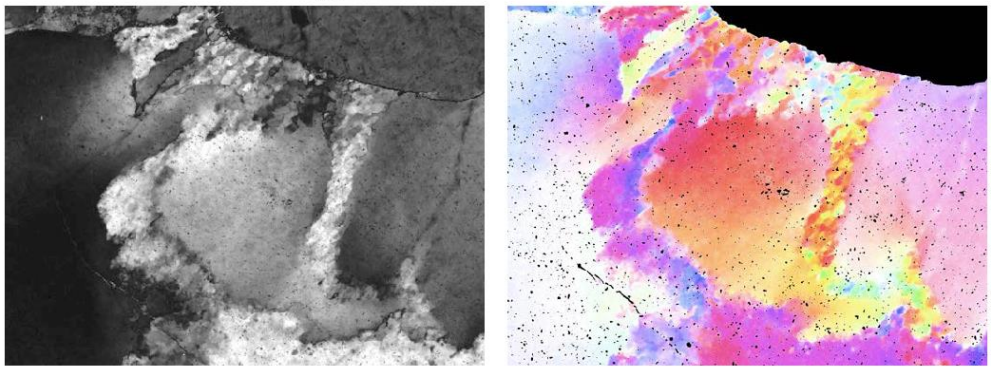

NNE-SSW

200 µm

inca **A44_g.POLFIG2_12.5_of_08**
incp **A44_g.POLFIG2_17.5_of_12**

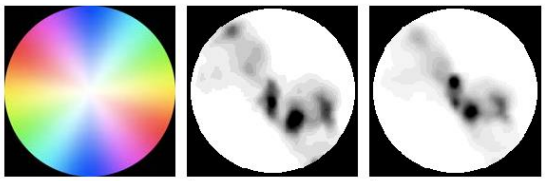

A44_10x_h

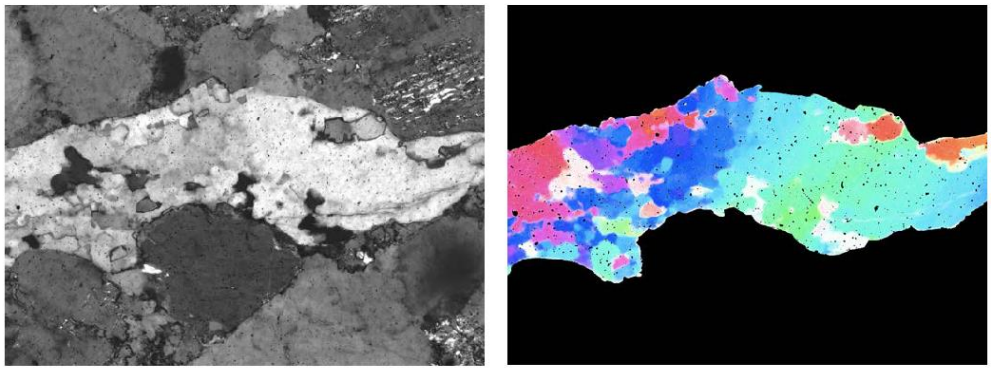

NNE-SSW

200 µm

inca **A44_h.POLFIG2_22.2_of_14**
incp **A44_h.POLFIG2_12.2_of_08**

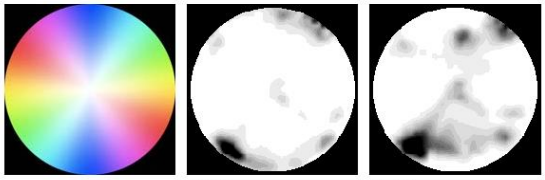

A44_10x_i

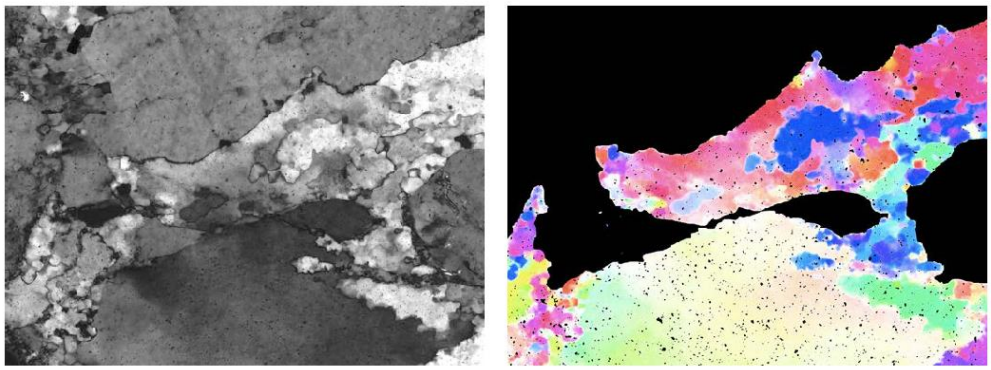

NNE-SSW

200 µm

inca A44_i.POLFIG2_24.1_of_16
incp A44_i.POLFIG2_29.5_of_20

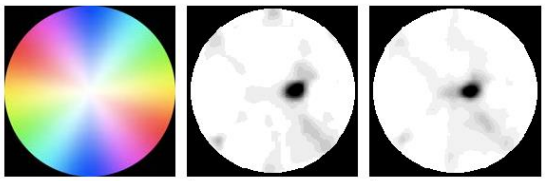

A45

A45_2.5x_a

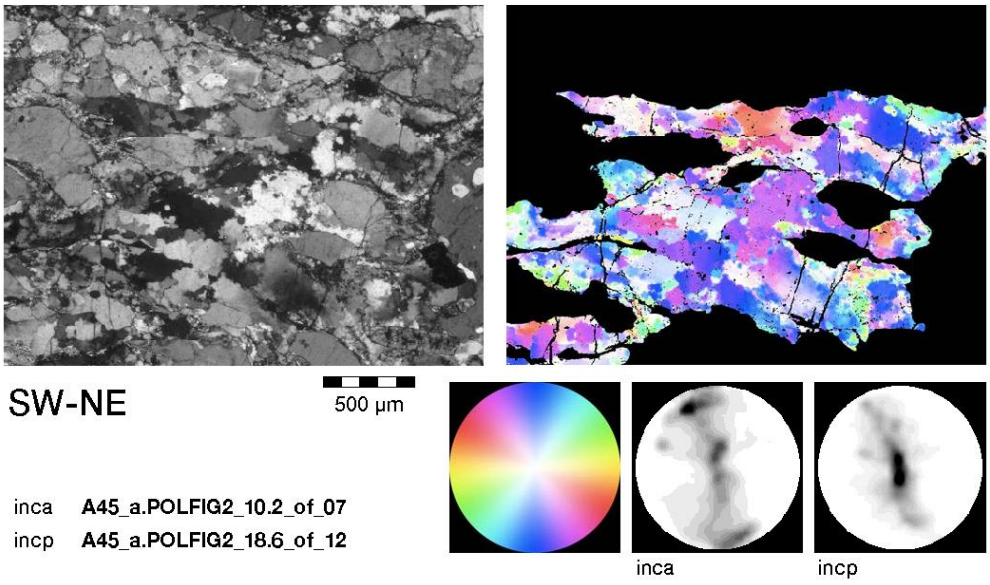

A45_5x_b

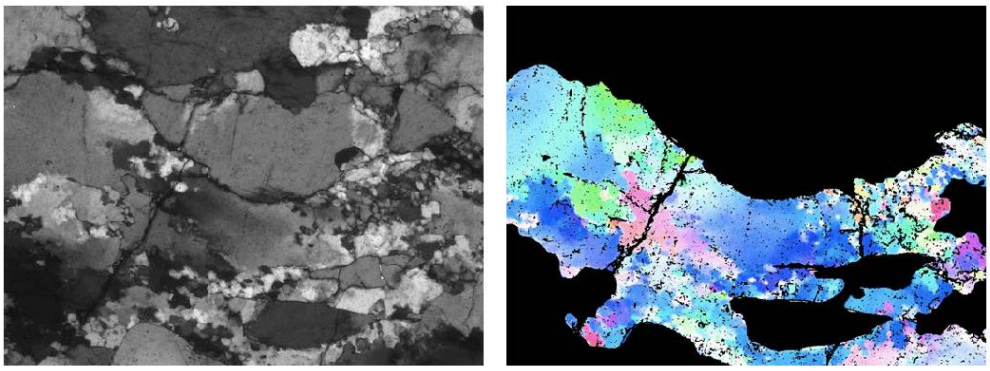

SW-NE

100 µm

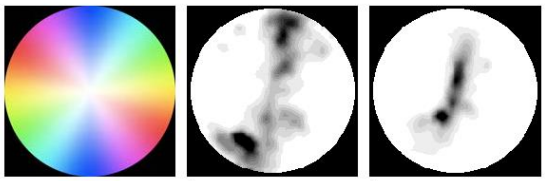

inca

incp

inca A45_b.POLFIG2_11.1_of_07
incp A45_b.POLFIG2_25.3_of_16

A45_5x_c

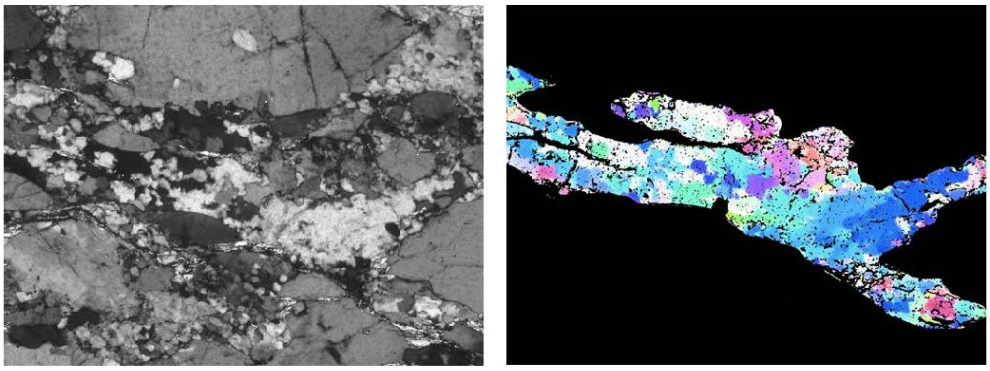

SW-NE

100 µm

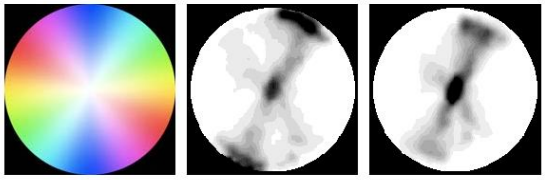

inca

incp

inca A45_5x_c.POLFIG2_10.3_of_07
incp A45_5x_c.POLFIG2_12.1_of_08

A45_5x_d

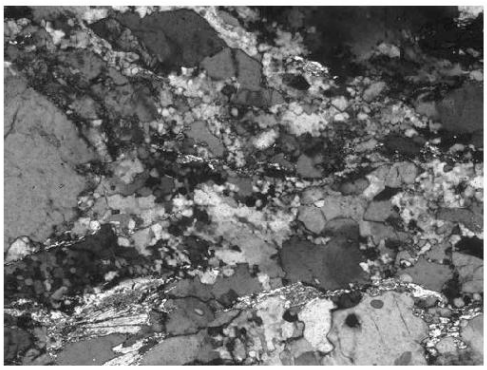

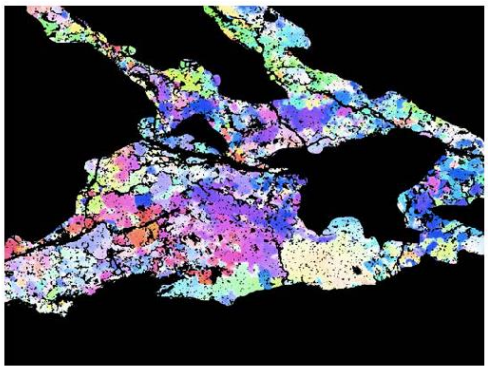

SW-NE

100 µm

inca A45_d.POLFIG2_06.2_of_04
incp A45_d.POLFIG2_13.5_of_09

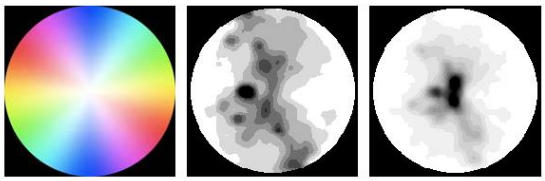

inca incp

A45_10x_e

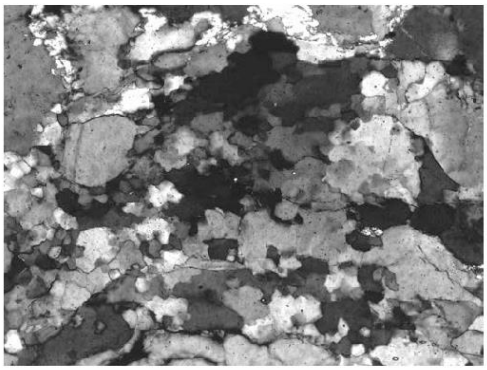

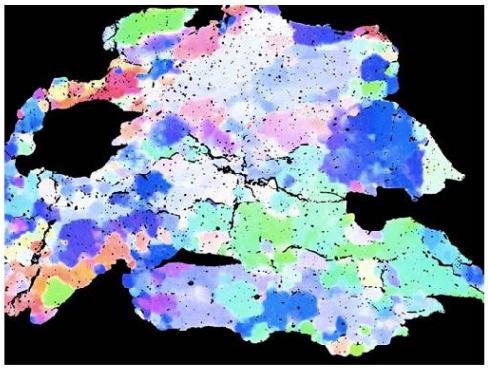

SW-NE

200 µm

inca A45_e.POLFIG2_11.1_of_07
incp A45_e.POLFIG2_18.3_of_12

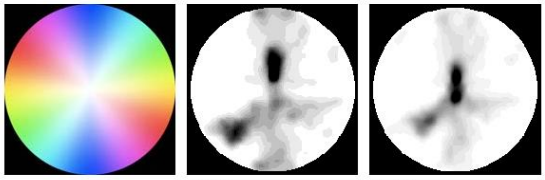

inca incp

A45_10x_f

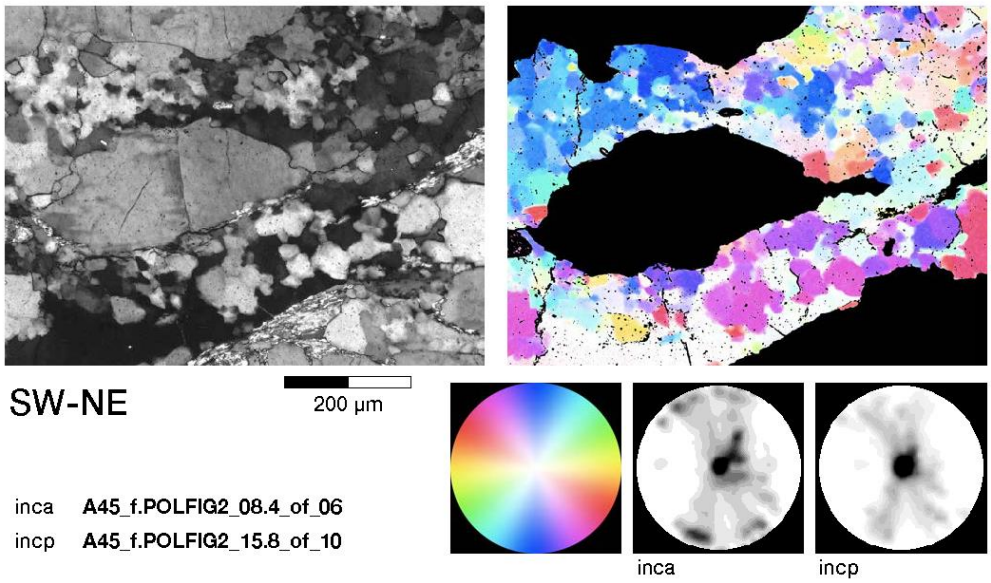

inca **A45_f.POLFIG2_08.4_of_06**
incp **A45_f.POLFIG2_15.8_of_10**

A46

A46_2.5x_a

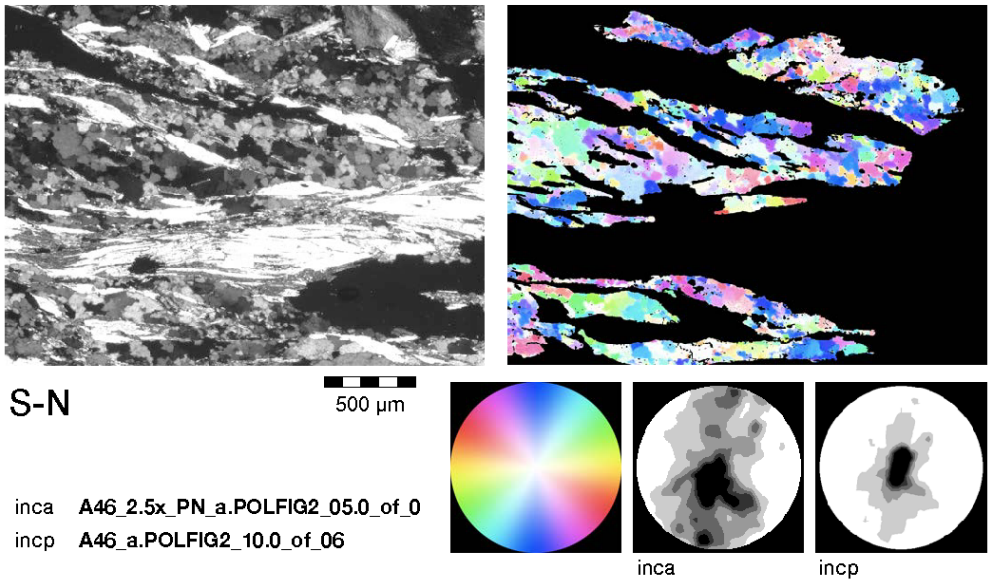

A46_2.5x_b

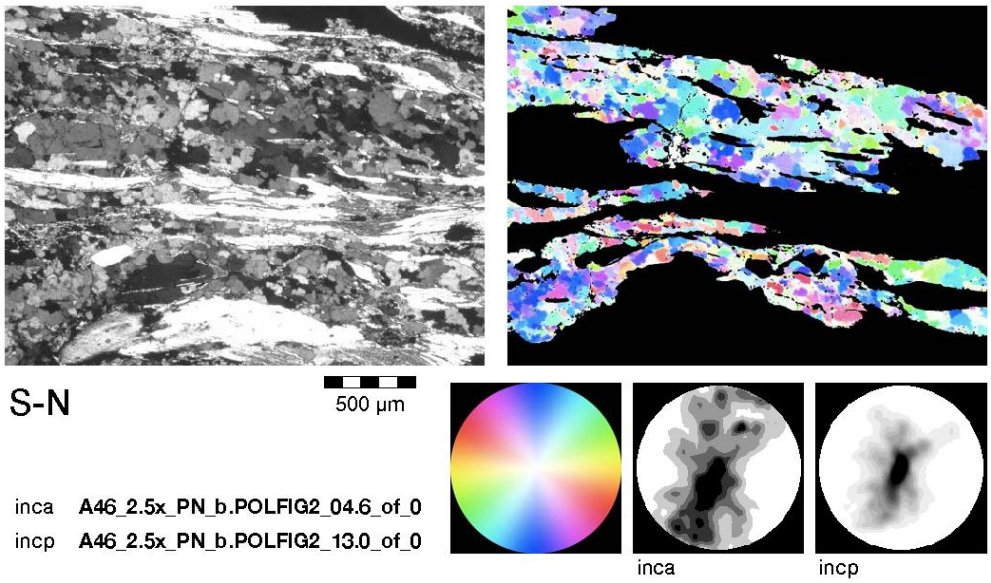

inca **A46_2.5x_PN_b.POLFIG2_04.6_of_0**
incp **A46_2.5x_PN_b.POLFIG2_13.0_of_0**

A46_2.5x_c

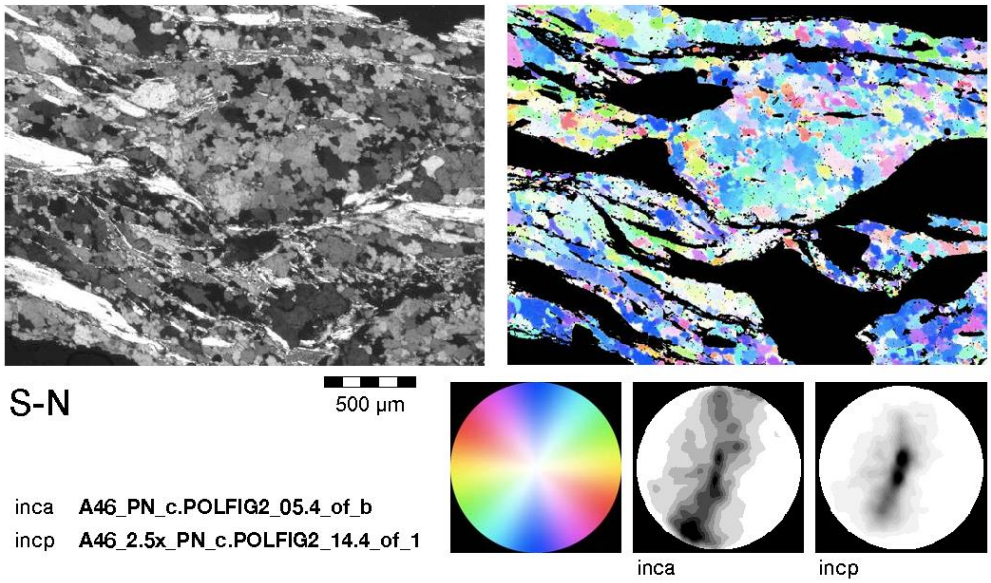

inca **A46_PN_c.POLFIG2_05.4_of_b**
incp **A46_2.5x_PN_c.POLFIG2_14.4_of_1**

A46_5x_d

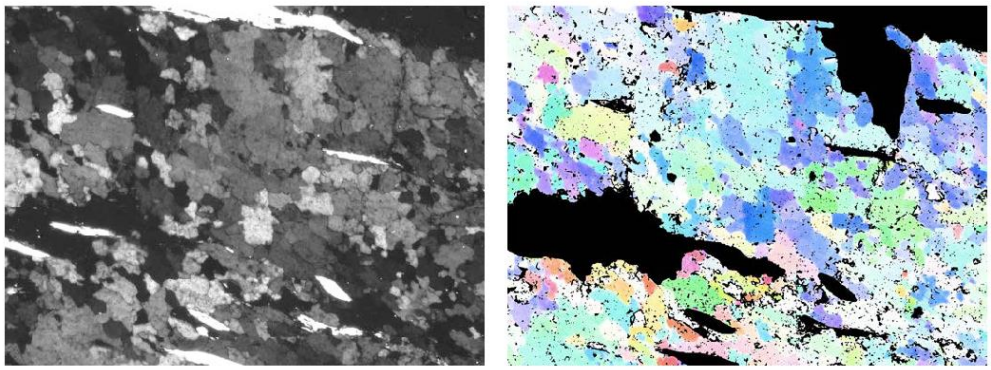

S-N

100 µm

inca A46_5x_PN_d.POLFIG2_13.3_of_09
incp A46_5x_PN_d.POLFIG2_18.5_of_12

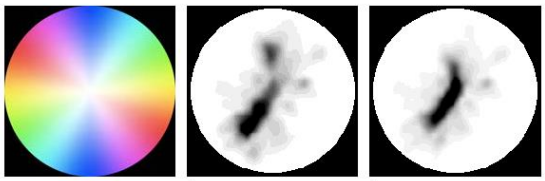

inca incp

A47

A47_5x_a

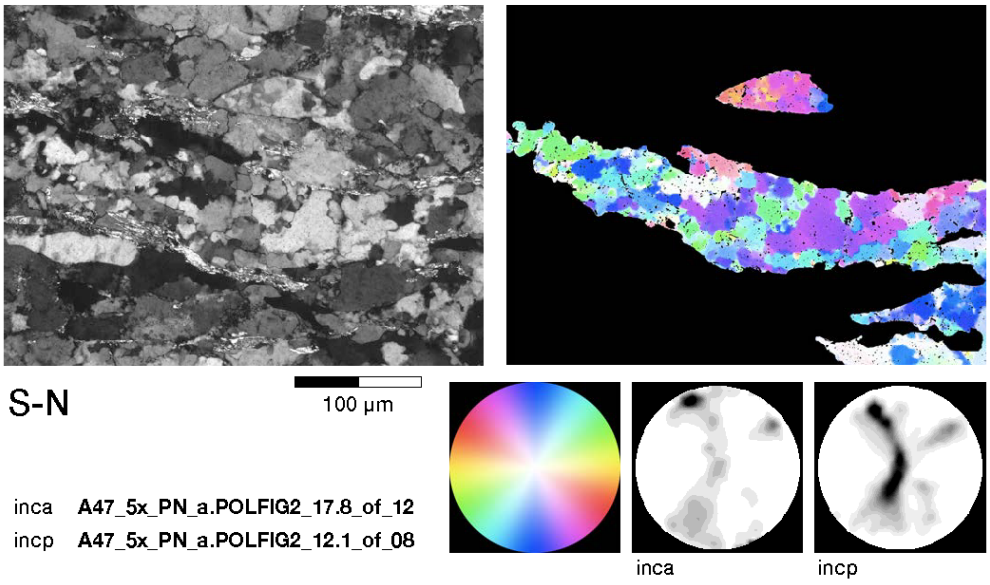

A47_5x_b

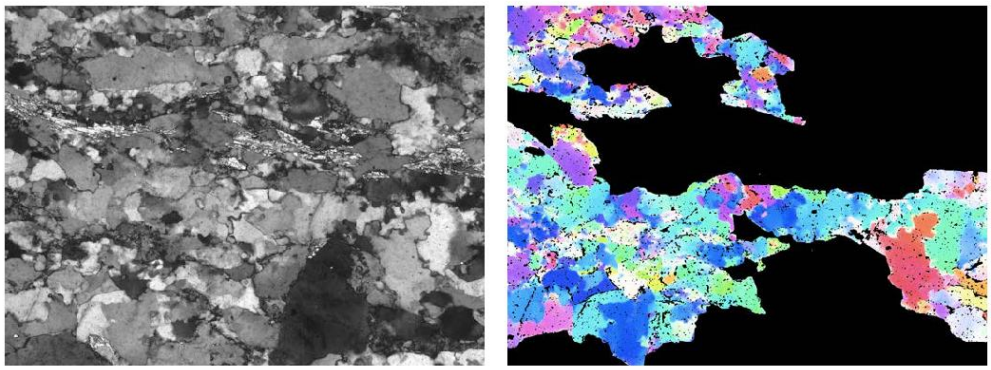

S-N

100 µm

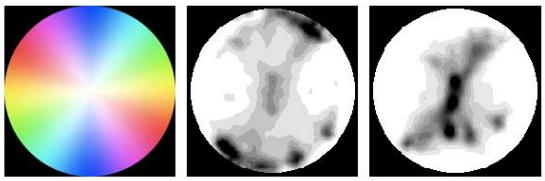

inca

incp

inca A47_5x_PN_b.POLFIG2_08.3_of_05

incp A47_5x_PN_b.POLFIG2_08.8_of_06

A47_5x_c

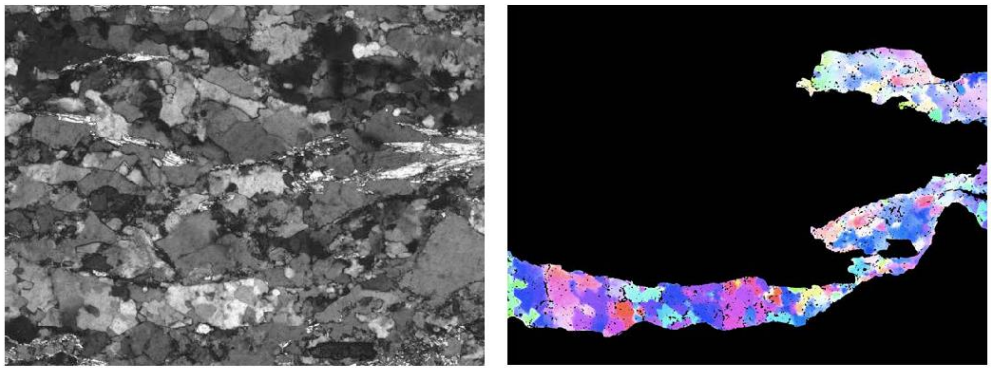

S-N

100 µm

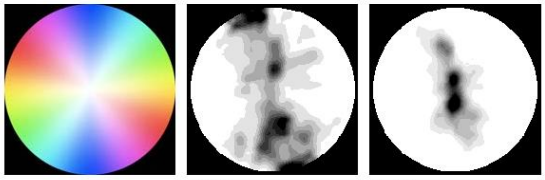

inca

incp

inca A47_5x_PN_c.POLFIG2_07.8_of_05

incp A47_5x_PN_c.POLFIG2_19.9_of_13

A47_5x_d

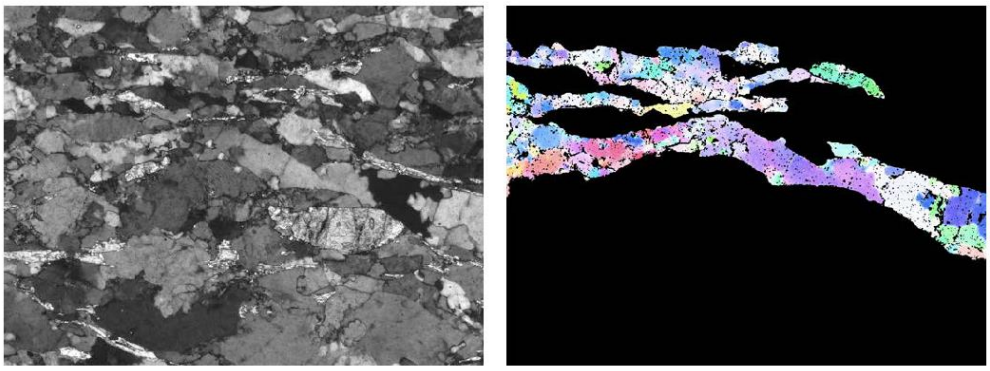

S-N

100 µm

inca

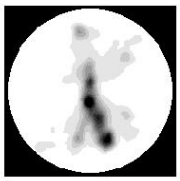

inca

incp A47_5x_PN_d.POLFIG2_17.2_of_11

incp

A47_5x_e

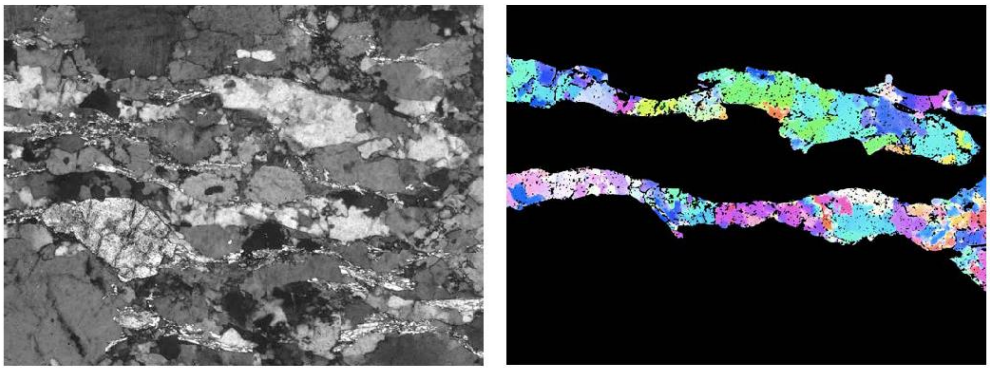

S-N

100 µm

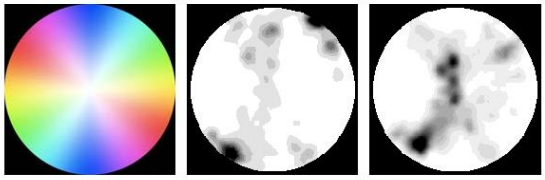

inca A47_5x_PN_e.POLFIG2_14.9_of_10

incp A47_5x_PN_e.POLFIG2_11.6_of_08

inca

incp

A47_5x_f

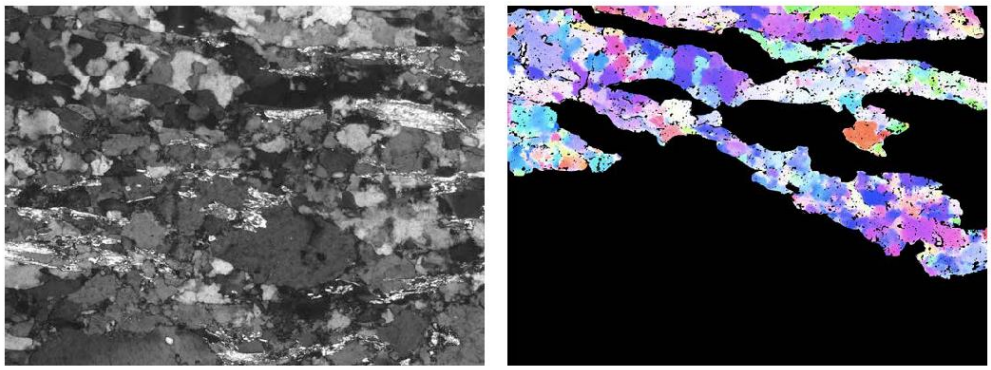

S-N

100 µm

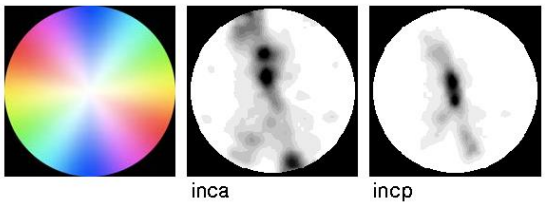

inca **A47_5x_PN_f.POLFIG2_09.9_of_07**
incp **A47_5x_PN_f.POLFIG2_22.8_of_15**

A47_5x_g

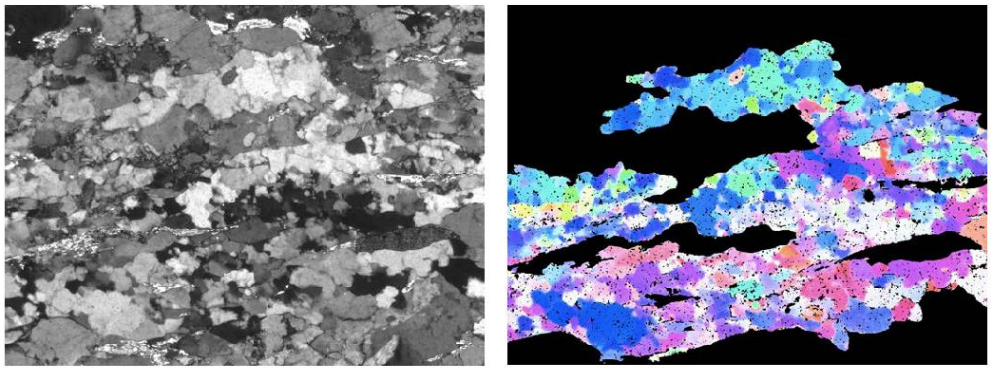

S-N

100 µm

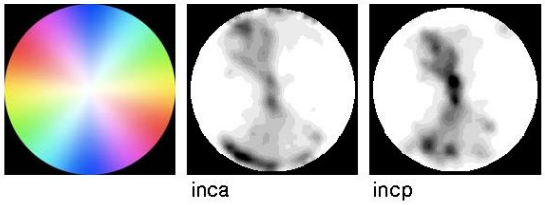

inca **A47_g.POLFIG2_09.7_of_07**
incp **A47_g.POLFIG2_09.8_of_07**

A48

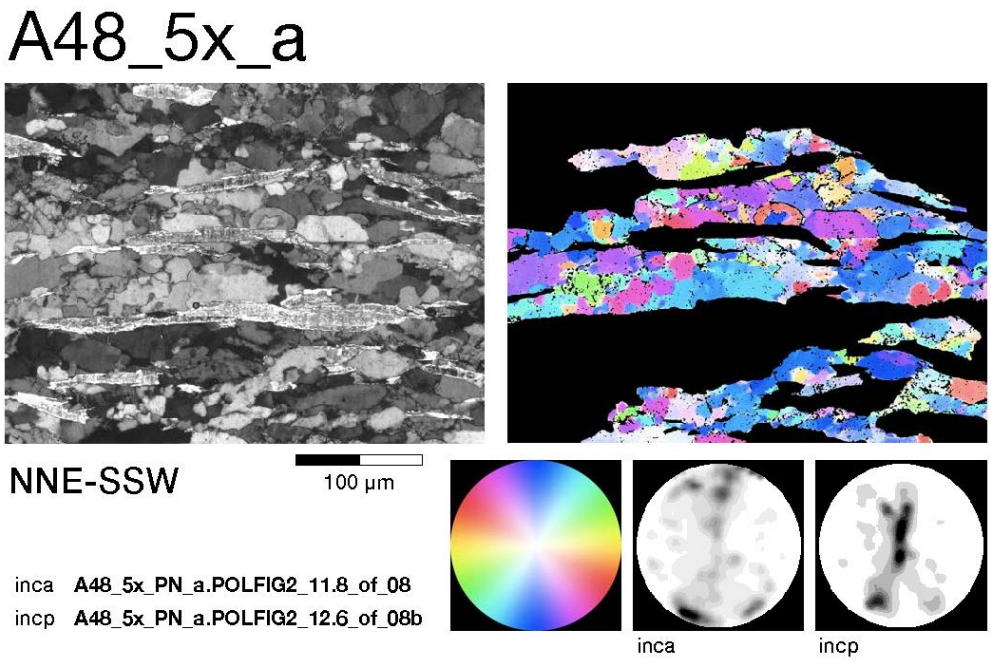

A48_5x_b

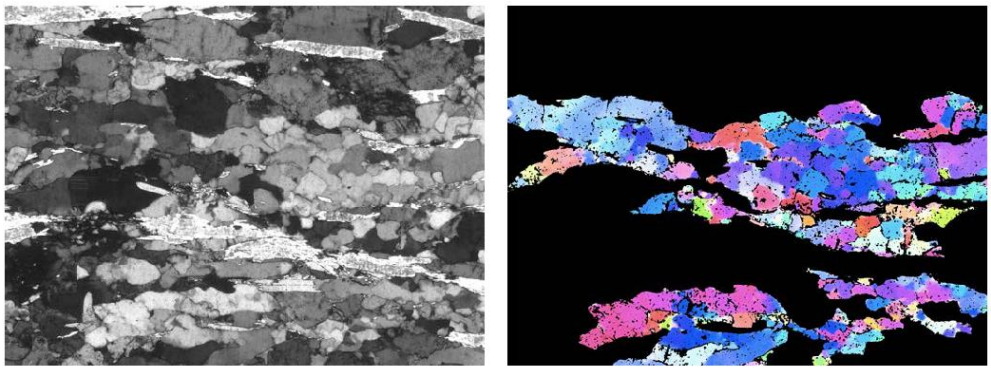

NNE-SSW

100 µm

inca A48_5x_PN_b.POLFIG2_08.6_of_05
incp A48_5x_PN_b.POLFIG2_20.1_of_14

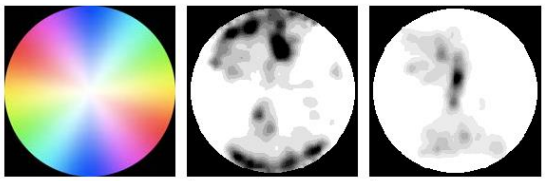

inca incp

A48_5x_c

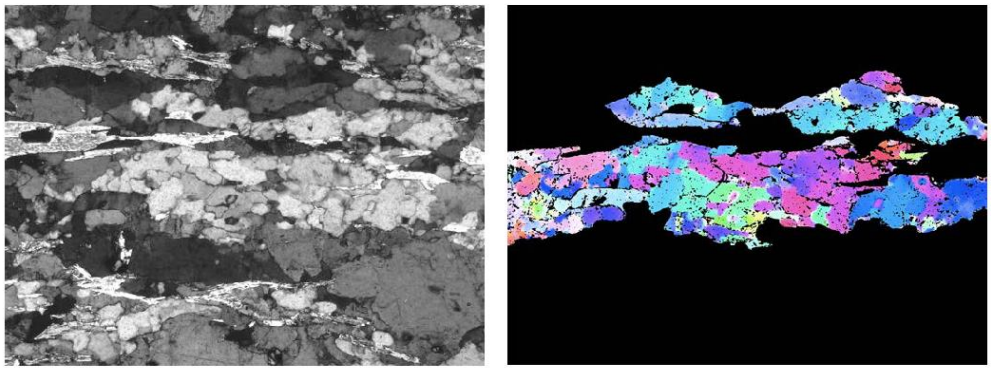

NNE-SSW

100 µm

inca A48_c.POLFIG2_15.9_of_10
incp A48_c.POLFIG2_09.3_of_06

inca incp

A48_5x_d

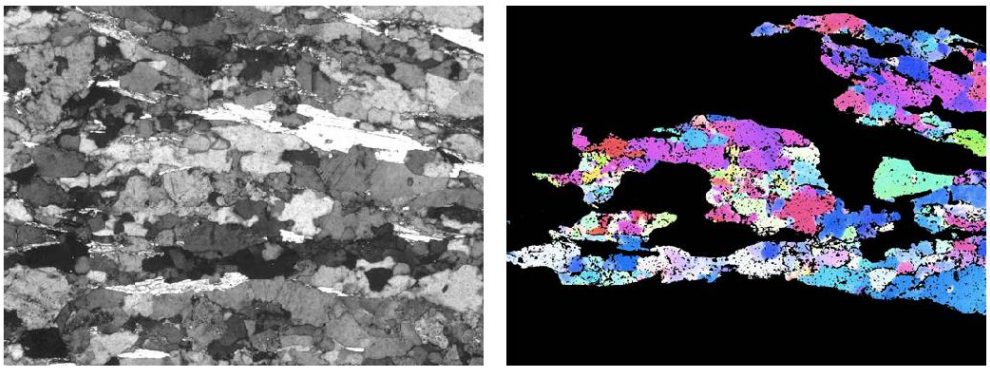

NNE-SSW

100 µm

inca A48_d.POLFIG2_13.0_of_08b
incp A48_d.POLFIG2_12.6_of_08b

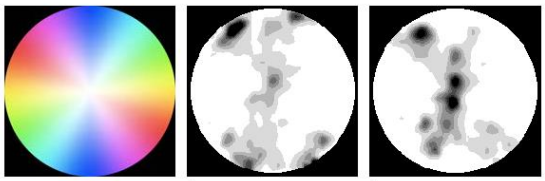

inca incp

A48_5x_e

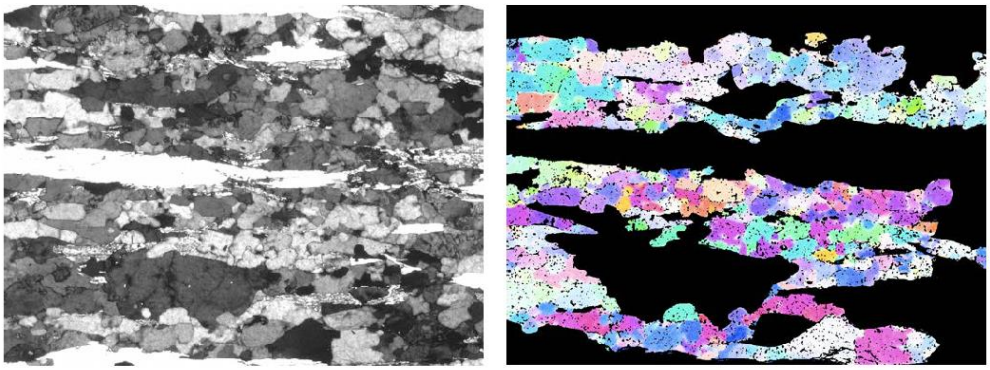

NNE-SSW

100 µm

inca A48_e.POLFIG2_08.5_of_06
incp A48_e.POLFIG2_07.9_of_05

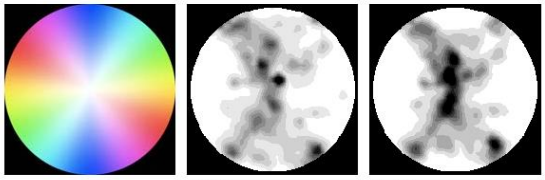

inca incp

A48_2.5x_h

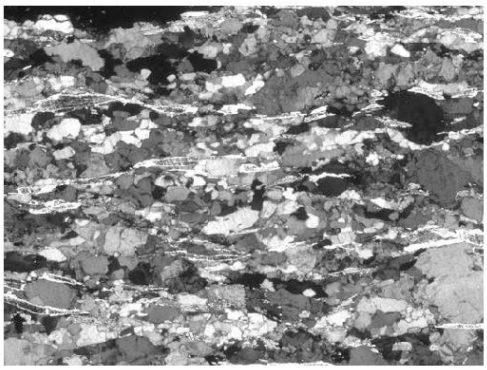

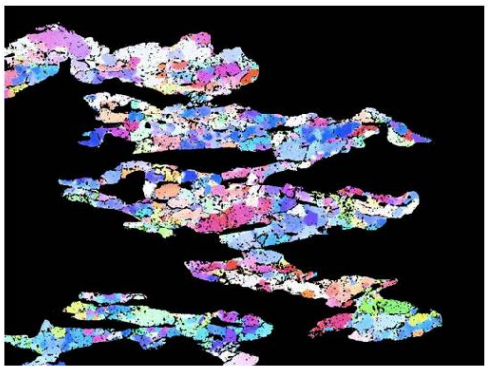

NNE-SSW

200 µm

inca **A48_h.POLFIG2_06.5_of_04**
incp **A48_h.POLFIG2_05.8_of_04**

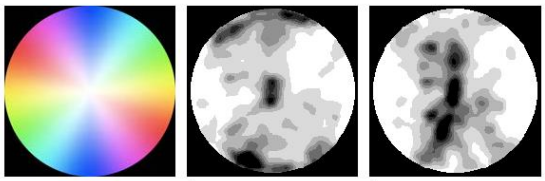

inca incp

C-AXIS POLE FIGURES PRODUCED WITH CIP ANALYSIS FOR EACH SAMPLE AND CIP SITE

A39 inca

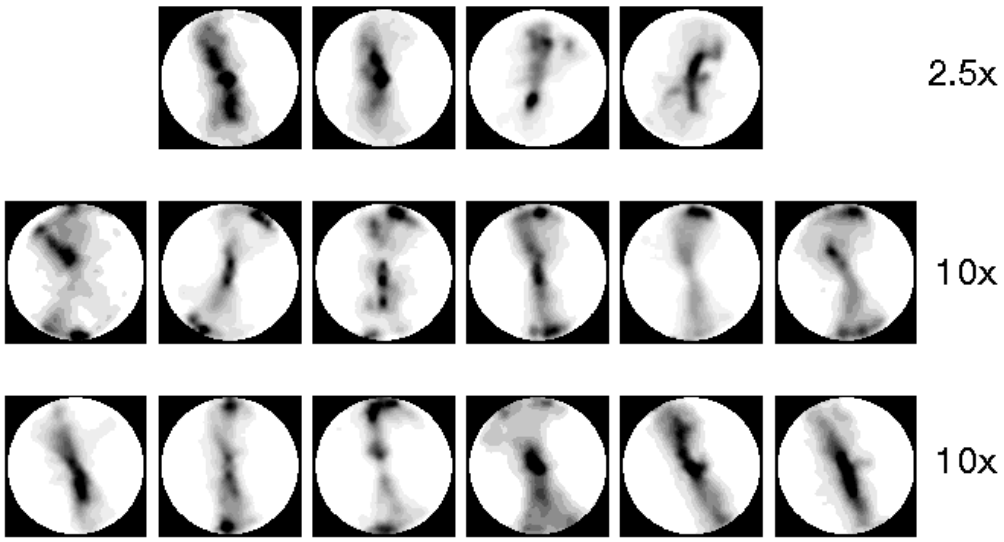

A39 incp

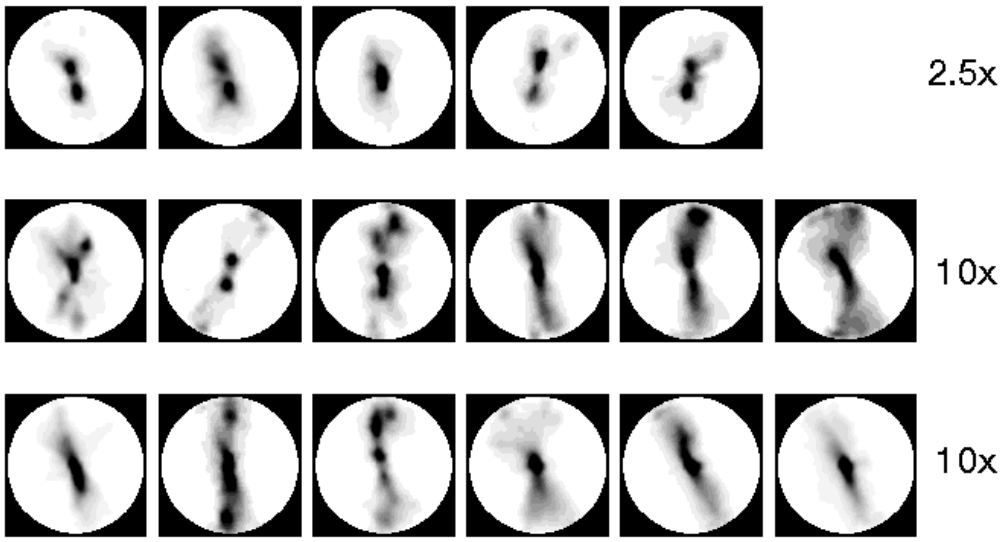

A40 inca

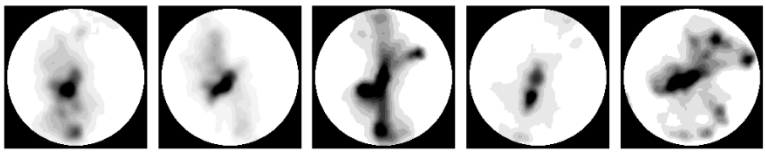

2.5x

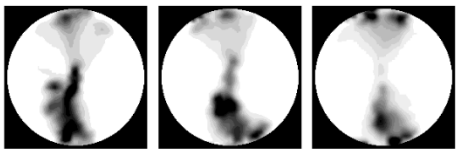

5x

A40 incp

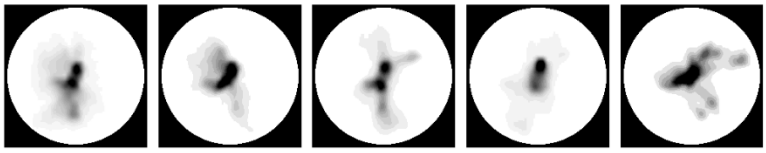

2.5x

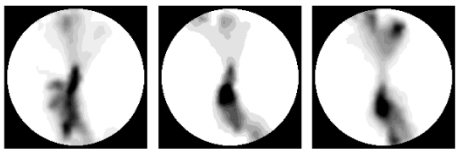

5x

A43 inca

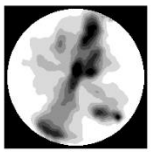

5x

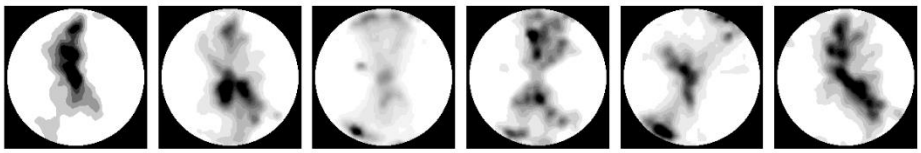

10x

A43 incp

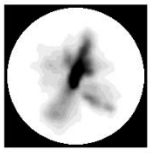

5x

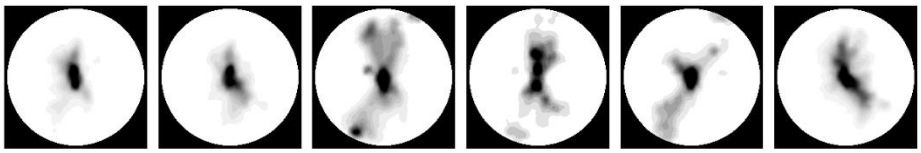

10x

A44 inca

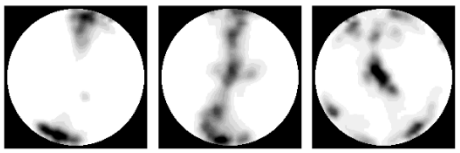

2.5x

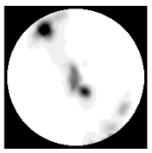

5x

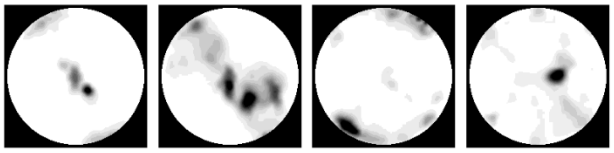

10x

A44 incp

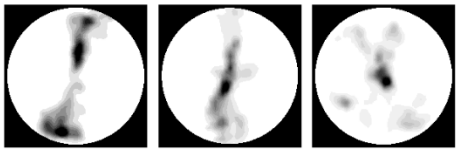

2.5x

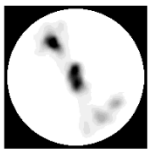

5x

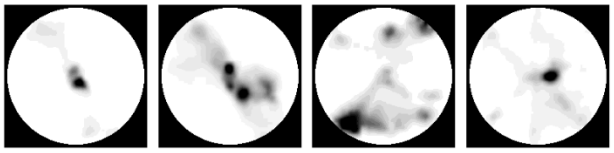

10x

A45 inca

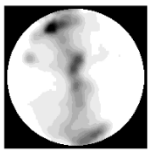

2.5x

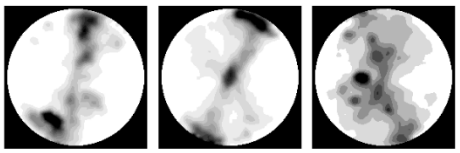

5x

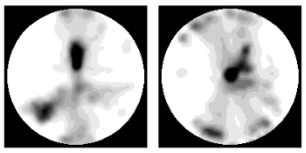

10x

A45 incp

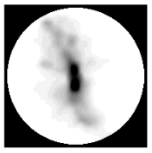

2.5x

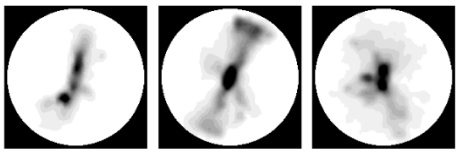

5x

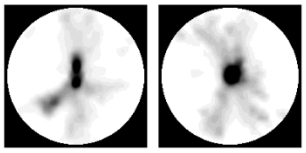

10x

A46 inca

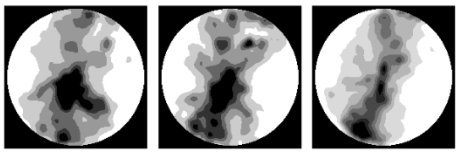

2.5x

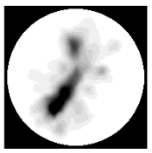

5x

A46 incp

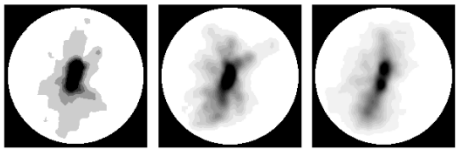

2.5x

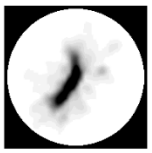

5x

A47 inca

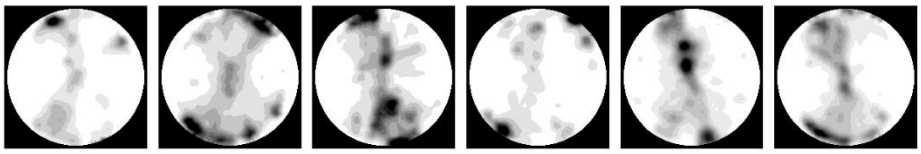

5x

A47 incp

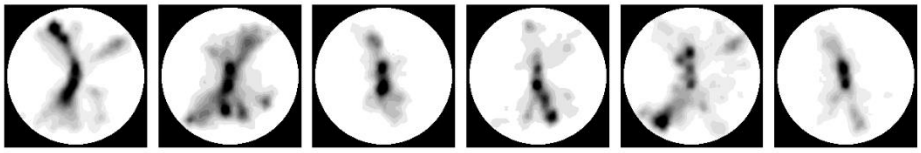

5x

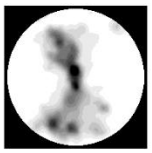

5x

A48 inca

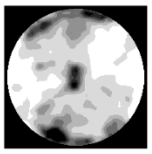

2.5x

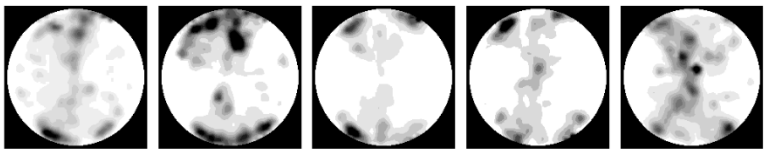

5x

A48 incp

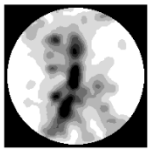

2.5x

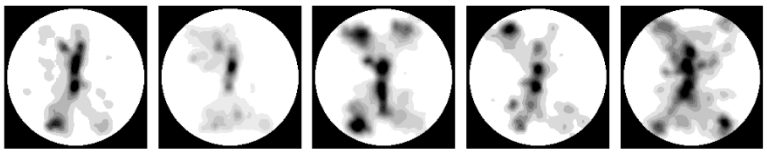

5x

Geological map of the northern part of Athos peninsula

GEOLOGICAL MAP OF THE NORTHERN PART OF THE ATHOS PENINSULA

Neofotistos Petros

DEPARTMENT OF GEOLOGY, ARISTOTLE UNIVERSITY OF THESSALONIKI

LEGEND

MAP UNITS

BASEMENT ROCKS

Serbo-Macedonian massif

Vertiskos Unit

Two mica gneiss: gray to brownish gray in colour, predominantly fine- to medium-grained, well-foliated and acquiring at places a flaser or even augen texture. Thickness varying from 500m at the eastern coast to 300m at the western coast, whereas the map unit fades out at the southwestern part of the study area.

Kerdyllion Unit

Biotite gneiss: dark gray to blueish gray in colour, medium- to coarse grained,well-foliated, exhibiting a lithological grading towards the amphibolite gneiss with biotite-amphibole-variations, frequenlt run-through by concordant, anatexitic, leucogneissic bodies and acquiring at places an augen texture. Thickness varying from 250-100m. Cross-marked areas indicate presence of leucogneissic bodies.

Amphibolite gneiss: dark green in colour, medium- to fine-grained, well-foliated, exhibiting a lithological grading towards the biotite gneiss with amphibole-biotite-variations, frequently run through by concordant, anatexitic, Leucogneissic bodies and acquining at places an augen texture. Thickness varying from 700 m at the eastern coast to 100-200m at the western coast. Cross-marked areas indicate presence of leucogneissic bodies.

Marble: white to blueish gray in colour, generally coarse-grained, well-foliated and intercalating with amphibolite gneis, calc-silicate and amphibole schists. Thickness >300m.

IGNEOUS ROCKS

Therma-Volvi-Gomati complex

Ultramafic/mafic rocks: dark to light green meta-peridotites, quite frequently serpentined, ljherzolitic at places subordinated by dark green pyroxenites, meta-gabbros and pale greenish white talc-schists. They appear in the form of up to tens of m in thickness elongate, lenticular bodies, tectonically emplaced within the other map units.

GEOLOGICAL / TECTONIC SYMBOLS

- Geological contact
- Tectonic contact / Shear zone
- Fault
- Fault inferred or concealed
- Strike and dip of S3 foliation
- Strike and dip of S3 foliation with the plunge of L3 lineation
- Strike and dip of S4 foliation
- Plunge of F3 fold axis
- Plunge of F4 fold axis

CROSS SECTIONS